37TH INTERNATIONAL MEETING

SMRA

Society for MR Angiography

2025

MRA Innovations Flowing Through Time

Budapest, Hungary

AUGUST 21–24, 2025

SMRA 2025 Scientific Chair:
Judit Csőre

SMRA President:
Jeremy Collins

SEMMELWEIS UNIVERSITY 1769

Free-breathing 3D high-resolution simultaneous grey-blood late gadolinium enhancement and MR angiography at 3T

Dongyue Si[1], Simon J. Littlewood[1], Michael G. Crabb[1], Karl P. Kunze[1,2], Claudia Prieto[1,3,4,5], René M. Botnar[1,3,4,5,6]

[1]School of Biomedical Engineering and Imaging Sciences, King's College London, London, UK, [2]MR Research Collaborations, Siemens Healthcare Limited, Camberley, UK, [3]School of Engineering, Pontificia Universidad Católica de Chile, Santiago, Chile, [4]Millennium Institute for Intelligent Healthcare Engineering, Santiago, Chile, [5]Institute of Biological and Medical Engineering, Pontificia Universidad Católica de Chile, Santiago, Chile, [6]Institute for Advanced Study, Technical University of Munich, Garching, Germany

Purpose: CMR is widely used for the assessment of different cardiac diseases, which can provide multi-contrast images including late gadolinium enhancement (LGE) for non-invasive myocardial tissue characterization[1], and cardiac MR angiography (CMRA) for anatomical information of coronary arteries[2]. A grey-blood (GB) phase-sensitive inversion recovery (PSIR) sequence has been proposed by nulling the signal of the blood pool using an inversion recovery (IR) preparation pulse, which demonstrated improved contrast for scar depiction than conventional bright-blood (BB) LGE imaging[3]. However, clinical LGE and CMRA images are usually acquired separately with unmatched spatial resolution and slice positions, limiting the joint evaluation of tissue characteristics and cardiac and coronary anatomy[4]. In this study, we propose a 3D free-breathing Grey-Blood and Bright-blOOd phase SensiTive inversion recovery (GB-BOOST) sequence for simultaneous assessment of coronary anatomy and myocardial tissue alterations.

Methods: The GB-BOOST research sequence acquires two interleaved 3D volumes prepared with IR and T2 preparation (T2prep) pulses respectively (**Fig.1**). The inversion time is set to null blood signal using a subject-specific Bloch equation simulation using T1 values measured by a scout post-contrast MOLLI T1 map. T2prep duration is 50ms. Image navigator (iNAV) enables free-breathing acquisition with 100% respiratory scan efficiency[5]. 2-point Dixon gradient echo using variable-density Cartesian trajectory with spiral-like profile order and golden-angle step is adopted with 5-fold undersampling[6]. Inline non-rigid motion corrected iterative SENSE reconstruction and water/fat separation is performed followed by offline high-dimensional patch-based low-rank (HD-PROST) denoising and PSIR reconstruction[7,8]. All experiments were performed on a 3T MR scanner (MAGNETOM Vida, Siemens Healthineers, Forchheim, Germany). Clinical breath-held 2D BB- and GB-PSIR, and free-breathing 3D GB-BOOST and 3D CMRA were sequentially acquired on 6 patients (2 males, 50±13 years) approximately 10-20 mins after the injection of contrast agent (GADOVIST® 1.0 (gadobutrol), Bayer Healthcare) at a dose of 0.15 mmol/kg. 3D sequences are performed in coronal orientation covering the whole heart with FOV = 340×340×~100mm^3, resolution = 1.2mm^3, TR/TE$_1$/TE$_2$ = 5.23/1.67/3.18ms. Qualitative analysis was performed to evaluate and compare the image quality of 3D T2prep GB-BOOST and 3D CMRA using a 4-point Likert scale (1: uninterpretable images, 2: poor image quality, 3: acceptable image quality, 4: excellent image quality).

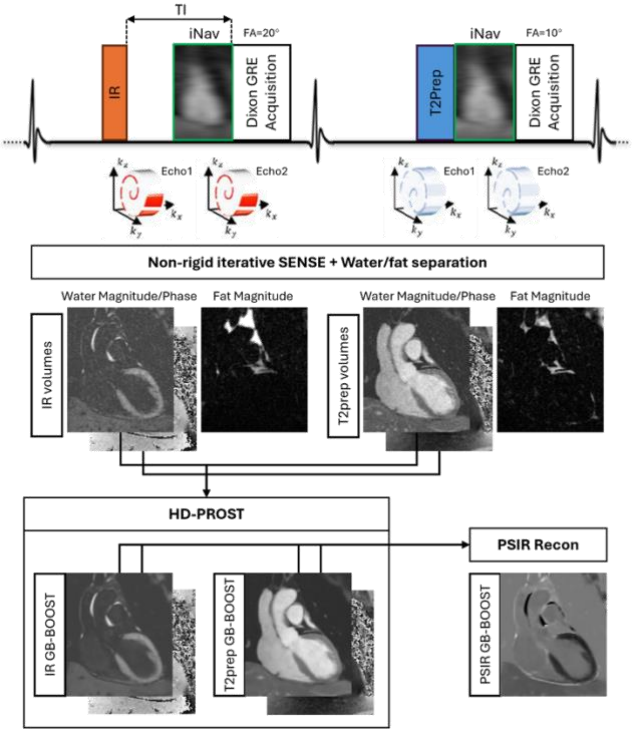

Fig.1. *Acquisition and reconstruction framework of GB-BOOST.*

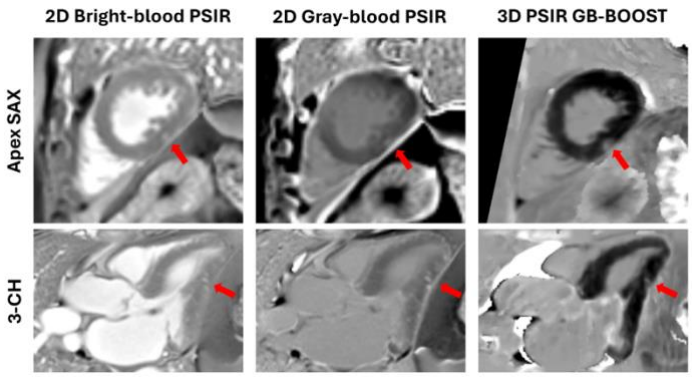

Fig.2. *Images of a 59-year-old female patient. Red arrows: scar*

Results: In-vivo experiments were successfully performed on the six subjects with scan time 9.8 ± 1.9 mins for 3D GB-BOOST and 4.8 ± 0.3 mins for 3D CMRA. 3D PSIR GB-BOOST was in good agreement with 2D BB- and GB-PSIR for detecting scar areas, providing excellent contrast between scar, blood and myocardium (**Fig.2**). According to visual comparison of curved planar reconstructions (**Fig.3**), 3D T2prep GB-BOOST provides image quality and contrast comparable with 3D CMRA for coronary visualisation. Qualitative image quality scores from all the patients of 3D T2prep GB-BOOST are also comparable with that of 3D CMRA (3.5 ± 0.8 vs 3.7 ± 0.5).

Discussion: We demonstrate the feasibility of simultaneous 3D GB-PSIR and 3D CMRA imaging in a single fast scan. 3D PSIR GB-BOOST achieves good contrast between scar, blood and myocardium, and 3D T2prep GB-BOOST is comparable with 3D CMRA.

References: 1.Kim RJ, et al. Circulation. 1999, 2.Stuber M, et al. JMRI. 2007, 3.Holtackers RJ, et al. JCMR. 2017, 4.Ginami G, et al. JCMR. 2017, 5.Henningsson M, et al. MRM. 2012, 6.Prieto C, et al. JMRI. 2015, 7.Cruz G, et al. MRM. 2017, 8.Bustin A, et al. MRM. 2019.

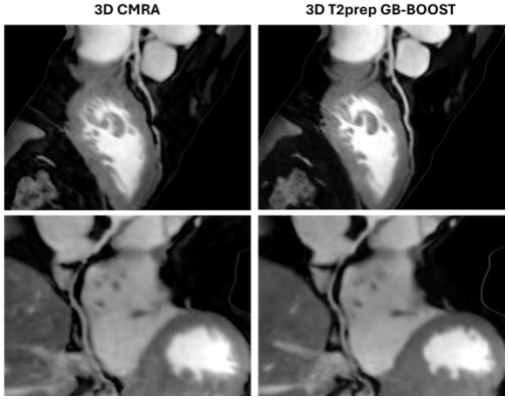

Fig.3. *Curved planar reconstruction of the patient in Fig.2.*

Dynamic Ferumoxytol-enhanced Imaging with 3D Whole-Ventricle Coverage using MR Multitasking

Xi Chen[1], Kim-Lien Nguyen[1,2,3,4], Anthony G. Christodoulou[1,2,4]

1. Department of Radiological Sciences, David Geffen School of Medicine at UCLA, Los Angeles, California, USA. 2. Physics and Biology in Medicine Graduate Program, David Geffen School of Medicine at UCLA, Los Angeles, California, USA. 3. Division of Cardiology, David Geffen School of Medicine at UCLA and VA Greater Los Angeles Healthcare System, Los Angeles, California, USA. Department of Bioengineering, UCLA, Los Angeles, California, USA.

Introduction: Ferumoxytol enhanced MRI allows fractional myocardial blood volume (fMBV) estimation using a multi-dose, slice-by-slice 2D cardiac-triggered T1 mapping protocol [1]. A dynamic contrast enhancement (DCE) single-dose protocol that is both 3D and cardiac-resolved may support fMBV by simplifying the workflow, improving spatial coverage, and potentially allowing for additional measurements such as cardiac function (from cine MRI) and blood flow (from DCE). In this work, we demonstrate the feasibility of a continuous-acquisition 3D whole ventricle cardiac phase-resolved dynamic ferumoxytol-enhanced MRI technique using the multitasking framework [2], which may provide the groundwork for a comprehensive assessment of myocardial perfusion in a single acquisition.

Methods: We used the multitasking framework to reconstruct a 5-way image tensor $I(x, t_1, t_2, t_3, t_4)$ where x represents 3D spatial coordinates, and t_1, t_2, t_3, t_4 represent: 1) cardiac motion, 2) respiration, 3) T1 recovery, and 4) DCE time dimensions, respectively. Dynamics along each dimension can be disentangled to enable motion resolved dynamic T1 mapping.

We performed in vivo experiments on 3 healthy subjects and 2 patients with ischemic heart disease at 3 T at rest. A patient with scar also had late gadolinium enhancement (LGE) and MOLLI scans. 3D multitasking images were acquired in the short-axis orientation with in-plane resolution = 1.7mm, slice thickness = 8 mm, and number of slices = 16–22, TR/TE=3ms/1.4ms, IR spacing=2160ms. Ferumoxytol 2 mg/kg was slowly infused starting 5 sec into the scan. Total acquisition time was 3 min.

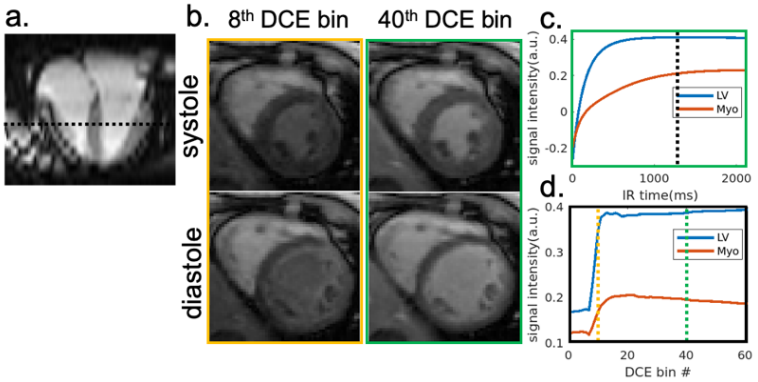

Fig.1. A healthy subject. a) A long-axis reformat image. b) End of systole and diastole short-axis images of the 8th and 40th DCE bins. The average signal intensity curves in LV and Myo ROIs along c) T1 recovery and d) DCE dimensions.

Results and Discussion: Fig.1 shows a healthy subject's long-axis reformat image (Fig.1a) and the end of systole and diastole images at two different DCE phases for one short-axis slice (Fig.1b), and average signal intensity curves in two ROIs drawn in the left ventricle (LV) and myocardium along the T1 recovery (1c) and DCE dimensions (Fig.1d respectively. Fig.2 shows the LGE, MOLLI T1w and T1map, and 3D multitasking T1w and T1map of a patient. The abnormally high T1 in multitasking T1 map, also seen to a lesser extent on the MOLLI images, correlates with scars shown in LGE, where lack of ferumoxytol-induced T1 shortening may indicate no blood supply.

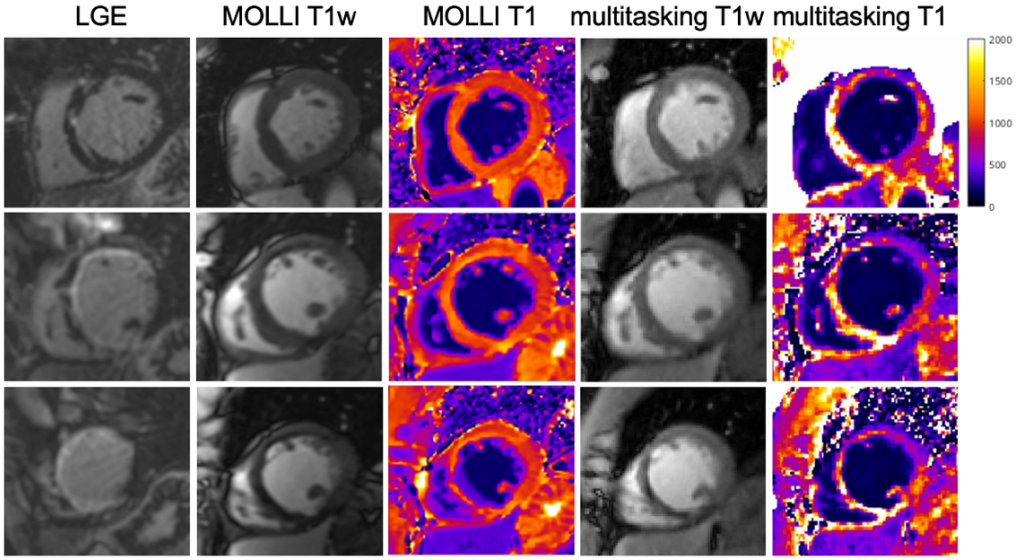

Fig.2. a) 2D LGE, MOLLI T1w, T1 map, and 3D multitasking T1w and T1map of a patient.

Conclusion: We proposed a dynamic ferumoxytol-enhanced cardiac MRI technique which has 3D whole ventricle coverage and is non-ECG gated and free-breathing. Preliminary results also show potential for detecting scar.

References: [1] Colbert, C.M., et al. *J Magn Reson Imaging* 2021. [2] Christodoulou, A.G., et al. *Nat Biomed Eng* 2018.

Saturated multi-delay renal arterial spin labeling technique at 5T ultrahigh-field MR: A comparative study with 3T MR

Xinyu Tong[1], Chen Chen[2], Zihan Ning[1,3], Ne Yang[4], Shuheng Zhang[2], Shuo Chen[2], Zuo-xiang He[5], and Xihai Zhao[1]

[1] School of Biomedical Engineering, Tsinghua University, Beijing, China, [2] Shanghai United Imaging Healthcare, Shanghai, China
[3] King's College London, Longdon, United Kingdom, [4] United Imaging Research Institute of Intelligent Imaging, Beijing, China,
[5] School of clinical medicine, Tsinghua University, Beijing, China

Purpose: The saturated multi-delay renal arterial spin labeling (SAMURAI) sequence enables simultaneous T1 quantification and renal perfusion measurement within a single scan at 3T [1]. This technique has demonstrated excellent reproducibility and holds significant potential for clinical applications [2]. Ultrahigh-field MR offers higher signal intensity and longer relaxation times, which may enhance ASL imaging [3]. This study aims to evaluate the feasibility and repeatability of the SAMURAI technique at 5T and compare image quality and renal perfusion measured by 3T and 5T.

Methods: ***Sequence design***: The SAMURAI sequence at the 5T retains the overall structure of such sequence at 3T. It consists of a pre-saturation pulse followed by a nonselective or slice-selective inversion pulse for FAIR ASL acquisition and Look-Locker spoiled gradient echo readout. To mitigate B1 inhomogeneity at 5T, a renal-specific symmetric shimming strategy, an optimized four-pulse saturation scheme, and an adiabatic inversion pulse were applied. ***In-Vivo experiment***: Ten healthy volunteers (27.5±4.7 years old, 4 males) were recruited with informed consent. The experiments were conducted on a 3T MR scanner (Ingenia CX, Philips Healthcare, The Netherlands) with a 16-channel dStream Torso coil and a 12-channel embedded posterior coil, and a 5T MR scanner (Jupiter, United Imaging Healthcare, Shanghai, China) with 24-channel Superflex body and 48-channel spine coils. The SAMURAI sequence was acquired once at 3T and twice at 5T during free breathing. ***Image analysis***: Image analysis was performed using Matlab R2022a following the SAMURAI pipeline, with modifications for 5T. Non-rigid registration employed a PCA-based group-wise strategy with B-spline interpolation. T1 maps were estimated via dictionary search, and voxel-wise T1 values were integrated into a stepwise kinetic model to quantify renal blood flow (RBF), arterial bolus arrival time (aBAT), and tissue bolus arrival time (tBAT). Signal-to-noise ratio (SNR) and corticomedullary contrast-to-noise ratio (CNR) were calculated from perfusion weighted images at different inversion times. ***Statistical analysis***: Differences between perfusion characteristics were assessed using paired t-tests, while repeatability at 5T was evaluated via the Intraclass Correlation Coefficient (ICC). All statistical analyses will be performed using SPSS 27.0.

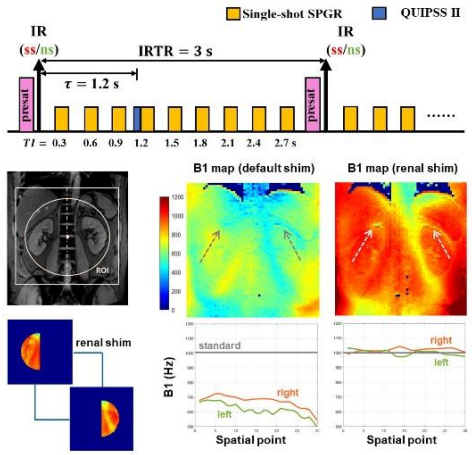

Figure 1. The sequence design and renal shim scheme at 5T

Results: All parameters measured at 5T exhibited good repeatability (ICC: T1: 0.868, RBF: 0.976, aBAT: 0.947, tBAT: 0.771, all *P*<0.001). Compared to 3T, cortical T1 was significantly higher at 5T (1410.9±77.5ms vs. 1009.2±81.4ms, *P*<0.001). Cortical RBF (329.3±42.9 mL/100g/min vs. 332.2±51.1 mL/100g/min, *P*=0.520) and aBAT (178.6±98.9ms vs. 191.1±72.0ms, *P*=0.492) showed no significant difference between 3T and 5T, while tBAT was significantly lower at 5T (2119.0±253.4ms vs. 2248.9±174.0 ms, *P*=0.021). All three perfusion parameters exhibited significant correlations between 3T and 5T (RBF: r=0.93, *P*<0.001; aBAT: r=0.61, *P*=0.005; tBAT: r=0.47, *P*=0.039). Additionally, the mean SNR (6.3±1.8 vs. 4.3±0.8, *P*=0.012) and CNR (4.7±1.5 vs. 2.2±0.5, *P*=0.002) were significantly higher at 5T than those at 3T.

Discussion and Conclusion: In this study, we demonstrated the feasibility and repeatability of the SAMURAI technique at 5T. Excellent agreement was found in the measurements of RBF between repeated scans and between 3T and 5T, indicating the robustness of multi-delay RBF measurements at 5T using SAMURAI. The lower tBAT at 5T may be influenced by field inhomogeneity affecting inversion pulse efficiency, leading to faster signal decay at long TI in some subjects. However, the accuracy of tBAT remains uncertain due to the lack of gold standard. The significantly improved SNR and CNR at 5T (1.5-2 times higher) may reduce the number of dynamics required, further shortening ASL scan time. **In conclusion, renal ASL using the SAMURAI sequence at 5T is feasible and repeatable, with excellent agreement with 3T and improved SNR and CNR, enhancing its potential for high-field renal imaging.**

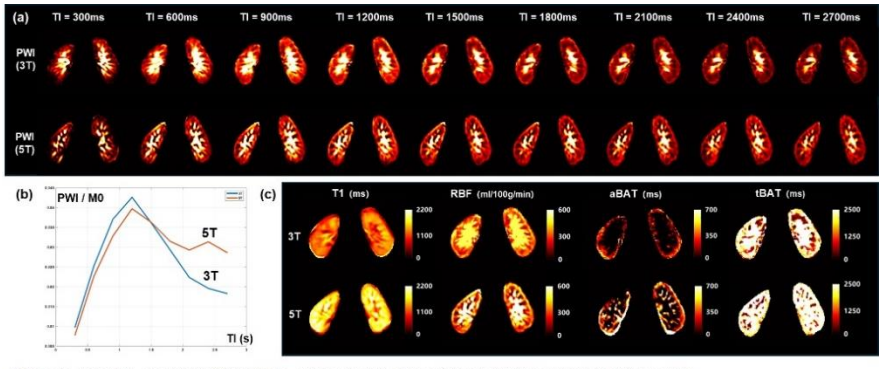

Figure 2. Example of PWI at different TIs, along with T1, RBF, aBAT, and tBAT measured at 3T and 5T.

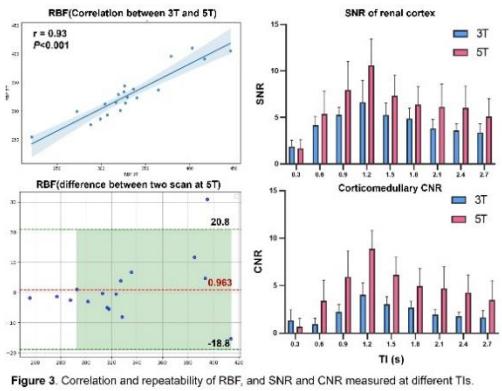

Figure 3. Correlation and repeatability of RBF, and SNR and CNR measured at different TIs.

References: [1] Ning Z, et al. Magn Reson Med, 2022. [2] Tong X, et al. Magn Reson Imaging, 2024. [3] Li X, et al. Magn Reson Med, 2018.

Deep learning accelerated reconstruction of radial whole-heart Ferumoxytol-enhanced free-running ultra-short echo time cardiac MRI

Kevin B Borsos[1,2], Augustin C Ogier[2], Christopher W Roy[2], Matthias Stuber[1,2,3], Milan Prša[4], Thomas Küstner[5], Jérôme Yerly[2,3]
[1]University of Lausanne, Lausanne CH, [2]Department of Radiology, Lausanne University Hospital, Lausanne CH, [3]Centre for Biomedical Imaging (CIBM), Lausanne CH, [4]Women, Mother and Child Department, Lausanne University Hospital, Lausanne CH, [5]Medical Image Data Analysis Lab (MIDAS.lab), University Hospital Tübingen, Tübingen DE

Purpose: Self-gated free-running cardiac magnetic resonance (CMR) constitutes a valuable alternative to traditional CMR methods, circumventing the need for breath holds and/or gating devices [1]. Ultra-short echo time (UTE) variants of free-running CMR [2] provide relief from high-velocity flow dephasing artifacts that can compromise image quality and obscure fine structures. Current reconstruction methods [3,4] rely on time-intensive iterative compressed sensing (CS) algorithms to produce diagnostic image quality. In this study we present and test a neural network to replace the CS reconstruction aiming to reduce reconstruction times of free-running UTE data from hours to minutes.

Methods: Training data was acquired using a 3D radial phyllotaxis UTE sequence in 50 pediatric patients with repaired congenital heart disease (CHD) imaged at 1.5T following intra-venous administration of Ferumoxytol. As fully sampled data is impractical to acquire, ground truths were taken to be CS images reconstructed using an XD-GRASP based algorithm [1,3] with motion-state binning to resolve respiratory and cardiac motion. A previously presented residual neural network [5] – initially trained on free-running Ferumoxytol-enhanced gradient-echo data, was fine-tuned to the UTE data (train/validation/test subjects=32/8/10). Reconstructed images were evaluated based on structural similarity index (SSIM), peak-signal-to-noise ratio (PSNR), mean-squared error (MSE) and reconstruction time. In addition, images were reformatted to generate short-axis view cines from which left ventricular ejection fraction (LVEF) was measured manually. Measurements were compared with a Bland-Altman analysis and paired t-test, where $p < 0.05$ was considered statistically significant.

Results: For a full 5D volume, our model achieved a mean reconstruction time of 3.4 minutes compared to 146 minutes with CS; a representative case from both methods is shown in Figure 1. Our neural network approach achieves a mean SSIM of 0.889, PSNR of 33.1 dB and MSE of 5.1×10^{-4} across the 10 test subjects indicating good agreement with ground truth CS images. Furthermore, Bland-Altman analysis of the LVEF of test subjects revealed a low bias of –0.38% between deep learning and CS reconstructions with narrow limits of agreement (-3.06% to 2.28%); p-value = 0.42, $R^2 = 0.98$.

Discussion: In this work we present a deep learning approach for the rapid reconstruction of Ferumoxytol-enhanced free-running UTE CMR data. Our model provides quantitatively comparable image quality to CS while reducing the reconstruction time by more than 40-fold. Moreover, the low bias and narrow limits of agreement observed between LVEF measurements suggests cardiac function is accurately preserved between the two reconstructions offering potential for direct integration into clinical workflows. Our work sets the stage for inline reconstruction making UTE free-running CMR a more clinically accessible protocol, suitable for both diagnostic and angiographic imaging in CHD patients.

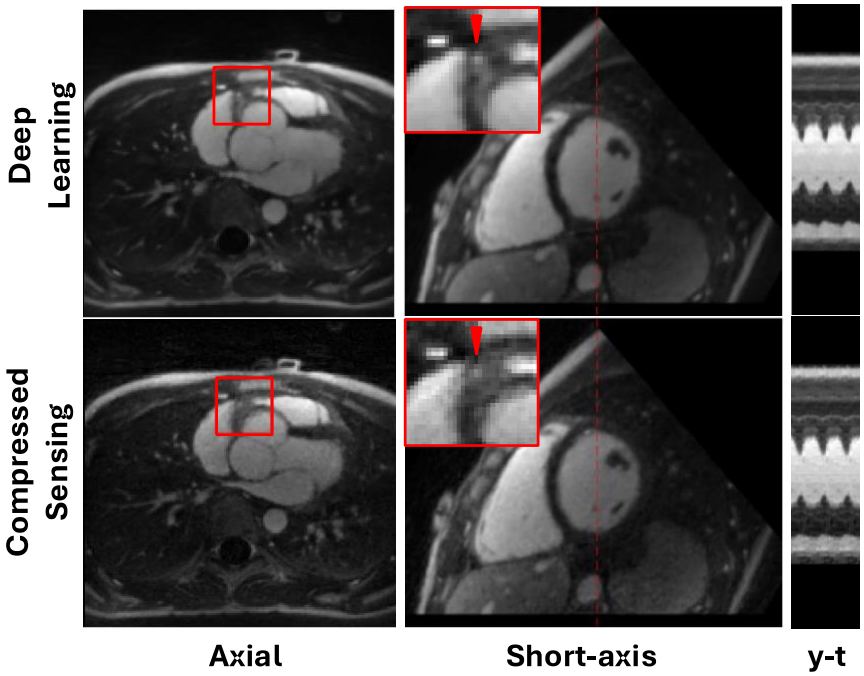

Figure 1: CS and deep learning (proposed) reconstruction of example test subject; axial, short-axis reformatted, and y-t projection views shown. Zoomed inset shows a section of the proximal segment of the right coronary artery.

References: [1] Di Sopra et al. MRM 2019; [2] Rossi et al. ISMRM 2022 (0333); [3] Feng et al. MRM 2018; [4] Yerly et al. MRM 2025; [5] Borsos et al. ISMRM 2025 (0043)

Application of a Tailored Bolus Injection to 3D CE-MRA of the Carotid Arteries; a Crossover Study

Jeffrey H. Maki[1], Mahmud Mossa Bossa[2,3], Pattana Wangaryattawanich[2], Noah Briller[2], Gregory J. Wilson[2]

1 – University of Colorado, Aurora, CO, USA 2 – University of Washington, Seattle, WA, USA 3 – University of North Carolina, Chapel Hill, NC, USA

Purpose: It has been shown that the arterial "impulse function" resulting from a small (1 mL) contrast test bolus can be used to "tailor" a venous contrast injection to achieve a desired arterial "shape", such as a longer and/or more uniform plateau phase[1]. It is theorized such bolus tailoring can improve 3D CE-MRA image quality[2]. We test this concept on 10 patients undergoing high-resolution 3D carotid CE-MRA.

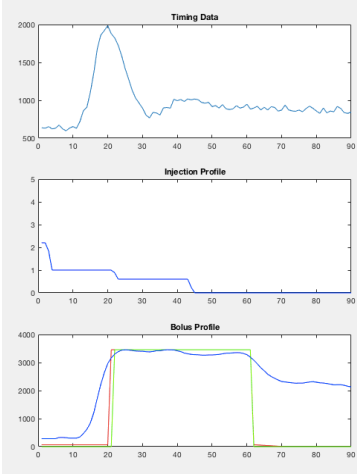

Fig 1. Example test bolus "impulse function" (top) - calculated 3 phase injection rates/durations (middle) to achieve a 40 sec plateau (bottom).

Methods: 10 patients scheduled for clinical carotid MRA were enrolled and randomized to receive two separate 3D CE-MRA exams in randomized order (3-30 days apart); one per standard clinical contrast injection protocol and one per research TIP (Tailored Injection Profile) protocol. 3D CE-MRA was performed on a Philips Ingenia 3T system (Philips, Best, the Netherlands) using identical scan parameters for both paired exams – TR/TE/flip = 4.5/1.6/27°, FOV 350 x 250 x 90 mm^3 (FH, RL, AP), acquired resolution 0.8 x 0.8 x 1.4 mm^3 (reconstructed to 0.5 x 0.5 x 0.7 mm^3), SENSE factor 2, scan time ~ 36 s, elliptical centric acquisition with flouroscopic triggering (n=6). A mid-study change in clinical protocol decreased FOV_z to 77 mm and changed to compressed SENSE such that scan time ~ 32 s (n=4).

Gadobenate dimeglumine (MultiHance, Bracco, Princeton, NJ) was used for all exams. For the clinical exam, 0.1 mmol/kg non-diluted contrast was injected at 1.6 mL/s followed by 30 mL normal saline (NS) flush at the same rate. For TIP a 1.0 mL test bolus was first administered at 2.0 mL/s followed by a 30 mL NS flush. A < 1 s temporal resolution SPGR scan of the upper thorax was performed per[1], and a small ROI was placed in the aortic arch. This ROI data was real-time exported to a custom Matlab (Mathworks, Natick, MA) program designed to calculate the appropriate 3-phase injection parameters[1] (0.1 mmol/kg contrast diluted with NS to 40 mL) such that a plateau of arterial SI is expected over 40 sec, approximately matching the duration of the CE-MRA (example of such shown in Fig. 1).

Qualitative and quantitative data was measured by blinded readers. SNR was calculated as average SI at the bilateral carotid bulbs divided by the standard deviation of a large ROI just outside of the carotid bulbs on subtractions. Vessel sharpness was measured in the left common carotid and vertebral arteries as the rise distance from 20-80% of maximum luminal signal and analyzed by Student's t-test. A preliminary single-reader analysis of overall image quality, SNR, edge sharpness, artifact level, homogeneity of arterial enhancement and venous enhancement was assessed using a 5-point Likert scale and analyzed by Wilcoxon Signed Rank Test.

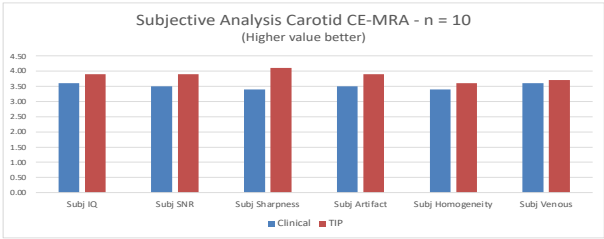

Fig 2. Preliminary subjective results - average 10 cases. TIP slightly better in all categories, however failed to achieve significance.

Results: All studies were successful and diagnostic. There was slightly improved average measured edge sharpness for TIP (6.5%), which did not achieve statistical significance. SNR was reduced by 25% for TIP (p=0.04). Subjective analysis (Fig. 2) demonstrated trending improvement with TIP, but again did not reach statistical significance for any of the 6 subjective measures.

Discussion: It was predicted that the expected lengthened and flattened arterial phase (designed to better align with acquisition duration) would decrease image blurring and artifacts, which was the trend for measured edge sharpness and all subjective assessments. None of these datapoints, however, reached statistical significance in this small sample. A separate arm of this study recently completed enrollment of 21 TIP thoracic aortic 3D CE-MRA exams in a similar cross-over fashion, and while results are still being tallied, this study will also be discussed.

While there was trending sharpness and IQ improvement, SNR was significantly decreased (25%) with TIP. This is not surprising as the original TIP study[1] noted a 19% SI loss as compared to standard injection, and some SNR loss should be expected given the contrast is injected over a longer duration and thus achieves lower peak concentration.

References:

1. Wilson, G. J. & Maki, J. H. Evaluation of a tailored injection profile (TIP) algorithm for uniform contrast-enhanced signal intensity profiles in MR angiography. *J Magn Reson Imaging* **44**, 1664–1672 (2016).
2. Clark, T. J., Wilson, G. J. & Maki, J. H. Effect of injection rate on contrast-enhanced MR angiography image quality: Modulation transfer function analysis. *Magn Reson Med* **78**, 357–369 (2016).

Hibernating vessels: Non contrast magnetic resonance angiography outperforms digital subtraction angiography in detecting below-the-knee arteries in CLTI patients

Alexander Crichton, Eniko Pomozi, Madeline Drake, Judit Csore, Janak Lamichhane. Bright Benfor, Paul Haddad, Alan B Lumsden, Trisha Roy.

Houston Methodist DeBakey Heart & Vascular Center

Introduction: Digital subtraction angiography is considered the gold standard for peripheral arterial imaging but has significant limitations. Not only does DSA pose safety risks as an invasive imaging technique requiring radiation and nephrotoxic contrast, but it can also be inaccurate without clinicians realizing it. Even with delayed acquisition, contrast may fail to reach patent portions of distal vessels, potentially missing viable targets for endovascular or surgical intervention ("hibernating vesels"). These limitations in current imaging have substantial implications for patient selection and treatment planning.

Quiescent-interval single shot (QISS) MRI offers a significant advancement, and provides a safe technique to image patients without exposure to nephrotoxic agents or ionizing radiation. QISS relies on intrinsic properties of blood itself rather than contrast agents that only highlight patent vessel lumens. The aim of this study was to evaluate whether QISS MRI detects patent vessels missed by DSA, and whether these findings resulted in lower TASC II and GLASS grading, potentially expanding treatment options for patients with PAD.

Methods: A retrospective review of patients presenting to Houston Methodist Hospital DeBakey Heart and Vascular Center with PAD undergoing QISS MRI and subsequent DSA was performed. Two examiners reviewed the imaging of each patient on both modalities. The vessels assessed were the popliteal tibioperoneal trunk (TPT), anterior tibial (AT), posterior tibial (PT), peroneal artery (PA) and dorsalis pedis (DP). All vessels were split into three sections (e.g AT1=proximal, AT2=middle, AT3=distal) and scored as either patent or occluded as individual segments (except the TPT and DP which were counted as one segment each). For vessel segment statistical analysis, a McNemar Chi test was performed. A weighted Cohen's Kappa was calculated to assess measurement agreement between the two scorers. In cases where there was disagreement, a third scorer provided imaging review to reach complete consensus for all segments. Following this TASC II and GLASS scoring was completed for QISS MRI and then DSA and compared to see if grades decided on DSA were downgraded to less severe grades when compared on QISS MRI. Statistical analysis of TASC and GLASS scoring was performed using a one-sided Wilcoxon test. Ethics approval was gained from the Houston Methodist Internal Review Board.

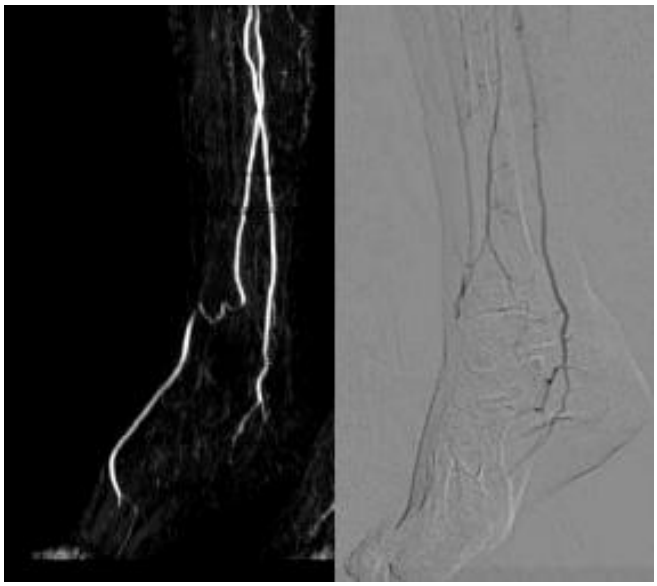

Figure 1. The DSA shows an absent DP artery, whereas the QISS MRI shows a patent DP being collateralized by the peroneal and providing branches to the digital arteries.

Results: 41 patients were included in the study (27 male, 14 female, mean age 65.7 years). Weighted Cohen's Kappa showed excellent agreement between both examiners (all Kappa scores >0.87, all p values <0.001). Overall, 570 vessel segments were analyzed, with a significantly higher number of patent vessel segments on QISS MRI compared to DSA (66% vs 58%, McNemar Chi 27.3, p<0.001) (figure 1). On single vessel analysis, there was also a higher level of patency seen on QISS MRI compared to DSA in the PA (72% vs 61%, McNemar Chi 7.0, p=0.001), PT (66% vs 52%, McNemar Chi 10.9, p=0.001), AT (73% vs 63%, McNemar Chi 7.1, p=0.01) and DP arteries (72% vs 61%, McNemar Chi 8.3, p=0.006). A combined analysis of the AT3/PT3/PA3/DP arteries as distal segments also showed statistical significance with a 16% higher number of vessels seen on QISS MRI (McNemar Chi 15.2, p<0.001). Overall TASC II and GLASS scoring did not significantly differ when comparing DSA and QISS MRI techniques. Subgroup analysis of TASC D and GLASS IV lesions however showed that vessels were significantly more likely to be downgraded to lower grade lesions when interpreting images using QISS MRI in comparison to DSA (TASC D 60% downgraded, W 45, r=0.75, p=0.002, GLASS IV 17.5% downgraded, W55, r=0.39, p=0.002).

Conclusion: Our study demonstrates that QISS MRI outperforms the current gold standard DSA in identifying more patent vessel segments. This advantage becomes increasingly significant in distal vessels where procedural planning is most critical. Prior studies have shown that these hibernating vessels have equivalent outcomes when used as bypass targets [6]. This study also suggests that QISS MRI may result in lower grading on TASC II and GLASS scoring of the most severe spectrum of arterial disease. Our study highlights the advantages of using QISS MRI when evaluating patients with complex below-the-knee disease in CLTI. Our findings encourage vascular surgeons/interventionalists to incorporate this imaging modality into pre-operative planning to enhance patient selection and decision-making.

Perfusion Quantification in Human Feet with Multi-PLD Time-SLIP MR Imaging

V. Malis,[1] Y. Kuwatsuru,[1] M. Miyazaki[1]

1. Dept. of Radiology, University of California-San Diego (UCSD), La Jolla, CA

Purpose: The purpose of this study was to evaluate the use of multi-post-labeling-delay (multi-PLD) Time-Spatial Labeling Inversion Pulse (Time-SLIP) arterial spin labeling (ASL) MRI [1] for quantifying peripheral perfusion in-vivo, with particular focus on the complex physiological conditions found in human feet. Specifically, the study aimed to assess the effects of multiple tagging pulses and high temporal resolution on perfusion measurements in the feet of healthy subjects, and to compare the in-vivo findings with previously validated theoretical and phantom models [2].

Methods: Five healthy volunteers (30 ± 3.7 years) were scanned on a 3T scanner (Vantage Galan 3T, Canon Medical Systems Corp., Japan) with Time-SLIP sequence featuring high temporal resolution of 100 ms for post-labeling delay (PLD) and employing two labeling configurations ("dark" and "bright", **Figure 1**) with 1–4 selective inversion pulses. Signal Increase Ratio (SIR) curves from muscle regions of interest were fitted with GKM to estimate perfusion coefficients and transit delays. Additionally, a continuous Γ-variate function was employed to characterize perfusion dynamics qualitatively. Fits were compared using goodness-of-fit metrics (R^2, RMSE).

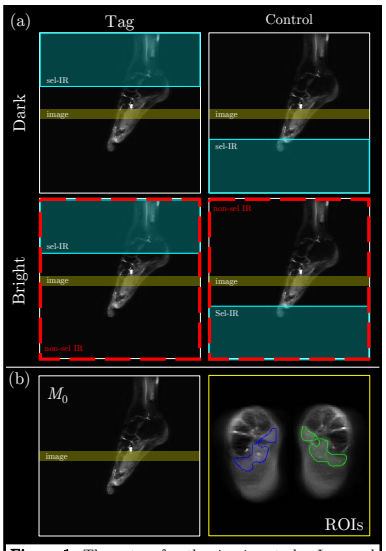

Figure 1: The setup for the *in-vivo* study. In panel **(a)** top row corresponds to the "dark" acquisition and bottom to the "bright. Panel **(b)** equilibrium magnetization (M_0) image on the left and an example of manually segmented muscle regions of interest (ROIs) used for perfusion quantification on the right.

Results: *In-vivo* results revealed significant differences from previously completed simulations and phantom experiments [2]. Contrary to constant-flow conditions, perfusion signals were highest with four selective inversion pulses, demonstrating increasing signal with more tag pulses. High temporal resolution allowed to capture complex perfusion patterns, including possible presence of multiple peaks suggesting multi-component flow. Perfusion colormaps for one of the subjects are shown in **Figure 2**, where higher signal can be observed in both "dark" and bright acquisitions with 4 tagging pulses. The SIR plots for the same subject as in Figure 2 are shown in **Figure 3**. While GKM fit provided absolute perfusion quantification, the Γ-variate function showed superior fitting metrics.

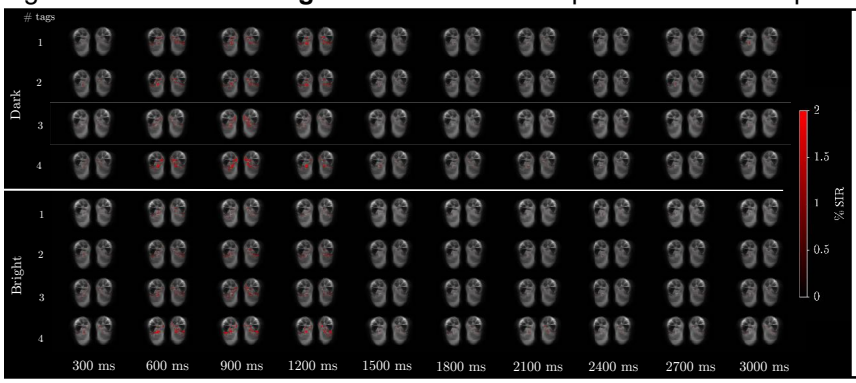

Figure 2: Perfusion colormaps of the foot from one of the study participants at selected inversion times (TIs). The top panel shows results obtained using the "dark" method, and the bottom panel using the "bright" method. Each row corresponds to acquisitions with 1, 2, 3, or 4 sel-IR pulses. The displayed perfusion maps are restricted to the manually segmented muscle regions of interest and are overlaid onto the equilibrium magnetization (M_0) image. Perfusion intensity is visualized using a colormap that transitions from transparent to a more opaque and vivid red with increasing perfusion.

Discussion: The observed discrepancies between phantom simulations and in-vivo results underscore physiological complexities such as pulsatile flow, variations in cardiac output, and heterogeneous vascular architecture that are not replicated in simplified experimental setups. High temporal resolution achieved with multi-PLD Time-SLIP allowed detailed visualization of perfusion evolution, enabling detection of intricate inflow patterns and transient flow phenomena that single-TI PASL approaches commonly miss. Multiple inversion pulses better captured delayed and staggered bolus arrivals common in peripheral vasculature, particularly in the foot. The Γ-variate fit, despite not offering absolute metrics, effectively characterized complex signal dynamics, emphasizing its utility for qualitative assessment in non-idealized, clinical scenarios. These findings highlight the necessity of utilizing advanced modeling and acquisition techniques capable of capturing physiological variability and provides a rationale for multi-tag acquisition with high temporal resolution.

Conclusion: Multi-PLD Time-SLIP MRI demonstrates strong potential for quantifying peripheral perfusion *in-vivo* under physiologically complex conditions. The observed perfusion complexity highlight the benefits of high temporal resolution and multi-tag strategies for accurate evaluation of peripheral perfusion.

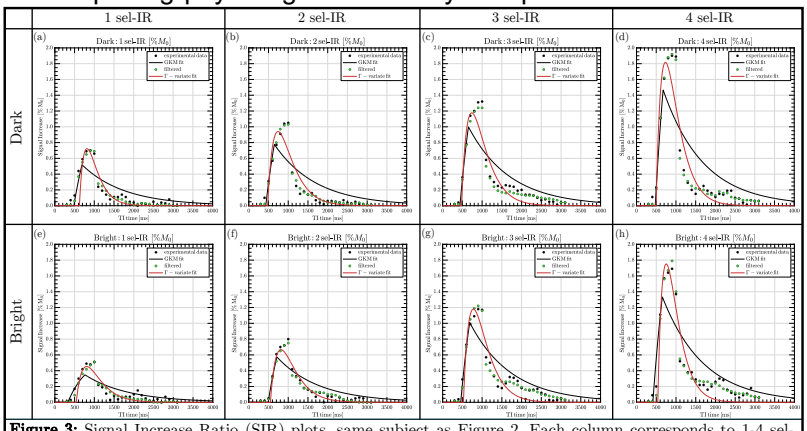

Figure 3: Signal Increase Ratio (SIR) plots, same subject as Figure 2. Each column corresponds to 1-4 sel-IR pulse(s). Top row with plots **(a-d)** for "dark" Time-SLIP acquisition and bottom row with plots **(e-h)** for "bright". Black curves indicate GKM fits, and red curves represent fits to the Γ-variate function.

References:

[1] Miyazaki M., *et al*., *Radiology*. 248, 20-43. (2008).
[2] Malis V., *et al*., SMRA 2024.

Acknowledgements: Research grants to M.M. from NIH NIA R01AG087407 and Canon Medical Systems Corp., Japan (35938).

Comparison of Vessel Length among T1-Mapping GOAL-SNAP MRA, SNAP MRA and TOF MRA

Haokun Li[1], Xiaoming Liu[2], Jiaqi Dou[1], Haozhong Sun[1], Huijun Chen[1]
[1]Center for Biomedical Imaging Research, Department of Biomedical Engineering, Tsinghua University, Beijing, China
[2]Union Hospital, Tongji Medical College, Huazhong University of Science and Technology, Wuhan, China

Purpose: Non-contrast Magnetic Resonance Angiography (MRA) techniques such as Time of Flight (TOF)[1] and Simultaneous Non-Contrast Angiography and Intraplaque Hemorrhage (SNAP)[2] are widely used in clinical medicine for the diagnosis of vascular stenosis. GOAL-SNAP[3] is an extension of SNAP which adopted 3D golden-angle radial sampling to allows reconstruction of images with different contrast. Comparisons among the three MRA techniques have been done on carotid arteries, but not yet on intracranial arteries. This study compares the vessel length of brain GOAL-SNAP MRA, SNAP MRA and TOF MRA to assess the ability of vessel imaging of these imaging techniques on intracranial arteries.

Methods Data Acquisition**:** This study was approved by the local institutional review board with all patients having provided written informed consent. Intracranial vessels of all subjects were imaged on a 3T scanner (Ingenia CX, Philips Healthcare, Best, The Netherlands) with a 32-channel head coil, using the three aforementioned sequences. The detailed scan parameters are as follows. GOAL-SNAP MRA: flip angle=8, FOV=200*200*200mm^3, spatial resolution=0.7*0.7*0.7mm^3, IRTR=2000ms, TFE factor=155. TOF MRA: flip angle=18 , FOV=200*200*84mm^3, spatial resolution=0.8*0.8*1.2mm^3 was acquired for comparison. SNAP MRA: flip angle=11, FOV=160*160*64mm^3, spatial resolution=0.4*0.4*0.4mm^3.

Method**:** Intracranial arteries in all MRA images were co-registered using the SimpleITK library in Python and cropped to the same FOV, and annotated using iCafe[4], a software for manual intracranial artery tracking and feature extraction, by a junior reviewer under guidance of a senior radiologist. Intensity inversion had been performed on SNAP MRA and GOAL-SNAP MRA to better suit the iCafe's preferences. Total artery length is defined by the sum of length of anterior cerebral artery (ACA), middle cerebral artery (MCA) and posterior cerebral artery (PCA), anterior communicating artery and posterior communicating artery following [4]. Total number of branches is defined by the number of bifurcation points in the cerebrovascular structure. Wilcoxon signed-rank tests were performed to assess the significance of the differences of each metric between each pair of techniques.

Comparison of Vessel Length**:** Seven patients with intracranial artery stenosis were recruited in this evaluation. The total artery length, ACA length, MCA length, PCA length, and total number of branches were calculated using the manual annotation in iCafe.

Table 1. Quantitative results of total valid length, lengths of ACA, MCA and PCA, and number of total branches in TOF MRA, SNAP MRA and GOAL-SNAP MRA.

Metric	GOAL-SNAP MRA	SNAP MRA	TOF MRA
Total Valid Length (mm)	1492±521	1413±583	1449±432
ACA Length (mm)	146±64	136±61	179±58
MCA Length (mm)	817±455	765±487	743±356
PCA Length (mm)	475±140	452±154	483±83
Total Branches	59.3±17.6	61.4±23.1	60.9±19.9

Table 2. Results of Wilcoxon signed-rank test on the quantitative results. *GS means GOAL-SNAP MRA. GS > SNAP means that the alternative hypothesis is the metric of GOAL-SNAP MRA is greater than that of SNAP MRA.*

Metric	GS > SNAP	GS > TOF	TOF > SNAP
Total Valid Length (mm)	0.109	0.344	0.188
ACA Length (mm)	0.173	0.976	0.008
MCA Length (mm)	0.086	0.109	0.594
PCA Length (mm)	0.188	0.594	0.289
Total Branches	0.656	0.531	0.542

Results: Table 1 shows the results of each measurement of TOF MRA, SNAP MRA and GOAL-SNAP MRA, while Table 2 shows the P value of Wilcoxon signed-rank tests. It is concluded that GOAL-SNAP MRA has the potential to visualize more arteries than TOF MRA and SNAP MRA, and this superiority is mainly in the imaging of MCA. The number of valid branches does not have an obvious difference among the three MRA techniques. Due to the relatively small number of total cases, a significant difference is not yet observed. Figure 1 shows the maximum intensity projection (MIP) image of the three MRA images of a patient, and the corresponding vessel tracing results. It is shown that both on the MIP images and the tracing results, GOAL-SNAP MRA can visualize more intracranial arteries than TOF MRA and SNAP MRA, especially at the positions of red arrow which is in the MCA region.

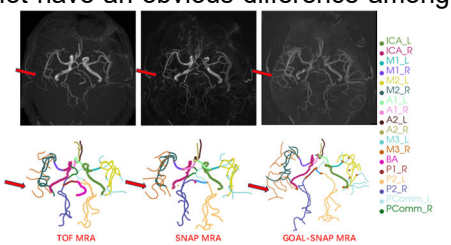

Fig. 1. Maximum intensity projection image (top) of TOF MRA, SNAP MRA and GOAL-SNAP MRA and the corresponding vessel tracing results (bottom). *Intensity inversion has been performed on SNAP MRA and GOAL-SNAP MRA. The different intracranial arteries are indicated with different colors in the vessel tracing results, and the red arrows indicate the positions where GOAL-SNAP MRA can visualize more intracranial arteries than TOF MRA and SNAP MRA.*

Conclusion: This study compared the vessel length of GOAL-SNAP MRA, SNAP MRA and TOF MRA, and shows that GOAL-SNAP MRA has the potential to visualize more intracranial arteries than the other two MRA techniques. More data will be included in the future work.

References [1] Laub, G. et al., Magn Reson Imaging Clin N Am 1995, [2] Wang, J. et al., Magn Reson Med 2013, [3] Qi, H. et al., Radiology 2018, [4] Chen, L. et al., Magn Reson Med 2018.

Gadoquatrane at a 60% reduced gadolinium dose for MR-Angiography of intracranial vessels

Authors: Giles Roditi[1], Sophie Hodge[2], Alex Liu[3], Mark Klemens[4], Birte M. Hofmann[4], Petra Palkowitsch[4], Genji Bai[5], Christopher Hancock[6], Seung Hong Choi[7]

Affiliations: [1]Department of Radiology, Glasgow Royal Infirmary, Glasgow, Great Britain, [2]Clinical Data & Analytics, Bayer Pharma R&D, Reading, Great Britain, [3]Clinical Data & Analytics, Bayer Pharma R&D, Whippany, NJ, USA; [4]Bayer AG, Pharma, Radiology R&D, Berlin, Germany, 5Huai'an First People's Hospital, Huaiyin District,Huai'an city, Jiangsu province, China, [6]HALO Diagnostics, Indian Wells, CA, USA, [7]Seoul National University, Seoul, South Korea

Purpose: To investigate efficacy of gadoquatrane, a low dose macrocyclic gadolinium-based contrast agent (GBCA) at a dose of 0.04 mmol gadolinium (Gd)/kg body weight (bw) compared to 0.1 mmol Gd/kg bw of standard of care (SoC) macrocyclic GBCAs (gadobutrol, gadoterate, gadoteridol) for CE-MR-Angiography of intracranial vessels in adults.

Methods: QUANTI CNS is a multicenter, randomized, prospective double-blind, Phase 3 cross-over study, conducted between July 2023 and May 2024. Adult patients with a known or suspected CNS pathology underwent two contrast-enhanced-MR-Angiographies (CE-MRA), one with gadoquatrane and the other one with a comparator SoC GBCA in a random order. Combined (including pre- and post-contrast images) and pre-contrast MR image sets were assessed in a blinded independent central review using three visualization parameters adapted to MRA, i.e. vessel lumen contrast enhancement, vessel border delineation and vessel diameter/dimension (internal morphology), as endpoints.

Results: Of 305 randomized patients, 14 underwent CE-MR-Angiography of intracranial vessels, 13 were evaluable for efficacy.

For the comparison of combined pre- and post-gadoquatrane MR images sets and combined SoC comparator MR images sets, the mean visualization parameters show similar scores with a difference close to 0 for all 3 readers and all 3 visualization parameters. Most of the mean differences are slightly below 0, indicating a tendency to slightly higher scores for the gadoquatrane enhanced image sets.

For the comparison of combined pre- and post-gadoquatrane vs pre-gadoquatrane MR image sets, the scores for the combined image sets showed a clear improvement for the 3 visualization parameters. The difference in mean scores for combined pre- and post-gadoquatrane vs pre-gadoquatrane MR image sets were close to or greater than 1 for all readers and all visualization parameters, showing clearly higher scores for gadoquatrane enhanced MRIs.

Discussion: Gadoquatrane at a dose of 0.04 mmol Gd/kg bw, which correlates to a 60% reduced gadolinium dose compared to SoC comparator GBCAs, shows consistent results for CE-MR-Angiography of intracranial vessels with the overall study population which demonstrated non-inferior efficacy of gadoquatrane to SoC comparator MRA. The study did not investigate the application of gadoquatrane in specific imaging protocols due to design requirements of the study. How to optimize the application of gadoquatrane in CE-MR-Angiography is to be investigated in future research.

Disclosure:
Authors SH, AL, MK, BMH and PP are employees of Bayer AG, Berlin, Germany and have indirect or direct financial interest in some of the products under investigation or subject matter discussed in the manuscript.
Authors GR, GB, CH, and SHC were investigators in the QUANTI CNS trial and received research funding from Bayer AG.

MRI-histology identifies impenetrable plaques not seen in conventional imaging: an amputated limb model and protocol for device development to cross impenetrable lesions

Alexander B Crichton, Eniko Pomozi, Judit Csore, Janak Lamichhane, Bright Benfor, Christof Karmonik, Alan B Lumsden, Trisha Roy - Houston Methodist Research Institute

Introduction: Immediate technical failure rates in randomized controlled trials of endovascular therapies range between 13-20%. and is most commonly due to an inability to cross lesions with a guidewire. Non-contrast MRI characterizes plaque composition and may identify patients at high risk for failed endovascular crossing. By identifying plaque characteristics and combining this with an amputated limb model, a process for evaluating new devices that can cross different plaque morphologies can be tested. This study evaluates a novel combined UTE/SSFP MRI protocol in an amputated limb model to identify impenetrable plaques. It then introduces the concept of device testing using the PowerWire® 14 Radiofrequency Guidewire (Baylis Medical Technologies, USA), which has an evidence basis in central venous disease in an amputated limb model to evaluate their ability to cross non-crossable arterial disease in chronic limb threatening ischemia (CLTI).

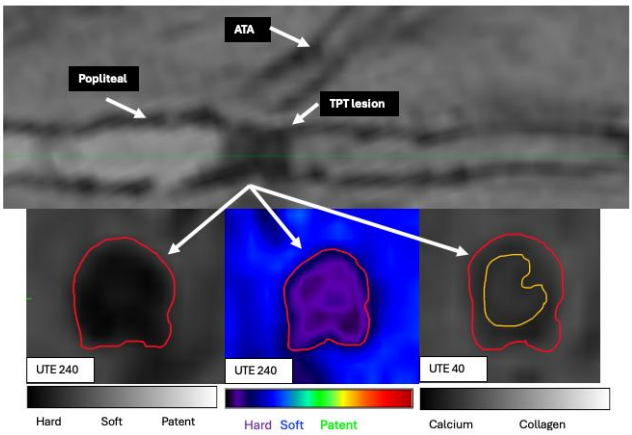

Figure 1. The UTE 240 sequence shows a hard lesion in the TPT artery, depicted by the black area. This is shown further with color enhancement, with purple identifying a significantly hard lesion. The UTE 40 sequence shows however that the predominant feature of this lesion is centrally minimally calcific, made up of collagenous tissue (yellow outline). This minimally calcific lesion was not crossable.

Methods: Patients with CLTI presenting to an academic vascular unit undergoing major limb amputation were included in the study. All patients underwent 3T non-contrast MRI. Lesions with >75% stenosis or occlusion in the below the knee arteries were evaluated and defined as either hard (>50% calcium/collagen) or soft (<50%). Hard lesions were further delineated into two groups: minimally calcific hard (<50% calcium) and significantly calcific hard lesions (>50% calcium). Lesions were also scored using TASC II and GLASS systems. Amputated limbs underwent percutaneous vascular intervention by a single board-certified vascular and endovascular surgeon in a hybrid operating room and an attempt was made to cross each lesion. The primary endpoint of this study was to compare crossing success in MRI-defined hard versus soft lesions. Secondary outcomes included comparing TASC C/D with TASC A/B lesions, GLASS III/IV and I/II lesion crossability, crossability in minimally versus significantly calcified hard lesions, stenotic versus total occlusions and demographic/medical risk factor predictors of crossing failure. In amputated limbs with impenetrable lesions, the 0.014 Powerwire was used to attempt vessel crossing and histological images outlining the effects of the wire are shown.

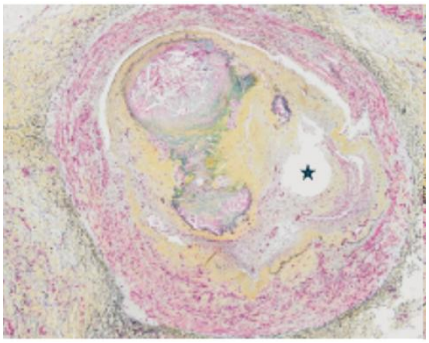

Figure 2. Movat's stained histological images following the Baylis Powerwire. The image shows that the wire has successfully passed intraluminally through a mixed calcific and dense collagenous lesion.

Results: The study included 27 patients with 46 below-knee arterial lesions, with end-stage CLTI. 12 (26%) lesions were defined as soft (<50% collagen/calcium) and 34 (74%) were hard (>50% collagen/calcium). The overall crossing failure rate was 70% (32/46 lesions), a finding consistent with the terminal disease state of these patients, 63% and 26% of whom had undergone previous failed endovascular and open revascularization attempts respectively. MRI plaque characteristics demonstrated a strong predictive value: hard lesions were significantly less likely to be crossable compared to soft lesions (91% vs 8%, p<0.001). Traditional classification systems showed variable predictive value: TASC C/D lesions had significantly higher crossing failure rates compared to TASC A/B (77% vs 33% p=0.039), while GLASS III/IV lesions did not achieve statistical significance when compared to GLASS I/II (73% vs 44%, p=0.129). Among hard lesions, there was no significant difference in crossability between minimally calcific and significantly calcific lesions (92% vs 90%, p>0.99) (figure 1). This key finding suggests that dense collagen, undetectable on conventional imaging, was visualized with MRI and plays a critical role in crossing failure independent of calcium burden. There was also no significant difference in the ability to cross occluded versus stenotic lesions (67% vs 80%, p=0.70). The 0.014 Powerwire underwent crossing experiments in two amputated limbs in lesions that were non-crossable prior to amputation and for other lesions that were non-crossable in the amputated limb model. Histological evidence shows that the wire can cross non-crossable plaque such as dense collagen (figure 2). This is highly important, as these collagenic lesions would not be visualized with currently available imaging techniques.

Conclusion: Non-contrast MRI with UTE/SSFP identifies critical plaque components that predict crossing failure, including dense collagen that is not visible on conventional imaging. This protocol offers an evidence-based approach to procedural planning, potentially reducing endovascular failures and a route to ensuring advanced crossing tools are available during endovascular procedures.

Generative MR Multitasking: Method and application to non-ECG, free-breathing, simultaneous multislice (SMS) cardiovascular T1-T2 mapping

Xinguo Fang[1,2] and Anthony G. Christodoulou[1,2]

[1]*Department of Radiological Sciences, David Geffen School of Medicine at UCLA;* [2]*Department of Bioengineering, UCLA*

Purpose: MR Multitasking[1] enables efficient multidimensional imaging for applications such as non-ECG, free-breathing T1 and T2 mapping. Conventional multitasking is built on low-rank tensor (LRT) models, which are scalable to many time dimensions but limited by motion binning and need for time-consuming spatial regularization. This work introduces a generative multidimensional model that is binning- and regularization-free, evaluated on 3-slice SMS T1-T2 mapping.

Methods: *Framework:* Like multitasking, generative multitasking (gMT) is a subspace imaging model; however, rather than modeling a temporal basis as a discrete low-rank tensor, gMT leverages a conditional variational autoencoder (CVAE) framework to generate a continuous multidimensional temporal basis. The CVAE receives sequence timings and real-time basis functions from self-gating data; it learns continuous latent vectors corresponding to motion states, bypassing discrete cardiac and respiratory binning. Its learned decoder can directly generate temporal basis functions for arbitrary combinations of motion states and contrast weightings (Fig. 1).

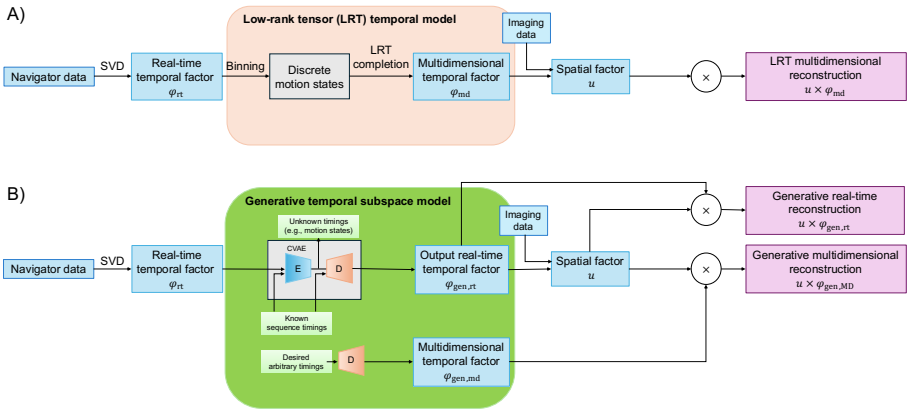

Figure 1: A. Multitasking framework; B, Generative Multitasking framework

Experiments: We evaluated the framework in *N*=5 human volunteers using a 2D SMS dual-flip-angle T1-T2 Multitasking pulse sequence[2] on a 3T scanner (MAGNETOM Vida, Siemens). Although conventional LRT Multitasking usually relies on nonlinear wavelet sparsity regularization for denoising, we performed both conventional Multitasking and generative Multitasking reconstructions without any spatial regularization here to evaluate intrinsic SNR and to avoid modification of noise properties by nonlinear regularization. SNR was measured as the ratio of the mean septal myocardial value to the standard deviation of air, both measured at the longest inversion time (closest to the GRE steady-state).

Results: We compared the reconstructions of conventional and generative Multitasking for T1-T2 mapping, displaying cardiac phase and respiratory dimensions as well as T1 and T2 maps (Fig. 2). The image SNRs are seen in Table 1.

Discussion: The generative Multitasking framework demonstrated several workflow and advantages over conventional Multitasking, including qualitatively higher SNR in images and T1/T2 maps. Meanwhile, gMT's high performance without time-consuming wavelet regularization addresses reconstruction time barriers to clinical translation. Understanding and improvement of latent motion space regularization are a useful area of future research.

Conclusions: Generative MR Multitasking may be an useful replacement for low-rank tensors, offering a new mechanism for multidimensional cardiovascular MR imaging.

SNR	Low-rank tensor Multitasking	Generative Multitasking
Subject 1	37.0	143.0
Subject 2	40.1	66.0
Subject 3	56.3	89.3
Subject 4	76.6	74.3
Subject 5	41.7	66.9

Table 1: Image SNR comparison

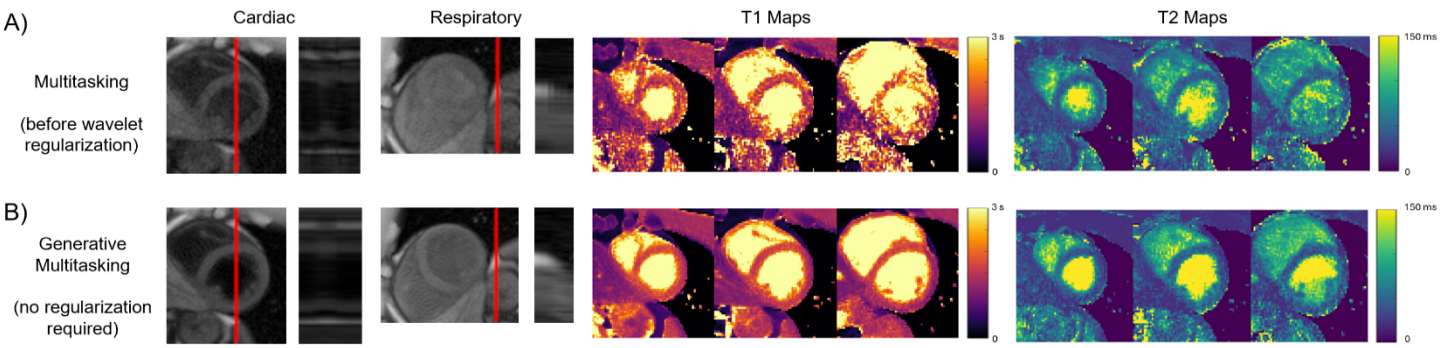

Figure 2: A. Multitasking reconstruction images before wavelet regularization; B. Generative Multitasking reconstruction, also without wavelet regularization. From left to right are cardiac cine, respiratory cine, T1 maps of all three slices, T2 maps of all three slices.

References: [1] Christodoulou AG et al., *Nat Biomed Eng* 2018. [2] Mao X et al. *Front Cardiovasc Med* 2022.

Free-breathing, ECG-free, IR-prepped Golden Angle Radial Imaging Technique for Myocardial T1 Mapping

Orhan Unal, Alexey Samsonov, Julia Velikina (Department of Radiology and Medical Physics - University of Wisconsin - Madison)

Purpose: Quantitative myocardial T1 mapping is critical for detecting and quantifying focal and diffuse myocardial fibrosis. Clinically, inversion recovery (IR)-based techniques such as MOLLI [2] are widely used due to higher precision and reproducibility. However, they tend to underestimate T1 values, largely due to heart rate dependence, often necessitating protocol adjustments. Saturation recovery (SR) methods like SASHA offer better T1 accuracy but at the cost of lower precision and greater sensitivity to noise. Both approaches require multiple breath-holds, which may be challenging for patients with cardiac or pulmonary conditions. In this work, we evaluate a free-breathing, ECG-free, IR-prepared T1 mapping approach using a Multitasking-like framework [3], comparing its accuracy and repeatability with MOLLI.

Methods: We implemented a free-breathing, ECG-independent, inversion recovery (IR)-prepared radial MRI technique using dual flip angles (FAs) and golden-angle sampling to account for $B1^+$ variations. Following each non-selective inversion recovery (IR) pulse, radial k-space data were continuously acquired using an interleaved scheme. Odd-numbered spokes were spaced by a constant increment of 111.25° (the golden angle), while even-numbered spokes were acquired at a fixed angle of 0° to serve as navigator lines. Each IR pulse resulted in the acquisition of 344 interleaved golden-angle projections along with 344 corresponding fixed-angle navigator projections. The number of IR pulses varied between 32 and 128 across different scans. For computational efficiency, a total of 377 unique golden-angle projections were generated before the acquisition pattern repeated itself [4]. Acquired data were retrospectively sorted into different cardiac (16), respiratory (5), and inversion time (344) phases. Phantom experiments were conducted using the RSNA QIBA DCE phantom with known T1 values to compare T1 estimates derived from Multitasking and MOLLI techniques. Additionally, we evaluated the impact of flip angle selection on T1 accuracy. Typical Multitasking acquisition parameters were as follows: FOV = 360×360 mm², matrix = 528×528, flip angles = 3°/10°, bandwidth = 125 kHz, TR/TE = 4.7/1.9 ms. For comparison, ECG-gated, breath-hold MOLLI 5(3)3 acquisitions used: FOV = 360×324 mm², matrix = 160×120, flip angle = 35°, bandwidth = 111 kHz, TR/TE = 3.0/1.2 ms, TI = 129 ms. Both Multitasking and MOLLI data were acquired in 15 healthy subjects at the mid-ventricular short-axis level using a 3T scanner (GE Healthcare, Waukesha, WI), following institutional review board (IRB) approval.

Results and Discussion: T1 maps were generated via voxel-wise fitting to a FLASH IR signal model, producing maps of T1, proton density (PD), B1+, and inversion efficiency. Acquisition parameters - flip angle, scan time, navigator lines, and regularization weights - were varied to assess their effects on image quality. Dual flip angle (FA) implementation enabled separation into cardiac, respiratory, and inversion time dimensions. T1 values from Multitasking were consistently higher than those from MOLLI, suggesting greater accuracy and reduced heart rate sensitivity. The dual-FA approach corrected for B1+ inhomogeneity compared to single-FA acquisition, therefore improving T1 accuracy. Multitasking performance depended on sampling near the null point during a specific respiratory phase, which varied across subjects. It is hypothesized that this variability may be reduced by instructing patients to breathe in a controlled rhythm, potentially improving repeatability to MOLLI-like levels. Table 1 shows T1 values measured using the dual FA Multitasking method compared to the known true T1 values in a phantom. The measured T1 values in phantom closely follow the true values across the full range, with slight underestimation at higher T1 times. Multitasking performance and accuracy were highly dependent on the SNR of source images, which was affected by FA choice and undersampling patterns. Poor SNR led to unreliable T1 estimates. Figure 1 demonstrates the impact of FA selection: the FA pair 2°, 12° (a) produced more noise than the 4°, 8° (b) pair.

True T1 (ms)	126	175	247	352	497	706	984	1454	1989
Measured T1 (ms)	130	181	244	349	488	692	952	1340	1718

Table 1: Dual flip angle T1 values obtained with Multitasking vs True T1 values in a phantom.

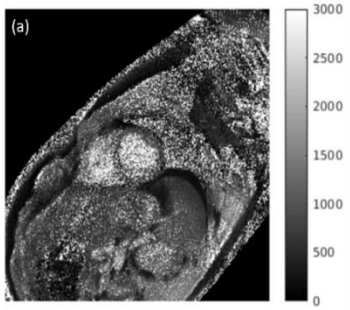

Figure 1: T1 maps obtained from the dual FA Multitasking acquisition with the FA pairs of 2, 12º (a) and 4, 8º (b).

Conclusion: This study demonstrates the feasibility of a free-breathing, ECG-free myocardial T1 mapping technique using a Multitasking-like approach. Initial results show improved accuracy over MOLLI and strong repeatability if inversion recovery sampling is uniform and sufficient. These findings support further investigation and development of self-gated T1 mapping for robust and patient-friendly myocardial tissue characterization.

References:

[1] Messroghli DR, Radjenovic A, Kozerke S, Higgins DM, Sivananthan MU, and Ridgway JP. Modified Look-Locker inversion recovery (MOLLI) for high resolution T_1 mapping of the heart. *Magn. Reson. Med.* 2004; 52:141

[2] Chow K, Flewitt JA, Green JD, Pagano JJ, Friedrich MG, and Thompson RB. Saturation recovery single-shot acquisition (SASHA) for myocardial T_1 mapping. MRM 2013; 71:2082

[3] Christodoulou AG, Shaw JL, Nguyen C, Yang Q, Xie Y, Wang N, Li D. Magnetic resonance multitasking for motion-resolved quantitative cardiovascular imaging. *Nat Biomed Eng*. 2018 Apr; 2(4):215-226

[4] Serry FM, Ma S, Mao X, Han F, Xie Y, Han H, Li D, Christodoulou AG. Dual flip-angle IR-FLASH with spin history mapping for B1+ corrected T1 mapping: Application to T1 cardiovascular magnetic resonance Multitasking. *Magn. Reson. Med.* 2021; 86:3182

Clinical Evaluation of a 3D Ultrafast Single Breath-Hold Sequence for cardiac functional assessment at 1.5T

Abdulhamid Haj Khalil[a], Kemal Furkan Kaldirimoglu[b], Monica Sigovan[a], Charles De-Bourguignon[c], Philippe Douek[a,c].
a. University Claude Bernard Lyon1, INSA-Lyon, CREATIS, 7 Avenue Jean Capelle O, 69100 Villeurbanne, France.
b.University of Health Sciences, Istanbul Training and Research Hospital, 34098 Istanbul, Turkey.
c.Department of Radiology, Louis Pradel Hospital, Hospices Civils de Lyon, 59 Boulevard Pinel, 69500 Bron, France.

Purpose: Cardiovascular magnetic resonance (CMR) is the gold standard for assessing heart volumes and function using 2D breath-hold cine imaging[1,2]. However, this technique requires multiple breath-holds and is time-consuming, which can reduce patient comfort and increase costs[3,4]. Researchers have introduced a novel ultrafast 3-dimensional (3D) cine sequence: Enhanced Sensitivity Encoding with Static Outer Volume Subtraction (ESSOS). While a study has been conducted at 3T MRI and with gadolinium[5], there is little evidence for its application at 1.5T MRI. This present study evaluated the ESSOS protocol at 1.5T MRI, using 3D cine imaging before gadolinium (pre-contrast) and after gadolinium (post-contrast) administration. The two ESSOS sequences were compared to standard 2D cine in terms of image quality and cardiac quantitative parameters.

Methods: 31 patients (21 males, 10 females) were initially included; 9 were excluded due to artifacts (motion or metal-related). Each patient underwent three sequences: standard 2D cine (pre-contrast), 3D cine ESSOS pre-contrast, and 3D ESSOS cine post-contrast (~8 minutes after gadolinium injection, 0.1 mmol/kg). All CMR exams were performed on a 1.5 Tesla (Philips Ingenia) MRI system using a phased-array cardiac multi coil. The 2D cine images were acquired in short-axis views using a balanced turbo field echo (TFE) sequence, covering the entire left ventricle. Parameters were reconstructed using pixel size 0.95 × 0.95 mm, matrix size 512 × 512, slice thickness 8 mm with no gap, field of view 486 × 486 mm, and 20 cardiac phases per slice. The 3D cine sequences used a fast coronal volume acquisition with high acceleration and ESSOS technology for ultrafast imaging. Post-processing allowed reconstruction into short-axis views. Image quality was rated on a 1–4 scale. Cardiac function parameters ejection fraction, wall thickness, volumes, and ventricular masses were measured for both right and left ventricles and compared using statistical analysis.

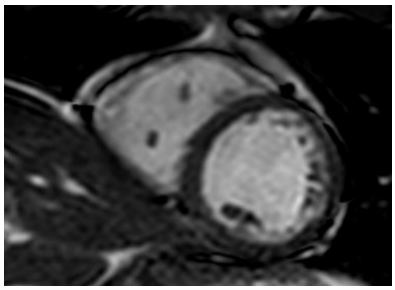

Fig 1: Image 2D Cine SA

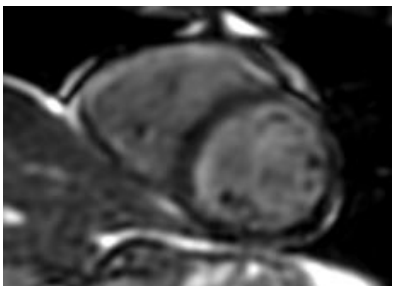

Fig 2: Image 3D Cine pre-contrast SA

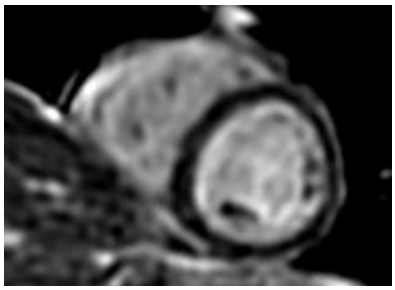

Fig 3: Image 3D Cine post-contrast SA

Results: Whole-heart acquisition time with 3D Essos was ~19 seconds (single breath-hold), compared to 14 × 12sec for 2D cine (multiple breath-holds). The 3D reconstruction was fast (~1 minute) and worked with standard MRI equipment. 2D cine provided the highest image quality (mean score 3.4), followed by 3D cine post-contrast (mean score 2.4). 3D cine pre-contrast had the poorest quality (mean score 1.7). Left ventricular ejection fraction (LVEF) from 3D cine post-contrast closely matched LVEF from 2D cine, with an intraclass correlation coefficient (ICC) of 0.959 [95% confidence interval (CI): 0.935–0.974]. In contrast, the ICC between 2D cine and 3D cine pre-contrast was 0.931 [95% CI: 0.890–0.956].Right ventricular ejection fraction (RVEF) from 3D cine post-contrast also showed better agreement with 2D cine (ICC 0.922 [95% CI: 0.879–0.950]) than 3D cine pre-contrast (ICC 0.906 [95% CI: 0.854–0.940]).

Discussion: Ultrafast 3D cine post-contrast at 1.5T is a rapid and practical method for cardiac functional imaging, providing clinically acceptable results. However, ultrafast 3D cine pre-contrast showed lower image quality, currently insufficient for clinical use. Ultrafast 3D imaging improves patient comfort and reduces scan time, but further studies are needed to enhance image quality at lower field strengths without contrast.

References:

[1] Puntmann VO, Valbuena S, Hinojar R, et al. Society for Cardiovascular Magnetic Resonance (SCMR) expert consensus for CMR imaging endpoints in clinical research: part I - analytical validation and clinical qualification. J Cardiovasc Magn Reson. 2018;20(1):67. Published 2018 Sep 20. doi:10.1186/s12968-018-0484-5

[2] Kilner PJ, Geva T, Kaemmerer H, Trindade PT, Schwitter J, Webb GD. Recommendations for cardiovascular magnetic resonance in adults with congenital heart disease from the respective working groups of the European Society of Cardiology. Eur Heart J. 2010;31(7):794-805. doi:10.1093/eurheartj/ehp586

[3] Craft J, Li Y, Nashta NF, Weber J. Comparison between compressed sensing and segmented cine cardiac magnetic resonance: a meta-analysis. BMC Cardiovasc Disord. 2023;23(1):473. Published 2023 Sep 21. doi:10.1186/s12872-023-03426-1

[4] Vincenti G, Monney P, Chaptinel J, et al. Compressed sensing single-breath-hold CMR for fast quantification of LV function, volumes, and mass. JACC Cardiovasc Imaging. 2014;7(9):882-892. doi:10.1016/j.jcmg.2014.04.016

[5] Gómez-Talavera S, Fernandez-Jimenez R, Fuster V, et al. Clinical Validation of a 3-Dimensional Ultrafast Cardiac Magnetic Resonance Protocol Including Single Breath-Hold 3-Dimensional Sequences. JACC Cardiovasc Imaging. 2021;14(9):1742-1754. doi:10.1016/j.jcmg.2021.02.031

Quantitative Myocardial Perfusion Using In-Line Cardiac MRI: Feasibility, Clinical Insights, and Comparison to PET imaging

Maya Gabbour[1], Enas Ahmed[1], Ahmed Negm[1], Jessica Magnuson[2], Holly Iverson[1], Chris Francois[1], Tim Leiner[1], Rachel Davids[2], Celvin Chow[2], Kara Dueker[2], Peter Kollasch[2], Xiaoming Bi[2], Ian Chang[1], Jeremy Collins[1]

[1]Department of Radiology, Mayo Clinic, MN, [2]Siemens Healthineers

Purpose: Myocardial quantitative perfusion (Myocardial QP) evaluates myocardial blood flow (MBF) in absolute units (ml/min/g). It is more sensitive than semiquantitative approaches for detecting inducible myocardial ischemia and shows promise in predicting major adverse cardiovascular events. In-line MQP analysis on MRI scanners enables efficient clinical translation by generating motion-corrected perfusion I mages, pixel-based blood flow maps, segmental MBF values, and signal intensity–time curves using a single-bolus, dual-sequence approach. We investigated MQP in consecutive patients referred for stress perfusion imaging and those undergoing contrast-enhanced cardiac MRI without stress at 1.5T.

Methods: IRB-approved study using a vendor-provided research prototype MQP sequence with in-line MBF calculation. All imaging was performed on a 1.5T scanner with a dedicated cardiac coil (MAGNETOM Aera, Siemens Healthineers, Forchheim, Germany). Stress perfusion was performed using a single 0.4 mg IV bolus of regadenoson (Lexiscan) over 10 seconds, followed by rest imaging after a 10-minute washout. Gadobutrol (0.075 mmol/kg at 2 cc/s) was used for both stress and rest imaging. Aminophylline (100 mg IV) was administered at the supervising physician's discretion for vasodilation reversal. An additional 0.05 mmol/kg Gadobutrol was given after rest imaging to complete a total dose of 0.2 mmol/kg for late gadolinium enhancement imaging. Stress and rest perfusion imaging included three short-axis slices (base, mid, apex), and a long-axis slice when the R-R interval allowed four slices per beat. LVEF and myocardial scarring were extracted from clinical cardiac MR reports. Participants were stratified by LVEF (≥50% vs. <50%) and by presence or absence of scar on conventional LGE. Resting MBF was compared between patients who received vasodilator and those with rest-only imaging using 2-tailed Student's t-tests. Where available, resting MBF was also compared between CMR and Ammonia PET using a Wilcoxon signed-rank test.

Results: A total of 146 patients (74 female, ages 19–87) were recruited for MQP imaging. Twenty-one were excluded due to workflow issues. In-line resting MQP data was analyzable in 124 of 125 completed cases (99%). Patients were stratified by LVEF and presence of scar; group means ± SD (Tables 1 and 2). Global resting perfusion was similar between patients with preserved and reduced LVEF without scarring ($p > 0.05$). However, patients with preserved LVEF and no scar had significantly higher global and endocardial MBF compared to those with preserved LVEF and scarring ($p < 0.001$). Resting MBF differed significantly between patients with and without aminophylline reversal ($p < 0.05$) but was similar between those with preserved LVEF and no scar and those undergoing stress imaging with reversal ($p > 0.05$). In 14 patients with LVEF >50% and no myocardial scarring, resting myocardial perfusion was assessed by both PET and MRI. CMR significantly underestimated MBF compared to PET ($p = 0.023$), with a median difference of -0.105 ml/g/min and a 95% confidence interval of -0.24 to -0.02 ml/g/min.

Discussion: This study demonstrates the feasibility of in-line MBF quantification in a heterogeneous clinical population, with 99% analyzability. Resting MBF was higher in patients with LVEF >50% without scarring compared to those with scarring. Residual vasodilatory effects of regadenoson persisted beyond a 10-minute washout, affecting MBF unless reversed with aminophylline. CMR systematically underestimated resting perfusion compared to PET in patients with preserved LVEF and no scarring, underscoring the need for modality-specific interpretation in clinical practice.

Group	N	Global Rest MBF (ml/g/min)	Resting Epi/Endo Ratio
LVEF>50%, No scar	70	0.9 (± 0.2)	1.1 (+/-0.06)
LVEF >50%, With scar	20	0.6 (+/-0.1)	1 (+/-0.06)
LVEF<50%, No scar	16	0.8 (+/- 0.2)	1.2 (+/-0.2)
LVEF<50%, with scar	8	0.64 (+/- 0.1)	1.1 (+/-0.1)

Table 1: Resting perfusion in patients not undergoing stress imaging. Values are reported as mean ± SD

Group	N	Stress MBF (ml/g/min)	Rest MBF (ml/g/min)	Stress Epi/Endo	Rest Epi/Endo
LVEF>50%, No scar, with reversal	6	1.8 (+/-0.5)	0.8 (+/-0.1)	0.9 (+/-0.07)	1 (+/-0.1)
LVEF>50%, No scar, No reversal	3	2.1 (+/-0.15)	1.46 (+/-0.03)	0.95 (+/-0.03)	1.01 (+/-0.07)

Table 2: Myocardial perfusion in patients undergoing stress imaging with or without reversal using aminophylline. Values are reported as mean ± SD.

Wideband joint myocardial bright- and black-blood imaging for patients with implantable cardiac devices at 1.5T

Pauline Gut[1,2], Hubert Cochet[1,3], Panagiotis Antiochos[4], Ambra Masi[4], Jürg Schwitter[4], Guido Caluori[1], Konstantinos Vlachos[1], Frederic Sacher[1,5], Pierre Jaïs[1,5], Matthias Stuber[1,2], Aurélien Bustin[1,2,3]
[1]IHU LIRYC, Heart Rhythm Disease Institute, Université de Bordeaux, France [2]Department of Diagnostic and Interventional Radiology, Lausanne University Hospital and University of Lausanne, Switzerland [3]Department of Cardiovascular Imaging, Hôpital Cardiologique du Haut-Lévêque, CHU de Bordeaux, France [4]Cardiovascular Department, Division of Cardiology, University Hospital of Lausanne and University of Lausanne, Switzerland [5]Department of Cardiac Pacing and Electrophysiology, Hôpital Cardiologique du Haut-Lévêque, CHU de Bordeaux, France

Purpose: Joint bright- and black-blood (SPOT) late gadolinium enhancement (LGE) cardiac imaging provides optimal scar localization and detection,[1] but image quality is degraded in patients with implantable cardioverter defibrillators (ICDs). Here we propose a wideband version of this technology by using a wideband T2 preparation [2,3].

Methods:
Sequence: A 2D, breath-held, ECG-triggered, single-shot, gradient recalled echo (GRE), wideband joint bright- and black-blood (wideband SPOT) LGE sequence was implemented on a 1.5T system (MAGNETOM Sola, Siemens). The black-blood images were acquired during odd heartbeats with an inversion-recovery pre-pulse (conventional bandwidth=0.8kHz, wideband bandwidth=3.8kHz) immediately followed by a T2 preparation (duration of 27msec) consisting of a tip down pulse, two adiabatic hyperbolic secant refocusing pulses[4] (conventional bandwidth=1.6kHz, wideband bandwidth=5.0kHz), and a tip up pulse. The bright-blood images were acquired without inversion-recovery during even heartbeats with the same T2 preparation adjacent to the imaging part of the sequence. Eight co-registered black- and bright-blood single-shot images were acquired for each slice position during mid-diastole and were reconstructed with GRAPPA. The following images were generated: i) averaged black-blood for scar detection, (ii) averaged bright-blood for scar localization and left ventricle (LV) wall segmentation, and (iii) superimposition of the scars detected with the black-blood image on the bright-blood image.
Patients: Wideband SPOT was compared to conventional GRE phase-sensitive inversion recovery (PSIR) and wideband GRE PSIR in eight patients (7 males, 57y±11y) with transvenous ICDs and known presence of myocardial scar (5 ischemic, 3 non-ischemic). Images were acquired in a randomized order, 15min after the administration of a continuous slow infusion of a total dose of 0.2 mmol/kg of Gadobutrol (bolus of 0.1 mmol/kg).
Analysis: An expert radiologist scored the subjective image quality (1=non-diagnostic, 2=less than adequate, 3=adequate, 4=excellent) and the overall ICD-artifact severity (1=severe, 2=large, 3=moderate, 4=minimal). LV wall and scar contours were drawn using Circle CVI42. Scar mass (in g), and size (as a % of LV) were assessed. The effect of the used sequence on the different metrics, that is, scar size, scar mass, image quality, and artefact severity, was assessed using a one-way ANOVA test. Each metric was then compared between the sequences using multiple pairwise testing with a Student's t-test using a Bonferroni correction post-hoc test.

Results: Out of eight patients, five had ischemic myocardial scars (four with transmural and one with subendocardial infarct) and three non-ischemic myocardial scars (one global epicardial (myocarditis), one global endocardial (fibrosis in the hypertrophic LV), and one mid-wall (myocarditis)). An example of wideband SPOT images compared to the other sequences in a patient with a subendocardial scar in the anterior segment is shown in **Fig.1**. The one-way ANOVA test showed that the sequence used influences the artefact severity score (P<0.01) and on the image quality (P<0.05). No significant differences were found between wideband SPOT and conventional PSIR for scar size (14.5%±9.6 vs. 24.2%±19.6 , P=0.606) and scar mass (3.0g±2.2 vs. 4.7g±3.4, P=0.551), but with wideband SPOT image quality was significantly improved (2.1±1.1 vs. 3.9±0.4, P<0.05) and device-related artefact drastically reduced (2.1±1.1 vs. 3.8±0.5, P<0.01), allowing improved scar detection and diagnostic. Similarly, no significant differences were found between wideband SPOT and wideband PSIR for scar size (21.9%±17.9 vs. 24.2%±19.6 , P=0.293), scar mass (4.4g±3.4 vs. 4.7g±3.4, P=0.457), device-related artefact (3.9±0.4 vs. 3.8±0.5, P=0.598), but wideband SPOT yielded better image quality (3.0±0.5 1 vs. 3.9±0.4, P<0.05).

Fig.2: Example of wideband SPOT images in a patient with a subendocardial scar and ICD.

Discussion: Wideband SPOT demonstrated comparable performance to wideband PSIR in assessing scar size and mass, but offered significantly improved image quality. Moreover, wideband SPOT sequence enabled device-related artefact-free images, enhancing scar detection and overall diagnostic confidence.
References:
[1] Bustin A, et al., *EP Europace*. 2022;24. doi:10.1093/EUROPACE/EUAC053.594 [2] Gut P, et al., *Magn Reson Med*. 2024;92(5):1851-1866. doi:10.1002/mrm.30162 [3] Gut P, et al., *Diagn Interv Imaging*. 2024. doi:10.1016/j.diii.2024.12.001 [4] Nezafat R, et al., *Magn Reson Med*. 2006;55(4):858-864. doi:10.1002/MRM.20835

In-vivo contrast enhanced T1 mapping for quantitative evaluation of intracranial atherosclerotic plaques

Xiaoqi Lin[1] , Shuwan Yu[1] , Haozhong Sun[1] , Jiaqi Dou[1] , Xiaoming Liu[2] , Ziming Xu[1] , Huijun Chen[1]

1. Center for Biomedical Imaging Research, Tsinghua University, Beijing, China;

2. Union Hospital, Tongji Medical College, Huazhong University of Science and Technology, Wuhan, China

Background and Purpose: Intracranial atherosclerosis is a leading cause of strokes especially in Asian countries [1]. High-resolution MR imaging has shown to enable in-vivo assessment of intracranial atherosclerotic plaques [2, 3]. However, previous research primarily focused on metrics such as plaque burden and relative plaque enhancement [3, 4]. T1 mapping has the potential to surpass traditional T1w MR images as a quantitative biomarker for intracranial plaques. This study attempts to evaluate contrast-enhanced T1 mapping of intracranial plaques using 3D SNAP with golden angle radial k-space sampling (GOAL-SNAP) [5] sequence. **This innovative approach holds promise for advancing our understanding of intracranial atherosclerosis, with ongoing efforts to validate its efficacy.**

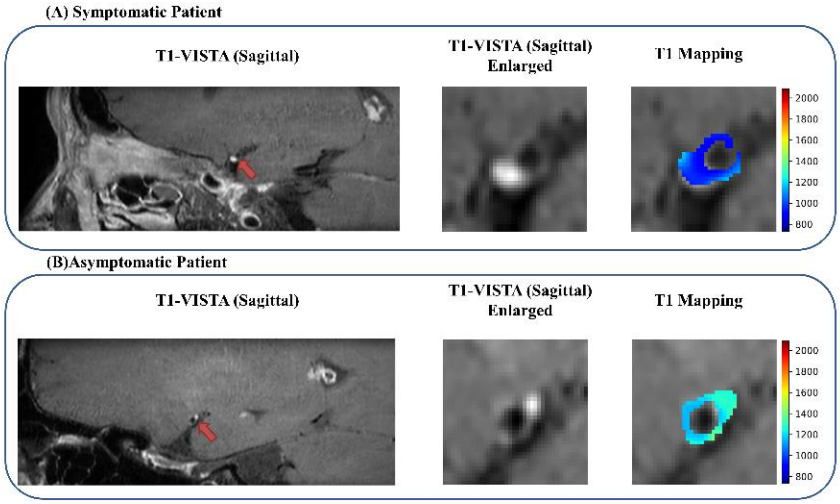

Figure 1. *Symptomatic patients (A) showing lower intracranial plaque T1 values compared to asymptomatic patients (B) on T1 mapping despite having similar intensity enhancement on T1-VISTA.*

Methods: This IRB-approved study enrolled 14 patients with middle cerebral artery (MCA) plaques. MR imaging was performed on a 3T scanner (Ingenia CX, Philips Healthcare, Best, The Netherlands) with a 32-channel head coil. MCA stenosis was localized using axial 3D time-of-flight (TOF) MR angiography. Both pre- and post-gadolinium enhanced 3D T1-weighted black-blood turbo-spin-echo sequences with variable flip angles with Delay alternating with nutation for tailored excitation (T1 DANTE-VISTA) and GOAL-SNAP images were acquired. The imaging parameters employed in this study are detailed in **Table 1**. Since plaques were less visible on post-contrast GOAL-SNAP, delineation was performed on post-contrast DANTE-VISTA images, which were then registered rigidly to align with post-contrast GOAL-SNAP images using SimpleITK [6]. Manual segmentation at the most stenotic site was conducted with CASCADE [7], and T1 values were extracted. Statistical analysis, including Mann-Whitney U tests, was performed in SPSS 24.0, with significance set at $p<0.05$.

Table 1. *Imaging Parameters used in this study*

Parameters	3D TOF	DANTE-VISTA	GOAL-SNAP
TR/TE(ms)	22/3.5	800/20	11.3/4.7
Flip Angle	18	90	8
FOV(mm^3)	200x200x84	200x200x60	100x100x100
Resolution(mm^3)	0.4x0.4x1.2	0.6x0.6x0.6	0.7x0.7x0.7
Orientation	Axial	Axial	Axial

Results: Among 14 patients (52.10±12.10 years; 12 males, 9 symptomatic), symptomatic plaques exhibited significantly lower post-contrast T1 values than asymptomatic plaques (804.20±211.06 vs.1176.45±267.35, p=0.029). **Figure 1** demonstrates two plaques with comparable signal intensities on T1-VISTA images, yet the T1 values of the symptomatic plaque are significantly lower than those of the asymptomatic plaque, highlighting its potential for assessing intracranial plaques and improving stroke risk evaluation.

Discussion and Conclusion: The study demonstrates that contrast-enhanced T1 mapping can differentiate symptomatic from asymptomatic intracranial plaques, with symptomatic plaques exhibiting significantly lower T1 values. This novel imaging technique may enhance the assessment of plaque characteristics and stroke risk. While promising, further validation with a larger cohort is needed to confirm its clinical utility.

References: [1] J. S. Kim et al., J Clin Neurol, vol. 1, no. 1, pp. 1-7,2005. [2] A. Lindenholz et al., Radiology, vol. 295, no. 1, pp. 162-170, 2020. [3] C. W. Ryu et al., Neurointervention, vol. 9, no. 1, pp. 9-20,2014. [4] J. W. Song, et al. Stroke, vol. 52, no. 1, pp. 193-202, 2021. [5] H. Qi et al., Radiology, vol. 287, no. 1, pp. 276-284, 2018. [6] R. Beare, et al., J Stat Softw, 86(8), 2018. [7] W. Kerwin et al., Topics in Magnetic Resonance Imaging, vol. 18, no. 5, pp. 371-378, 2007.

Cardiac Multitasking T1/T1ρ: Initial Evaluation in Porcine Myocardial Infarction Model

Haoran Li[1,2], Archana Malagi[2], ChiChi Yang[2], Hsu-Lei Lee[2], Hsin-Jung Yang[2], Suvai Gunasekaran[2]

[1]UCLA, Department of Bioengineering, Los Angeles, California, United States, [2]Biomedical Imaging Research Institute, Cedars-Sinai Medical Center, Los Angeles, California, United States

Purpose: T1ρ mapping is an emerging non-contrast pulse sequence for detecting myocardial fibrosis that would provide enormous potential for assessing myocardial scar in pediatric and adult patients with poor renal function.[1] While cardiac T1ρ mapping has been examined in chronic myocardial infarction tissue, T1ρ has not yet been well understood in regard to what it is measuring in vivo at different stages of myocardial disease.[2] Additionally, using native T1 mapping in conjunction with T1ρ mapping could be a way to further elucidate myocardial tissue characterization.[3] Therefore, we aim to develop a robust Multitasking (MT) T1/T1ρ sequence that can characterize myocardial tissue without the need for contrast. In this study we propose a MT T1/T1ρ multitasking sequence that is being initially evaluated in baseline scans in a porcine myocardial infarction model. **Methods:** Pulse Sequence: We modified a previously described MT T1/T1ρ sequence that was designed for imaging the brain at 3T.[4] The sequence was updated to three spin locking times of 0, 28, and 56 ms. The sequence was imaged in a short axis view with field-of-view of 240 x 240 mm^2 in-plane resolution of 1.0x1.0mm^2, and slice thickness of 3.5 mm with a scan time was 3:06 minutes. Phantom: An ISMRM/NIST phantom (model 106, CaliberMRI, Boulder, Colorado) was scanned on a 3T scanner (Biograph mMR, Siemens). Reference protocols for phantom study included inversion recovery spin echo for T1 mapping and previously published T1ρ values from the same phantom for T1ρ mapping.[5] Animals**:** For this initial evaluation in vivo, this study included 3 pigs during their baseline scan prior to myocardial infarction. Scans were performed on a 3T scanner (MAGNETOM Vida, Siemens). The protocol included the proposed MT T1/T1ρ mapping at base, mid, and apex slices. Image Reconstruction and Processing: T1ρ data were reconstructed using the multitasking reconstruction framework. The reconstructed images are represented as a sixteen-dimensional low-rank tensor consisting of spatial factor matrix and the temporal dimensions containing information of T1 and T1ρ recovery. Multiparametric maps were fitted from reconstructed image series.[6]

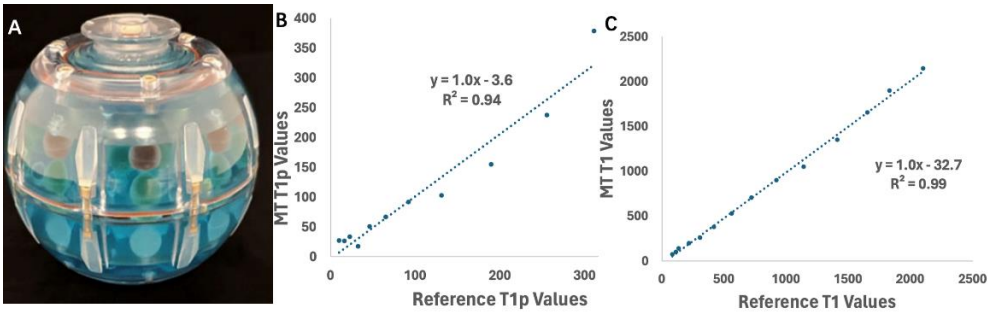

Figure 1. (A) ISMRM/NIST phantom. (B) Correlation of MT T1 and reference T1. (C) Correlation of MT T1ρ and reference T1ρ.

Results: Our phantom results demonstrate a strong correlation between MT T1 mapping and reference and MT T1ρ with reference (Pearson correlation of 0.99 and 0.96, respectively) (Fig. 1). In vivo our T1 and T1ρ mapping we demonstrate good image quality (Fig. 2,3). Average T1 was 1500 ± 36 ms T1ρ was 39.1 ± 1.1 ms. **Discussion:** This study demonstrates that our proposed MT T1/T1ρ is a robust sequence that correlates strongly with reference protocols. Additionally, we can see excellent image quality in vivo at 3T (Figure 2,3). Average T1 values were in the same range as previously published values.[7] Average T1ρ values were a bit lower than previously published values, but this could be due to our pigs being scanned baseline while previous research only scanned after chronic infarction.[2] As this study has just begun, we could only test our sequence on healthy pigs but we will be following the animals after infarction to see changes in T1 and T1ρ and comparisons to LGE over time. Furthermore, we will examine the myocardium ex vivo to compare the T1 and T1ρ tissue characterization with histology.

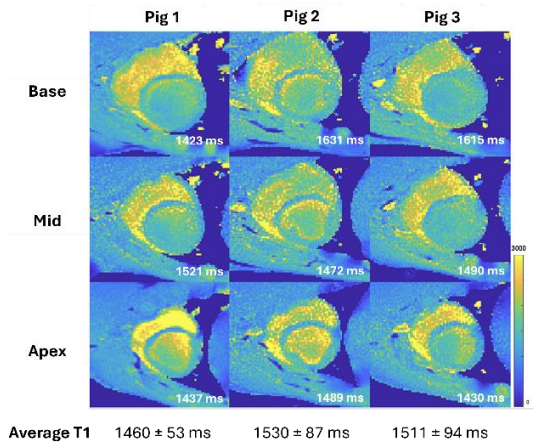

Figure 2. Base, mid, and apex T1 maps for each animal with slice T1 measurements

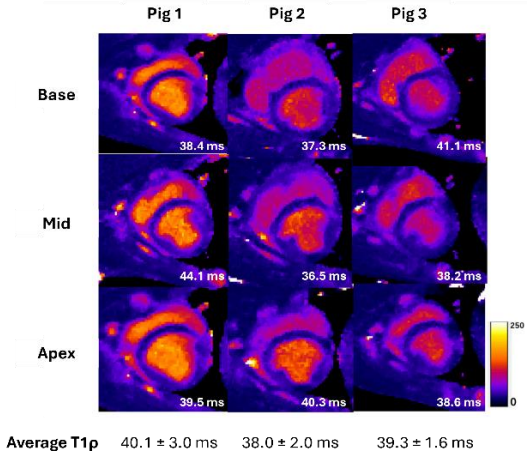

Figure 3. Base, mid, and apex T1ρ maps for each animal with slice T1ρ measurements

References: 1. Bustin et. al. JCMR 2023, 2. Witschey et. al. JCMR 2012, 3. Kali et. al. JACC: CI, 4. Ma et. al. MRM 2021, 5.Monga et. al. JMRI, 6. Cao et. al. MRM 2021, 7. Zhuang et. al. RCTI 2023

Myocardial oxygenation is compromised only in severe fibrotic regions in patients with ischemic heart failure

Jinhan Qiao, MD[1], Keyan Wang, MD[1], Ran Li, PhD[2], Cihat Eldeniz, PhD[2], Liya Dai, MD[2], Caleb Berbert, BS[2], Qi Huang, PhD[2], Yang Yang, PhD[3], Jie Zheng, PhD[2]

[1] The First Affiliated Hospital of Zhengzhou University, Zhengzhou, China

[2] Washington University in St Louis, St. Louis, Missouri, USA

[3] University of California at San Francisco, San Francisco, California, USA

Purpose Altered myocardial oxygenation was indicated in patients post-myocardial infarction (MI) due to impaired mitochondrial function, reduced microvascular integrity, and/or increased fibrotic tissue [1]. Past studies used positron emission tomography (PET) to demonstrate non-invasive and quantitative assessment of changes in myocardial oxygen metabolism in patients with myocardial ischemia, but the PET modality involves a relatively long scan time (> 2 hours), irradiation, and is much less available. Hence, we are leveraging our new cardiovascular MR (CMR) technique in quantification of myocardial oxygen extraction fraction (mOEF) to evaluate such oxygen metabolic changes in patients with ischemic heart failure.

Methods Twenty three patients (Age: 62 ± 12 years, 16 Male, left ventricle ejection fraction or LVEF: 35 ± 14%, NYHA II: 5/23, III: 15/23, IV: 3/23) with ischemic heart failure (HF) determined by x-ray angiography, clinical history, and/or echocardiography were prospectively recruited after signing consent forms. Additional 10 patients (Age: 40 ± 13 years, 9 Male, LVEF: 63 ± 10%) without any cardiovascular disease/history were recruited as a control group. The CMR were performed on a 3T clinical MR scanner (Skyra, Siemens healthineer, Erlangen, Germany). All subjects underwent cine imaging for strain quantification, as well as native T1, mOEF, post-contrast T1, and late gadolinium enhancement (LGE) scans. Myocardial extracellular volume (ECV) was quantified based on native and post-contrast T1. Myocardial mOEF maps were reconstructed by a supervised deep learning network [2]. Segmental measurements on maps based on 16-segment AHA model was performed for statistical analysis.

Results (1) In patients, myocardial global mOEF correlates moderately with rate-pressure product (RPP) (r = 0.42, p = 0.04), where ECV and native T1 are not related to RPP. This indicates mOEF may be the only index related to myocardial oxygen consumption.
(2) Comparing to the controls, patients with heart failure had lower mOEF (0.52 ± 0.1 vs. 0.59 ± 0.05, p< 0.001) and higher ECV (34 ± 9% vs, 25 ± 2%, p<0.001). Between mOEF and ECV in these patients, no correlation was observed when ECV < 40%, but a mild negative correlation exists when ECV >= 40% (r = -0.34, p = 0.002). This is similar to observation with the LGE presence (mOEF: 0.54 ± 0.08, LGE< 50% vs. 0.43 ± 0.12, LGE ≥ 50% p < 0.001)
(3) Myocardial segmental mOEF is significantly lower subtended by obstructive coronary artery stenosis (≥ 50%) than those by non-obstructive stenosis (< 50%), regardless 1-, 2-, or 3-vessel obstruction.
(4) Using a model combining mOEF, native T1, and myocardial strain values, the non-contrast imaging can predict LGE > 50% with AUC = 0.85 and sensitivity/specificity = 83% / 79%.

Examples of mOEF map, ECV map, and LGE are shown in the **Figure**, in which the patient at top panel had only severe LAD stenosis and the patient at bottom panel had three mild or moderate coronary artery stenosis. The color scale for ECV is 0-100% and for mOEF is 0-1.

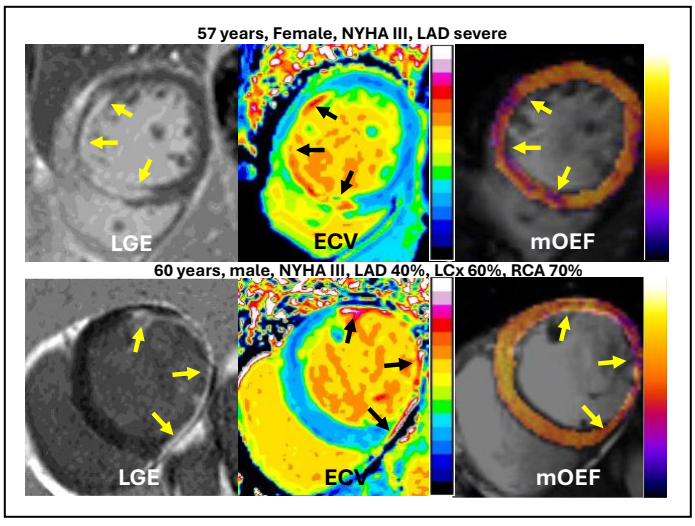

Discussion The novel non-contrast mOEF technique reveals that relatively severe myocardial fibrosis with ECV larger than 40% induces reduced oxygen metabolism in ischemic heart failure. This altered cardiac oxygenation appears to be related to severity of stenosis, but not to number of stenotic coronary arteries.

References 1. Frantz S, et al. European Heart Journal. 2022;43: 2549-2561. **2**. Li R, et al. Radiology Advances, 2024; 1(4).

Multi-echo Propeller Sampling for T_1-T_2-T_2^*-FF Cardiac MR Multitasking

Lingceng Ma[1,2], Hsu-Lei Lee[3], Debiao Li[1,3], Aleksandra Radjenovic[2], and Anthony G. Christodoulou[1,2]
[1]University of California, Los Angeles; [2]University of Glasgow; [3]Cedars-Sinai Medical Center

INTRODUCTION Myocardial T_1, T_2, T_2^* and fat fraction (FF) mapping can diagnose and prognosticate myocardial diseases[1,2]. MR Multitasking allows free-breathing, non-ECG-triggered simultaneous myocardial T_1/T_2/T_2^*/FF mapping[3], with multi-echo readouts acquiring the same radial line within each TR. To increase multi-echo sampling efficiency of T_1-T_2-T_2^*-FF Multitasking and thus SNR/precision, we introduced propeller-like EPI sampling into Multitasking with a randomized pre-phase gradient, thus providing more complementary/incoherent spatiotemporal information along the multi-echo dimension.

METHOD The proposed propeller Multitasking sequence for T_1-T_2-T_2^*-FF mapping (Fig. 1A) introduces a randomized pre-phase gradient before each echo train (Fig. 1B), resulting in a uniform-random phase encoding perpendicular to the radial direction (Fig. 1C); blip gradients between the multi-echo readouts achieve a propeller-like asymmetric EPI blade (Fig. 1D); rational-approximation-of-golden-angle (RAGA)[4] temporal ordering satisfies Nyquist sampling requirements with limited unique trajectories to preserve computational efficiency. Healthy volunteer scans (n=9) were performed on a 3T scanner (Prisma, Siemens). T_1-T_2-T_2*-FF Multitasking data were acquired with the originally published radial sequence[3] and the proposed propeller sequence with 11 echoes, at 1.7mm x 1.7mm x 8mm spatial resolution. Each scan lasted 2.5 min during free-breathing and without ECG triggering. T_1, T_2, T_2*, and FF maps were estimated from the reconstructed multidimensional images and then were analyzed. Agreement between radial and propeller Multitasking was assessed by Bland-Altman analysis. Local precision (related to SNR) was assessed by the within-septum coefficient of variation (CoV); a one-tailed paired t-test tested whether propeller sampling increased T_1/T_2/T_2^*/FF mapping precision (decreased CoV).

RESULTS Propeller Multitasking maps qualitatively displayed higher SNR (Fig. 2A). Septal values from radial and propeller generally agreed (Fig. 2B). Quantitative analysis confirmed the higher SNR of propeller, indicated by a lower within-septum CoV for T_2^* (P = 0.008) and FF (P = 0.008) measurements when compared to radial (Table 1).

DISCUSSION The propeller Multitasking sequence provides more multi-echo incoherence than radial Multitasking, producing more precise T_2^* and FF measurements in the septum. Future enhancements to the reconstruction model to incorporate stronger multi-echo modeling may further exploit the incoherence offered by the proposed propeller sequence, potentially improving precision further or reducing scan times.

CONCLUSION We presented a non-ECG free-breathing propeller Multitasking sequence for T_1/T_2/T_2^*/FF mapping in the myocardium. This sequence offers a foundation for incorporating multi-echo modeling to further improve imaging efficiency.

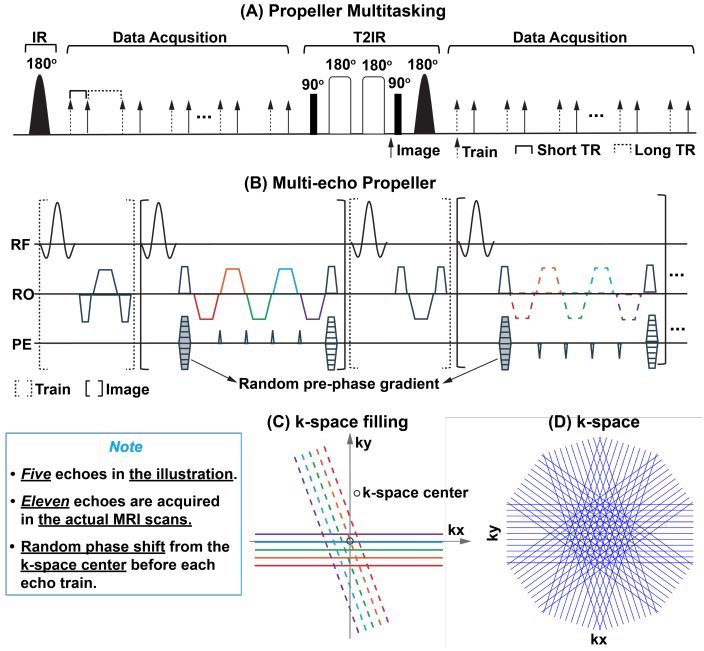

Fig.1. (A) T_1-T_2-T_2^*-FF Multitasking sequence. (B) Random pre-phase gradients between multi-echo readouts realize propeller k-space filling (C). (D) RAGA propeller k-space.

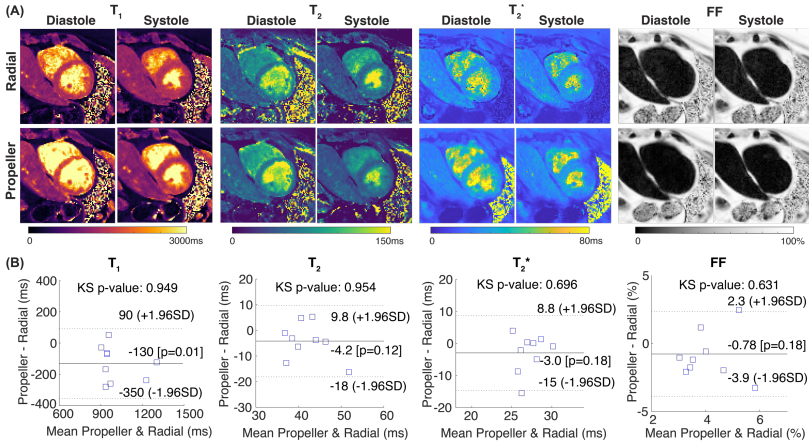

Fig.2. (A) T_1, T2, T2*, FF maps from radial and propeller Multitasking. (B) Bland-Altman plots for measurements from radial and propeller Multitasking.

Table 1 Within-septum CoV of T_1, T_2, T_2^* and FF values

	T_1 Cov	T_2 Cov	T_2^* Cov	FF Cov
Radial	0.205 ± 0.064	0.203 ± 0.062	0.233 ± 0.067	0.235 ± 0.067
Propeller	0.174 ± 0.051	0.173 ± 0.050	0.163 ± 0.043	0.164 ± 0.044
One-tail P value	0.099	0.097	0.008	0.008

1. Pennell DJ, et al. *Circulation*. 2013;128(3):281-308.
2. Kenchaiah S, et al. *J Am Coll Cardiol*. 2021;77(21):2638-2652.
3. Cao T, et al. *Magn Reson Med*. 2022 88(4):1748-1763.
4. Scholand N, et al. *Magn Reson Med*. 2025; 93(1): 51-66.

High accuracy cardiac MR images acquired with autonavigator software in patients with implantable cardiac devices

Hadas Shiran[1], Raymond Y. Kwong[2], Michael Salerno[3], Bob S. Hu[1,4]
[1]Palo Alto Medical Foundation, Palo Alto, CA, USA. [2]Brigham and Women's Hospital, Boston, MA, USA.
[3]University of California, San Francisco, CA, USA. [4]Vista.ai, Palo Alto, CA, USA

Purpose: The main objective of this research is to examine the accuracy of artificial intelligence (AI)-driven auto-navigation software for localizer sequences for cardiac MR studies in an initial set of patients with implantable cardiac devices. The goal is to achieve adequate localization in the presence of significant device artifacts.

Methods: We identified 30 patients with implantable cardiac devices with images acquired between 4/2023 and 3/2025 at Palo Alto Medical Foundation in Palo Alto, CA using the acquisition software from Vista.ai (Palo Alto, CA). While this software incorporates navigation, sequence parameter tuning, image quality monitoring, and analysis, we focused only on the navigation component in this study. Of the study patients, 4 were excluded due to incomplete image availability. Of the remaining 26 patients, 9 female and 17 male, with an average age of 71 years, images were reviewed for accuracy of the AI navigation localization process. Secondarily, image quality was assessed for diagnostic utility. All patients had implantable cardiac devices, of which 2 were implantable loop recorders, 19 were dual chamber pacemakers, and 5 were implantable cardioverter-defibrillator (ICD). Some patients had additional implants including prosthetic valves and prior valve repairs (n=4). Localization accuracy was judged based on how much auto-scanning required manual adjustment.

Results: Auto localization performed extremely well with few needed adjustments. Of the 2 patients with implantable loop recorders, both had excellent accuracy (no adjustments needed). Of the 19 patients with dual chamber pacemakers, we classified patients based on adjustments needed with 17 requiring no adjustment, of which 6 were noted to have substantial artifacts that did not affect localization but did affect image quality. One study required one significant adjustment. One patient had a large pleural effusion that necessitated aborting the study and sending the patient to the emergency department. Of the ICDs, 4 patients did not require adjustments and in 1 patient we were unable to eliminate artifacts despite multiple attempts at shimming and wide-band imaging, and the study was aborted. In total, 90% of pacemaker patients and 80% of ICD patients had excellent or good slice placements without the need to adjust AI-driven protocols.

Discussion and conclusions: This is the first study to demonstrate that auto-navigator localizer sequences can be used in the setting of implantable cardiac devices. Other studies with Vista.ai software have already demonstrated AI-guided cardiac MR leads to improved image quality and reliability in >1000 patients(1). A much smaller study of 82 patients, using different software, excluded device patients(2). Diagnostic performance in patients with devices(3),(4) with assessments of image quality and which sequence types are most prone to artifacts(5),(6) is also known. However, to date, there has not been significant experience for use of automated techniques in patients with cardiac devices. We have demonstrated feasibility of use of auto-localization with no need for manual adjustment to the protocols despite substantial artifacts in up to 90% of patients. However, in the limited number of studies in which adjustments were needed, image artifacts were substantial. Image quality remains a challenge, especially with ICDs, which will require further research and may be difficult to improve with AI techniques.

References: 1. Kwong RY, et al. *JACC* 2023; 81(8_Supplement):1363–1363. 2. Glessgen C, et al. *Eur Radiol* 2025. 3. Schwitter J, et al. *Circ Cardiovasc Imaging* 2016; 9:e004025. 4. Sasaki T, et al. *Circ Cardiovasc Imaging* 2011; 4:662–670. 5. Naehle CP, et al. *Am Heart J* 2011; 161:1096–1105. 6. Muthalaly RG, et al. *Radiology* 2018; 289:281–292.

RV diastolic function evaluated by CMR-derived metrics

Dana C. Peters[1], Jie Xiang[2], Jerome Lamy[3], Ipek Buber[1], [1]Yale University Department of Radiology, and [2]Biomedical Engineering. . [3] Interdisciplinary University of Paris, Paris, France.

Introduction: Right ventricular (RV) diastolic dysfunction is observed in various conditions, including pressure and volume overload pathologies, primary and secondary lung diseases, pulmonary arterial hypertension, ischemic heart disease, congenital heart disease, cardiomyopathies, and the physiological aging process. It may also serve as a marker of elevated right-sided pressure. While echocardiography is the most common technique used to evaluate diastolic function, the assessment of RV diastolic function is often overlooked. In this study, we aimed to investigate RV diastolic function parameters (RV E/A ratio and RV E/e') using MRI and compare them to tricuspid regurgitant jet velocity (TRV), which reflects elevated right-sided pressure when exceeding 2.8 m/s, as per ASE guidelines.

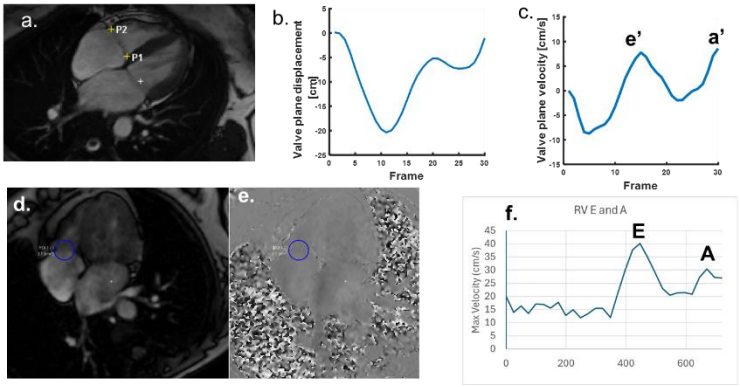

Figure 1: Methods for RV diastoilc function evalution of e', a' and E and A. A-C. RV valve-tracking for e'. D-F. Earlly diastolic tricuspid filling measurement of RV E and A, using an RV ROI.

Methods: Eighteen patients (4 men, mean age 54 ± 15 years) with suspected left ventricular (LV) diastolic dysfunction and preserved RV and LV systolic function, as determined by echocardiographic evaluation were prospectively enrolled. All patients underwent transthoracic echocardiography (with a measurable tricuspid regurgitant jet) and cardiac MRI within 52 ± 48 days. Using a deep learning network to track tricuspid valve motion (Figure 1A–C), we measured RV early (e') and late (a') diastolic velocities. RV E and A wave velocities were analyzed using long-axis-encoded phase contrast imaging (Figure 1D–F). Additionally, indexed RV volumes and EF were obtained. These RV metrics were compared to estimated pulmonary artery systolic pressure (PASP), calculated from tricuspid regurgitant jet velocity (PASP = $4v^2$), and to the presence of abnormal LV diastolic function.

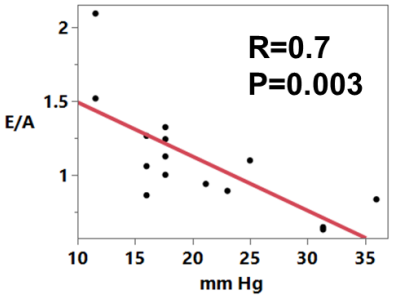

Figure 2:RV E/A was a strong correlate of echo-derived PASP.

Results: RV E/A exhibited a very strong correlation to PASP pressure (Figure 2, R=-0.70, p=0.003). Other tested RV metrics of RVEDVi, RVESVi, RVEF, E, A, E/e', A/a', and e'/a' were not correlated to estimated PASP. LV E/A and E/e' were also not correlated, although LV E/A was correlated well to RV E/A (R=0.66, p=0.005). In analysis of RV diastolic metrics, based on presence or absence of any LV diastolic dysfunction, we found that PASP was elevated in diastolic dysfunction (19 ±6 mm Hg vs. 29 ±9 mm Hg, p=0.01), and that RV E/A trended lower (1.2 ±.4 vs. 095. ±0.20, p=0.14).

Discussion: An early echocardiographic study (1) identified the E/A ratio as a strong correlate of (PASP) estimated by echocardiography. More recently, another echocardiography study (2) reported that the ratio of indexed right atrial area to RV systolic velocity was the strongest surrogate for RV end-diastolic elastance, as estimated by catheterization, while E/A and E/e' ratios failed to show significant correlations. Recent reviews (3) highlight that RV diastolic dysfunction may represent an early marker of RV heart failure, underscoring the importance of its evaluation. Furthermore, the RV E/e' ratio has been shown to estimate mean right atrial pressure (RAP) with reasonable accuracy (4). According to our findings, RV diastolic E/A was correlated with LV diastolic parameter E/A, with RV E/A demonstrating a particularly strong relationship with PASP. A decreasing trend in the E/A ratio, driven by an increase in the A wave—like the pattern seen in LV early diastolic dysfunction—may reflect elevated RAP.

1. Yu CM et al., Circulation 93(8) 1996. 2. Yogeswaran A et al. ERJ Open Res 2023 Sep 18;9(5):00226-2023. 3. YH Jung et al, Heart Failure Reviews 2022. 4. D'Andrea A et alJ Cardiol. 2017

Simultaneous magnetic resonance imaging technique of carotid artery perivascular adipose tissue and vessel wall: A feasibility and repeatability study

Shuwan Yu[1], Shuo Chen[2], Zihan Ning[1], Huiyu Qiao[1], Ning Xu[1], Xihai Zhao[1]

[1] Center for Biomedical Imaging Research, Tsinghua University, Beijing, China

[2] Shanghai United Imaging Healthcare, Shanghai, China

Background and Purpose: Studies have demonstrated that both atherosclerotic (AS) plaque vulnerability and perivascular adipose tissue (PVAT) inflammation are independently associated with cerebrovascular symptoms[1,2]. Therefore, it is essential to conduct non-invasive joint assessment of carotid AS plaque and PVAT for better stratifying the risk of ischemic cerebrovascular events. This study aimed to develop a simultaneous magnetic resonance (MR) imaging technique for carotid artery PVAT and vessel wall.

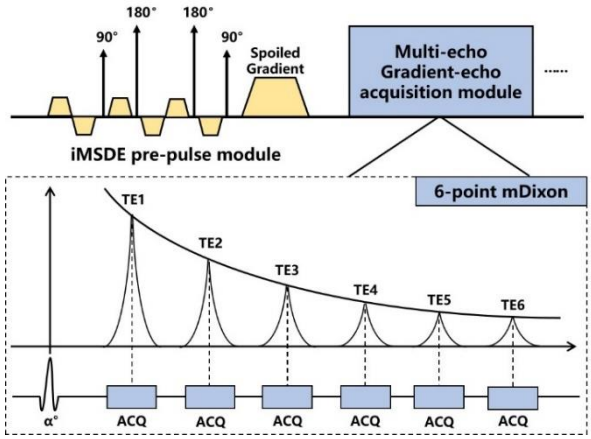

Figure 1. iMSDE-mDIXON sequence design diagram.

Methods: We proposed an integrated MR imaging protocol combining iMSDE with mDIXON, termed iMSDE-mDIXON (Figure 1). Seventeen healthy subjects and nine patients with carotid AS underwent MR imaging experiments, including five healthy subjects selected for repeatability testing. The iMSDE-mDIXON, MERGE, and mDIXON sequences were performed for bilateral carotid imaging. The reliability of iMSDE-mDIXON sequence was assessed by evaluating its agreement with MERGE sequence in measuring carotid wall morphology (lumen area [LA], wall area [WA], mean wall thickness [MWT], normalized wall index [NWI]) and with mDIXON sequence in quantifying carotid PVAT (PVAT area, PVAT area index [PVAT-AI], PVAT volume index [PVAT-VI], proton density fat fraction [PDFF]). The interclass correlation coefficient (ICC) and Bland-Altman plots were used for statistical analysis.

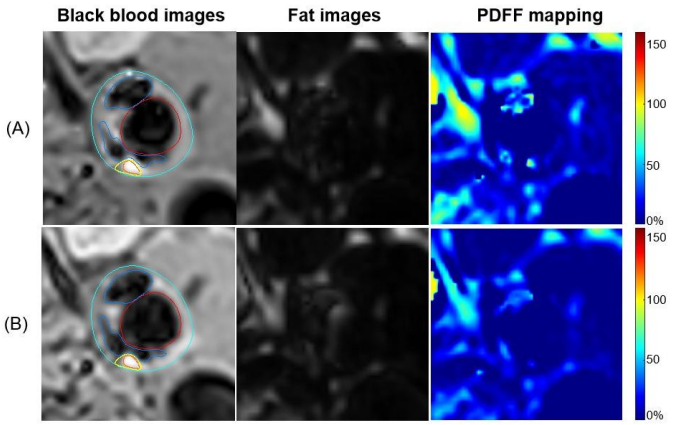

Figure 2. Comparison of iMSDE-mDIXON and reference sequences (MERGE and mDIXON). (A) iMSDE-mDIXON images of a carotid AS patient (male, 81 years); (B) reference images of the same carotid AS patient.

Results: The example of MR imaging results is shown in Figure 2. The iMSDE-mDIXON technique exhibited high reliability in assessing carotid vessel wall morphology (ICC: healthy subjects, 0.903-0.997; patients: 0.928-0.999) and PVAT morphology (ICC: healthy subjects: 0.906-0.988; patients: 0.957-0.996) (Table 1). While the technique demonstrated potential for carotid AS assessment, it exhibited a substantial bias (>20%) in PDFF quantification. Notably, a moderate to excellent agreement was maintained between iMSDE-mDIXON and mDIXON in measuring PVAT PDFF in both healthy subjects (ICC: left, 0.782; right, 0.740) and AS patients (ICC: left, 0.790; right, 0.628) (Table 1). In addition, the proposed sequence showed excellent agreement in quantifying carotid vessel wall (ICC = 0.845-0.999) and PVAT morphology (ICC = 0.841-0.989) between the repeated scans.

Table 1. ICC between iMSDE-mDIXON and reference sequences.

	Healthy subjects		AS patients	
	Left	**Right**	**Left**	**Right**
LA, mm^2	0.994	0.997	0.999	0.998
WA, mm^2	0.990	0.989	0.979	0.980
MWT, mm	0.989	0.974	0.985	0.928
NWI	0.903	0.934	0.940	0.950
PVAT area, mm^2	0.988	0.951	0.996	0.979
PVAT-AI	0.974	0.929	0.990	0.957
PVAT-VI	0.968	0.906	0.992	0.970
PVAT PDFF, %	0.782	0.740	0.790	0.628

Discussion and Conclusion: This study proposed an iMSDE-mDIXON sequence which enables simultaneous imaging of the carotid vessel wall and PVAT in a single scan with high efficiency, reliability, and repeatability. This technique has considerable potential for joint characterization of the changes of PVAT and pathology of vessel wall in carotid artery.

References: [1] Bos D., J Am Coll Cardiol, 2021, 77(11):1426-1435. [2] Baradaran H., J Am Heart Assoc, 2018, 7(24): e010383.

Aspirin Use is Associated with Reduced Aneurysm Wall Enhancement in Patients with Unruptured Intracranial Saccular Aneurysms: a Large-scale Multi-center Study

Pengjun Jiang[1], Qingyuan Liu[1], Shuo Wang[1], Chengcheng Zhu[2]

1. Neurosurgery, Tiantan Hosptial, Beijing, China 2. Radiology, University of Washington, Seattle, USA

Background: Aneurysm wall enhancement (AWE) on vessel wall MRI is a critical risk factor for the symptomatic presentation of intracranial aneurysms [1] and it is associated with aneurysm growth and rupture. Histology validation studies showed that it is associated with aneurysm wall inflammation and remodeling. However, the role of aspirin, a classic nonsteroidal anti-inflammatory drug (NSAID), in modulating AWE in intracranial saccular aneurysms remains inconclusive [2]. Previous studies studying AWE and medication use were limited by small sample sizes and single study design [3]. This study aims to investigate the relationship between Aspirin use and AWE in a large-scale multi-center cohort.

Methods: This study conducted a cross-sectional analysis of patients with unruptured intracranial saccular aneurysms from three prospective clinical trails: IARP-CP cohort (unique identifier: ChiCTR1900024547) , the 100-Project phase I cohort (NCT04872842) and phase II cohort (NCT05608122). The cohorts were from 82 medical centers in China. All included patients underwent high-resolution vessel wall imaging (HR-VWI) with 3.0T MRI scanners, including pre- and post-Gd enhancement images, with a resolution of 0.6mm isotropic. Clinical data and imaging information were collected, and AWE patterns were classified into three grades based on HR-VWI: Grade 0 (no enhancement), Grade 1 (focal wall enhancement), and Grade 2 (circumferential wall enhancement). Aspirin use was defined as ≥100 mg at least three times per week for 6 months or longer. Ordinal logistic regression was employed to identify independent factors associated with AWE pattern.

Results: A total of 1270 patients (age 56 (IQR 48-63), 704 female) with complete HR-VWI data, encompassing 1333 aneurysms (size median 5.8mm), were included. Among these, 720 aneurysms (54.0%) exhibited no enhancement (Grade 0), 372 (27.9%) Grade 1 enhancement, and 241 (18.1%) Grade 2 enhancement. Ordinal multi variable logistic regression analysis revealed that aspirin use, hypertension (HP), aneurysm size, non-ICA locations, BMI and irregularity were independent risk factors for AWE (Table). Aspirin use was associated with lower AWE with OR 0.50 (0.35, 0.73). Notably, atorvastatin use did not demonstrate statistical significance.

Conclusions and Discussion: This study indicate a strong association between long-term aspirin use and reduced AWE severity, suggesting that aspirin may delay clinical progression through mitigating aneurysm wall inflammation. This study provides novel insights to the role of nonsteroidal anti-inflammatory drug on aneurysm wall inflammation and provides new evidence for the pharmacological management of patients with intracranial aneurysm. Future longitudinal studies are required to confirm these findings.

Variables	Univariate		Multivariate	
	P	OR (95%CI)	*P*	OR (95%CI)
Sex	0.619	0.95 (0.77 ~ 1.17)		
Hypertension	**<.001**	1.91 (1.54 ~ 2.36)	**<.001**	1.99 (1.58 ~ 2.51)
Diabetes	0.536	1.15 (0.74 ~ 1.79)		
Dyslipidemia	0.147	1.24 (0.93 ~ 1.67)	0.157	1.31 (0.90 ~ 1.90)
ICCD	0.449	1.15 (0.80 ~ 1.66)		
Aspirin	**<.001**	0.54 (0.38 ~ 0.76)	**<.001**	0.50 (0.35 ~ 0.73)
Statin	**0.002**	1.67 (1.21 ~ 2.30)	0.057	1.46 (0.99 ~ 2.14)
Irregularity	**<.001**	1.70 (1.32 ~ 2.19)	**0.046**	1.32 (1.01 ~ 1.74)
Age	0.103	1.01 (1.00 ~ 1.02)	0.759	1.00 (0.99 ~ 1.01)
Size	**<.001**	1.27 (1.22 ~ 1.33)	**<.001**	1.22 (1.17 ~ 1.28)
BMI	**<.001**	0.78 (0.74 ~ 0.82)	**<.001**	0.86 (0.81 ~ 0.90)
Location (ICA ref)				
ACA/ACOM	**<.001**	2.18 (1.55 ~ 3.06)	**0.015**	1.55 (1.09 ~ 2.22)
MCA	**<.001**	1.58 (1.21 ~ 2.05)	**0.024**	1.38 (1.04 ~ 1.82)
PCA/PCOM	**<.001**	2.14 (1.44 ~ 3.19)	**0.027**	1.61 (1.05 ~ 2.46)

ICCD: Ischemic cerebrovascular and cardiovascular diseases, OR: Odds Ratio, CI: Confidence Interval

References:

[1] Zhu C, Wang X, et,al Eur Radiol. 2020 Dec;30(12):6413-6420.

[2] Weng JC, et al. Stroke. 2020 Oct;51(10):3045-3054.

[3] Xia J, et al. Transl Stroke Res. 2024 Dec;15(6):1133-1141.

A 3D steady-state CEST sequence for non-invasive measurement of cerebral blood components at 3T

Chuyu Liu[1], Zhensen Chen[2,3], Zhongsen Li[1], Nan Gao[1], Xiaolei Song[1]

[1]Center for Biomedical Imaging Research (CBIR), School of biomedical engineering, Tsinghua University, Beijing, China [2]Institute of Science and Technology for Brain-Inspired Intelligence, Fudan University, Shanghai, 200433, China [3]Key Laboratory of Computational Neuroscience and Brain-Inspired Intelligence (Fudan University), Ministry of Education, 200433, China

Purpose: Cerebral blood components can reflect the metabolism of focal lesions. As a molecular imaging tool that can detect many labile protons on glucose, proteins and peptides, etc., CEST is potential to observe the spatial-temporal metabolic changes in cerebral arteries and veins [1-3]. In this study, we developed a 3D steady-state CEST sequence for non-invasive measurement of cerebral blood components at 3T.

Methods: ***Sequence Design*** The schematic of the proposed pulse sequence is shown in Figure 1, where each unit contains a series of Gaussian-shape saturation pulses and a gradient echo acquisition. The acquisition window is short enough to ensure the small interval between saturation blocks, and further allows the in-flow blood to be continuously labeled. To obtain z-spectra of blood in a 3D FOV within an acceptable scan time, we adopted a steady-state CEST strategy. Since CEST effect accumulates over time, the proposed sequence uses a high-low view order to ensure the k-space center signals have more CEST effect. Besides, the saturation field is much larger than the imaging field to avoid unsaturated blood flow into imaging FOV. Noteworthy, the gradient echo acquisition brings bright blood contrast to the image. ***MRI experiments*** We conducted repeated experiments to verify the repeatability of the proposed sequence. Eight healthy subjects were scanned at a 3T scanner (Ingenia, Philips Healthcare) with a 32-channel coil. All volunteers signed the written informed consent. 34 frequency offsets varying from -8 to 8 were performed at 2.5 μT within 14 minutes. Other scan parameters were: saturation time of 100 ms, FOV of 160 x 160 x 60 mm^3 (2 imaging slabs), resolution of 1 x 1 x 1.2 mm^3, TFE factor of 15. The blood CEST sequence was repeated twice within the scan sessions to evaluate the measurement repeatability, by calculating the intraclass correlation coefficient (ICC) at 4 vessel locations (i.e., right M1, left M1, basilar artery and vein around the torcular). Paired t-test was performed between 4 vessel locations.

Results: ***Repeatability analysis*** The ICC values and the corresponding P values are shown in Table 1. Moderate to excellent repeatability was obtained for both the normalized Z spectra and MTR asymmetry. ***3D metabolic maps of cerebral vessels*** 3D maps of MTRasym and LD at 2 ppm are depicted in Figure 2, illustrating the capacity of the proposed sequence to obtain 3D spatial metabolism distribution of blood. Noteworthy, signals of arteries and veins are quite different. One possible reason is that arterial blood contains more oxygen and glucose than venous blood.

Conclusion: This study proposed a 3D steady-state CEST sequence for non-invasive measurement of cerebral blood components. Preliminary results illustrated the potential value in the diagnosis and evaluation of blood metabolism-related diseases.

	Normalized Z value @1.2 ppm		Normalized Z value @2 ppm		MTR asymmetry @1.2ppm		MTR asymmetry @2ppm	
	ICC	*P*	ICC	*P*	ICC	*P*	ICC	*P*
Right M1	0.663	0.022	0.867	0.001	0.828	0.002	0.797	0.015
Left M1	0.649	0.033	0.873	0.001	0.896	0.002	0.79	0.037
BA	0.842	0.04	0.829	0.008	0.983	<0.001	0.883	<0.001
Vein	0.523	0.047	0.723	0.008	0.541	0.062	0.691	0.018

Table 1. Repeatability of the proposed CEST sequence for human cerebral vessels at 1.2 ppm and 2 ppm.

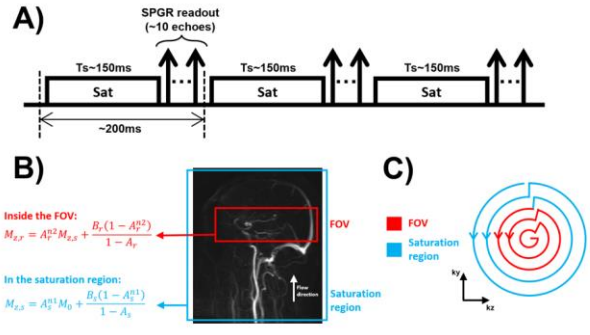

Figure 1. Principle of the proposed CEST sequence for vessel imaging. (A) The schematic of the steady-state pulse sequence. (B) The imaging FOV and saturation field. (C) The sequence adopted spiral high-low view-order to ensure the k-space center signal has more CEST effect.

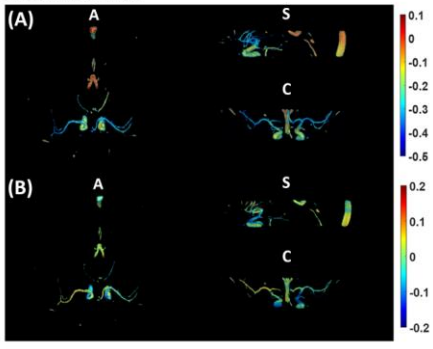

Figure 2. 3D spatial distribution of MTR asymmetry (A) and Lorentzian Difference (B) at 2 ppm. Blood CEST signals in arteries and veins have significant differences.

References: [1] Cui J, et al. Magn Reson Med. 2022. [2] Shah SM, et al. Neuroimage.2017. [3] Zheng S, et al. Magn Reson Med. 2014.

Reduced perivascular cerebrospinal fluid pulsation in patients with ischemic stroke

Qiuting Wen[1], Xiaopeng Zhou[2], Caixia Fu[3], Bing Tian[4], Chengcheng Zhu[5]

[1] Indiana University School of Medicine, Indianapolis, IN, USA; [2] School of Health Sciences, Purdue University, West Lafayette, IN, USA; [3] Siemens Shenzhen Magnetic Resonance Ltd., Shenzhen, China. [4] Changhai Hospital, Shanghai, China. [5] University of Washington School of Medicine, Seattle, WA, USA

PURPOSE: Over half of stroke survivors develop cognitive impairment within a year, with glymphatic dysfunction potentially contributing to neurodegeneration. pCSF flow, driven by arterial pulsation, is crucial for waste clearance[1]. Rodent studies show that arterial ligation reduces arterial pulsatility, leading to impaired glymphatic exchange[2]. However, how cerebrovascular abnormalities affect pCSF pulsation in humans remains unclear. This study aimed to investigate pCSF alterations in ischemic stroke patients with unilateral middle cerebral artery (MCA) stenosis, using the contralateral hemisphere as a control. Dynamic diffusion-weighted imaging (dynDWI) was used to assess pCSF pulsation around major cerebral arteries.

METHODS: We recruited 97 ischemic stroke patients (age 58±13, 27 males, 70 females) with unilateral MCA-M1 atherosclerotic plaque from a tertiary hospital. Stenosis severity was classified as Uni50- (<50% narrowing), Uni50+ (>50% narrowing), and Bi50-50+ (bilateral stenosis with asymmetry). MRI was performed on a Siemens Skyra 3T scanner. DynDWI (b=150 s/mm²) was acquired along three diffusion directions (60 repetitions), with concurrent finger photoplethysmography recording. Data-driven segmentation identified pulsatile pCSF regions. Paired t-tests and Wilcoxon tests (if non-normal) compared pCSF volume between hemispheres, with false discovery rate correction.

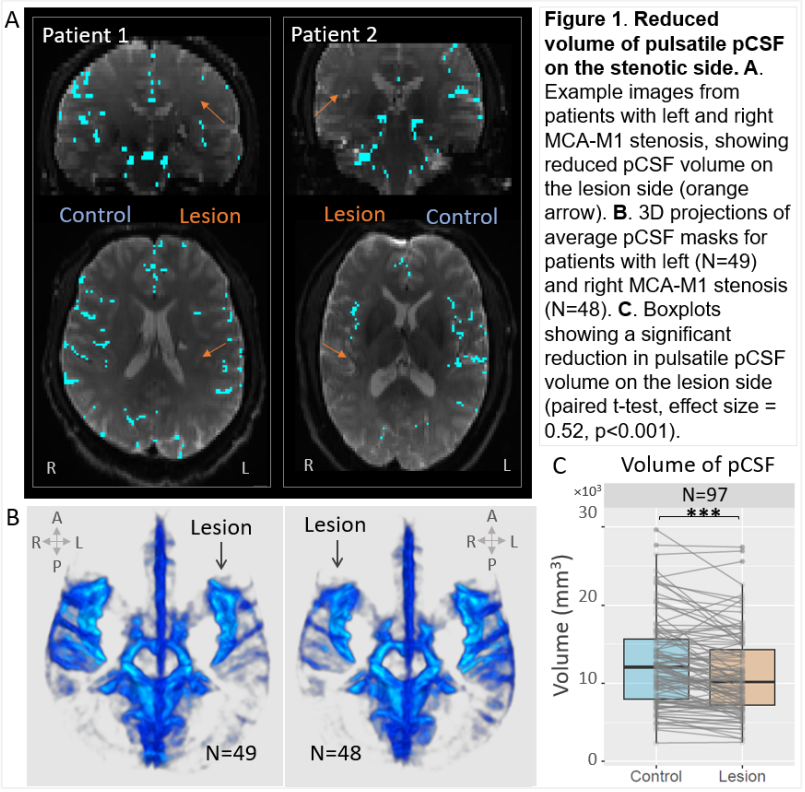

Figure 1. Reduced volume of pulsatile pCSF on the stenotic side. A. Example images from patients with left and right MCA-M1 stenosis, showing reduced pCSF volume on the lesion side (orange arrow). **B**. 3D projections of average pCSF masks for patients with left (N=49) and right MCA-M1 stenosis (N=48). **C**. Boxplots showing a significant reduction in pulsatile pCSF volume on the lesion side (paired t-test, effect size = 0.52, p<0.001).

RESULTS: Significant reduction in pulsatile pCSF volume was observed on the lesion side (**Figure 1**), both individually (**Figure 1A**) and at the group level (**Figure 1B**). The lesion side had a 12% volume reduction compared to the control side ($p < 0.001$, Cohen's $d = 0.52$, **Figure 1C**).

Specific reductions along MCA: Among three main arteries, pCSF reduction was significant only along the MCA ($p < 0.001$, Cohen's $d = 0.43$), but not along the PCA or ACA. Interestingly, PCA displayed a slight increase in pCSF volume, likely indicative of compensatory effects ($p = 0.02$, effect size = -0.28). MCA reductions were primarily in the m2 segment distal to the stenosis ($p < 0.001$, Cohen's $d = 0.65$), with no reduction in MCA-m1 ($p = 0.9$).

Greater stenosis, greater pCSF reduction (**Figure 2**): Patients with Uni50+ stenosis exhibited the largest between-hemispheric pCSF reduction (14% reduction than control side, $p < 0.001$, Cohen's $d = 0.6$), followed by Bi50-50+ (10%, $p < 0.05$, Cohen's $d = 0.43$) and Uni50- (3%, $p = 0.34$, Cohen's $d = 0.3$). On the control side, pCSF volumes ranked as follows: Uni50- > Uni50+ > Bi50-50+ (**Figure 2B**).

DISCUSSION: These findings provide human evidence that arterial stenosis reduces pCSF pulsatility, consistent with animal studies linking reduced arterial pulsatility to impaired glymphatic flow. The most pronounced reductions occurred downstream in MCA-M2, indicating broader disruptions to CSF circulation and waste clearance. This diminished pCSF pulsation may contribute to the high incidence of neurodegeneration in stroke patients, highlighting the dual impact of cerebrovascular conditions on both blood flow and CSF dynamics.

1. Mestre et al, Nat Commun 2018, PMID: 30451853; 2. Iliff et al, J Neurosci 2013, PMID: 2422772.

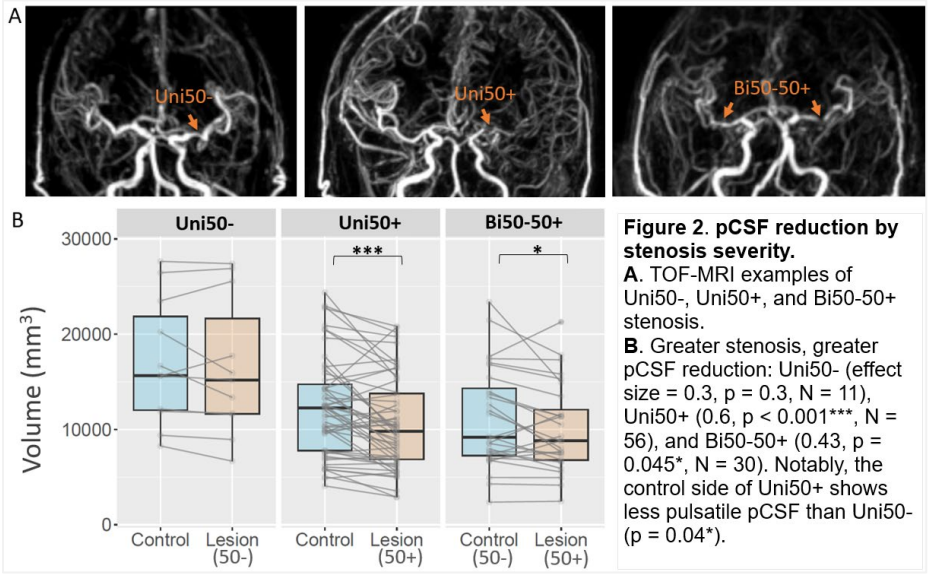

Figure 2. pCSF reduction by stenosis severity.
A. TOF-MRI examples of Uni50-, Uni50+, and Bi50-50+ stenosis.
B. Greater stenosis, greater pCSF reduction: Uni50- (effect size = 0.3, p = 0.3, N = 11), Uni50+ (0.6, p < 0.001***, N = 56), and Bi50-50+ (0.43, p = 0.045*, N = 30). Notably, the control side of Uni50+ shows less pulsatile pCSF than Uni50- (p = 0.04*).

Motion-Robust Quantitative Multi-Contrast Atherosclerosis Characterization

Meng Lu[1], Yin-Chen Hsu[1], Debiao Li[1,2], and Yibin Xie[1], on behalf of the DTECT Consortium

[1]Biomedical Imaging Research Institute, Cedars-Sinai Medical Center, Los Angeles, CA, United States, [2]Department of Bioengineering, University of California Los Angeles, Los Angeles, CA, United States

Purpose: Carotid atherosclerosis is a major etiology for ischemic stroke. Multi-contrast vessel wall imaging is effective in identifying high-risk atherosclerotic plaques. However, carotid vessel wall imaging is susceptible to various types of motion, such as arterial pulsatile, breathing, and bulk motion resulting from swallowing and coughing. A substantial proportion of carotid scans are corrupted by motion artifacts resulting in nondiagnostic exams or patient recalls. A multi-center carotid imaging study reported that 15% of the scans acquired had unacceptable imaging quality due to motion[1]. Recently we proposed a new vessel wall imaging method, quantitative multi-contrast characterization of atherosclerosis (qMATCH), which markedly shortens scan time and provides an all-in-one dataset for carotid plaque imaging. However, motion artifacts and data corruption may still manifest in challenging patients. In this work, we propose improved imaging reconstruction and post-processing methods to increase the motion robustness of qMATCH.

Methods: Two motion compensation (MoCo) strategies were developed to address the impact of motion. First, motion binning was applied during the image reconstruction of qMATCH data. Navigator data were analyzed and clustered for up to 6 distinct motion states and the entire scan data were separated into 6 different motion bins accordingly. An additional motion dimension was introduced in the image model and all motion states were individually resolved [2]. The motion bin with the least intra-bin motion variation was chosen for the subsequent post-processing and image synthesis. Second, residual motion artifacts were suppressed by region-optimized virtual (ROVir) coils method. The ROVir method determines the optimal coil weightings to maximize the signal-to-interference ratio, which enhances the signal from the ROI and suppresses the signal outside [3]. ROI was defined as a rectangular area containing the carotid arteries. To test the effectiveness of the proposed motion compensation strategies, 8 qMATCH datasets with different magnitudes of motion artifacts were selected from the DTECT multi-center study for testing. The datasets were reconstructed twice, one with the proposed MoCo method and the other without. Imaging precision was qualified using coefficient of variance (CoV) analysis of the carotid vessel wall regions and compared between the two reconstructions.

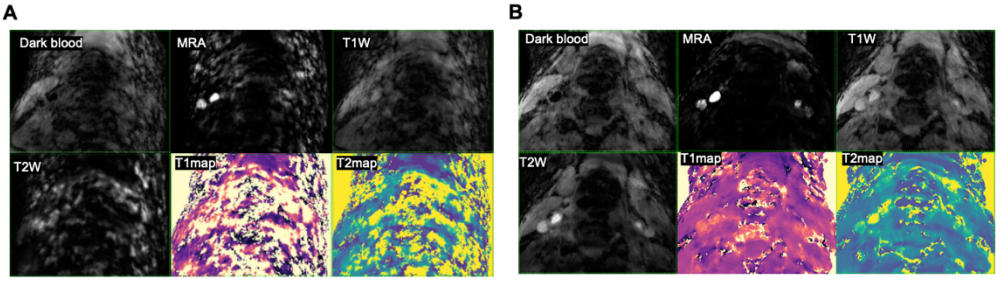

Fig 1. Comparison of image quality and vessel wall visualization before and after the proposed MoCo method in a representative case. Panel A shows the original qMATCH image set without MoCo and Panel B shows the images after the application of MoCo.

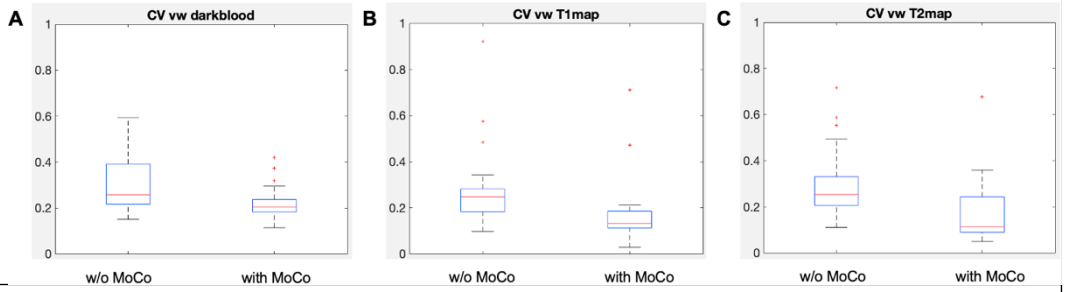

Fig 2. Comparison of imaging precision (CoV) before and after the proposed MoCo method. For each subplot, the left box plot shows the results from the original motion corrupted images; and the right box plot shows the results from the proposed method.

Results: The proposed MoCo method substantially reduced the level of motion artifacts and enhanced the delineation of the vascular anatomies in all 8 testing cases. **Fig 1** shows a representative qMATCH dataset before and after the application of the proposed MoCo method. **Fig 2** shows the comparison in image precision, indicating that the resultant images exhibited significant improvements in image precision for vessel wall signal values, T1 values, and T2 values, as evidenced by a lower CoV value in all cases after MoCo ($p<0.001$).

Discussion: The proposed motion compensation method effectively mitigates motion artifacts and enhances vessel wall visualization for qMATCH carotid vessel wall imaging. It also improves the precision of quantitative mapping. Further validation in a larger cohort is required to validate the current findings.

References:

1. Boussel L, et al. *Radiology* 2009, 252(3):789–796
2. Ma S, et al. *Magn Reson Med* 2022, **87**(1):102-119.
3. Kim D, et al. *Magn Reson Med* 2021, **86**(1):197-212.

Acknowledgement:

This work was partly supported by NHLBI R01HL159200, VA-MERIT I01CX002208 and VA-MERIT I01CX001901.

Carotid MRA using Centric k_y-k_z 3D FFE and Black Blood Imaging with T_2 Prep before BB pulses

V. Malis,[1] H. Jung,[1] Y. Kuwatsuru,[1] M. Miyazaki[1]

1. Dept. of Radiology, University of California-San Diego (UCSD), La Jolla, CA

Introduction: Carotid MRA and vessel wall imaging remains challenging due to the long scan times associated with Time of Flight (TOF) and Black Blood (BB) imaging. In BB vessel wall imaging, the major issue is the contrast between the vessel wall and dark blood, which affects visualization of the vessel wall and surrounding tissues, especially at the carotid bifurcation. This study aims to develop fast, non-contrast carotid WB MRA and vessel wall BB imaging utilizing a zigzag centric k_y-k_z 3D trajectory and T_2 Prep.

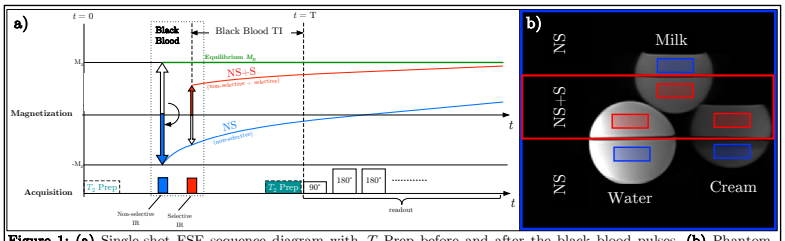

Figure 1: (a) Single-shot FSE sequence diagram with T_2 Prep before and after the black blood pulses. **(b)** Phantom contains water (T_1/T_2=2500/1300 ms), milk (T_1/T=1500/70 ms), and cream (T_1/T_2=900/50 ms), mimicking long T_2 fluid, venous blood, and muscle tissue, respectively. The imaging plane experiences double inversion (non-selective (NS) and selective (S)) pulses and is marked by red box, blood experiences only NS pulse and is marked by blue box.

Methods: For WB imaging, coronal 3D cFFE was optimized with T_2 Prep TE of 65 ms to suppress venous and tissue signals. For vessel wall imaging we developed a simulation tool to optimize sequence configuration and improve the contrast of vessel wall over dark blood. In BB imaging T_2 Prep module was implemented 1) before (T_2 Prep-BB-ACQ) and 2) after (BB-T_2 Prep-ACQ) the BB double inversion and tested it on a phantom containing various T_2 components. **Figure 1a** shows the sequence diagram of vessel wall imaging using 3D single-shot FSE with T_2 Prep module before and after the BB pulses. **Figure 1b** shows phantoms with various T_1/T_2 values: water (T_1/T_2=2500/1300 ms) for long T_2 components like fluid, milk (T_1/T_2=1500/70 ms) for venous blood, and cream (T_1/T_2=900/50 ms) for muscle tissues.[1] After the simulation and phantom studies, four healthy subjects underwent the carotid MRA and vessel wall imaging on a clinical wide-bore 3T scanner (Vantage Galan 3T, Canon Medical Systems Corp., Japan). A zigzag centric k_y-k_z k-space trajectory[2-4] was utilized in both: WB MRA used 3D FFE (cFFE) and BB employed 3D single-shot FSE (cSSFSE).

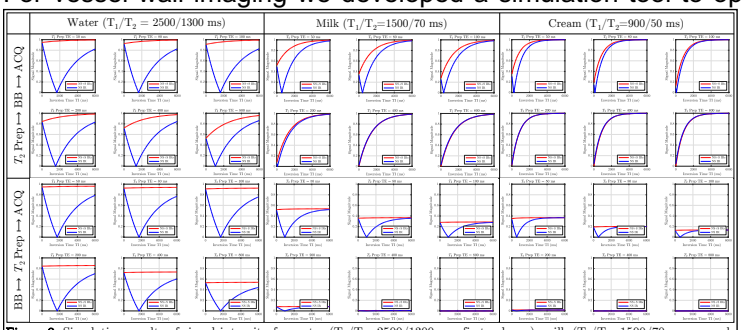

Figure 2. Simulation results of signal intensity for water (T_1/T_2=2500/1300 ms, first column), milk (T_1/T_2=1500/70 ms, second column), and cream (T_1/T_2=900/50 ms, third column) under two configurations T_2 Prep before BB (top row) or BB before T_2 Prep (bottom row) followed by ACQ. The red line indicates non-selective (NS) and selective (S) IR pulses and blue line shows only non-selective IR pulse. With increasing T_2 Prep TE from 50 to 800 ms, T_2 Prep after BB (bottom row) shows decreasing signals as T_2-weighted, whereas T_2 Prep before BB (top row) shows similar curves in NS+S and S in shortening T_2 values.

Results: **Figure 2** shows the simulation plots for water, milk, and cream, mimicking fluid, venous blood, and muscles, respectively. The phantom results show similar signal magnitude to the simulation (not shown). **Figure 3** presents the phantom images of water, milk, and cream. T_2 Prep before BB shows good signal intensities, even with short T_2 components, while T_2 Prep after BB shows regular T_2-weighted images with diminishing short T_2 signals. **Figure 4** shows cTOF, peripheral pulse-gated (PPG) cFFE (coronal acquisition), and vessel wall imaging using T_2 Prep before BB with T_2 Prep=300 and 400 ms. Coronally acquired cFFE using PPG show good signal intensity of carotid arteries like cTOF MIP. T_2 Prep before BB gave good background signals of muscle and vessel wall signals similar to the phantom study of short T_2 components.

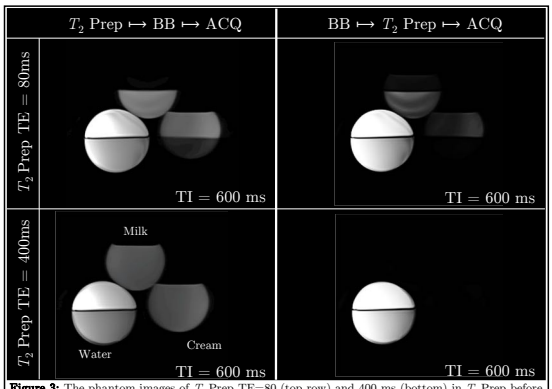

Figure 3: The phantom images of T_2 Prep TE=80 (top row) and 400 ms (bottom) in T_2 Prep before BB (left panel) and after BB (right panel). Note that T_2 Prep after BB shows T_2-weighted images with diminishing short T_2 values of milk (T_2=70 ms) and cream (T_2=50 ms). On the other hand, T_2 Prep before BB pulses shows enhanced signals of shorter T_2 values of milk and cream.

Discussion: The simulation results closely matched the phantom results, validating the accuracy of simulation tool. The analysis demonstrated that placing the T_2 Prep module after the BB pulses provided the most effective suppression of short T_2 signals (**Figure 3**). For WB imaging, T_2 Prep with TE=65 ms was applied just before the readout to suppress the background signals (**Figure 4b**). For BB imaging, applying T_2 Prep before BB pulses achieves regaining of short T_2 signals in muscle and vessel walls in black blood imaging.

Conclusion: We developed WB cFFE by applying T_2 Prep TE=65 ms to suppress vein and background signals in sub-60-seconds imaging. In BB imaging, we also achieved good contrast between vessel walls and black blood by regaining surrounding signals using T_2 Prep before BB pulses.

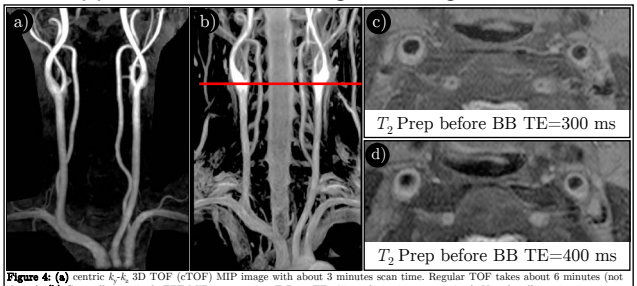

Figure 4: (a) centric k_y-k_z 3D TOF (cTOF) MIP image with about 3 minutes scan time. Regular TOF takes about 6 minutes (not shown). **(b)** Coronally acquired cFFE MIP image using T_2 Prep TE=65 ms (<1 minute scan time). Vessel wall imaging images at the red line in b) using T_2 Prep before BB images using T_2 Prep TE 300 ms in **(c)** and 400 ms in **(d)**. T_2 Prep after BB gives T_2-weighted images with diminished background signals (not shown). T_2 Prep TE=300 and 400 ms in c) and d) show good contrast between vessel wall and black blood with higher surrounding signals.

References:

[1] Jones C., *et al*., *Magn Reson Imaging.* 1998;16(1):83-5.
[2] Miyazaki M., *et al*., *Magn Reson Med Sci.* 23(2), 171-83 (2024).
[3] Malis V., *et al*., *Magn Reson Med Sci.* 23(1), 66- 79 (2024).
[4] Ota H., *et al*., *MAGMA;* 37:1105-117 (2024).

Acknowledgements: Research grant to M.M. from Canon Medical Systems Corp., Japan (35938).

High-resolution 3D carotid vessel wall MRI without a custom-designed coil using deep-learning denoising

Xiangjian Hou[1,2], Bradley D. Bolster, Jr.[3], David Carpenter[4], Hua Guo[5], Chun yuan[1], and Xiaodong Ma[1]

[1]Department of Radiology and Imaging Sciences, University of Utah; [2]Department of Electrical and Computer Engineering, University of Utah; [3]Siemens Medical Solutions USA, Inc., Salt Lake City; [4]SiemensMedical Solutions USA, Inc., Denver; [5]Center for Biomedical Imaging Research, Department of Biomedical Engineering, Tsinghua University.

Purpose: 3D vessel wall MRI (VWI) has emerged as a new imaging tool for evaluating carotid atherosclerosis[1,2]. To achieve high spatial resolution ($< 1mm$) necessary for good visualization of wall morphology and plaque components, 3D carotid VWI usually combines with a custom-designed carotid coil to ensure adequate SNR. However, the custom-designed carotid coil is not available for all institutes or hospitals, limiting the broad application of 3D carotid VWI in research studies and clinical practice. In this study, we aim to develop a deep-learning-based denoising framework to achieve high-resolution 3D carotid VWI without a custom-designed carotid coil.

Methods: *Data acquisition and preprocessing:* 3D carotid vessel wall MRI data were acquired on a Siemens 3T Prisma-fit scanner using a vendor-provided 20-channel head-neck coil combined with a custom-designed neck-shape-specific carotid surface coil.[3] The simultaneous non-contrast angiography and intraplaque hemorrhage (SNAP) sequence[4] were applied for demonstrative purposes, with a spatial resolution of $0.83\ mm$ isotropic and acquisition time of 6.5 minutes (coronal view, no acceleration was used). The images without custom-designed coil (i.e., noisy images) were reconstructed offline by removing k-space data acquired with custom-designed coil elements. There were 13 patients in the sample, each providing 80 slices. We then applied z-normalization to the noisy images to ensure the noise distribution is not clipped. We retained pixel values between the 0.6% and 99.5% quantiles for the ground truth, followed by normalization. The threshold selection was based on manual evaluation.

Deep-learning-based denoising framework: We proposed to use a Transformer-based model, Restormer [5], for denoising carotid vessel wall MRI data. Specifically, we implemented a channel-wise attention block as the backbone of the reconstruction model, which has lower demand in computation resources and also better performance (Fig. 1). CNN-based method, DnCNN[6] and traditional denoising method, BM3D[7] were also implemented for comparison purposes.

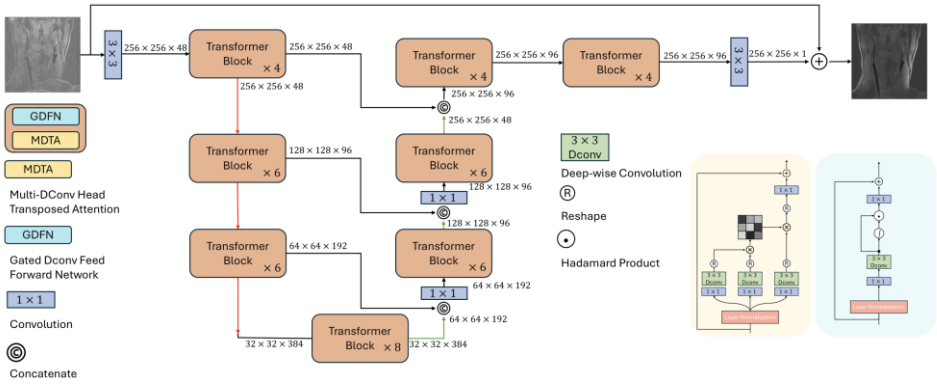

Fig. 1. Overview of the Restomer model, image adapted from [5].

Model training and evaluating: We employed the AdamW optimizer with a learning rate of 0.001. The data was split into training/validation/test sets in a $9:2:2$ ratio. Early stopping was implemented when the SSIM on the validation set did not increase by 0.02 over 5 epochs to prevent the model from converging to a local optimum. We used random rotations and flips for data augmentation and adopted the l_1 loss function. Since the model uses $2D$ inputs, all normalization was completed during preprocessing to avoid brightness differences between slices. The batch size was set to 4, and all experiments were conducted on a single NVIDIA RTX A100 80GB GPU. We used PSNR and SSIM metrics to evaluate the model's performance.

Results and Discussion: As shown in Fig. 2, Restormer significantly outperforms the other methods in metrics and visualization. During visual assessments, we observed that the model's output (i.e., denoised images) have well-maintained vessel wall structures, although they tend to be overly smooth. Additionally, slight brightness flickering between slices existed since only coronal views were used as 2D input. Validation on patient data will be done in future.

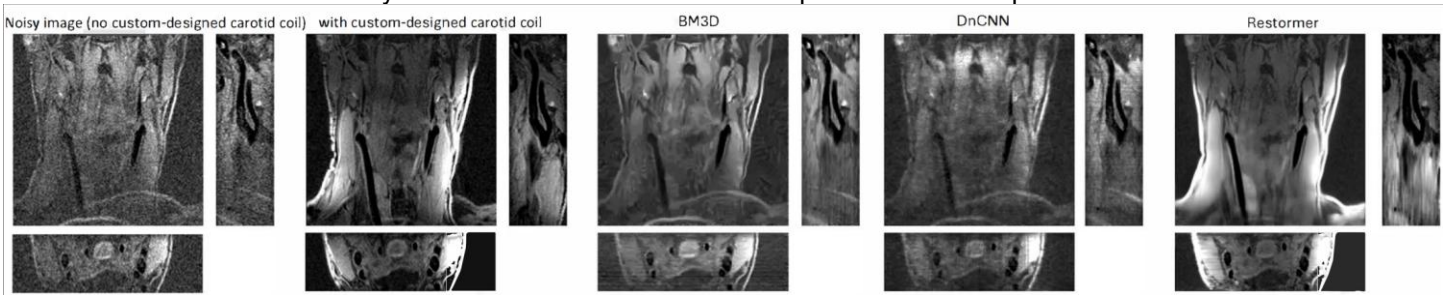

Fig 2. Results on one test subject. The representative slices in 3 views around the bifurcation were displayed.

Conclusion: Using the proposed deep-learning denoising framework, Restormer, the image quality of 3D carotid VWI without custom-designed carotid coil is comparable with VWI with carotid coil. It shows promise for enabling high-resolution 3D carotid VWI in institutes where a custom-designed carotid coil is unavailable.

References: [1] Yuan C, et al, Radiology 2001, 221(2), 285–29 [2] Tobias Saam, et al, Radiology 2007, 244(1):64–77 [3] Michael J Beck, et al, MRM 2017, 78(6):2460–2468 [4] Jinnan W, et al, MRM 2013, 69(2):337–345 [5] Syed W Zamir, et al, CVPR 2022 [6] Kai Z, et al, TIP 2017, vol. 26, no. 7, pp. 3142-3155 [7] Kostadin D, et al, TIP 2007, 16(8):2080–2095

Simultaneous High-Spatial-Resolution Quantitative Brain T1 Mapping and MR Angiography Using 3D Golden-Angle Radial k-Space Sampling in 5T

Haozhong Sun[1], Ne Yang[2], Yajie Wang[1], Haikun Qi[3], Haokun Li[1], Rui Li[1], Jiaqi Dou[1], Ziming Xun[1], Xiaoqi Lin[1], Runyu Yang[1], Zhongsen Li[1], Huijun Chen[1]

1. School of Biomedical Engineering, Tsinghua University, Beijing, China; 2. United Imaging Research Institute of Intelligent Imaging, Beijing, China; 3. School of Biomedical Engineering, ShanghaiTech University, Shanghai, China

PURPOSE: Intracranial atherosclerosis is a major cause of ischemic stroke [1] and is associated with a high risk of recurrence [2]. Despite its clinical significance, research on intracranial atherosclerosis remains challenging and insufficient. Moreover, while magnetic resonance angiography (MRA) detects stenosis, it alone cannot fully explain the risk of atherosclerotic stroke [3]. Quantitative MR imaging (qMRI) using T1 mapping has been reported [4] to identify elevated stroke risk. This study aims to propose a sequence for simultaneous quantitative brain T1 mapping and MRA at 5T, enabling a comprehensive assessment of intracranial atherosclerosis with high spatial resolution.

METHODS: Simultaneous non-contrast angiography and intraplaque hemorrhage (SNAP) imaging with 3D golden-angle radial k-space sampling (GOAL-SNAP) [5] was originally proposed for carotid intraplaque hemorrhage imaging, as shown in Fig. 1. In this study, we adapted GOAL-SNAP for simultaneous quantitative brain T1 mapping and MRA, developing it on a 5T platform (uMR Jupiter, United Imaging Healthcare) to achieve high isotropic resolution suitable for the small intracranial arteries. First, we assessed the accuracy of T1 mapping in a phantom study using nine tubes with T1 values ranging from 200 to 900 ms at 5T. A 2D IR turbo spin-echo (TSE) sequence served as the reference The GOAL-SNAP was set with the following parameters: field of view (FOV) = 100×100×100 mm³, spatial resolution = 0.69×0.69×0.69 mm³, TR = 14.4 ms, IRTR = 2000 ms, TFE factor = 155, and scan time = 6 min 51 s. A healthy male volunteer (61 years old) provided consent for GOAL-SNAP scanning at both 3T (Philips Healthcare, Best, The Netherlands) and 5T. Additionally, axial 3D time-of-flight (TOF) MR angiography (FOV = 200×188×84 mm³, spatial resolution = 0.6×0.85×1.2 mm³, scan time = 2 min 05 s) was acquired for comparison.

RESULTS: Fig. 2a shows the T1 maps obtained using the reference IR-TSE, while Fig. 2b presents the T1 maps acquired with GOAL-SNAP at 5T. The scatter plot demonstrates a strong correlation between the T1 values of the nine tubes, with a R^2 of 0.99. The percentage error of GOAL-SNAP at 5T is 6.93% ± 4.83%. Fig. 3 compares MRA images acquired using 3T GOAL-SNAP, TOF, and 5T GOAL-SNAP. In the MIP maps along axial, sagittal, and coronal projections, 5T GOAL-SNAP MRA provides better visualization of small blood vessels (indicated by arrows). The SNR/CNR near small vessels for 5T GOAL-SNAP, 3T GOAL-SNAP, and TOF are 11.9/9.8, 10.5/8.9, and 16.0/15.0, respectively. Fig. 4 displays multi-frame T1-weighted images at different inversion times (TI) to illustrate signal evolution, while the estimated T1 map from GOAL-SNAP at 5T highlights tissue differences but exhibits more noise compared to GOAL-SNAP at 3T.

DISCUSSION: We implemented GOAL-SNAP at 5T for high-spatial-resolution simultaneous quantitative brain T1 mapping and MRA. The phantom study demonstrated excellent accuracy in T1 mapping at 5T. Additionally, 5T GOAL-SNAP provided superior MRA visualization of small arteries compared to 3T GOAL-SNAP (with higher SNR and CNR) and TOF-MRA (revealing more small vessels), which could enhance the detection of small lesions in clinical practice. However, further improvements in image quality are needed to enhance T1 mapping SNR, and field inhomogeneities at 5T should be addressed and corrected. More quantitative comparisons are required for a comprehensive evaluation between 3T and 5T.

REFERENCES: [1] Suri M F K, Johnston S C, et al. Journal of Neuroimaging, 2009, 19(S1): 11S-16S. [2] Chimowitz MI, Lynn MJ, Howlett-Smith H, et al. N Engl J Med 352: 1305–1316. [3] de Havenon, A., Mossa-Basha, M., Shah, L. et al. Neuroradiology 59, 1193–1202 (2017). [4] Steen R G, Langston J W, Reddick W E, et al. Journal of Magnetic Resonance Imaging, 1996, 6(1): 226-234. [5] Qi H, Sun J, Qiao H, et al. Radiology, 2018, 287(1): 276-284.

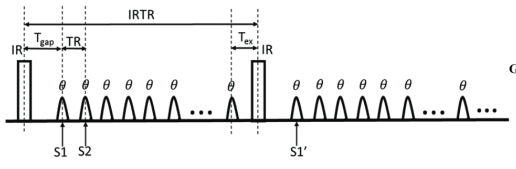

Fig 1. Schematic of GOAL-SNAP sequence.

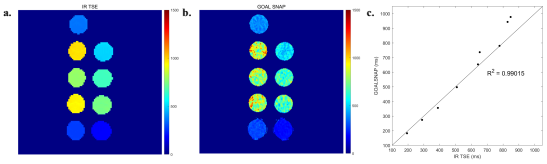

Fig 2. Phantom study in 5T.

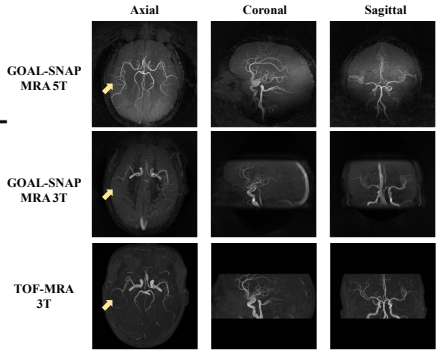

Fig 3. Comparison of MIPs between GOAL-SNAP in 5T, GOAL-SNAP in 3T and TOF-MAR in 3T.

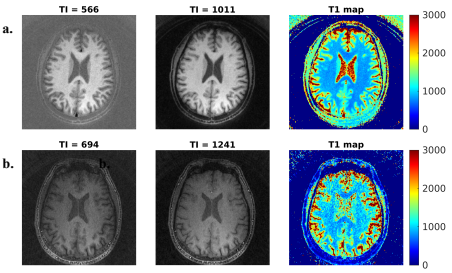

Fig 4. The multi-frame T1-weighted images and estimated T1 map of GOAL SNAP in 3T (a) and 5T (b).

Application of Mask-guided Hybrid Decouped Fourier Block in Carotid Artery Wall Segmentation

Meng Haoding[1], Zheng Chong[2], Ma Peijiang[1], Lu Jie[2], Li Rui[1]
[1]Tsinghua University, Beijing; [2]Xuanwu Hospital, Beijing

Purpose

This study aims to explore a novel mask-guided modulation strategy based on deep learning and its impact on carotid artery vessel wall segmentation performance by fully utilizing multi-frequency information.

Method

Fourier Block Design and Integration The core innovation consists of 5 key sub-modules (Fig1 Left): **Fourier Transform Module:** Converts input feature maps from spatial to frequency domain. **Input Masking Module:** Divides frequency features into bands using masks generated from Manhattan distance calculations. **Nonlinear Frequency Modulation Module:** Applies nonlinear transformations within each frequency band. **Output Masking Module:** Reorganizes processed frequency features using output masks. **Inverse Fourier Transform Module:** Converts features back to spatial domain. The frequency band division strategy involves calculating Manhattan distance from the frequency domain center to generate center distance maps, guiding the creation of input and output masks for partitioning the frequency domain into multiple bands. ***Dataset and Preprocessing*** Experiments were conducted on a clinical head and neck artery MRI dataset with 16 cases, including T1, T2, T1C, TOF, and annotated vessel wall masks. Images have a 64x64x64 field of view and 0.4x0.4x0.8 spacing. ***Network Architecture and Training*** The Fourier blocks are placed in the skip connections of the nnU-Net, combining low-level spatial details with high-level semantic information. 5 fold cross validation training were conducted three times for both the baseline and improved networks with these settings: Learning rate: 1e-2, Weight decay: 1e-4, Epochs: 500, GPU: A800, Bin: 2, Bout: 2.

Result

Results demonstrate significant improvements as shown in Fig1 Right and Tab1 in segmentation performance: **Visual Comparison:** The blue regions represent model predictions, green denotes manual annotations, and red indicates overlaps. The proposed method shows better alignment with manual annotations, particularly in distinguishing vessel walls from surrounding tissues. **Quantitative Metrics:** The improvements are statistically significant across all components compared to the baseline model.

Discussion

This module uses mask-guided frequency division and decoupling to divide the frequency domain feature map into multiple bands, allowing for independent processing of different frequency information and avoiding frequency domain information confusion caused by traditional linear convolution. Additionally, it is a plug-and-play structure that can be easily transplanted into various medical image segmentation tasks.

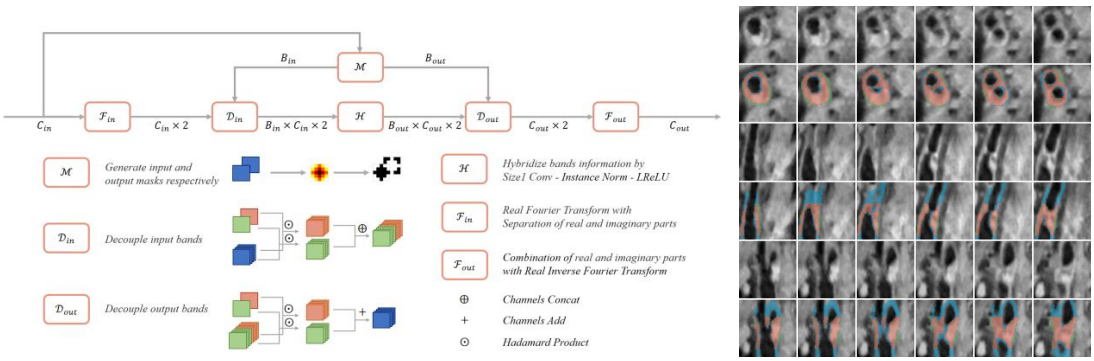

Fig1. The Overview of MHD-Fourier Block (Left) and A Visual Comparison (Right)

Metric	Without	With
Outer Wall	0.6567 ± 0.0105	$\mathbf{0.6827 \pm 0.0084}$
Inner Lumen	0.6209 ± 0.0100	$\mathbf{0.6405 \pm 0.0087}$

Tab1. The Metirc of Models without/with Proposed Design

Surface Coil-Informed Deep Learning Denoiser for Carotid Vessel Wall Imaging

Lisha Zeng[1,2], Lixia Wang[1], Debiao Li[1,2], Yibin Xie[1] on behalf of the DTECT Consortium

[1]Biomedical Imaging Research Institute, Cedars-Sinai Medical Center, Los Angeles, CA, United States, [2]Department of Bioengineering, University of California Los Angeles, Los Angeles, CA, United States

Purpose: Carotid vessel wall imaging yields vital diagnostic insights into atherosclerotic conditions including luminal stenosis and high-risk plaque features - applications that demand high-resolution images with superior signal-to-noise ratio (SNR). However, standard MR head-and-neck are positioned far from the carotid arteries and often fail to provide adequate receiver sensitivity. Specialized carotid surface coils have been developed to boost SNR; however, they are not widely accessible and add substantial workflow challenges. This work aimed to **develop a deep learning (DL) denoiser capable of enhancing images acquired with standard head-and-neck coils alone, achieving SNR and image quality comparable to those acquired with specialized carotid coils.**

Methods: A total of 28 carotid MRI scans acquired as part of an ongoing multicenter study (3.0 T, Siemens Healthineers) were used in this experiment. The scans involved the simultaneous use of a standard 20-channel head-and-neck OEM coil, and a specialized Neck-Shape-Specific (NSS) carotid surface coil [1]. Multi-contrast carotid vessel wall imaging sequences, including 2D T1w TSE, T2w TSE, TOF-MRA, and MPRAGE, were used for image acquisition. Paired images were retrospectively reconstructed from the standard coil elements with and without the NSS coil elements, and used as the input and reference data, respectively. Each contrast-weighted image set was trained by a separate DL model; 5 scans (from 150 to 590 slices per sequence) were reserved for testing, and the other 23 scans (from 690 to 2714 slices per sequence) were used for training and validation at a ratio of 8:2. The network architecture used was an adapted Residual-UNet with skip connections [2]. Before data were fed into the model, preprocessing was performed, including 3D N4 bias correction, background masking, histogram matching and normalization. All slices were zero-padded to squares. Test outputs of the trained networks were qualitatively and quantitatively evaluated using objective metrics including noisiness by σ (signal intensity) in small 5x5 ROIs in the lumen, PSNR, and SSIM. A randomly selected subset of test slices was scored by an expert radiologist for image sharpness at carotid arteries on a 5-point scale. The performance of the proposed method was also compared to two conventional general denoising methods on all the metrics measured.

Results: Figure 1 shows a representative case from the testing dataset, including the DL output, and results from two conventional denoising methods, compared with the input and reference images. Table 1 summarizes the statistics of quantitative metrics of the comparisons on all test sets, including metrics of image sharpness, noisiness, PSNR, and SSIM.

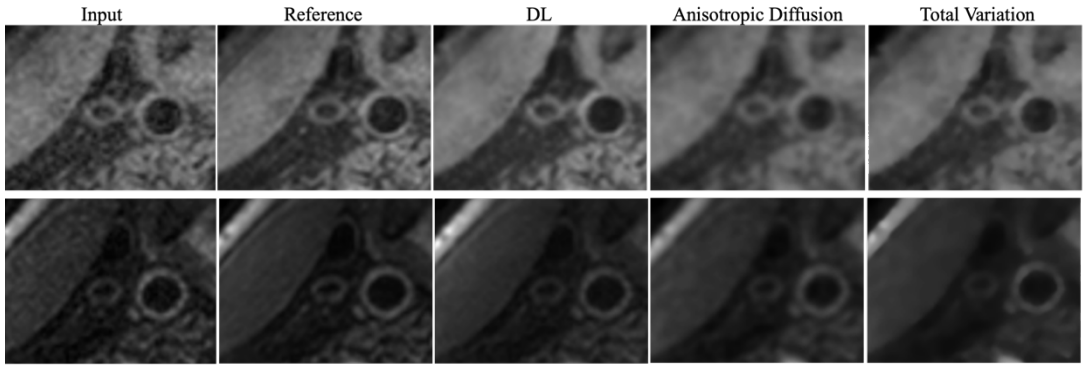

Figure 1. Sample test outputs of DL network for image enhancement vs conventional denoising algorithms. Zoomed-in at the one carotid artery and muscle tissue adjacent, in the transverse view. Images shown are T1w TSE (upper row) and T2w TSE (lower row).

Table 1: Comparison of Quantitative Image Metrics. Slices Mean ± SE are presented. Paired t-tests or Wilcoxon tests were performed between DL output and input for Noisiness (n=25), PSNR, and SSIM; and between traditional methods and DL for the sharpness score (n=10). (*p < 0.05 ** p < 0.01)

Sharpness Score	**Input**	**Output DL**	**Anisotropic**	**TV**	**Reference**
T1w TSE	3.2±0.20	3.5**±0.17	2.2±0.14	2.6±0.22	3.8±0.14
T2w TSE	3.2±0.20	3.8**±0.13	2.8±0.13	2.4±0.22	3.7±0.21
MPRAGE	2.8±0.38	3.4**±0.17	1.1±0.19	0.9±0.28	3.8±0.13
TOF-MRA	2.7±0.22	3.1**±0.18	2.3±0.15	2.3±0.15	3.1±0.23
Noisiness	**Input**	**Output DL**	**Anisotropic**	**TV**	**Reference**
T1w TSE	0.039±0.002	0.016**±0.002	0.013±0.001	0.008±0.001	0.020±0.002
T2w TSE	0.019±0.001	0.007**±0.001	0.007±0.001	0.006±0.001	0.012±0.001
MPRAGE	0.029±0.003	0.020**±0.002	0.011±0.002	0.007±0.002	0.026±0.003
TOF-MRA	0.037±0.003	0.028*±0.002	0.022±0.002	0.018±0.002	0.029±0.002
PSNR	**Input vs Ref**	**DL**	**Anisotropic**	**TV**	**Output vs Ref**
T1w TSE	25.48±0.28	28.10**±0.30	25.67±0.25	25.67±0.25	
T2w TSE	27.20±0.33	30.49**±0.22	27.51±0.30	27.29±0.29	
MPRAGE	28.23±0.18	31.03**±0.15	26.36±0.13	26.69±0.12	
TOF-MRA	27.87±0.09	31.27**±0.09	27.93±0.08	27.79±0.08	
SSIM	**Input vs Ref**	**DL**	**Anisotropic**	**TV**	**Output vs Ref**
T1w TSE	0.832±0.007	0.874**±0.005	0.808±0.006	0.800±0.006	
T2w TSE	0.860±0.005	0.899**±0.013	0.868±0.003	0.850±0.003	
MPRAGE	0.782±0.006	0.887**±0.003	0.636±0.006	0.629±0.005	
TOF-MRA	0.844±0.002	0.904**±0.002	0.830±0.002	0.807±0.002	

Discussion: The proposed DL denoiser achieved a significant reduction of noise from the input images, matching or outperforming the reference images for all sequences. Compared to traditional denoising methods, the proposed method showed significantly better preservation of image details and sharpness. Further validation of the proposed method's diagnostic performance for the detection of plaque features is currently underway.

References:

[1] Beck, M.J., et al., MRM, 2017
[2] Qiu, S., et al., MRM, 2022

Acknowledgement:

Grant support by NHLBI R01HL159200, VA-MERIT I01CX002208 and VA-MERIT I01CX001901

Evaluation of AI-assisted Compressed Sensing in intra- and extra-cranial MR vessel wall imaging

Ran Huo[1], Decheng Meng[1], Shuo Chen[2], Hualu Han[2], Qiang Zhao[1], Jiajia Xu[1], Ying Liu[1], Huishu Yuan[1]

1. Department of Radiology, Peking University Third Hospital, Beijing, China; 2. United Imaging Research Institute of Intelligent Imaging, Beijing, China.

Background and Purpose: The United Compressing Sensing (uCS) has been used to evaluate the MR vessel wall features. Artificial intelligence-based accelerated MR imaging has shown great promise in recent years [1]. However, its potential of AI-assisted Compressed Sensing (ACS) for evaluating vessel wall features remains unexplored. In this study, **we aimed to evaluate the value of in ACS in characterising intra- and extra-cranial MR vessel wall features compared to uCS.**

Methods: **Study sample**: Patients with carotid stenosis referred for carotid endarterectomy were enrolled. **MR imaging**: All participants underwent MR imaging for ntra- and extra-cranial artery on a 3.0T MR scanner to acquire following sequences: 1) 3D ACS T1-weighted imaging (T1WI): FSE, slice thickness 0.6 mm, bandwidth 500 Hz/pixel, TR 800 ms, TE 13.26 ms, FOV 268 mm × 200 mm, voxel size 0.60 × 0.60 × 0.60, and scanning time 3 min 2s; 2) 3D ACS T2-weighted imaging (T2WI): FSE, slice thickness 0.6 mm, bandwidth 550 Hz/pixel, TR 1800 ms, TE 220.48 ms, field of view 268 mm × 200 mm, voxel size 0.60 × 0.60 × 0.60, and scanning time 4 min 2s; 3) 3D uCS T1WI: FSE, slice thickness 0.6 mm, bandwidth 500 Hz/pixel, TR 800 ms, TE 13.26 ms, FOV 268 mm × 200 mm, voxel size 0.60 × 0.60 × 0.60, and scanning time 5 min 58s; and 4) 3D uCS T2WI: FSE, slice thickness 0.6 mm, bandwidth 550 Hz/pixel, TR 1800 ms, TE 220.48 ms, FOV 268 mm × 200 mm, voxel size 0.60 × 0.60 × 0.60, and scanning time 6 min 2s. **Image review**: Both qualitative and quantitative vascular analysis was performed on 2D cross-sectional slices at 5 locations on bilateral artery, namely Common Carotid Arteries (CCA), carotid bifurcation (BULB), Internal Carotid Arteries (ICA), C2, C5, M1 segment. Qualitative vascular analysis was used to evaluated the Image Quality (IQ) on all above 5 segment artery using a 4-point scale. Only images with IQ ≥2 was included for further quantitative analysis. The Signal-to-Noise Ratio of the lumen (SNR lumen = SI lumen/SD muscle or white matter) and wall (SNR wall = SI wall/SD muscle or white matter), Contrast-to-Noise Ratio (CNR = SNR wall - SNR lumen) and wall-lumen sharpness (Sharpness = 1/d[mm-1]) were computed. **Statistics**: Wilcoxon's rank sum test was used to conduct a statistical analysis of the qualitative ratings of the two sets of images. For the quantitative ratings of the two sets of images, the paired t-test was used for statistical analysis.

Results: In total, 44 subjects with total of 82-88 blood vessels were included. The examination time of ACS was significantly lower than that with uCS. There were statistically significant differences in the subjective image quality ratings between ACS- and uCS-T1WI, as well as between ACS- and uCS-T2WI across five segments of the carotid artery (all P <0.05). Specifically, the p-values for the CCA/BULB/C2/C5/M1 segments between ACS T1WI and CS T1WI were 0.0002, 0.0023, <0.0001, <0.0001, and <0.0001, respectively. The p-values for ACS- versus uCS-T2WI were all <0.0001. For ACS and uCS groups, in all five segment, the wall SNR of T1WI/T2WI showed statistically significant differences (P < 0.0001), while part of lumen SNR exhibited no statistical difference. For CNR, there were statistically significant differences in the objective image quality ratings of ACS- versus uCS-T1WI, as well as ACS- versus uCS-T2WI across five segments of the carotid artery (all P < 0.0001). For wall-lumen sharpness, statistically significant differences were found between ACS- and uCS-T1WI, as well as between ACS-) and uCS-T2WI across five segments of the carotid artery (all P < 0.0001).

Discussion and conclusions: ACS shortens examination time for intra- and extra-cranial MR vessel wall imaging, while improving the image quality compared to uCS.

		ACS	uCS	*P*
CCA	T1W	34.0 ± 16.2	20.0 ± 8.3	<0.0001
(n=88)	T2W	11.6 ± 8.1	6.4 ± 4.1	<0.0001
BULB	T1W	36.8 ± 16.9	22.0 ± 9.1	<0.0001
(n=86)	T2W	11.9 ± 7.7	6.7 ± 4.2	<0.0001
C2	T1W	14.9 ± 6.5	9.6 ± 3.8	<0.0001
(n=83)	T2W	9.1 ± 5.9	4.7 ± 3.4	<0.0001
C5	T1W	16.1 ± 5.3	10.6 ± 3.9	<0.0001
(n=84)	T2W	14.0 ± 8.7	7.8 ± 5.5	<0.0001
M1	T1W	18.8 ± 7.5	13.4 ± 4.8	<0.0001
(n=87)	T2W	32.3 ±15.7	17.3 ± 6.9	<0.0001

Table 1 Comparisons of CNR between ACS and

		ACS	uCS	*P*
CCA	T1W	2.0 ± 0.3	1.4 ± 0.4	<0.0001
(n=88)	T2W	2.0 ± 0.4	1.5 ± 0.6	<0.0001
BULB	T1W	1.9 ± 0.4	1.4 ± 0.4	<0.0001
(n=88)	T2W	2.0 ± 0.5	1.5 ± 0.6	<0.0001
C2	T1W	2.2 ± 0.4	1.8 ± 0.4	<0.0001
(n=83)	T2W	2.5 ± 0.7	2.1 ± 0.6	<0.0001
C5	T1W	2.1 ± 0.4	1.7 ± 0.4	<0.0001
(n=82)	T2W	2.4 ± 0.6	1.9 ± 0.6	<0.0001
M1	T1W	2.2 ± 0.3	1.9 ± 0.4	<0.0001
(n=85)	T2W	2.9 ± 0.8	2.5 ± 0.6	<0.0001

Table 2 Comparisons of wall-lumen sharpness between ACS and uCS.

References: [1] Johnson PM, et al. Semin Musculoskelet Radiol 24:12–20.

A Carotid Artery ROI Localization Pipeline in Head and Neck MRI Based on Slice Classification and Iterative Non-Maximum Suppression

Meng Haoding[1], Zheng Chong[2], Ma Peijiang[1], Lu Jie[2], Li Rui[1]
[1]Tsinghua University, Beijing; [2]Xuanwu Hospital, Beijing

Purpose

This study aims to develop a complete and omission-free ROI extraction pipeline from raw medical images, specifically targeting the localization of carotid artery regions in head and neck magnetic resonance imaging (MRI).

Method

Pipeline Design and Integration The core innovation of our proposed pipeline consists of two key components (Fig1 Left): the pre-trained ResNet-50 slice networks for classification and the iterative Non-Maximum Suppression (NMS) technique for precise localization. **Slice Classification:** Leveraging transfer learning, we fine-tune pre-trained ResNet-50 models to classify 2D slices from axial, sagittal, and coronal directions of 3D MRI images. Input slices, resized to 224x224 and normalized via min-max scaling and z-score standardization, generate 1D probability vectors. Each vector element indicates the probability of a slice containing a Region of Interest (ROI). **Iterative Non-Maximum Suppression:** This module processes the probability vectors. The NMS window size is determined based on ROI index distribution in training data. The iterative process has two stages: initially, a longer non-overlapping window constrains the range of carotid arteries; then, a smaller window within this range precisely locates each artery. This approach mitigates overfitting from limited and unevenly labeled datasets. ***Dataset and Preprocessing*** Experiments use a clinical head and neck artery MRI dataset with 16 cases, including T1, T2, T1C, and TOF modalities with annotated masks. Images have a 512x512x256 field of view and 0.4x0.4x0.8 spacing. Preprocessing includes 224x224 resizing, z-score standardization, and data augmentation for consistency and model generalization. ***Network Architecture and Training*** For classification : Alpha: 0.9, Gamma: 2, Learning rate: 1e-3, Epochs: 100, GPU: A800, Batch size: 128. For suppression in different directions: X direction: first stage for x uses two 110 length windows, second stage one 64 length window; Y and Z directions: first stage uses one 100 length window, second stage one 64 length window.

Result

The pipeline generates ROI regions (Fig2) that fully cover necessary foreground areas while minimizing irrelevant background regions. Visualization and assessment by physicians confirm that the generated ROIs are centered on the vascular wall for cases with labels and accurately locate the vascular wall imaging area for cases without labels.

Discussion

This study offers a standardized and effective pipeline for ROI cropping from clinical raw images, providing high-quality ROIs for subsequent segmentation tasks. The integration of mature pre-trained models with iterative NMS not only enhances the robustness of ROI localization but also addresses the challenge of model overfitting in scenarios with limited and imbalanced datasets.

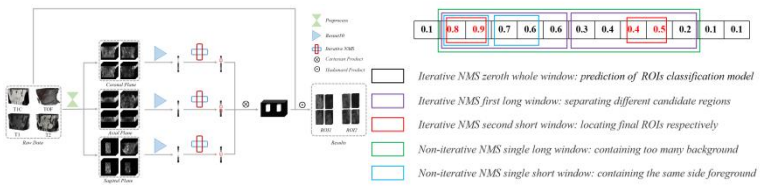

Fig1. The Proposed Pipline (Left) and An Example of Iterative NMS (Right)

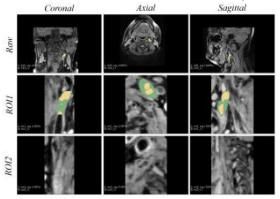

Fig2. A Visualization of Cropped ROIs from The Raw Data

A Nomogram Model for Predicting Subsequent Vascular Events in Patients with Acute Ischemic Cerebrovascular Disease Based on Plaque Characteristics and Clinical Factors

Jiayuan Hu[1,2], Shu Wu[1], Yange Chang[1,2], Juan Huang[1], Sheng Jiao[1], Yan Song[1,2]

1. Department of Radiology, Beijing Hospital, Beijing, China
2. Graduate School of Peking Union Medical College, Beijing, China

Purpose: Recurrent vascular events following ischemic stroke typically exhibit greater disability and fatality. This study aims to establish a model incorporating imaging characteristics of culprit plaques and clinical factors to predict the 1-year recurrence risk of vascular events in patients with acute ischemic cerebrovascular disease.

Methods: This prospective study recruited patients with acute ischemic stroke or TIA who were admitted to the Neurology Department of Beijing Hospital from January 2020 to August 2023. High-resolution magnetic resonance vessel wall imaging (HR-VWI) was performed. Patients were randomly divided into a training set and a validation set at a 3:1 ratio. Telephone follow-ups were conducted every three months. Univariate and multivariate Cox regression analyses were employed to identify risk factors for the recurrence of subsequent vascular events, based on clinical information and imaging characteristics of the culprit plaques. The accuracy and calibration of the prediction model were assessed using the C-index, the area under the receiver operating characteristic curve (AUC), and calibration plots. Decision curve analysis was used to evaluate the clinical utility of the nomogram. Patients were categorized into high-risk and low-risk groups using the X-tile to calculate the cutoff value. The log-rank test was used to compare the intergroup Kaplan-Meier survival curves.

Results: The study enrolled 129 patients, with a median follow-up of 12.0 months. A total of 29 individuals (22.48%) experienced endpoint events during the follow-up period. The training set comprised 96 individuals, while the validation set comprises 33 individuals. Plaque length (HR 0.89, *P*=0.039), coronary artery disease (HR 5.29, *P*<0.001), and an NIHSS score >4 (HR 4.20, *P*=0.008) were identified as independent risk factors for recurrent vascular events. These factors, along with intraplaque hemorrhage, sex, age, and diabetes were included to construct a predictive model for 1-year recurrence risk of vascular events. The model exhibited good predictive performance with AUCs of 0.807 in the training group and 0.916 in the validation group. The cutoff value for high-risk and low-risk patients is 110.6, with the high-risk group experiencing vascular events at a rate 6.201 times higher than that of the low-risk group (HR 6.201, *P*< 0.001).

Conclusion: The model constructed in this study can effectively predict the 1-year recurrence risk of vascular events in patients with acute ischemic cerebrovascular disease. Based on the findings, it is possible to identify a high-risk population for recurrent vascular events, thus providing a basis for clinicians to tailor more targeted, individualized treatment plans.

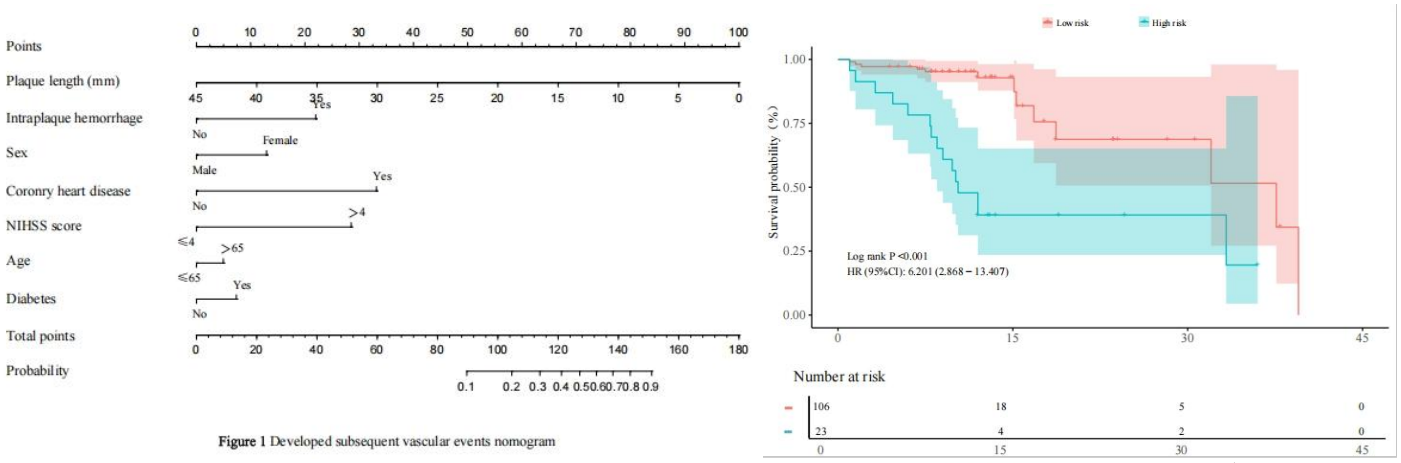

Figure 1 Developed subsequent vascular events nomogram

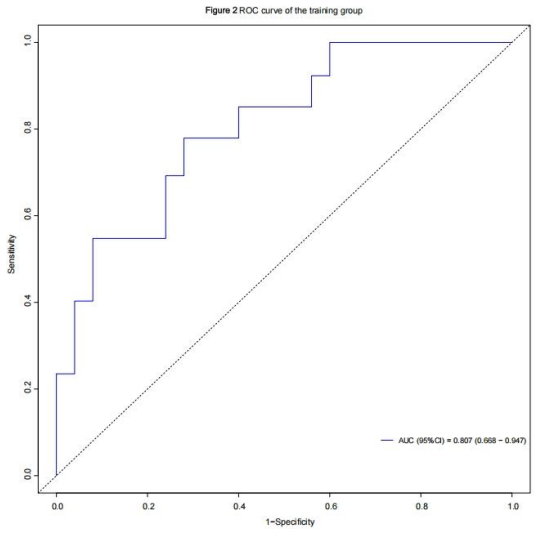

Figure 2 ROC curve of the training group

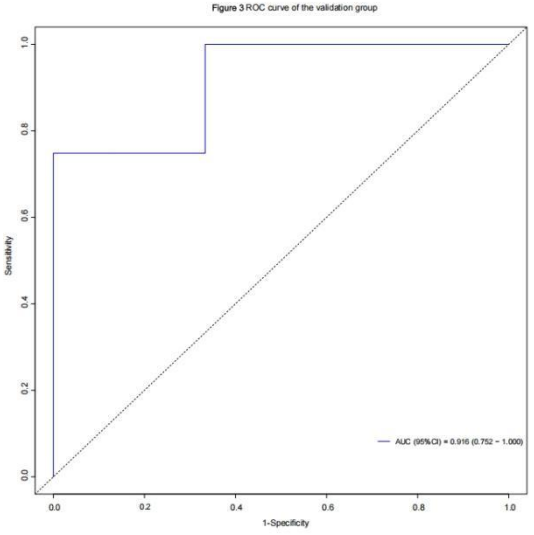

Figure 3 ROC curve of the validation group

Spatial Feature Extraction of Calcification from MRI and Its Correlation with Fibrous Cap Rupture of Carotid Plaque

Qinxin Wang[1], Ran Huo[2], Huiyu Qiao[3], Liu Ying[2], Tao Wang[4], Decheng Meng[2], Xihai Zhao[1]

[1]Center for Biomedical Imaging Research, School of Biomedical Engineering, Tsinghua University, Beijing, China
[2]Department of Radiology, Peking University Third Hospital, Beijing, China
[3]School of Biomedical Engineering, Capital Medical University, Beijing, China
[4]Department of Neurosurgery, Peking University Third Hospital, Beijing, China

Purpose： Fibrous cap rupture (FCR) in carotid atherosclerosis plaque is one of the critical pathological mechanisms underlying acute ischemic stroke[1]. Studies indicate that spatial heterogeneity of intraplaque calcification(CA) is a critical modulator for mechanical stress and FC stability[2]. **This study aims to develop a pipeline for extracting spatial features of intraplaque CA from MR vessel wall imaging and determine their relationships with FCR.**

Methods: The MRI dataset of this study was collected from a cohort of patients with moderate-to-severe carotid stenosis referred to carotid endarterectomy. All patients underwent carotid MR vessel wall imaging on a 3T scanner (uMR 880, United Imaging, Shanghai, China). The study protocol was approved by institutional review board and all patients provided consent form. ***Image analysis and postprocessing:*** The MR images were analyzed by two radiologists with consensus blinded to clinical profiles using vessel analysis software. The vulnerable plaque features (intraplaque hemorrhage [IPH), large lipid-rich necrotic core (LRNC), CA and FCR), plaque burden of normalized wall index (NWI) and luminal stenosis were evaluated. A postprocessing pipeline was developed for extracting spatial features of intraplaque CA from MRI including morphology and spatial distribution (Fig 1). Patients with coexisting CA and IPH in carotid plaques were included in statistical analysis. ***Statistical analysis:*** Morphological features of CA were compared between patients with and without FCR utilizing Mann-Whitney U test. Multivariate logistic regress ion was used to assess the association of the CA morphological features with FCR by adjusting confounding factors: Model 1, sex, age, and body mass index (BMI); Model 2, model 1 plus clinical confounding factors (P<0.1 in univariate analysis); Model 3, model 2 plus luminal stenosis, NWI, and IPH volume. The morphology-FCR correlations were used to screen for morphologically high-risk CAs, then stratify them by FC status before analyzing spatial distributions via Hotelling's T^2 test and density mapping to identify high-risk zones. The spatial proximity of CAs to rupture layers was further validated in FCR cases.

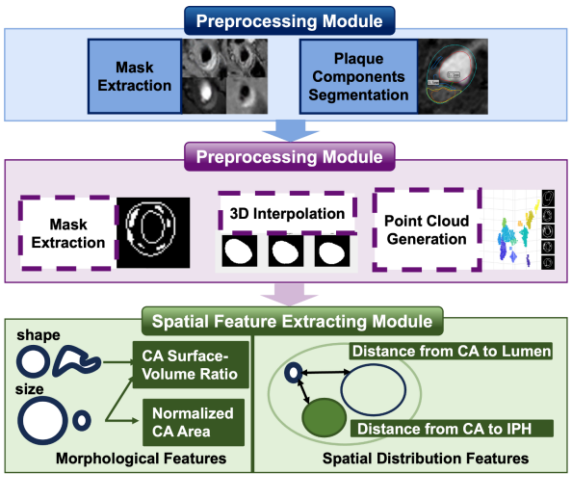

Fig 1. Pipeline for extracting spatial features of intraplaque calcification

Table 1: Multivariable Logistic Regression Analysis of Morphological Features

Variable	FCR		
	OR	95% CI	P-value
Model 1			
Mean Normalized CA Area	0.55	0.30, 0.10	0.049
CA Surface Volume Ratio	1.79	1.00, 3.19	0.049
Model 2			
Mean Normalized CA Area	0.53	0.30, 0.94	0.030
CA Surface Volume Ratio	1.79	1.03, 3.12	0.040
Model 3			
Mean Normalized CA Area	0.65	0.30, 1.42	0.283
CA Surface Volume Ratio	2.54	1.07, 6.06	0.035

Model 1, demographics of sex, age, and BMI; Model 2, model 1 plus baseline HDL level; Model 3, model 2 plus luminal stenosis, NWI, and IPH volume. Increment for all CA features was 1 standard deviation.

Results: In 86 patients (mean age=65.5 years;73 males) with coexisting IPH and CA, 36 (41.9%) had FCR. Patients with FCR showed significantly smaller mean CA area, greater surface-volume ratio, luminal stenosis, NWI, and IPH volume compared to those without (all P<0.05). Logistic regression revealed that surface-volume ratio had significant association with FCR in all models (all P<0.05). The exhibited mean normalized CA area diminishing significance from Model 1 (P<0.05) to Model 3 (P=0.283). Thus, the high-risk CAs were screened using the following criterion: surface-volume ratio >75th percentile of the FCR group's IQR. Spatial distribution analysis of these high-risk CAs revealed significant inter-group distribution differences (P<0.05). Spatial density mapping further delineated a characteristic clustering of high-risk CAs in FCR patients within specific domains: 0.80–3.00 mm from lumen and 0.30–0.75 mm from IPH. No analogous spatial concentration was observed in non-FCR cases. MR imaging in FCR patients revealed spatial concordance between rupture sites and CAs meeting morphological and positional criteria. Of 16 high-risk CAs, 10 (62.5%) localized within the ruptured fibrous cap layer, while 2 (12.5%) occupied adjacent layers.

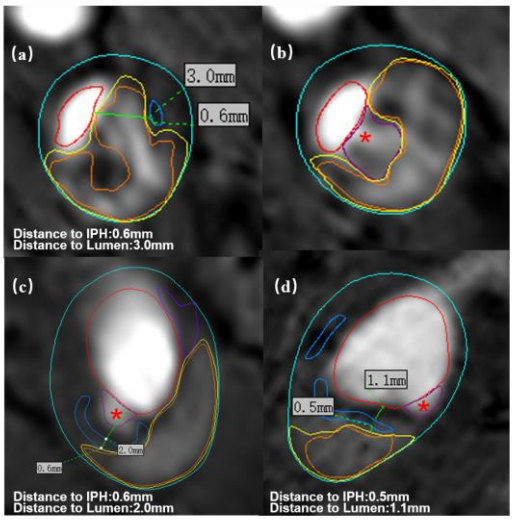

Fig 2. High-risk CA distribution relative to FCR planes. (a,b) FCR plane with ulceration (*), lumen (red), wall (blue), IPH (orange), LRNC (yellow) and high-risk CA (blue) proximal to rupture in the adjacent superior plane. (c,d) Two FCR cases: CA(blue) co-localized with rupture in the same plane. Distances between CA, lumen, and IPH marked.

Conclusions: This study developed a spatial feature extraction pipeline and demonstrated that high-risk intraplaque CAs associated with FCR are characterized by reduced surface-volume ratio, and within vulnerability zones (0.80–3.00 mm from lumen, 0.30–0.75 mm from IPH). The co-localization of 62.5% of these CAs localized in rupture layers suggests their potential role as biomechanical stress amplifiers. Future studies will expand sample size, further validate spatial accuracy through CT and pathology and integrate hemodynamic models to unveil mechanisms.

References: [1] Yuan C, et al. Circulation. 2002. [2] Gu S, et al. Front Cardiovasc Med. 2022

3D Whole Heart Coronary Angiography at Low-Field: A Clinical Feasibility Study

Simon J. Littlewood[1], Carlos Castillo-Passi[2,3,4], Michael G. Crabb[1], Dongyue Si[1], Anastasia Fotaki[1], Tiago Sequeiros[1], Filippo Bosio[1], Karl P. Kunze[5], Claudia Prieto[1,7,8], René M. Botnar[1,6,7,8,9]

[1]School of Biomedical Engineering and Imaging Sciences, King's College London, London, United Kingdom. [2]Department of Radiology, Stanford University, Stanford, California, USA. [3]Division of Radiology, Veterans Administration Health Care System, Palo Alto, California, USA. [4]Stanford Cardiovascular Institute, Stanford, California, USA. [5]MR Research Collaborations, Siemens Healthcare Limited, Camberley, United Kingdom. [6]Institute for Biological and Medical Engineering, Pontificia Universidad Católica de Chile, Santiago, Chile. [7]School of Engineering, Pontificia Universidad Católica de Chile, Santiago, Chile. [8]Millenium Institute for Intelligent Healthcare Engineering, Santiago, Chile, [9]Institute for Advanced Study, Technical University Munich, Germany.

Purpose: Interest in low-field (<1.0T) MRI is growing due to lower costs, reduced energy and helium use, and improved accessibility for claustrophobic and bariatric patients.[1,2] Recently, we demonstrated the feasibility of high-resolution free-breathing 3D coronary magnetic resonance angiography (CMRA) at 0.55T in healthy subjects.[3] This study evaluates 0.55T CMRA as a potential clinical tool for assessing coronary anatomy and coronary artery disease (CAD).

Methods: Twenty-one patients with a range of cardiovascular conditions were recruited and scanned at 0.55T (MAGNETOM Free.Max, Siemens Healthineers, Forchheim, Germany). The CMRA research sequence framework (Figure 1) has previously been described[4] at 1.5T[4] and has was recently adapted for low-field.[3] The sequence consists of an ECG-triggered, free-breathing 3D whole-heart bSSFP acquisition with a 3x under-sampled variable density spiral-like Cartesian (VD-CASPR) trajectory. The following specific parameters were utilised: FoV = 312x312x88-108 mm^3, TR/TE = 4.87/2.20 ms, isotropic spatial resolution=1.5 mm^3, bandwidth = 801 Hz/Px. A T2 preparation pulse (60 ms duration, MLEV-4 refocusing scheme) was applied to enhance blood pool contrast and a fat saturation pulse with a flip angle of 180° was used to suppress epicardial fat. Low-resolution 2D image navigators (iNAV)[5] were incorporated into the sequence at each heartbeat to enable 100% respiratory scan efficiency and predictable scan times. The acquired data were reconstructed with non-rigid motion corrected iterative-SENSE followed by patch-based low-rank denoising (PROST)[6] performed directly in the scanner software. Image acquisition was performed in diastole when heart rate (HR) < 70 beats-per-minute (bpm) or systole otherwise. Qualitative image quality analysis using a 4-point Likert scale (1: uninterpretable images, 2: poor image quality, 3: acceptable image quality, 4: excellent image quality) was performed by a clinical expert to analyse the quality of the images for the three major coronary arteries.

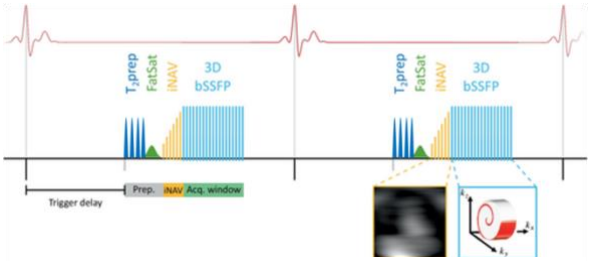

Fig. 1 Proposed CMRA sequence

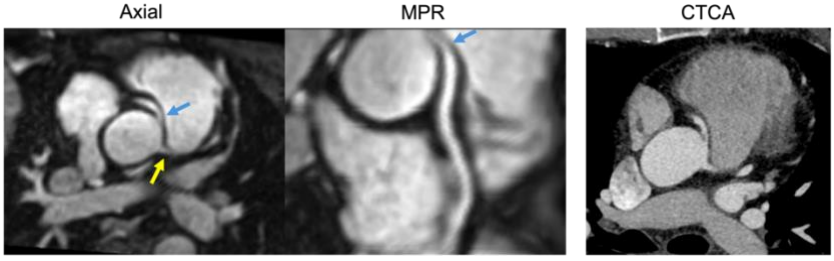

Fig. 2 Axial and MPR images from the CMRA sequence in a patient with anomalous RCA (blue arrow) arising from the left coronary cusp. The left main stem (LMS) is depicted by the yellow arrow. Corresponding CTCA confirms the findings.

Results: All twenty-one patients (eighteen males, mean age 57±14 years, HR 62±9 bpm) were successfully scanned in 7±1 min. Three patients with HR >70 bpm were scanned in systole. Proximal segments of all three major vessels were well visualised. Mean image quality scores: left anterior descending (LAD) 3.1±0.8, left circumflex (LCx) 2.8±0.8, right coronary artery (RCA) 3.5±0.5. Fig. 2 shows a patient with anomalous RCA origin. Fig. 3 demonstrates coronary stenoses in a patient with CAD.

Discussion: This study demonstrates the feasibility of 0.55T CMRA in patients with cardiovascular disease, with an ~7 min scan time. Despite a lower signal-to-noise ratio compared to higher-field scanners, this protocol accurately depicted coronary arteries, including anatomical variations. One patient's congenital anomaly was clearly visualised, showing RCA's inter-arterial course which was confirmed on CTCA. CAD was detected in the LAD and RCA proximal segments in 2 patients. Limitations include a small sample size and low CAD prevalence. Future work will focus on assessing more CAD cases to evaluate the diagnostic potential for guiding revascularisation.

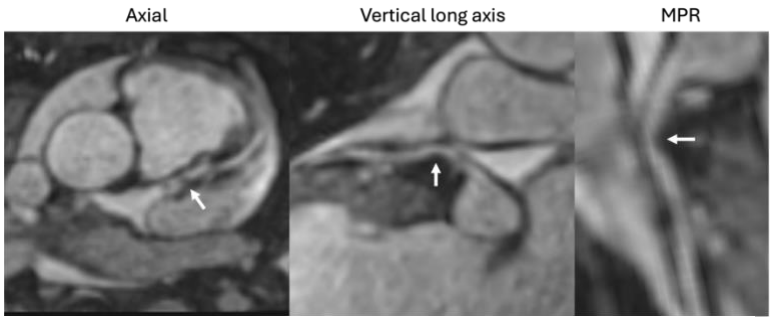

Fig. 3 Axial, vertical long axis and MPR images of the LAD. CAD is demonstrated by the white arrows.

References: **(1)** Arnold TC, et al. *Journal of Magnetic Resonance Imaging*. 2023;57(1):25-44. **(2)** Campbell-Washburn AE, et al. *Journal of Magnetic Resonance Imaging*. 2023. **(3)** Castillo-Passi C, et al. *Magn Reson Med*. 2024 **(4)** Bustin A, et al. *Journal of Cardiovascular Magnetic Resonance*. 2020;22(1):24. **(5)** Henningsson M, et al. *Magn Reson Med*. 2012;67(2):437-445. **(6)** Bustin A, et al. *Magn Reson Med*. 2019;81(6):3705-3719

Risk Factors for Co-existing Extracranial Carotid and Intracranial Artery High-Risk Atherosclerotic Plaques: An MR Imaging Study

Xiaoyi Chen[1]; Dandan Yang[2]; Xiaowei Song[3]; Shuo Chen [4]; Huiyu Qiao[5]; Chun Yuan[6]; Zhuozhao Zheng[1]; Xihai Zhao[4]

1. Department of Radiology, Beijing Tsinghua Changgung Hospital, School of Clinical Medicine, Tsinghua University, Beijing, China. 2. Department of Radiology, Beijing Geriatric Hospital, Beijing, China. 3. Department of Neurology, Beijing Tsinghua Changgung Hospital, School of Clinical Medicine, Tsinghua University, Beijing, China. 4. Center for Biomedical Imaging Research, School of Biomedical Engineering, Tsinghua University, Beijing, China. 5. School of Biomedical Engineering, Capital Medical University, Beijing, China. 6. Department of Radiology, University of Washington, Seattle, USA.

Purpose: Atherosclerosis is a systematic disease that usually affects multiple vascular beds, such as coexisting plaques [1,2]. High-risk atherosclerotic plaques (HRPs) more likely lead to ischemic events [3]. Determination of risk factors for HRPs is important for clinical management. This study sought to investigate the risk factors for co-existing extracranial carotid and intracranial artery HRPs using MR vessel wall imaging (MR-VWI).

Methods: Study sample: Patients with co-existing extracranial carotid and intracranial atherosclerotic plaques were recruited from a multicenter clinical trial and clinical information was collected. **MR imaging:** All patients underwent carotid MR-VWI and intracranial artery MRA on 3.0T MR scanner (Achieva TX, Philips Healthcare, Best, The Netherlands) with a dedicated 8-channel carotid artery coil and head coil. The carotid MR imaging protocol and parameters are as follows: 3D-TOF: TR/TE 20/4.9 ms, flip angle 20°; T1W: QIR, TR/TE 800/10 ms; T2W: multislice DIR, TR/TE 4800/50 ms; MP-RAGE: TR/TE 8.8/5.3 ms, flip angle 15°. All imaging sequences were acquired with the identical FOV 14×14 cm and resolution 0.5×0.5 mm. The parameters of 3D-TOF MRA for intracranial artery were as follows: TR/TE 25/3.5 ms, flip angle 20°, FOV 24×24 cm, resolution 0.7×0.7 mm. **Data analysis**: All the MR images were reviewed by two experienced radiologists to access the wall thickness, lumen area, wall area, total vessel area and NWI. The presence and size of CA, LRNC, IPH and FCR were identified and measured. The luminal stenosis of carotid and intracranial artery was measured on the 3D-TOF MRA. The carotid HRP was defined as luminal stenosis ≥50% or plaques with IPH, FCR, or large LRNC. The HRP of intracranial artery was defined as luminal stenosis ≥50%. **Statistical analysis:** The patients were divided into non-HRP group (no carotid HRP and MCA stenosis <50%), single HRP group (had carotid HRP or MCA stenosis ≥50%) and co-existing HRPs group (presence of both carotid HRP and MCA stenosis ≥50%). Multivariate logistic regression analysis was used to determine the associations between clinical risk factors and the three groups.

Results: Among the 190 recruited patients, 77 (40.5%) were in non-HRP group, 78 (41.1%) were in single HRP group, and 35 (18.4%) were in co-existing HRPs group. The prevalence of diabetes and family history of cardiovascular disease (CVD) was highest in co-existing HRPs group (57.1%, 51.4%), followed by single HRP group (39.7%, 38.5%) and non-HRP group (29.9%, 24.7%) (P=0.023, P=0.017). Patients in co-existing HRPs group were more likely to have higher prevalence of diabetes (OR: 3.92, 95% CI: 1.53-10.04, P=0.004) and family history of CVD (OR: 3.37, 95% CI: 1.26-8.98, P=0.015) compared to those in non-HRP group after adjusting for age, sex, HDL, and smoking (Table 1). Similarly, patients in co-existing HRPs group also showed more likely to have higher prevalence of diabetes (OR: 2.49, 95% CI: 1.04-5.95, P=0.040) compared to single HRP group after adjusting for age, sex, and HDL. Figure 1. shows the representative example with co-existing extracranial and intracranial artery HRPs.

Table 1 Comparison of risk factors between 3 groups by multivariate logistic regression analysis

	OR (95% CI)	p
Single HRP group vs. Non-HRP group		
Age	0.99 (0.96-1.03)	0.614
Sex	1.73 (0.89-3.35)	0.107
Family history of CVD	1.91 (0.93-3.91)	0.078
Co-existing HRPs group vs. Non-HRP group		
Age	0.96 (0.91-1.01)	0.137
Sex	2.91 (0.80-10.66)	0.107
Smoking	1.33 (0.40-4.41)	0.640
HDL	5.13 (1.25-21.17)	0.024
Diabetes	3.92 (1.53-10.04)	0.004
Family history of CVD	3.37 (1.26-8.98)	0.015
Co-existing HRPs group vs. Single HRP group		
Age	0.97 (0.92-1.02)	0.225
Sex	1.58 (0.61-4.10)	0.346
HDL	4.67 (1.29-16.91)	0.019
Diabetes	2.49 (1.04-5.95)	0.040

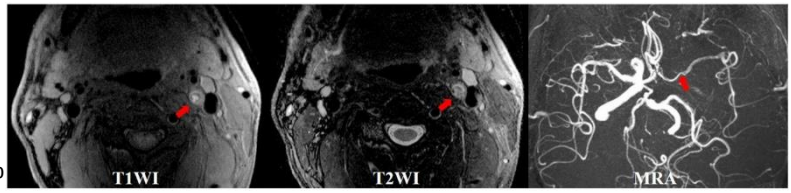

Figure 1. The black-blood T1W, black-blood T2W and 3D-TOF MR images from a 55 years old male patient with acute stroke in the left cerebral hemisphere, and the patient has the risk factors of diabetes and family history of cardiovascular disease. The T1W and T2W images indicate the atherosclerotic plaque with IPH in the C1 segment of the left ICA. The MRA represents the luminal stenosis ≥50% in the ipsilateral MCA.

Discussion: Co-existing extracranial carotid and intracranial artery high-risk atherosclerotic plaques are prevalent in middle-aged and elderly symptomatic atherosclerotic patients. Diabetes and family history of cardiovascular disease are independent risk factors for co-existing high-risk plaques.

References: 1. Lancet 2014; 383: 984-988. 2. Stroke Vasc Neurol 2021; 6: 595-602. 3. Radiology 2014; 271: 381-389.

Longitudinal Study of Intracranial Atherosclerosis and Stroke Risk in Brain Tumor Patients: Preliminary Results

Beibei Sun, Mohamed HD Hassan, Mohamad Hosaam Mosi, Dan Cheng, Ahmed Amr Safwat, Charles Watt, Chengcheng Zhu, Mahmud Mossa-Basha

Department of Radiology, University of Washington, Seattle, Washington, USA.

Purposes: Cancer patients have twice the stroke risk of the general population, with brain tumor patients at particularly high risk [1]. As cancer survival rates have improved in recent years [2], it is crucial to identify those at elevated stroke risk to potentially guide primary prevention. Since intracranial atherosclerotic disease (ICAD) is a leading cause of stroke globally [3], we developed a unique longitudinal vessel wall MRI (IVW) database to assess ICAD and track acute ischemic stroke (AIS) incidence in brain tumor patients, offering valuable insights into the vascular health of this high-risk group.

Methods: We retrospectively reviewed a prospective database of brain tumor patients (diagnosed from 1984 to 2025) who underwent MRI brain at our oncology center from 2018 to 2025. Collected data included demographics, cardiovascular risk factors, tumor type (primary/metastatic), WHO grade, IDH mutation status, and treatment details (surgery, radiation, chemotherapy). Three neuroradiologists reviewed IVW MRIs to assess ICAD features, including plaque prevalence, total plaque count, plaque enhancement, enhancement grade, and lumen stenosis at baseline and follow-up. AIS occurrence was recorded as an endpoint.

Results: To date, 1,000 patients have been enrolled. A preliminary analysis of 350 patients (mean age 51.9 years, 38.9% male) showed that 78.9% had primary brain tumors, and 72.0% underwent surgery. Median follow-up was 3.5 years, with 37.7% mortality. Of the tumors, 230(65.7%) were classified by WHO grade I to IV (Grade I: 6.2%, Grade II: 16.5%, Grade III: 17.4%, Grade IV: 25.6%). 74.5% patients underwent radiation therapy, 52.3% patients underwent chemo; and 45.2% underwent concurrent. Table presents the IVW findings of intracranial arteries. At baseline, no cases of vasculitis, moyamoya disease, or arterial dissection were observed. However, 4 patients (1.1%) were found to have an aneurysm, and 2 patients (0.8%) had arterial dissection. Atherosclerosis was present in 36.5% of patients, with 22.3% having multiple plaques. A total of 291 plaques were identified, of which 238 (81.8%) showed enhancement. Specifically, 194 (66.7%) plaques exhibited grade 1 enhancement, while 48 (16.5%) had grade 2 enhancement. Over time, plaque prevalence increased to 41.4%, with 25.7% having multiple plaques. Among these, 81.5% plaques showed enhancement, including 64.8% with grade 1 enhancement and 61 18.2% with grade 2 enhancement. AIS occurred in 5.1% of patients, with 8 out of 12 cases having plaques in the stroke-affected vascular territory.

Conclusion: In this study, we observed a significant prevalence of ICAD among brain tumor patients with an increase in plaque burden over time. The presence of ICAD in this population suggests an elevated risk of cerebrovascular complications, possibly exacerbated by cancer and treatment-associated factors. Additionally, the incidence of acute ischemic stroke in brain tumor patients, albeit low, underscores the need for vigilant cardiovascular monitoring in this high-risk group. These findings highlight the importance of early detection and management of ICAD to mitigate stroke risk and improve patient outcomes.

Table. Vessel wall images findings during follow up

Baseline	
Vasculitis	0(0%)
Moyamoya	0(0%)
Aneurysm	4(1.1%)
Dissection	2(0.6%)
Atherosclerosis plaques (%)	128(36.5%)
Multiple plaques (%)	78(22.3%)
Total Plaque numbers (n)	291
Plaque with stenosis (>50%)	3(1.0%)
Plaque enhancement (yes or no)	238(81.8%)
Plaque enhancement (grade1)	194(66.7%)
Plaque enhancement (grade2)	48(16.5%)
Follow up (median [IQR], years)	3.5 [1.3-6.0]
Atherosclerosis plaques (%)	145(41.4%)
Multiple plaques (%)	90(25.7%)
Total Plaque numbers (n)	335
Plaque with stenosis (>50%)	3(0.9%)
Plaque enhancement (yes or no)	273(81.5%)
Plaque enhancement (grade1)	217(64.8%)
Plaque enhancement (grade2)	61(18.2%)
Stroke prevalence (%)	18(5.1%)

Reference

[1] Zaorsky NG, et al. Stroke among cancer patients. Nat Commun. 2019;10:5172.

[2] Siegel RL, et al. Cancer Statistics, 2021. CA Cancer J Clin. 2021;71:7-33.

[3] Gutierrez J,et al. Lancet Neurol. 2022;21:355-368.

Characterizing Dynamic Changes of Carotid Morphology in Patients with Carotid Atherosclerosis by Black-Blood MR Cine Imaging

Huiyu Qiao[1]; Qiansu Yang[2]; Ning Xu[3];Jiachen Liu[3]; Ran Huo[4]; Shuhao Wang[5]; Jingli Cao[6]; Tao Wang[7]; Xihai Zhao[3]

[1.] School of Biomedical Engineering, Capital Medical University, Beijing, China. [2.] Center of Medicine Clinical Research, Department of Pharmacy, Medical Supplies Center of PLA General Hospital, Beijing, China. [3.] Center for Biomedical Imaging Research, School of Biomedical Engineering, Tsinghua University, Beijing, China. [4.] Department of Radiology, Peking University Third Hospital, Beijing China. [5.] Thorough Images, Beijing, China. [6.] China National Clinical Research Center for Neurological Disease, Beijing Tiantan Hospital, Capital Medical University, Beijing China. [7.] Department of Neurosurgery, Peking University Third Hospital, Beijing, China.

Purpose: The atherosclerosis usually leads to the structural changes, such as lumen stenosis, wall thickening, complex plaque components[1], while also affecting the vascular function including compliance, distension, wall shear stress, plaque structure stress and so on[2]. This study aims to evaluate the capability of BB-cine imaging in assessing dynamic changes of carotid lumen and vessel wall in patients with carotid atherosclerosis.

Methods: Study sample: Twenty-nine subjects (mean age, 64.9±7.6 years; 22 males) with carotid atherosclerosis referred to CEA were enrolled. **MR imaging:** Carotid BB-cine imaging was performed for all subjects on a 3T MR scanner (Achieva TX, Philips Healthcare, Best, The Netherlands) with a dedicated 8-channel carotid coil. The imaging parameters of BB-cine are as follows: SPGR acquisition, TE/TR 4.5/9.1 ms, flip angle 8°, turbo factor 15, acquisition resolution 0.8×0.8×3 mm^3, FOV 160×160×24 mm^3, cardiac phases 12. **Histological and MR analysis**: All the H&E stained specimens were interpreted by histologists with >5 years' experience to access the presence and area of IPH, LRNC, CA and LM. The MR BB-cine images were matched with histological images and reviewed by two radiologists. The contours of lumen and wall for each dynamic image were outlined. **Statistical analysis:** For each matched BB-cine slice, the dynamic changes of LA, WA, MaxWT and NWI were calculated as (Maximum value - Minimum value) / Minimum value. The values of dynamic change were compared between groups with and without IPH, LRNC, CA or LM using Mann-Whitney U test. Spearman rank correlation analysis was performed to determine the relationship between the dynamic changes and the area of each plaque components when present.

Results: Eighty MR cine slices from 29 patients were successfully matched with histological sections. Of the 80 slices, 48(60.0%) had IPH, 62(77.5%) had LRNC, 58(72.5%) had CA, and 40(50.0%) had LM on the corresponding histological sections. The mean area of IPH, LRNC, CA and LM on histology was 9.7±6.8mm^2, 10.3±8.8mm^2, 3.9±3.4mm^2 and 3.9±3.5mm^2, respectively. The dynamic changes of WA were significantly lower in the images with IPH (P=0.019) and LRNC (P=0.016) compared to those without. The dynamic changes of MaxWT were significantly different between the cine images with or without CA (P=0.036) and LM (P=0.032) (Table 1) . Significant correlations were found between the dynamic changes of MaxWT and the area of IPH (r=-0.40, P=0.005) and LRNC (r=-0.40, P=0.001). The dynamic changes of WA were significantly correlated with the area of CA (r=-0.35, P=0.007). The dynamic changes of LA were significantly correlated with the area of LM (r=0.37, P=0.018). The dynamic changes of NWI were not correlated with the area of all components (all P>0.05). Figure 1 were typical cine images and histological sections with LRNC and LM, alongside their corresponding dynamic changes of carotid morphology.

Table 1. Dynamic changes of carotid morphology in images with or without plaque components.

Dynamic Change	IPH		P	LRNC		P	CA		P	LM		P
	-	+		-	+		-	+		-	+	
MaxWT, %	13.6(9.8,23.3)	12.3(9.0,18.7)	0.473	14.2(8.5,25.9)	12.4(9.2,19.2)	0.489	18.2(11.0,28.2)	11.9 (8.9,17.9)	0.036	10.8(8.7,17.1)	14.9(11.4,23.2)	0.032
LA, %	27.7(14.0,42.5)	35.6(26.6,52.3)	0.071	27.2(17.0,36.0)	34.7(22.3,52.0)	0.120	40.8(27.5,55.1)	31.1(18.0,45.9)	0.070	28.0(16.2,40.9)	33.6(26.8,58.1)	0.082
WA, %	8.3(4.1,16.2)	4.3(2.9,8.3)	0.019	8.8(4.7,17.1)	4.7(2.8,8.8)	0.016	7.8(2.3,13.9)	5.2(3.2,10.2)	0.714	6.3(3.3,12.1)	4.9(2.8,10.0)	0.248
NWI, %	18.5(11.6,26.3)	13.4(11.0,19.0)	0.138	19.3(11.6,26.4)	14.1(10.9,20.4)	0.178	14.1(10.4,25.2)	15.0(11.4,21.0)	0.813	14.5(10.9,23.5)	14.2 (11.6,20.2)	0.950

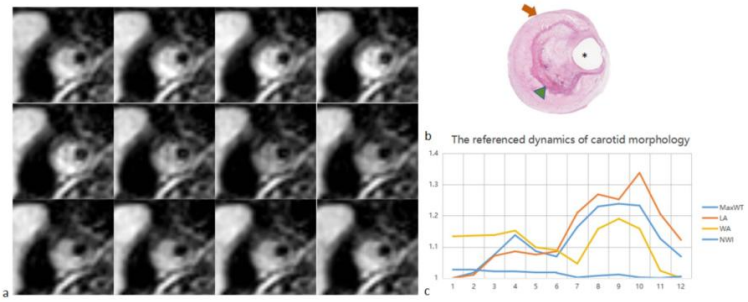

Figure 1. The BB-cine images, histological sections, and corresponding referenced dynamics of the right carotid artery in a sixty-two female subjects. This slice was histologically identified as having LRNC (yellow arrow) and LM (green arrow head).

Discussion: The dynamic changes of arterial lumen calculated by BB-cine indicate the distension of lumen. In this study, the dynamic changes of LA increased with the size of LM, revealing that the distension of lumen can be enhanced. The size of IPH, LRNC and CA was mainly impact the distension of wall.

References: 1. Atherosclerosis. 2021;319:42-50. 2. JACC Cardiovasc Imaging. 2020;13(3):817-819.

Association between the amount of carotid perivascular adipose tissue measured by MR imaging and carotid atherosclerotic plaque vulnerability

Shuwan Yu[1], Ran Huo[2], Decheng Meng[2], Jiachen Liu[1], Ning Xu[1], Ying Liu[2], Xihai Zhao[1]

[1]Center for Biomedical Imaging Research, Tsinghua University, Beijing, China

[2]Department of Radiology, Peking University Third Hospital, Beijing, China

Background and Purpose: Pathophysiological studies have established that Inflammatory changes in PVAT play a critical role in the progression of AS disease[1]. This study aimed to explore the association between carotid perivascular adipose tissue (PVAT) amount and vulnerable plaque characteristics using magnetic resonance (MR) vessel wall imaging.

Methods: ***Study sample:*** We enrolled 153 patients (64.5±8.1 years; 123 men) with moderate-to-severe atherosclerotic stenosis awaiting carotid endarterectomy. ***MR imaging:*** Participants underwent preprocedural 3.0T carotid MR imaging (8-channel coil) including 3D TOF, 2D T1w/T2w black-blood, and 3D SNAP[2] sequences (2mm slice thickness). The imaging was performed with the field of view centered on the bifurcation of surgical target artery. ***Image analysis:*** As shown in Figure 1, axial slices were analyzed to delineate lumen-wall boundaries and identify plaque components including calcification (CA), lipid-rich necrotic core (LRNC), intraplaque hemorrhage (IPH), and fibrous cap rupture (FCR) using established criteria[3,4]. PVAT within the region of interest (twice the lumen-wall area) was segmented using k-means clustering based on the inherent adipose hypointensity on SNAP reference images. The PVAT amount measurements included maximum area, PVAT-AI (PVAT/lumen-wall area ratio), and PVAT-VI (PVAT/lumen-wall volume ratio). ***Statistical analysis:*** Associations between carotid PVAT amount and plaque features were evaluated using logistic regression.

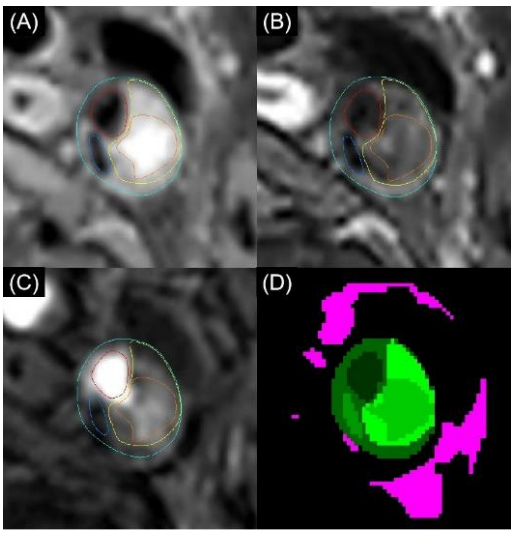

Figure 1. Representative image with vulnerable plaque. (A-C) Plaque delineation on T1w, T2w, and TOF sequences (green=outer wall, red=lumen, blue=CA, yellow=LRNC, orange=IPH). (D) Carotid (green)/PVAT (pink) mask comparison.

Table 1. Logistic regression analysis results.

	Univariate model		Multivariate model	
	OR (95%CI)	***P***	**OR (95%CI)**	***P***
Maximum PVAT area, mm²				
CA	1.009(0.998,1.020)	0.099	1.004(0.991,1.018)	0.522
LRNC	1.001(0.986,1.017)	0.887	0.999(0.974,1.026)	0.958
IPH	1.007(1.000,1.014)	0.045	1.003(0.995,1.011)	0.479
FCR	1.011(1.004,1.018)	0.004	1.007(0.999,1.016)	0.083
Maximum PVAT-AI				
CA	1.173(0.765,1.798)	0.464	0.961(0.545,1.697)	0.891
LRNC	2.006(0.689,5.837)	0.201	2.894(0.684,12.250)	0.149
IPH	2.257(1.501,3.396)	<0.001	1.917(1.209,3.040)	0.006
FCR	2.241(1.524,3.293)	<0.001	1.847(1.209,2.822)	0.005
PVAT-VI				
CA	0.826(0.365,1.870)	0.647	0.374(0.117,1.190)	0.096
LRNC	0.986(0.247,3.935)	0.984	1.283(0.153,10.756)	0.818
IPH	2.071(1.061,4.041)	0.033	1.419(0.664,3.034)	0.367
FCR	3.280(1.611,6.678)	0.001	2.365(1.076,5.199)	0.032

* Multivariate model adjusted for age, gender, BMI, history of smoking, diabetes, alcohol, hypertension, hyperlipidemia and coronary heart disease.

Results: Significant associations can be found between all PVAT amount measurements and IPH (OR=1.007-2.257, *P*<0.05) and FCR (OR=1.011-3.280, *P*<0.05). No significant associations were observed between all PVAT measurements and CA/LRNC (*P*>0.05). After adjustment of cardiovascular risk factors, significant associations remained between maximum PVAT-AI and IPH (OR=1.917, *P*=0.006) and between maximum PVAT-AI/PVAT-VI and FCR (OR=1.847-2.365, *P*<0.05) (Table 1).

Discussion and Conclusion: Carotid PVAT amount measured by MR imaging is independently associated with vulnerable plaque features, suggesting its potential as an effective indicator of plaque vulnerability.

References: [1] Tanaka K., Front Physiol, 2018, 9: 3. [2] Wang J., Magn Reson Med, 2013; 69(2): 337-345. [3] Saam T., Arterioscler Thromb Vasc Biol, 2005; 25(1): 234-239. [4] Chen S., J Magn Reson Imaging, 2018; 47(3): 634-639.

Free-breathing rapid T_1 mapping for coronary blood supply quantification through dynamic response of contrast-enhanced whole-heart myocardium

Bowei Liu[1], Rui Guo[2], Haiyan Ding[1]

[1] Center for Biomedical Imaging Research, Tsinghua University, Beijing, China

[2] School of Medical Technology, Beijing Institute of Technology, Beijing, China

Purpose:

The myocardium's response to contrast agents reflects the relationship between coronary artery blood supply and myocardial uptake, which can be captured by first-pass perfusion[1] or early/late gadolinium enhancement (EGE/LGE)[2-3]. However, EGE has not widely adopted due to complex signal variations from contrast agent kinetics[4]. Quantitative T_1 mapping can address this issue but current techniques are limited to static T_1 measurements at one "still" time point. Therefore, this study developed the Dynamic Approach for Rapid T_1 mapping (DART) sequence to dynamically quantify whole-heart contrast-enhanced myocardial response.

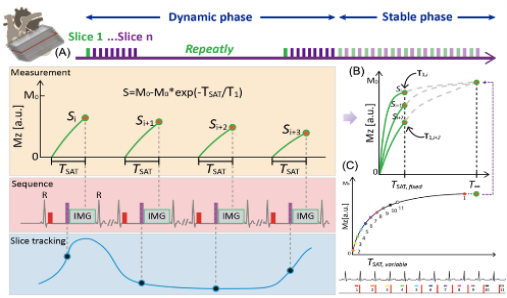

Fig 1 Sequence diagram for the proposed Dynamic Approach for Rapid T_1 mapping (DART).

Methods: The dynamic and stable phase were combined into a single free-breathing scan protocol (**Fig 1**). Following contrast administration, T_1-weighted imaging was performed repeatedly for interleaved multi-slice (typically nine slices) acquisition using slice tracking[5] covering entire ventricle until contrast agent distribution stabilized (~10 mins post-injection). During dynamic phase, saturation-prepared single-shot bSSFP image with fixed saturation-recovery time ($T_{SAT,\ fixed}$) was acquired continuously, reaching a temporal resolution of 9 heartbeats for all slices. Followed by multiple saturation-prepared images acquired like conventional SASHA[6] with linearly increasing $T_{SAT,\ variable}$, which were used to estimate the equilibrium magnetization M_0 and dynamic T_1 using model: $S_i = M_0\,(1 - \exp\,(-T_{SAT,i}/T_1))$, where S stands for signal intensity. In-vivo studies were conducted on a 3T MR scanner (Ingenia CX, Philips Healthcare, Best, The Netherlands). Seven healthy controls (age: 43 ± 11 years, 2 males) were scanned without contrast injection, while another five healthy volunteers (age: 64 ± 10 years, 3 males) with a bolus injection of Gd-DTPA (0.2 mmol/kg). The method was further verified in one patient with an infarction zone.

Results: Representative dynamic T_1 maps were shown in **Fig 2**. No significant difference was found for myocardial T_1 in contrast-free group (1468 ± 56 v.s. 1462 ± 51 ms, P = 0.34) between DART and traditional T_1 estimation. T_1 quantification during ten-minute non-contrast scan was stable, with averaged CV of 2.7 ± 1.1%. Homogeneous dynamic T_1 maps were obtained in the contrast-injected healthy group. T_1-time curves unveiled the consequential T_1 elevation trends in myocardium (normal versus lesion) and blood as contrast agent flowed out.

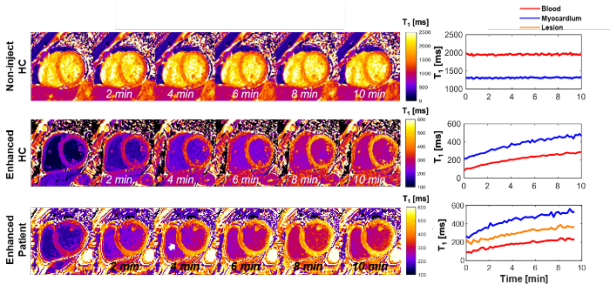

Fig 2 Representative T_1 maps and T_1-time curves of blood and myocardium by DART per one slice from three testify groups.

Discussion: This study proposed a free-breathing T_1 mapping sequence with whole-heart coverage for measuring the dynamic response of contrast-enhanced myocardium. Employing the proposed method, qualified T_1 maps were acquired every nine heartbeats for each of nine slices, enables quantification of contrast agent distribution during EGE phase, reflecting the whole process of coronary blood supply .

Reference: 1. Kellman P et al. JCMR 2017. 2. Toupin S et al. JMRI 2022. 3. Hammer-Hansen S et al. JACC: CVI 2017. 4. Arheden H. JACC: CVI 2017. 5. Sachs TS et al. MRM 1994. 6. Chow K et al. MRM 2014.

Exploring the Link: Atrial Fibrillation and Atherosclerotic Intraplaque Hemorrhage in the setting of Cerebral Acute Infarct

Authors: Ahmed A. Safwat, Mona Kharaji, Maoxue Wang, Cristina Sanchez, Marina Ferguson, M Mossa-Basha

Institution: University Of Washington

Purpose:

Stroke is a significant global health concern, with over 12.2 million new cases reported annually according to the World Stroke Organization. Several risk factors contribute to the likelihood of experiencing a stroke, with atrial fibrillation (A-Fib) and Intraplaque hemorrhage (IPH) being significant factors, accounting for approximately 45-50% of all stroke cases(1). The occurrence of IPH at extracranial ICA in patients with concurrent A-Fib, along with other vascular risk factors such as hypertension & hyperlipidemia, raises various concerns about the relationship between these conditions and the underlying stroke etiology. Understanding these correlations is crucial for developing targeted prevention and treatment strategies.

Materials and methods:

At the University of Washington, all acute stroke patients undergo vessel wall MRI (VWI) covering the intracranial and carotid vasculature on their post-stroke MRI. We reviewed 550 stroke patients with VWI and collected cases with acute infarct or TIA and carotid IPH or A-Fib. Clinical information and risk factors were collected from the medical system. Carotid IPH was identified based on VWI, acute infarct on diffusion-weighted imaging, and A-Fib based on clinical reports. The patients were divided into three groups: 1) A-Fib+IPH, 2) only A-Fib, and 3) only IPH. Multiple logistic regression was used to assess the relationship between high-risk factors and patients with IPH and A-Fib.

Results:

A total of 103 patients were included in the study, 26 patients with A-Fib + IPH, 28 patients with only A-Fib, and 49 patients with only IPH. Hypertension was significantly higher in group 1 (1: 100% vs 2: 82.63% vs 3: 75%, p<0.03). Additionally, LDL absolute level was the lowest in group 1 (1: 69.92 ±32.75 vs 2: 83.86 ±32.07 vs 3: 102.5 ±34.78, p<0.002) (Table 1). Sex was significantly related to patients with both of IPH and A-Fib (p=0.048, OR 0.288, 95%CI 0.084, 0.989).

Conclusion:

The study consistently identified hypertension in A-Fib+IPH group. In addition, A-Fib+IPH group had lower dyslipidemia compared to the other two groups. Finally, there was a male predilection among the three groups, suggesting males are at higher risk for A-Fib and/or IPH. Further investigation determining the relationship and contribution to stroke is necessary.

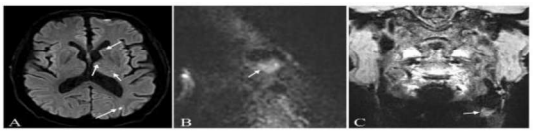

Figure 1. An 80 years old male with atrial fibrillation. Diffusion restriction at the left head of caudate, thalamus, and occipital lobe on the diffusion weighted image (A). Intraplaque hemorrhage of the left carotid bifurcation on the pre-contrast vessel wall imaging (B,C: Axial, Coronal planes)

Table 1: Clinical information and vascular risk factors among the three groups

	Only A-Fib n=49	Only IPH n=28	IPH and A-Fib n=26	p
Age (years old)	71±13.89	71±10.64	77±9.98	0.114
Sex (male)	26/49	19/28	21/26	0.052
Dyslipidemia	36/49	23/28	22/26	0.464
Hypertension	40/49	21/28	100%	0.03
Diabetes	15/49	6/28	9/26	0.539
Smoking	18/49	12/28	17/26	0.057
BNP (pg/ml)	367.18±437.42	157.5±271.53	270.73±328.04	0.076
Hgb A1c (mmol/mol)	6.13±1.79	6.54±1.87	6.08±1.14	0.525
LDL (mg/dl)	83.86±32.07	102.5±34.78	69.92±32.75	0.002
Acute infarct	34/49	23/28	19/26	0.471

1. Kamtchum-Tatuene J, Wilman A, Saqqur M, Shuaib A, Jickling GC. Carotid Plaque With High-Risk Features in Embolic Stroke of Undetermined Source. Stroke. 2020;51(1):311-4.

Advancing Endovascular PAD Treatment: Overcoming Critical Knowledge Gaps with MRI-Histology: an NIH funded study

Alexander Crichton, Eniko Pomozi, Judit Csore, Janak Lamichhane, Alan B Lumsden, Trisha Roy
Houston Methodist DeBakey Heart & Vascular Center

Introduction: There are critical gaps in our understanding of why endovascular treatments fail, particularly in the below the knee arteries. Randomized literature has shown opposing outcomes, with BEST CLI suggesting a bypass first approach, and BASIL-2, which was specific to infra-popliteal disease suggesting an endovascular first approach (1,2). Immediate technical failure remains stubbornly common, with rates of 13-20% quoted in randomized literature (1-3). It is clear that patient selection for treatment has not been optimized, resulting in poor outcomes. Imaging technology has made incredible advances in visualizing blood vessels, and more specifically plaque morphology. Ultrashort Echo Time (UTE) Magnetic Resonance Imaging (MRI) is a non-contrast technique that has been validated in ex vivo samples to evaluate plaque characteristics. Our hypothesis is that plaque characteristics will define procedural outcomes and that this study will advance our understanding of arterial plaque composition that can be utilized to specifically tailor treatment to the patient's disease. The aim of this study was to evaluate the effect of plaque characteristics on immediate technical failure in patients undergoing peripheral vascular intervention.

Methods: Patients attending a large volume academic vascular center with chronic limb threatening ischemia (CLTI) undergoing a planned peripheral vascular intervention were included in the study Inclusion criteria were: age >40 years old, target vessel with at least 50% stenosis defined by pre-operative imaging, Rutherford peripheral artery disease classification grade 4, 5 or 6. Exclusion criteria included refusal or failure to provide consent and MRI contraindications. All patients included underwent a 3T research non-contrast MRI using a UTE sequence. The key feature to identify was whether the lesions being treated were made up of predominantly >50% soft (thrombus, cholesterol/lipid plaque) or predominantly hard (calficic/collagenous plaque) components. Surgeons were blinded to the MRI images analysis and proceeded with the procedure based on clinical pre-operative imaging. The key measure of outcome was immediate technical failure. Fishers Exact test was used for statistical analysis using DATAtab (e.U, Graz, Austria 2025). Institutional Board Review approval for this study was granted.

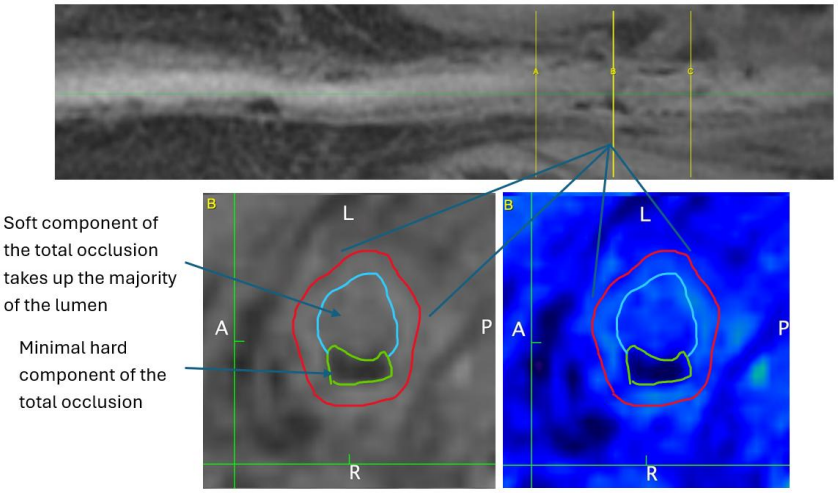

Figure 1. The image above shows a centerline visualization of the popliteal artery where white = patent, grey = soft and dark = hard. In the color image, blue = soft and dark/purple = hard. This shows a predominantly soft total occlusion. This lesion was easily crossable.

Results: 27 lesions underwent MRI evaluation and peripheral vascular intervention (median age 69 years old, 18.2% female, 81.8% male). 3 lesions were excluded because of one being crossed with a guidewire but not being treated and two had MRI image artefacts (e.g. due to movement during image acquisition) leaving 24 lesions for analysis. 54.2% of lesions were defined as soft and 45.6% of lesions were predominantly made up of hard components (figures 1 and 2). Immediate technical failure occurred in 25% of lesions and the only reason for this was an inability to cross the lesion. All lesions that were majority soft had a 0% rate of immediate technical failure whereas 36.4% of predominantly hard lesions had immediate failure due to an inability to cross the lesion which was a statistically significant difference (p=0.031). Subgroup analysis of lesions that had at least a 75% stenosis/total occlusion showed that hard lesions were significantly more likely to result in immediate technical failure compared to soft lesions (57.1% vs 0%, p=0.026). The presence of a totally occlude vessel however did not predict immediate technical failure when compared to a stenosis though (27.3% vs 7.7%, p=0.30).

Conclusions: MRI-histology analysis of plaque characteristics acts as a key predictor of immediate technical failure, yet the ability to evaluate the diseased vessel wall characteristics prior to peripheral vascular intervention remains heavily underutilized. This imaging technique can clearly delineate differences in vessel wall morphology and their close relationship with patient outcomes provides a significant translational finding that could revolutionize patient selection and approaches to treatment.

Preoperative White Matter Lesions on the Fazekas Scale Predict Postoperative Ischemia: The Role of MRI in Risk Stratification for Carotid Endarterectomy

Mark Matus MD[1,2], Andrea Varga MD PhD[2], Peter Sótonyi Jr Prof[2], Zsuzsanna Mihály MD PhD[2]

[1] Department of Vascular Surgery, Hungarian Defense Forces Medical Center - Military Hospital, Budapest, Hungary

[2] Department of Vascular and Endovascular Surgery, Heart and Vascular Center, Semmelweis University

Purpose:

This study aimed to investigate the predictive value of preoperative MRI in operative risk stratification by exploring the relationship between white matter lesions, intraoperative cerebral oxygen desaturation—particularly after carotid clamp release—and the development of new ischemic lesions on postoperative cranila MR diffusion-weighted imaging (DWI).

Methods:

A prospective cohort study (NCT03840265) was conducted, including patients who underwent carotid endarteerctomy (CEA) with available pre- and postoperative MRI scans and intraoperative near-infrared spectroscopy (NIRS) monitoring. The Fazekas scale was assessed on preoperative cranial MRIs. Intraoperative cerebral desaturation was evaluated using NIRS, focusing on the maximum drop in regional cerebral oxygen saturation (rSO_2) after clamp release. On the postoperative MRI scans, DWI was used to detect new ischemic lesions. Statistical analyses included Pearson correlation coefficients and logistic regression models to determine associations between variables.

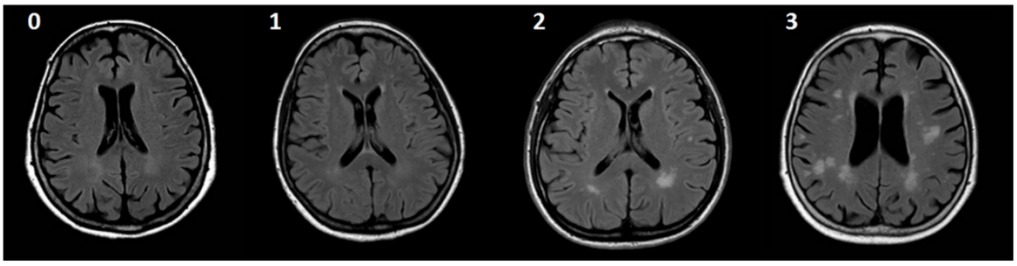

Preoperative MRI scans of patients undergoing carotid endarterectomy, demonstrating white matter hyperintensities graded using the Fazekas scale from 0 to 3.

Results:

A total of 75 patients with both pre- and postoperative MRI and complete intraoperative NIRS monitoring were included. The mean age was 69.6 (SD: ±7.3) years. White matter lesions were graded using the Fazekas scale, with the following distribution: Fazekas 0 (n = 19), Fazekas 1–2 (n = 52), and Fazekas 3+ (n = 4). A significant correlation was observed between the ipsilateral Fazekas score and the presence of new ipsilateral ischemic lesions on postoperative diffusion-weighted imaging ($r = 0.23$, $p = 0.045$). While the association between Fazekas score and intraoperative cerebral desaturation on the contralateral side did not reach statistical significance ($r = 0.12$, $p = 0.300$), the trend may warrant further investigation in larger cohorts.

Discussion:

The correlation between Fazekas scores and postoperative ischemic lesions suggests that MRI-based evaluation can identify patients at higher risk of hemodynamic instability, particularly due to cerebral desaturation due to carotid clamping. Integrating MRI findings into preoperative planning may improve patient selection and perioperative management strategies. Further prospective studies are warranted to validate these findings and refine MRI-based risk assessment protocols.

4D flow using bSSFP at 3T for improved diastolic function evaluation

Jie Xiang[1], Maolin Qiu[2], Gigi Galiana[1,2], Ipek Buber[2], Jeremy Steele[3], Dana C. Peters[1,2]

[1] Department of Biomedical Engineering, Yale University [2] Department of Radiology and Biomedical Imaging, Yale University [3]Pediatric Cardiology, Yale School of Medicine

Purpose: One major limitation of 4D flow MRI is poor contrast. We recently developed a 2D balanced steady state free precession (bSSFP) phase contrast (PC) method. In two tested applications[1,2], we observed accurate velocity measurement and enhanced image contrast. In this work, we extended our method to 4D flow, for comparison of flow velocity and volume, with conventional spoiled GRE based 4D flow, and 2D methods.

Methods: Figure 1 shows the 4D flow bSSFP sequence plotting the gradients in all 3 directions and their corresponding 1st moments. Gradients were designed to null the 0th and 1st moments at TEs and through TRs, achieved by adding extra bipolar. We performed 4D flow bSSFP on 11 healthy volunteers (6 females, 32±13y) on a Siemens 3T Vida scanner. Scan parameters included 3D Cartesian short-axis volume planned at the valve with retro-ECG-gating and navigator-gating. RF was turned off for navigator-skipped heartbeats to reduce SAR, and additional steady state preparation was added after each navigator. TR/TE/θ= 4.1ms/1.8ms/35°, spatial resolution ~3x3x3 mm^3, temporal resolution ~33ms, 12 slices zero-filled to 24, in short axis, 250cm/s through-plane and 200cm/s in-plane VENC. GRAPPA R = 2 coupled with UNFOLD, 67% asymmetric echo, 0.6ms RF pulse with time-bandwidth product of 6, total scan time ~8min. Parameters for GRE 4D flow were similar except TR/TE/θ= 4.3ms/2.1ms/15°. We compared early and late mitral inflow velocities (E and A) and stroke volume (SV) by 4D flow bSSFP to both GRE based 4D flow, 2D 4ch PC and 2D axial PC (for SV). 2D 4ch bSSFP was used for valve velocity estimation[3] and volume correction.

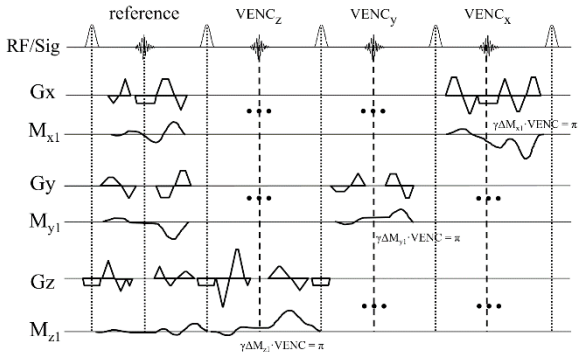

Figure 1 – 4D flow bSSFPsequence diagram and M1

Results: Figure 2 shows one example comparing 4D flow bSSFP and conventional 4D flow, demonstrating better myocardium-blood contrast in both spatial and temporal domain, and similar velocity measurement. Figure 3 shows plot examples of velocity and volume measurements from different acquisitions, and their correlation and Bland-Altman analysis. 4D flow bSSFP agreed with both 2D PC and conventional 4D flow approaches (all R > 0.75), indicating no significant difference for E, A, SV, except an average of 5.27cm/s higher A measured vs. 2D PC (p<0.05).

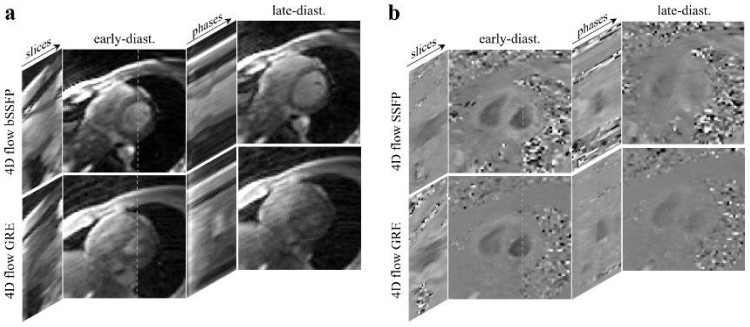

Figure 2 – magnitude and phase images of 4D flow bSSFP vs GRE

Discussion: The feasibility of 4D flow bSSFP, for improved contrast, and consistent E, A and SV measurements vs. conventional GRE based 4D flow and 2D PC was demonstrated. The anatomical information can be obtained in the same scan, with no need of extra anatomical overlays or image registration. Our proposed methods may provide comprehensive evaluation of diastolic dysfunction and may perform better at lower field (1.5T or a recent study tested at 0.6T[4]) vs. the 3T scanner used here (i.e. with reduced off-resonance and SAR).

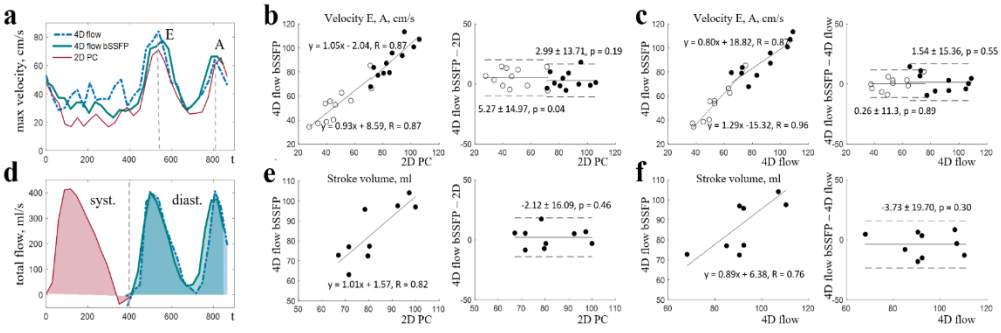

Figure 3 – Mitral inflow E, A, SV measurement by 4D flow bSSFP vs GRE and 2D PC

Reference: [1] Xiang J, et al. Magn Reson Med. 2024;91(3):911-925. [2] Xiang J, et al. J Cardiovasc Magn Reson. 2024 Winter;26(2):101098. [3] Gonzales RA, et al. J Cardiovasc Magn Reson. 2021;23(1):137 [4] McGrath C, et al. Magn Reson Med. 2025 Mar 19.

Improved 5D flow MRI with 3D RING gradient delay correction

Thara Nallamothu[1], Justin Baraboo[1], Daniel Kim[1], Christopher Roy[2], Matthias Stuber[2], Michael Markl[1]
[1]Department of Radiology, Northwestern University, [2]Department of Radiology, University Hospital Lausanne (CHUV)

Purpose: 5D flow is an emerging free-running 3D radial imaging acquisitions with inherent self-gating (ECG, respiration) that captures 3-directional cardiac blood flow[1]. 5D flow data is based on radial k-space sampling, which is subject to gradient delay trajectory errors, where the actual k-space positions may be shifted from the expected position. There are multiple approaches for correcting gradient delay errors in k-space following the acquisition that have been applied with success to cine anatomical MRI. One strategy models the gradient delays as an ellipse fit to the intersections between spokes (RING), which can be extended to 3D[2]. However, flow imaging quantifies the phase of the acquired data, and the impacts of gradient delay errors on measured flow from 3D phase data are not well-characterized. Here, we aim to quantify how a 3D RING correction vs. a simple 1D correction in k-space impacts 5D flow magnitude and velocity image quality.

Methods: 5D flow was acquired in 10 healthy volunteers (age 40±22, 2 female). Each subject's data was processed with no trajectory delay correction (original), 3D RING correction, or 1D shift correction (Fig. 1). 3D RING was performed according to the method proposed by Rosenzweig et al. 2018 with 3D modifications described in Figure 1. 500 reference k-space spokes were used in the 3D RING fit. We first reconstructed one fully sampled static data set per subject, i.e. averaged over cardiac and respiratory cycles. We compared image quality of static magnitude images by quantifying signal-to-artifact ratio (SR) as (maximum signal in image) / (mean signal in segmentation outside body). We then performed full cardiac and respiratory-resolved compressed sensing (CS) 5D flow reconstructions to evaluate the impacts on velocity. 5D flow images were post-processed using a 3D eddy current correction and velocity anti-aliasing. In fully resolved data, we computed SR of magnitude images, aorta mean velocity, and ascending aorta peak systolic velocity.

1D shift
Corrects each readout by shifting k-space peak to the center of k-space

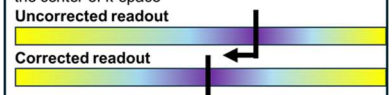

3D RING
Corrects k-space trajectory in 3D by estimating shifts from expected trajectory using ellipsoid fit to k-space intersections

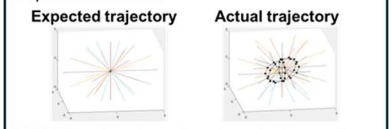

3D RING is performed according to the method proposed by Rosenzweig et al. 2018 with normal vector:

$$\hat{n}_{\theta\phi} = \begin{pmatrix} \sin\theta\cos\phi \\ \sin\theta\sin\phi \\ \cos\theta \end{pmatrix}; \text{ Eqn 1}$$

To describe ellipsoidal spoke shifts as the vector:

$$S = \begin{pmatrix} S_x & S_{xy} & S_{xz} \\ S_{xy} & S_y & S_{yz} \\ S_{xz} & S_{yz} & S_z \end{pmatrix}; \text{ Eqn 2}$$

K-space trajectory positions are modeled as

$$r_{\theta\phi} = S\hat{n}_{\theta\phi} + a_{\theta\phi}\hat{n}_{\theta\phi}; \text{ Eqn 3}$$

where $a_{\theta\phi}$ is the index of each readout point. **S** is computed by identifying the intersecting points of orthogonal k-space lines according to the methods described by Rosenzweig et al. 2018. The corrected k-space trajectory is then computed by Eqn 3.

Figure 1: Methods. 1D shift and 3D RING gradient delay corrections

Figure 2: Effect of trajectory correction on magnitude images. 3D RING and a 1D shift correction were applied and static images were reconstructed without compressed sensing (one zero-filled cardiac and respiratory frame). Sagittal slices of the same image volume are shown. 3D RING reduced the artifact visible in the original image, while 1D shift did not and introduced further errors.

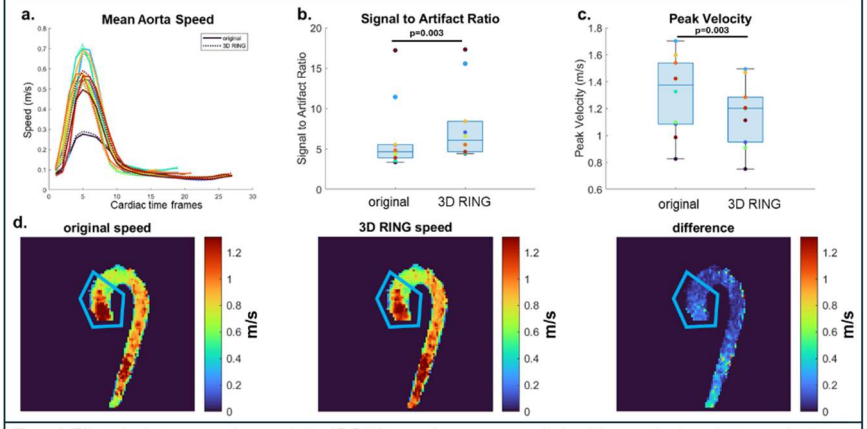

Figure 3: Effect of trajectory correction on velocity. 3D RING correction was were applied and time-resolved, respiratory-resolved images were reconstructed with compressed sensing. A) the velocity profiles in the aorta over time were altered with a decrease in velocity in most cases. B) signal to artifact ratio was increased. C) ascending aorta peak velocity was decreased. D) Example maximum intensity projections of aorta speed are shown, with ascending aorta ROI highlighted. 3D RING altered the velocity profile, with the greatest differences at the edges of the aorta and the edges of the image.

Results: Compared to original data, 3D RING correction led to a decrease in the apparent streaking artifact outside the body, while 1D shift correction was less effective (Fig. 2). 3D RING increased SR by 38% in static images (p=0.01). For the fully resolved 5D flow data, aorta mean velocity profiles were similar but with decreased velocity (Fig. 3a). 3D RING increased SR by 29% (p=0.003, Fig. 3b) and decreased peak velocity by 10% (p=0.003, Fig. 3c).

Conclusions: 3D RING significantly reduces artifacts in 5D flow and impacts the quantified velocities. Future studies are needed to investigate the impacts of 3D RING parameters on flow in comparison to a cartesian ground truth.

1. Ma, L. E. *et al.* 5D Flow MRI: A Fully Self-gated, Free-running Framework for Cardiac and Respiratory Motion-resolved 3D Hemodynamics. *Radiol Cardiothorac Imaging* **2**, e200219 (2020).
2. Rosenzweig, S., Holme, H. C. M. & Uecker, M. Simple auto-calibrated gradient delay estimation from few spokes using Radial Intersections (RING). *Magnetic Resonance in Medicine* **81**, 1898–1906 (2019).

A comparison between MRI based pulmonary flow measurement: 2D phase-contrast, 4D flow and lung perfusion with matrix pencil decomposition

Stefan Gherca[1], Jens Bremerich[1], Daniel Hinck[1], Tanja Haas[1,2], Daniel Giese[3], Markus Klarhöfer[3], Oliver Bieri[1,2], Grzegorz Bauman[1,2], Maurice Pradella[1]

[1]Department of Radiology, Clinic of Radiology and Nuclear Medicine, University Hospital Basel, University of Basel, Basel, Switzerland

[2]Department of Biomedical Engineering, University of Basel, Basel, Switzerland

[3]Magnetic Resonance, Siemens Healthineers AG, Forchheim, Germany

Purpose: To assess accuracy and agreement between cardiac output (CO) from 2D phase-contrast (2D-PC) and 4D flow with lung perfusion using matrix pencil decomposition (Q(MP)).

Methods: This prospective study included 10 healthy individuals (aged 20-35 years, with an equal male/female ratio and an average BMI of 24 kg/m²). All imaging was conducted using a 1.5T clinical MR scanner (MAGNETOM Avanto-Fit, Siemens Healthineers AG, Forchheim, Germany).

Flow measurements in the main pulmonary artery (MPA) were obtained for each participant using both 2D-PC and 4D flow MRI techniques. A prototype coronal 4D-flow sequence provided by the vendor with retrospectively ECG-gating and compressed sensing reconstruction but without respiratory navigator was used. For MRI lung function analysis, time-resolved coronal image sets covering the entire lung were acquired during free breathing with an ultra-fast balanced steady-state free precession (uf-bSSFP) sequence [1].

2D-PC MRI image analysis was conducted using Circle Cardiovascular Imaging (cvi42, Calgary, Canada) by a cardiothoracic radiologist with 5 years of experience in cardiovascular imaging. The 4D flow MRI images were analyzed using suiteHEART® (Neosoft, Pewaukee, Canada) by a cardiothoracic radiologist with 2 years of experience in cardiovascular imaging. CO was calculated for flow measurements and reported in ml/min.

Functional lung data acquired with the uf-bSSFP sequence were analyzed using a fully automated image processing pipeline - TrueLung [2]. The pipeline combined several processing steps including a non-rigid image registration for the compensation of respiratory motion, artificial neural network image segmentation [3] and spectral analysis with the matrix pencil method to generate perfusion images; perfusion was automatically reported as ml/min [4]. Quantitative lung perfusion evaluation was performed using a method proposed by Kjørstad et al [5]. Data was checked for normal distribution and reported as median and interquartile range. The Friedman test was applied with pairwise comparisons to detect specific differences among the three methods. We used Pearson correlation to quantify linear correlation strength between each method pair: 2D-PC vs. 4D flow, 4D flow vs. Q(MP), and 2D-PC vs. Q(MP). Bland-Altman plots were used to assess agreement between methods.

Results: Median pulmonary blood flow was 6580±1317.5 ml/min for 4D MPA, 6882.5±2133.75 ml/min for 2D MPA, and 6239±1715.25 ml/min for Q(MP). The Friedman test (statistic = 0.20, p = 0.905) showed no significant differences between the methods. Pearson correlations were strong: 0.940 (2D-PC vs. 4D flow), 0.711 (4D flow vs. Q(MP)), and 0.808 (2D-PC vs. Q(MP)). In the Bland-Altman analysis, the mean differences between the methods were generally small, indicating good agreement (Figure 1). Absolute differences were smallest between 2D-PC and 4D flow (496.2 ml/min; 7% of median 4D MPA), followed by 2D-PC and Q(MP) (638.6 ml/min; 10% of median Q(MP)) and 4D flow and Q(MP) (840 ml/min; 12.7% of median Q(MP)).

Conclusion: The three pulmonary blood flow methods show strong correlations and agreement, whereas 2D-PC showed better agreement with Q(MP) than 4D flow.

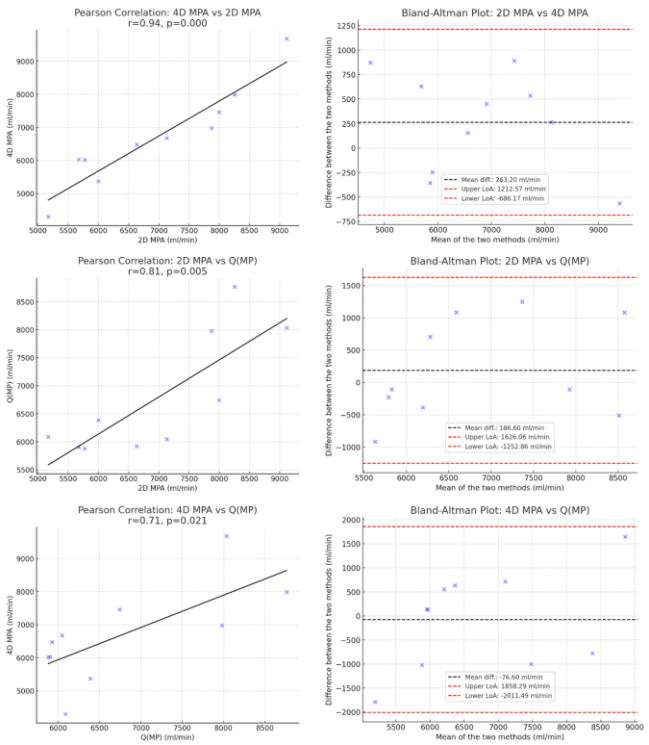

Figure 1. Pearson correlation plots (left) show strong correlations between each pair, especially 4D MPA vs 2D MPA (r=0.94). Bland-Altman plots (right) display the mean differences and limits of agreement, revealing minor discrepancies, with notable outliers in the 4D MPA vs Q(MP) comparison.

References:

1.Bauman, G., O. Pusterla, and O. Bieri, *Ultra-fast Steady-State Free Precession Pulse Sequence for Fourier Decomposition Pulmonary MRI.* Magn Reson Med, 2016. **75**(4): p. 1647-53.

2.Pusterla, O., et al., *An automated pipeline for computation and analysis of functional ventilation and perfusion lung MRI with matrix pencil decomposition: TrueLung.* Z Med Phys, 2024.

3.Pusterla, O., et al., *MRI lung lobe segmentation in pediatric cystic fibrosis patients using a recurrent neural network trained with publicly accessible CT datasets.* Magn Reson Med, 2022. **88**(1): p. 391-405.

4.Bauman, G. and O. Bieri, *Matrix pencil decomposition of time-resolved proton MRI for robust and improved assessment of pulmonary ventilation and perfusion.* Magn Reson Med, 2017. **77**(1): p. 336-342.

5.Kjørstad, Å., et al., *Quantitative lung perfusion evaluation using Fourier decomposition perfusion MRI.* Magn Reson Med, 2014. **72**(2): p. 558-62.

High-Temporal-Resolution Pulse-Gated Single-Venc vs. ECG-Gated Dual-Venc 4D Flow MRI for Intracranial Hemodynamic Assessment

Anahita Najafi, MD MPH[1], Adam Richter, BSE[1], Anna Lytchakov, BA[1], Theresa Benson, BS, BA[1], Ning Jin, PhD[2], Rachel Davids, BS[2], Susanne Schnell, PhD[1,3], Ann Ragin, PhD[1], Emily Rogalski, PhD[4], Kelly Jarvis, PhD[1]

[1] Dept. of Radiology, Northwestern University, USA. [2] Siemens Medical Solutions USA, Inc. [3] Dept. of Medical Physics, University of Greifswald, Germany. [4] Healthy Aging & Alzheimer's Research Care Center, The University of Chicago, USA

Purpose Age-related hemodynamic changes have been linked to structural brain changes and cognitive decline, but the underlying mechanisms remain unclear [1]. 4D flow MRI [2] enables comprehensive evaluation of blood flow dynamics such as peak velocity and pulsatility index [3] and is useful for studying heart-brain hemodynamic coupling. Our previously reported heart-brain imaging protocol [4] used dual-venc 4D flow MRI with prospective ECG gating (DV-ECG) for intracranial flow imaging. While DV-ECG increases dynamic velocity range and velocity to noise ratio [5], it poses challenges. First, prospective gating cannot capture the full cardiac cycle and introduces scan time variability. Second, balancing high temporal resolution with feasible scan times in a comprehensive heart-brain protocol remains difficult [2]. In contrast, a high-temporal-resolution single-venc approach with retrospective pulse gating (highRes-SV-Pulse) could capture the full cardiac cycle with feasible scan times. However, single-venc acquisition can increase velocity noise. Additionally, pulse-gating can introduce variable timing delay, potentially causing timing disagreement between and within subjects. This study compared DV-ECG and highRes-SV-Pulse 4D flow MRI for velocity noise and quantification of hemodynamic parameters.

Methods DV-ECG and highRes-SV-Pulse 4D flow prototype MRI sequences were acquired at 3T clinical scanner (MAGNETOM Prisma, Siemens Healthineers, Forchheim, Germany) in 11 cognitively normal mid-to-later-life adults. One participant was excluded due to ECG signal loss that occurred during DV-ECG acquisition (10 participants analyzed; age=65.5±8.5 years; 8 females and 2 males). DV-ECG (venc=60–120 cm/s; TR/TE/FA=6.0 ms/3.4 ms/15°; k-t GRAPPA, R=5; resolution=1x1x1mm^3/84.0ms; scan time=13.0±3.5[9-19]min), and highRes-SV-Pulse (venc=120 cm/s; TR/TE/FA=5.2 ms/2.9 ms/15°; GRAPPA, R=3; resolution=1x1x1mm^3/41.3ms; scan time=15.8±1.5[14-18]min) were acquired. Standard preprocessing steps, including corrections for Maxwell terms and eddy currents, noise filtering, and velocity anti-aliasing were applied [6]. Manual segmentation of Circle of Willis (CoW) for both scans, and automated time-delay correction via pulse wave detection for highRes-SV-Pulse were performed. Automated voxelwise hemodynamic parameter mapping [7] quantified mean velocity (Vmean), systolic mean velocity (SystVmean), peak velocity (Vmax), pulsatility index (PI), and time-to-peak (TTP), after denoising (see Figure 1). Velocity noise was estimated as the voxelwise standard deviation of static tissue velocities over time ($\sigma_v = std(v)$) and reported as a percentage of venc.

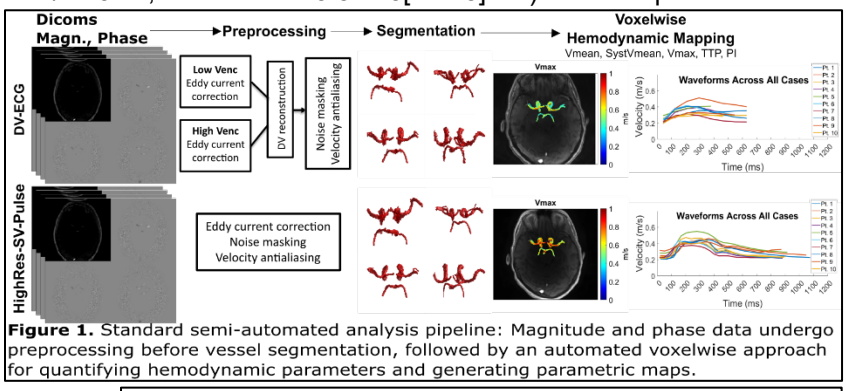

Figure 1. Standard semi-automated analysis pipeline: Magnitude and phase data undergo preprocessing before vessel segmentation, followed by an automated voxelwise approach for quantifying hemodynamic parameters and generating parametric maps.

Results Qualitative assessment of velocity waveforms (Figure 1) indicated that highRes-SV-Pulse showed sharper systolic peaks and greater pulsatility. Moderate correlations were observed for Vmean, SystVmean, Vmax, and TTP (r=0.73, 0.71, 0.64, and 0.46; p<0.001); the correlation for PI was not significant. As shown in Figure 2, Bland-Altman plots indicated no significant bias in Vmean and TTP (p>0.05; LOA=0.08 m/s [24%], and 120 ms [37%]). However, highRes-SV-Pulse measured higher values for SystVmean, Vmax, and PI (mean difference: 0.07 m/s, 0.13 m/s, and 0.64; p<0.01; LOA=0.11 m/s [27%], 0.22 m/s [34%], and 0.50 [41%]). Velocity noise estimates were significantly lower in DV-ECG compared to highRes-SV-Pulse (0.027±0.006 m/s [2.27±0.54% of high venc] vs. 0.054±0.007 m/s [4.50±0.58% of venc]; p<0.01).

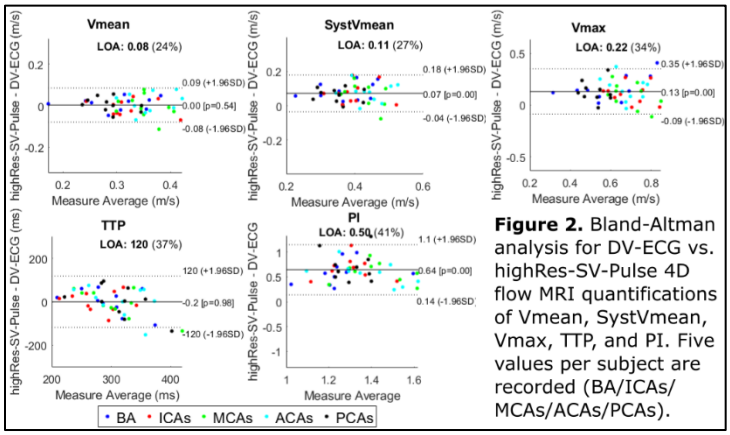

Figure 2. Bland-Altman analysis for DV-ECG vs. highRes-SV-Pulse 4D flow MRI quantifications of Vmean, SystVmean, Vmax, TTP, and PI. Five values per subject are recorded (BA/ICAs/MCAs/ACAs/PCAs).

Discussion HighRes-SV-Pulse 4D flow MRI captured pulsatile velocity waveforms and higher systolic velocities compared to DV-ECG, while maintaining comparable mean velocity quantifications and scans times. Despite its higher velocity noise, highRes-SV-Pulse demonstrates utility for studying regions with a narrow velocity range (e.g. CoW), when scan time is constrained. Findings highlight acquisition trade-offs, supporting highRes-SV-Pulse for time-limited intracranial flow imaging within the heart-brain protocol. Acquisition-related differences must be considered when comparing or pooling data across studies. Next steps include assessing intra- and inter-observer reproducibility and comparing results to 2D PC-MRI.

Acknowledgements NIH NIA P30AG059988, K01AG080070

References [1] de Roos. Circulation. 2017. 35(22):2178 [2] Markl. JMRI. 2012. 36(5):1015 [3] Roberts. Radiology. 2023. 307(3):e222685 [4] Jarvis. ISMRM. 2022 [5] Schnell. JMRI. 2017. 46(1):102 [6] Bock. ISMRM. 2007 [7] Jarvis. JMRI. 2020.

Quantitative evaluation of temperature-induced vessel changes using 3D PC MRA: A 5T MRI study

Jiachen Liu[1], Huilin He[2], Qian Wang[2], Dong Xu[2], Shuo Chen[3], Hualu Han[3], Xihai Zhao[1]

1. School of Biomedical Engineering, Tsinghua University, Beijing, 100084 China.

2. Department of Rheumatology, Peking Union Medical College Hospital, Beijing, 100730, China.

3. Shanghai United Imaging Healthcare, Shanghai, 201815, China.

Purpose

Systemic sclerosis (SSc) is a rare disease with the highest mortality among rheumatic diseases [1]. Raynaud's phenomenon, typically characterized by vascular compromise due to cold and/or emotional stressors, is a typical early feature [2]. Quantifying temperature-induced vessel changes is crucial for vasculopathy assessment but lacks effective tools. Therefore, this study aims to develop a semi-automated method to assess temperature-induced vessel changes using 3D PC MRA at 5T.

Methods

Imaging protocol: The MR imaging was performed on a 5T whole-body MR scanner (uMR Jupiter, United Imaging Healthcare, Shanghai) with a 24-channel SuperFlex body coil. SSc patients and healthy controls underwent 3D PC-MRA before and after 5-minute warm water immersion (WWI) (40°C) within one hour. MR imaging parameters are as follows: FOV = 240×155×45 mm³, spatial resolution = 0.6×0.6×0.6 mm³, flip angle = 15°, TR/TE = 72.4/8.9 ms, VENC = 3 cm/s, compressed sensing factor = 4. Total scan time: 4 min 54 sec. ***Postprocessing***: A semi-automated pipeline (Fig. 1) was developed for morphologic evaluation. Temperature-induced vessel changes were assessed via normalized vessel volume change (NVVC), vessel dynamic changing rate (VDCR), and vascular thermo-sensitivity index (VTSI): $VNNC = nVol_1 - nVol_0, VDCR = VNNC/nVol_0, VTSI = VDCR - \ln(nVol_0)$, where $nVol_0$ and $nVol_1$ are normalized hand volumes before and after WWI. ***Statistical analysis***: Group differences were analyzed using independent samples *t*-test ($p < 0.05$ considered significant).

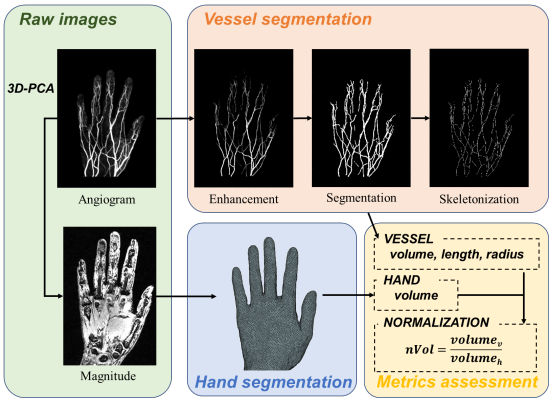

Fig. 1 Flowchart of the quantitative evaluation of hand vessel using 3D PCA.

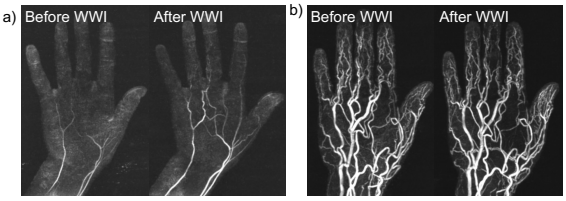

Fig. 2 Example MIP of 3D PCA from a) 62 year old female RP patient, and b) 64 year old female patient before and after WWI.

Table 1 Quantitative evaluation of vessel-to-temperature sensitivity between groups.

	RP (n=10)	HC (n = 7)	*P-value*
NVVC, ‰	0.72±0.79	1.24±1.92	0.527
VDCR	0.23±0.26	0.13±0.16	0.475
VTSI	5.75±0.89	4.65±0.37	0.018*

NVVC=Normalized vessel volume change, VDCR=vessel dynamic changing rate, VTSI=vascular thermo-sensitivity index. Data are presented as mean ± standard deviation. *p<0.05 and **p<0.01.

Results

Ten SSc patients (42±14 years) and seven healthy controls (55±12 years) were recruited. Figure 2 shows representative MIP of 3D PCA. VTSI was significantly higher in SSc patients (5.76 vs. 4.65, p=0.018), while other metrics showed no significant differences between groups (all p>0.05) (Table 1).

Discussion

This study proposes a semi-automated, 3D PC MRA based technique for quantifying temperature-induced vessel changes. VTSI shows is useful for detecting vasculopathy among SSc patients.

References

[1] Volkmann, et al. Lancet. 2023. [2] Markousis-Mavrogenis G, et al. Curr Opin Rheumatol. 2023.

Interaction of aortic hemodynamics with myocardial and vascular remodeling in symptomatic and asymptomatic aortic stenosis examined by 4D Flow CMR

Roberto Visintini[1,2], Ralf Felix Trauzeddel[1,3], Elias Daud[1], Maximilian Müller[1], Jan Gröschel[1], Darian Viezzer[1], Thomas Hadler[1], Edyta Blaszczyk[1], Ning Jin[4], Daniel Giese[5], Sebastian Schmitter[6], Sascha Treskatsch[3], Jeanette Schulz-Menger[1,2]

[1]Working Group on Cardiovascular Magnetic Resonance, Experimental and Clinical Research Center, a joint cooperation between Charité Universitätsmedizin Berlin and the Max-Delbrück-Center for Molecular Medicine, Berlin, Germany; [2]Department of Cardiology and Nephrology, HELIOS Klinikum Berlin Buch, 13125 Berlin, Germany; [3]Charite - Universitätsmedizin Berlin, corporate member of Freie Universität Berlin and Humboldt-Universität zu Berlin, Department of Anesthesiology and Intensive Care Medicine, Charité Campus Benjamin Franklin, Hindenburgdamm 30, 12203 Berlin, Germany; [4]Cardiovascular MR R&D, Siemens Medical Solutions USA, Inc., Cleveland, Ohio, USA; [5]Magnetic Resonance, Siemens Healthineers AG, Erlangen, Germany; [6]Physikalisch-Technische Bundesanstalt, Braunschweig and Berlin, Germany

Purpose

Aortic valve stenosis (AS) is the most common valvular heart disease in Europe[1] with a subgroup of these patients being asymptomatic despite severely reduced aortic valve orifice area. Their current management remains controversial[1,2]. Our goal was to examine the role of cardiovascular magnetic resonance (CMR) in their risk stratification.

Methods

Asymptomatic and symptomatic patients with moderate to severe AS underwent CMR at one of three sites of the Berlin research network for-CMR (BER-CMR) (site I: 3T MAGNETOM Skyra FIT; site II and III: 3T MAGNETOM Prisma FIT, all Siemens Healthineers, Forchheim)[3]. A three-dimensional (3D) cine (time-resolved) phase-contrast CMR with three-directional velocity-enconding (4D Flow CMR) research sequence covering the thoracic aorta with respiratory navigation and retrospective triggering was applied with the following imaging parameters: Temporal resolution 38.96 ms, echo time 2.17 ms, nominal flip angle 15°, voxel size of 2.25 x 2.25 x 2.5 mm^3, compressed sensing acceleration factor 7.6, three-directional velocity-encoding 250 cm/sec. 4D Flow CMR was analyzed regarding maximum wall shear stress (WSS) across 9 planes over the entire thoracic aorta in CAAS MR Solution (Pie Medical Imaging BV, Maastricht, The Netherlands). They were compared to 19 healthy volunteers. Absolute values and percentages and mean ± standard deviation (SD) are given. Significance was tested using one way Anova. Statistical analysis was done using SPSS (IBM, Armonk, USA).

Results

There were no differences in ventricular function and fibrosis between both groups. WSS differed significantly between asymptomatic and symptomatic stenoses at Plane 2, 3, 4, 5, 6 and 9. Healthy volunteers differed significantly from asymptomatic stenoses only in Plane 5, 6, 7, 8 and 9 but not in the ascending aorta and the beginning of the aortic arch (Table 1 and Figure 1).

Discussion

Symptomatic AS patients showed higher WSS than asymptomatic patients and volunteers in the ascending aorta. In the later aortic arch and descending aorta healthy volunteers revealed higher WSS than both stenoses groups.

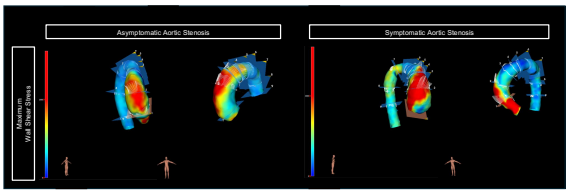

Figure 1: Representative examples ofwall shear stresses in a patient with asymptomatic and patient with symptomatic aortic stenosis

	Healthy volunteers	Asymptomatic aortic stenosis	Symptomatic aortic stenosis	p-value
Max WSS Plane 1 (mPa)	1380 ± 301	1652 ± 1049	1305 ± 476	0.48
Max WSS Plane 2 (mPa)	916 ± 189	1116 ± 233	1494 ± 365	< 0.01
Max WSS Plane 3 (mPa)	999 ± 198	889 ± 279	1248 ± 374	< 0.01
Max WSS Plane 4 (mPa)	952 ± 156	741 ± 253	1077 ± 349	< 0.01
Max WSS Plane 5 (mPa)	1070 ± 166	691 ± 239	1000 ± 377	< 0.01
Max WSS Plane 6 (mPa)	1096 ± 158	612 ± 177	856 ± 373	< 0.01
Max WSS Plane 7 (mPa)	1190 ± 170	586 ± 201	695 ± 276	< 0.01
Max WSS Plane 8 (mPa)	1175 ± 189	524 ± 108	663 ± 230	< 0.01
Max WSS Plane 9 (mPa)	1209 ± 188	536 ± 67	577 ±150	< 0.01

Table 1: Comparison of wall shear stresses along the thoracic aorta

[1]Vahanian A, et al. Eur Heart J 2022;43(7):561-632; [2]Rafique AM, et al. Am J Cardiol 2009;104(7):972-7; [3]Müller M, et al. Front Cardiovasc Med 2024;11:1456814

Foramen Ovale Shunt Visualization and Quantification using Particle Tracking and 4D Flow MRI in Normal Fetal Hearts

Reagan M Tompkins[1], Takashi Fujiwara[2], Eric M Schrauben[1], Lorna P Browne[2], Joost van Schuppen[1], Sally-Ann Clur[3], Richard M Friesen[4], Erin K Englund[2], Alex J Barker[2,5], Pim van Ooij[1]

[1]Department of Radiology & Nuclear Medicine, Amsterdam University Medical Center, NL; [2]Department of Radiology, Section of Pediatric Radiology, Children's Hospital Colorado, University of Colorado Anschutz Medical Campus; [3]Department of Pediatric Cardiology, Emma Children's Hospital, Amsterdam University Medical Center, NL; [4]Department of Pediatrics, Section of Cardiology, Children's Hospital Colorado, University of Colorado Anschutz Medical Campus; [5] Department of Bioengineering, University of Colorado Anschutz Medical Campus

Purpose In fetal circulation, oxygenated blood from the ductus venosus (DV) preferentially shunts through the foramen ovale (FO), a critical fetal atrial connection, while de-oxygenated blood from the inferior vena cava (IVC) is largely directed to the right ventricle. Visualizing these flow patterns with 4D Flow MRI is challenging due to the high spatiotemporal resolution required and fetal motion present during acquisition. This study demonstrates the ability of motion-corrected 4D Flow MRI to visualize and quantify this preferential DV flow shunting in third-trimester fetuses.
Methods 4D flow MRI with Prospective Undersampling in Multiple Dimensions was acquired in 5 healthy fetuses at gestational ages ranging between 33-37 weeks[1]. Scan parameters were: acquired/reconstructed spatial resolution of $(2.5mm)^3/(1.25mm)^3$, temporal resolution of 38-50ms, 10 cardiac phases, VENC of 150cm/s, TR/TE/FA of 2.99-3.30ms/1.77-2.04ms/6.5°, and scan time of ~6 minutes. Retrospective motion correction and compressed sensing reconstruction was applied, and data was filtered for noise[2,3]. A phase-contrast magnetic resonance angiogram (PC-MRA) of the fetal heart and major vasculature was segmented in 3D Slicer to include the DV, IVC, and all visible intracardiac structures[4]. Flow analysis was performed in GTFlow (Gyrotools, Zurich, Switzerland), enabling the generation of particle traces to visualize and quantify shunting through the FO. Particles were released from contours placed in the distal IVC and DV (before the junction with the IVC, Figure 1). The density of particle seeding was normalized to the DV and IVC contours' mean flow values. To quantify flow distribution, virtual particles were semi-continuously released from these two contours into the upstream vessel at each heart phase over one cardiac cycle[5]; their arrival was tracked across a contour drawn at the FO using the PC-MRA. The percentage of particle arrivals at the FO, out of total released particles per contour, was calculated and averaged over the cardiac cycle.
Results Flow through the FO was successfully visualized in all fetuses (Figure 1), with a higher proportion of emitted particles arriving from the DV contour in all but one case. Participant-specific values can be found in Table 1. Particle arrivals are reported as both a non-zero average (excluding phases where no particles arrived) and a total average (including all 10 phases, even when no particles arrived).

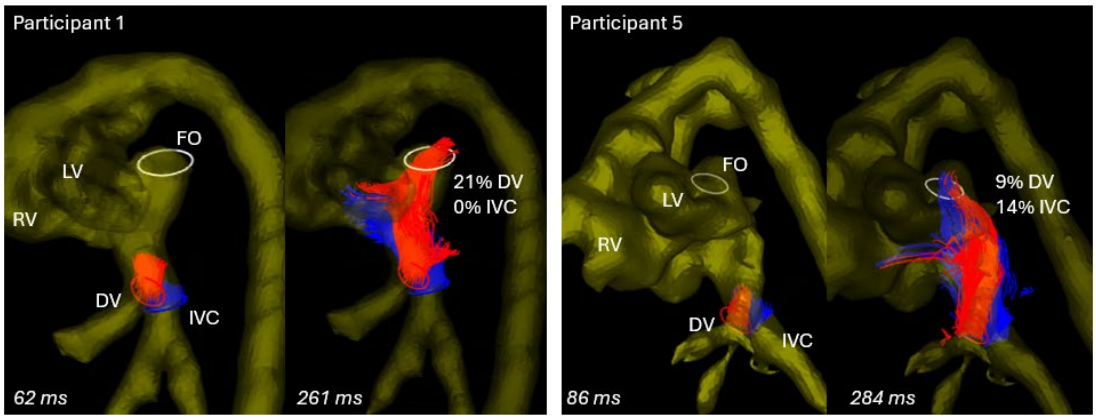

Figure 1. Generated particle tracings from contours at the DV (red) and IVC (blue), with the FO contour at the atria. The PC-MRA segmentation guided contour placement.

Table 1. Quantitative results for FO flow in each fetus. The flow ratio was used in determining seeding density. Particle arrivals are reported as non-zero average (total average).

Participant	DV/IVC flow ratio	%DV arriving at FO	%IVC arriving at FO
1	1.11	23.7 (21.4)	0 (0)
2	1.30	18.0 (18.0)	8.67 (6.17)
3	2.66	43.3 (43.3)	13.3 (6.67)
4	1.25	35.5 (34.5)	10.7 (1.07)
5	0.73	18.26 (9.23)	24.1 (14.4)

Discussion This work explored the potential for motion-corrected 4D flow MRI in assessing key fetal hemodynamic features, demonstrated here with the preferential shunting, compared to the IVC, of oxygenated blood from the DV in normal fetal circulation. The quality and accuracy of particle tracking is highly dependent on the quality of imaging data, emphasizing the importance of motion correction. The ability to visualize small flow patterns can serve as an assessment of the quality of newly developed 4D flow fetal imaging protocols. Inaccuracies, such as pathlines leaving the blood pool, suggest the presence of noise and tracking errors. These inaccuracies may result from imperfections in segmentations, due to the movement of fetal structures, and the use of a relatively high velocity encoding parameter. Optimizing both imaging acquisition and processing techniques is necessary to improve tracking accuracy and overall data reliability.

References [1] Gottwald LM, et al. *NMR Biomed*. 2020; [2] Tompkins RM, et al. *Magn Reson Med*. 2025; [3] Arshad SM, et al. *Magn Reson Med*. 2024; [4] Kikinis R, et al. 3D Slicer. *Intraoperative Imaging and Image-Guided Therapy*. 2014; [5] Roos PR, et al. *J Magn Reson Imaging*. 2023.

Convolutional variations for computationally efficient training of spatiotemporal super-resolution 4D Flow MRI

Jessica Schmidt[a], Pia Callmer[a], Mia Bonini[b], Alexander Fyrdahl[a,c], David Nordsletten[b], David Marlevi[a,d]

[a] Karolinska Institutet, Sweden, [b] University of Michigan, USA, [c] Karolinska University Hospital, Sweden, [d] Massachusetts Institute of Technology, USA

Purpose: Time-resolved four-dimensional phase-contrast magnetic resonance imaging - more commonly: 4D Flow MRI - allows for full-field imaging of various hemodynamic metrics[1]. While inherent trade-offs between resolution, image quality, and scan time limit applicability, the emergence of trained super-resolution networks has opened up for high-resolution recovery through previously unexplored domains[2]. Whereas various setups have been explored, convolutional approaches have so far been limited to either spatial *or* temporal upsampling. Expanding into spatiotemporal upsampling would enable for broader applicability, however, would require the use of higher-order convolutional operations; a matter associated with an exponential increase in both model parameters and training time. To address this, this study aims to investigate different convolutional variations for computationally efficient spatiotemporal super-resolution training, mitigating the effects of the curse of dimensionality while achieving accurate hemodynamic recovery.

Methods: Using the existing residual network 4DFlowNet[3], this work investigates five different alternatives to achieve a spatiotemporal super-resolution. First, a naive *Standard 4D Convolution* approach is implemented, representing a baseline from which to optimize efficiency (**Fig.1A.I**). Second, for computational speed-up a *Nested 3D Convolution* was implemented, assuming temporal independence in noise and artifact distribution separating temporal and spatial convolutions (**Fig.1A.II**). As a third and fourth alternative, a *(3+1)D convolution* [5] and *4D Hybrid kernel* convolution was implemented, both reducing the number of convolutional parameters by neglecting spatiotemporal cross-correlation (either by serial, **Fig.1A.III**, or parallel combinations, **Fig.1A.IV**). As a fifth alternative, the notion of *Sparse 4D Convolutions*[6] are used to leverage the natural spread of data in high-dimensional feature spaces and introduce implicit model regularization (**Fig.1A.V**). Lastly, by combining the Hybrid kernel with the sparse 4D convolution a *Sparse Hybrid 4D Convolution* is evaluated (**Fig.1A.VI**). All methods were evaluated using synthetic 4D Flow MRI generated from six patient-specific computational fluid models used in previous work[4]. Discretized at low (dx = 4mm; dt = 40ms) and high (dx = 2mm; dt = 20ms) resolution, and using image patches of 12x12x12x5 voxels at low resolution, a total of 23'328, 2'496 and 2'502 patches were generated for training, validation, and testing, respectively. Network speed was evaluated with respect to training and inference time, while network accuracy was assessed by the relative error (RE), mean absolute error (MAE), and linear regression fit between super-resolved and reference high-resolution velocities in the test data.

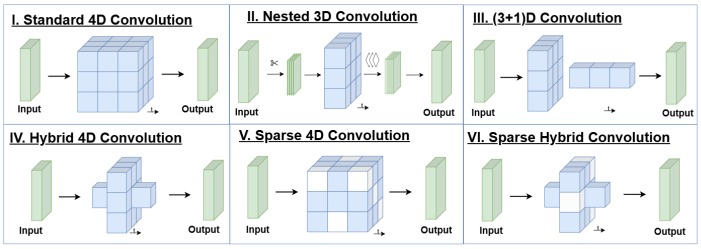

Fig A

Model Name	RE [%]	MAE [m/s]	R^2	Number of Parameters	Computation Time
Standard 4D Convolution	26.8002	0.0201	0.8982	3705283	4060 sec
Nested 3D Convolution	26.0078	0.0189	0.8865	2603331	3445 sec
(3+1)D Convolution	25.5941	0.019	0.9014	1797591	988 sec
Hybrid 4D Convolution	27.3143	0.0193	0.8954	1561795	3180 sec
Sparse Hybrid Convolution	**25.5934**	**0.0175**	**0.9036**	**681024**	**763 sec**

Fig B

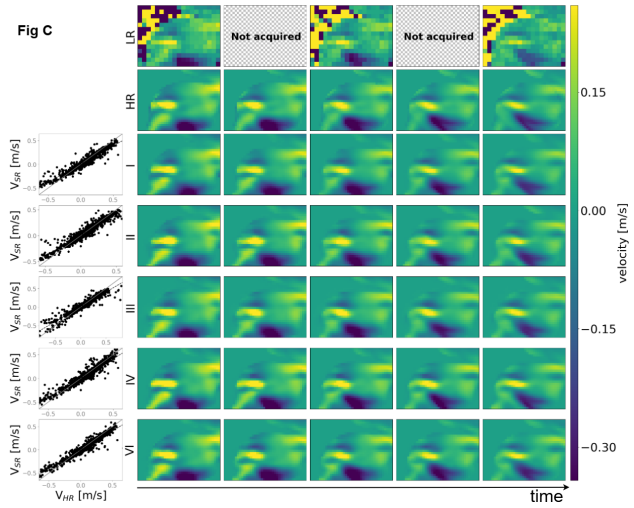

Figure 1: (**A**) Convolutional Kernels of the 4D Convolution Variants (**B**): Table of Test Set Metric Evaluations (**C.1**) Comparison between high-resolution (HR), low-resolution (LR) and super-resolution (SR) variants on the Test Set (**C.2**): Correlation of V_x at peak flow frame.

Results: As per **Fig.1C**, all convolutional variations achieve similar levels of denoising and qualitative alignment with the high-resolution reference. As per **Fig.1B**, the optimized convolutional approaches all achieve substantial speed-up as compared to the standard implementation, with the sparse hybrid computing a single epoch at 20% of the time required for the full setup. Notably, this did not impact prediction accuracy with RE, MAE, and regression statistics all similar between approaches (even being slightly improved with the sparse hybird approach).

Discussion: This study demonstrates how convolutional modifications can achieve substantial improvements in computational time needed to train neural networks for spatiotemporal super-resolution 4D Flow MRI. Notably, the sparse hybrid implementation achieved a five-fold speed-up while maintaining comparably super-resolution accuracy to the baseline model, highlighting potential for future investigation.

References: [1]Bissell et al, JCMR 2023 [2]Ferdian et al, MedIA 2023 [3]Ferdian et al., Frontiers 2020 [4]Bonini et al., JHLT 2022 [5]Küstner et al, Sci Rep 2020 [6]Choy et al, CVPR 2019

Evaluating the Clinical Suitability of 4D Flow MRI in Paediatric Cardiac Imaging: Insights and Experiences

P Hall Barrientos, J Black, P Gupta, R Allen, T Savage
Royal Hospital for Children, Glasgow, UK

Purpose

4D flow offers advanced blood flow visualisation and quantification, surpassing conventional 2D flow MRI in versatility and detail. Its application in routine clinical paediatric cardiac imaging remains underexplored, particularly regarding its feasibility and potential benefits across diverse cardiovascular pathologies. This study implemented 4D flow sequences in all CMR protocols requiring flow measurements, evaluating its benefits in time efficiency and 3D blood flow visualisation.

Materials and Methods

Thirty-three paediatric patients (age range 12- 18 years, 16 female), with varying cardiac pathologies were studied between 2023-2024. Scans were performed on a 1.5 T Aera Siemens scanner at the Royal Hospital for Children, Glasgow. For each patient 2D flow MRI was acquired followed by 4D flow imaging. Data included flow measurements, image quality assessment, acquisition times and flow conservation of the pulmonary artery vessels. Cardiac pathology was confirmed through prior clinical diagnosis and echocardiographic findings. Fourteen patients were confirmed with structural issues (pectus excavatum, tetralogy of Fallot, VSD, AS and coarctation of the aorta), four with valve related issues, four with functional and rhythmic concerns, five with congenital/complex conditionals and three to rule out cardiomyopathy.

Results

The average acquisition time for 4D flow MRI was 13 minutes, shorter than the cumulative 19 minutes for 2D flow imaging (fig.1). Flow conservation was more accurate with 4D flow (2%) compared to 2D flow (19%). The quality of 4D flow images were adequate in 97% of cases, with only one case with severe artefact due to metal being present. There were no significant differences between 2D and 4D flow measurements in the main pulmonary artery and ascending aorta, $p = 0.46$ and $p = 0.78$ respectively. However, differences were observed in the left pulmonary artery and right pulmonary artery, $p < 0.05$, due to suboptimal 2D plane positioning across these vessels.

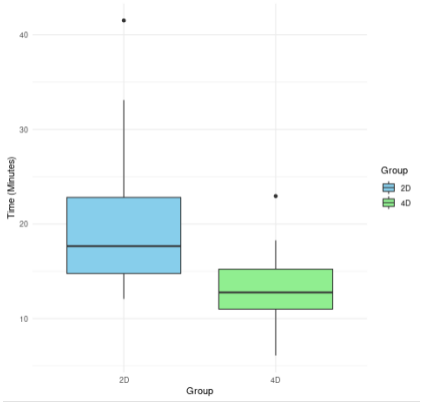

Fig 1. Total time 2D vs. 4D

Discussion

4D flow data acquisition is time-saving and beneficial to patients. However, prolonged scans occasionally led to breathing pattern changes, such as sighs or positional shifts, which introduced breathing artifacts and reduced image quality. Signal-to-noise ratios were notably better in patients who received contrast, although we found that administering contrast is not essential for 4D flow imaging. 4D flow is not necessarily required for all cardiac patients, for example of the pectus excavatum it is more than enough to implement 2D flow measurements. Furthermore, the ability to visualise complex anatomy (fig.2), and associated flow patterns, allows a comprehensive assessment of haemodynamics.

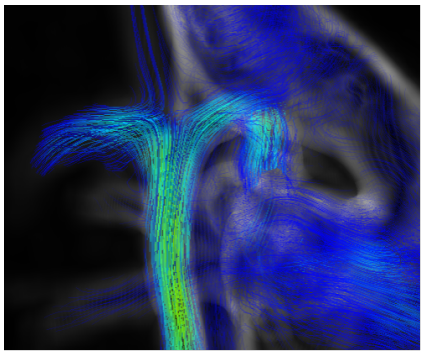

Fig 2. Visualisation of Fontan vessel

References:

1. Sena, L. (2008). Cardiac MR imaging: from physics to protocols. Pediatric Radiology, 38, 185.
2. Kramer, C. M., Barkhausen, J., Bucciarelli-Ducci, C., Flamm, S. D., Kim, R. J., & Nagel, E. (2020). Standardized cardiovascular magnetic resonance imaging (CMR) protocols: 2020 update. Journal of Cardiovascular Magnetic Resonance, 22(1), 17.
3. Stankovic, Z., Allen, B. D., Garcia, J., Jarvis, K. B., & Markl, M. (2014). 4D flow imaging with MRI. Cardiovascular diagnosis and therapy, 4(2), 173.

Assessment of Pulmonary Artery Pressure Gradients in Pulmonary Arterial Hypertension Patients Derived from MRI 4D Flow

Pauline Hall Barrientos[1],S Lua[2], G Roditi[1], C Church[2]

[1]Queen Elizabeth University Hospital Glasgow, UK

[2]Scottish Pulmonary Vascular Unit, Golden Jubilee University Hospital, Glasgow, UK

Purpose: Diagnosis of Pulmonary Arterial Hypertension (PAH) is diagnosed using right heart catheterisation (RHC). However, it is an invasive procedure carrying many risks. Cardiac Magnetic Resonance Imaging (CMR) can potentially be a non-invasive alternative to evaluating and assist in the follow up and management of pulmonary hypertension [1,2]. This proof-of-concept study measures pressure differences with the pulmonary arteries with correlation to RHC-derived haemodynamics in patients with chronic thromboembolic disease with (CTEPH) and without pulmonary hypertension (CTED).

Methods: Five patients with CTEPH, four patients with CTED and seven healthy volunteers were recruited and underwent MR 4D-flow imaging of the pulmonary vessels. All scans were performed using a 3 T Prisma MRI system. All acquisitions used a VENC of 150 cm/s and 4D flow data was processed and analysed using cvi42. Pressure gradients were measured from the proximal of the MPA to distal LPA/RPA (fig 1).

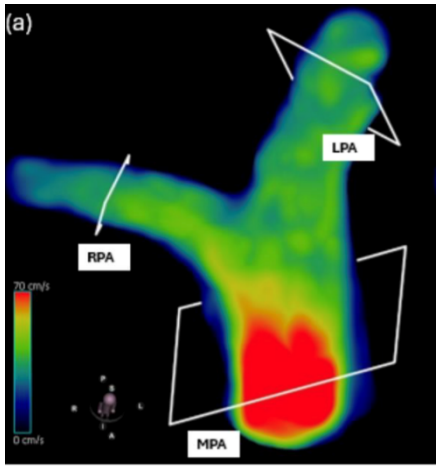

Fig. 1. Analysis planes

Results: In the healthy cohort a substantial pressure difference was observed at peak systole, from MPA to RPA, when compared to CTED/CTEPH patients (fig. 2). It was also noted pressure differences between CTED and CTEPH patients, as shown in figure 2, with a mean pressure difference of –1.48±1.06 mmHg and –0.484±0.707 mmHg respectively.

Conclusions: Our findings show the pressure difference within the RPA as potential marker for PAH diagnosis. However, a larger sample size is needed to confirm if there a statistical difference between CTED and CTEPH patients.

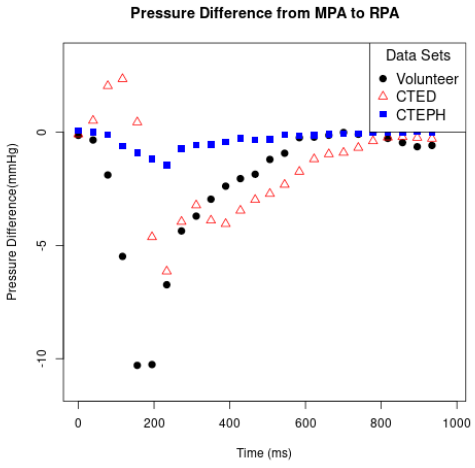

Figure 2. Pressure differences groups

References:

1. Reiter, U., Kovacs, G., Reiter, C., Kräuter, C., Nizhnikava, V., Fuchsjäger, M., ... & Reiter, G. (2021). MR 4D flow-based mean pulmonary arterial pressure tracking in pulmonary hypertension. *European Radiology*, *31*, 1883-1893.

2. Cerne, J. W., Pathrose, A., Gordon, D. Z., Sarnari, R., Veer, M., Blaisdell, J., ... & Carr, J. C. (2022). Evaluation of pulmonary hypertension using 4D flow MRI. *Journal of Magnetic Resonance Imaging*, *56*(1), 234-245.

Impact of Sequence Types and Field Strengths on 4D Flow CMR Measurements: A Multi-Center Study at 3T and 7T

Elias Daud[1], Ralf Felix Trauzeddel[1], Katja Degenhardt[2], Felix Krüger[2], Nico Egger[3], Armin M Nagel[3], Rob J van der Geest[4], Ning Jin[5], Daniel Giese[6], Jeanette Schulz-Menger[1], Sebastian Schmitter[2]

[1]Working Group on Cardiovascular Magnetic Resonance, Experimental and Clinical Research Center, a joint cooperation between Charité Universitätsmedizin Berlin and the Max-Delbrück-Center for Molecular Medicine, Berlin, Germany; [2]Physikalisch-Technische Bundesanstalt, Braunschweig and Berlin, Germany; [3]Institute of Radiology, Friedrich-Alexander-University Erlangen-Nürnberg, Erlangen Germany; [4]Department of Radiology, Leiden University Medical Centre, Leiden, The Netherlands; [5]Cardiovascular MR R&D, Siemens Medical Solutions USA, Inc., Cleveland, Ohio, USA; [6]Magnetic Resonance, Siemens Healthineers AG, Erlangen , Germany

Purpose

Four-dimensional (4D) Flow CMR provides a comprehensive evaluation of blood flow hemodynamics. This study investigated the comparability and reliability of 4D Flow CMR across different scanners and field strengths.

Methods

In a prospective multi-site study, nine healthy volunteers underwent CMR at two locations in Germany: site I (3T and 7T) (MAGNETOM Skyra Fit and MAGNETOM 7T, respectively) and site II (7T) (MAGNETOM Terra X) (all Siemens Healthineers, Forchheim, Germany). 4D Flow CMR data were acquired using a research sequence, with additional scans at site II performed with and without respiratory navigation. Forward flow volume (FFV) and peak velocity (PV) were analysed at four standardized aortic planes (Figure 1) using MASS research software. Correlation and intraclass correlation coefficient (ICC) analyses assessed measurement comparability and reliability.

Results

A representative example of 4D Flow CMR phase images of one healthy volunteer across all three scanning sites is displayed in Figure 2. Moderate to good agreement was observed when comparing 3T and 7T scanners: FFV: Site I (7T) vs. 3T: r=0.50, P<0.002, ICC=0.651; Site II (7T) vs. 3T: r=0.76, P<0.001, ICC=0.794, PV: Site I (7T) vs. 3T: r=0.82, P<0.001, ICC=0.904; Site II (7T) vs. 3T: r=0.77, P<0.001, ICC=0.873. Between 7T scanners, PV showed good agreement (r=0.68, P<0.001, ICC=0.812), but FFV varied significantly. Respiratory navigation had minimal impact, with excellent agreement for both FFV (r=0.95, P<0.0001, ICC=0.992) and PV (r=0.95, P<0.0001, ICC=0.842) (Figure 3).

Discussion

4D Flow CMR at 7T demonstrated feasibility and good agreement with 3T, though FFV differences between 7T scanners warrant further investigation. Respiratory navigation had minimal impact on measurement reliability

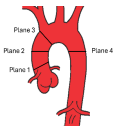

Figure 1: Plane positions

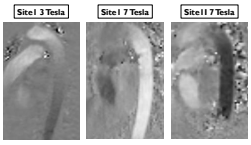

Figure 2: Examples of 4D Flow CMR phase images

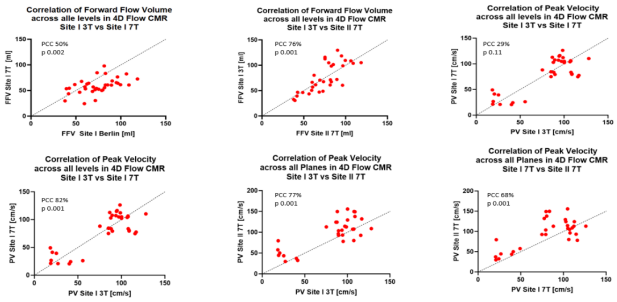

Figure 3: Correlation of FFV and PV measured across the different sites

Highly Efficient, Free-Breathing Whole-Chest Equilibrium Phase bT1RESS MR Angiography: Initial Clinical Experience

Robert R. Edelman[1,2], Nondas Leloudas[1], Hang Chen[3], Reza Nezafat[3,4], Tess Wallace[5], Ioannis Koktzoglou[1,6].
[1]Endeavor Health; [2]Radiology, Feinberg School of Medicine, Northwestern University; [3]Beth Israel Deaconess Medical Center; [4]Harvard Medical School; [5]Siemens Healthineers; [6]Pritzker School of Medicine, University of Chicago

Purpose: A fundamental limitation of both CTA and contrast-enhanced MRA (CEMRA) is that angiographic image quality greatly deteriorates when scans are obtained after the first pass (i.e., during the "equilibrium phase" of contrast enhancement). To overcome this limitation, we recently described a breath-hold, slab-selective equilibrium phase CEMRA technique called *balanced T1 relaxation-enhanced steady-state (bT1RESS)* (1). Further improving upon this technique, we implemented a highly efficient free-breathing version with >9-fold scan acceleration that enables very rapid whole-chest imaging and tested it in a series of patients undergoing clinically-indicated cardiac MRI (CMR) exams.

Methods: This study was IRB approved. 33 patients were imaged using a standard CMR protocol with the addition of a prototype navigator-gated, whole-chest bT1RESS sequence which was obtained post-contrast (0.15 mmol/kg gadobutrol). Scan parameters included: isotropic 2-mm resolution (1-mm^3 with interpolation), TI = 500 ms, SPAIR, sampling bandwidth ~1500 Hz/pixel, TE = 1.15 ms, slice and phase partial Fourier, temporal resolution ~200 ms. The first 14 patients were obtained with 2x2 (slice x phase) GRAPPA acceleration, while the last 19 patients used 3x2 GRAPPA acceleration.

Results: Median scan time for the 19 patients using 3x2 acceleration was 1.27 minutes (min = 0.91 minutes, max = 3.02 minutes) vs. 2.21 minutes for the 14 patients using 2x2 acceleration. For 3x2 acceleration, 2 patients had a scan time >2 minutes and 3 patients had a scan time <1 minute. Mean blood pool-to-muscle contrast was 6.5 for bT1RESS scans obtained <5 minutes post-contrast vs. 5.7 for bT1RESS scans obtained >20 minutes post-contrast, so that diagnostic bT1RESS studies could be obtained without concern for post-contrast scan delay. Good-to-excellent image quality and visualization of the aorta, pulmonary arteries and veins, coronary origins, coronary sinus, LAA, atria and ventricles **(Figs. 1 and 2)** were obtained in all cases with 3x2 acceleration and all but one case with 2x2 acceleration (the exception being a patient in whom ghost artifacts were caused by motion of ferromagnetic sternal wires). There was excellent correlation (0.92/0.93, p<0.001) between left/right end-diastolic ventricular volumes obtained from short axis cine stacks vs. bT1RESS.

Discussion: Free-breathing, whole-chest equilibrium phase bT1RESS shows promise as a highly efficient and useful method for cardiac and vascular imaging. Using 3x2 GRAPPA acceleration, good-to-excellent image quality was reliably obtained with scan times <2 minutes. Multiplanar reconstructions of the heart and great vessels were of diagnostic quality and off-resonance effects were insignificant. In practice, the short acquisition time allows whole-chest bT1RESS to be obtained during the 4-minute waiting interval between the resting perfusion scan and TI scout, while rapid inline image reconstruction (<15 seconds for the entire data set) permits contemporaneous image review without disrupting the normal CMR workflow. Alternatively, the scan can be acquired tens of minutes later with comparable image quality, similar to a ferumoxytol-enhanced exam but with the major benefit of using a standard extracellular gadolinium-based contrast agent. The technique also shows promise for rapid 3D functional evaluation of the heart.

References: 1. Edelman et al. JCMR 2024;26(2):101046. **Acknowledgements:** NIH 1R01CA263091, 1R21CA273280.

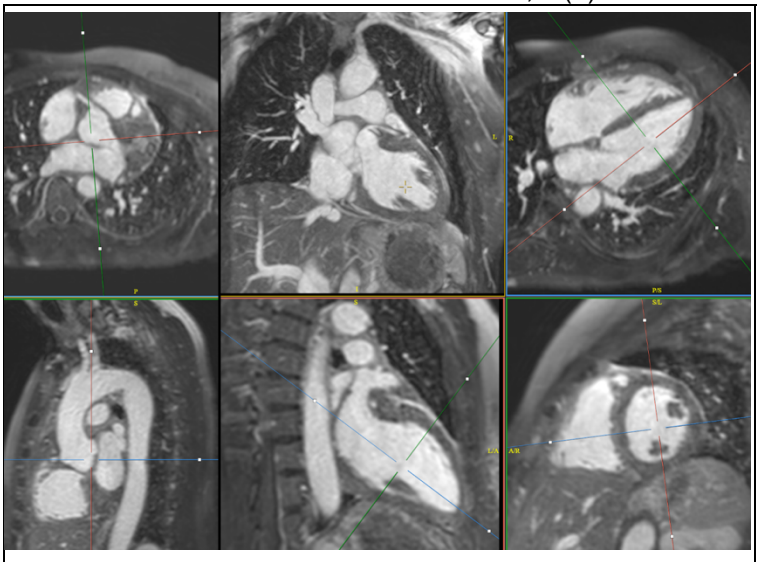

Fig. 1. 51-year-old female with non-sustained ventricular tachycardia. Multiplanar reconstructions from whole-chest bT1RESS (3x2 acceleration, scan time = 1 min 46 sec) show excellent delineation of the entire thoracic aorta, pulmonary vessels, and intracardiac structures.

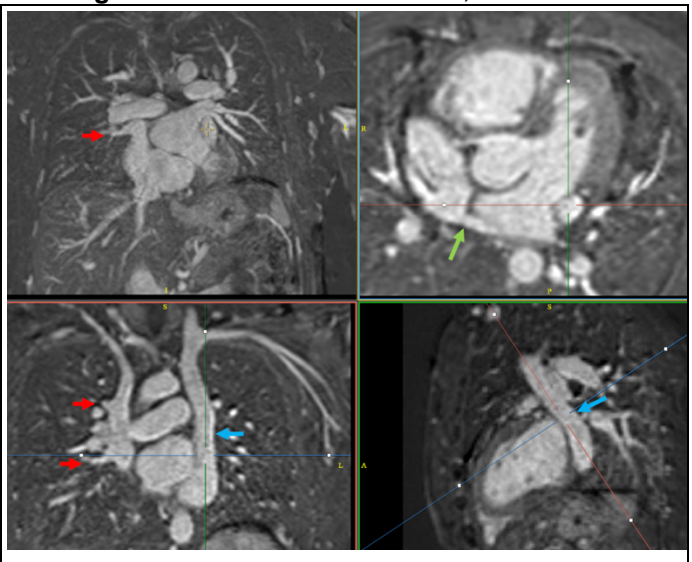

Fig. 2. Whole-chest bT1RESS in a 37-year-old male with partial anomalous pulmonary venous return (red arrows), left superior vena cava (blue arrow), and sinus venosus defect (green arrow). There is excellent depiction of the congenital anomalies.

Detecting abnormal aortic motion in Marfan syndrome

D. Bosshardt[1,2], R. Merton[1], A. Reilink[1], D. Robbers-Visser[2], E. M. Schrauben[1], M. Groenink[1,2], P. van Ooij[1]
[1]*Department of Radiology & Nuclear Medicine, Amsterdam UMC, the Netherlands*
[2]*Department of Cardiology, Amsterdam UMC, the Netherlands*

Purpose: To detect abnormal motion in Marfan patients by a comparison with a 3D average of healthy controls.
Methods: 47 healthy volunteers (aged 34 [22-50] years, 23 women) and 84 Marfan patients of which 33 had aortic root replacement surgery (RR) (aged 36 [24-50] years, 11 women) and 51 native aortas (aged 34 [19-50] years, 26 women) were included as part of a prospective study investigating aortic motion in Marfan [1]. All participants underwent MRI imaging of the thoracic aorta using a free breathing, time-resolved and three-dimensional (3D) balanced steady-state free precession (bSSFP) without contrast agent administration on a 3T Philips scanner (Best, NL) [2]. ECG or PPU-gated PROspective Undersampling in multiple Dimensions acceleration was used with acceleration factor R~19 and scan time of ~4:30 min. Automated self-gating was used to retrieve the respiratory signal and retrospectively register and average four respiratory bins to expiration. Scan parameters were acquired/reconstructed spatial resolution of (1.6/1.0 mm)^3, temporal resolution of 30 cardiac phases, TR/ TE / FA = 2.9 ms / 1.4 ms / 40°. NnU-net [3] was used to segment the aorta in 3D at all timeframes. Three-dimensional displacement was quantified by iterative closest point (ICP) registration of all timeframes to the end-diastolic timeframe [4]. The timeframe with the highest 3D displacement was selected for analysis. ICP registration and nearest neighbour interpolation was used to create 3D average and standard deviation (SD) maps of the volunteers and to project these onto the patient geometries. Increased/ decreased displacement (cm^2) was defined as higher/lower displacement than the average+/-1.96*SD (95% confidence interval) of the volunteer maps. Proximal and distal ascending and descending aorta regions (AAo and DAo) were manually selected relative to the right pulmonary artery and the supra-aortic arteries (see figure 1h). Multivariate analysis of abnormal motion for each of these regions was performed with RR, betablocker use, sex, angiotensin blockers, left ventricular function (LVF), aortic insufficiency (AoI), mutation effect, age, mean arterial pressure, body surface area, heart rate, root diameter and tortuosity index (TI) [5]. Incidence maps showing the number of patients with abnormal motion per wall point were created as well [6].

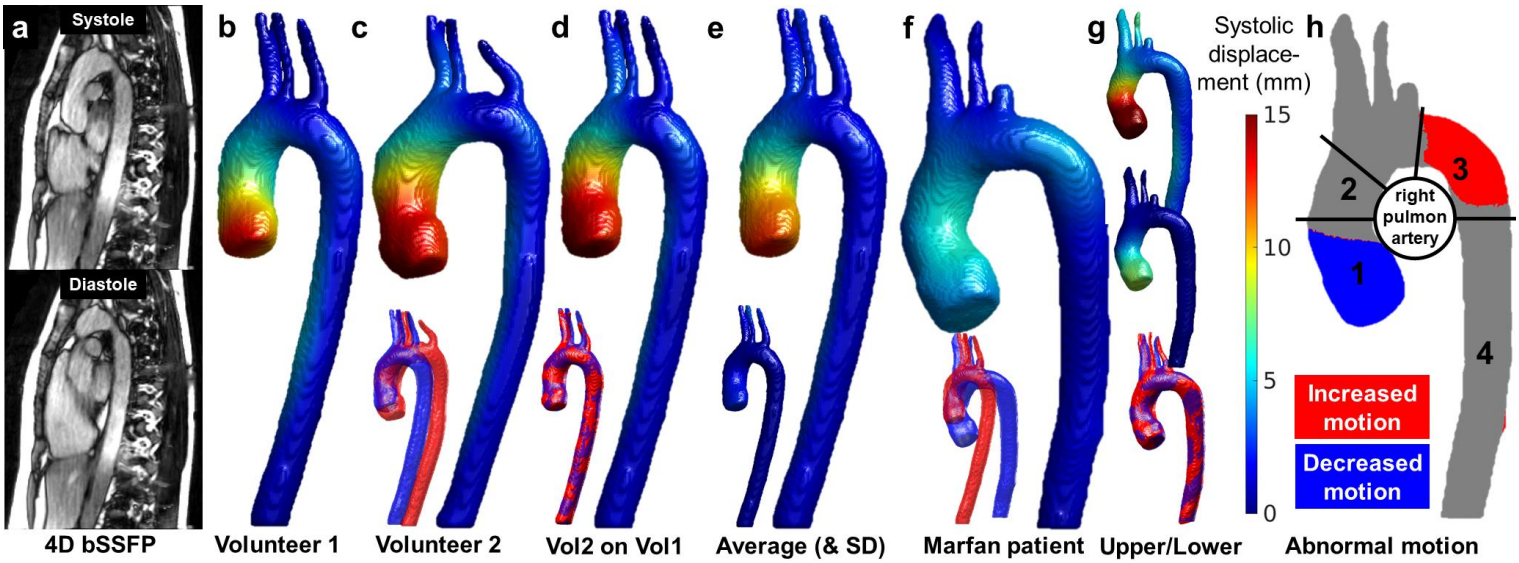

Figure 1. a) 3D bSSFP images for one slice at the systolic and diastolic timeframe, b) peak systolic displacement of volunteer 1 and c) volunteer 2, d) displacement of volunteer 2 projected to volunteer 1, insets show pre- and post-registration, e) the average displacement and standard deviation of all 47 volunteers, f) displacement of an exemplary Marfan patient, g) the upper and lower limits of the volunteer 95% confidence interval projected on the patient geometry, insets show pre- and post-registration, h) red/blue regions show higher/lower systolic displacement than upper/lower thresholds of the volunteers.

Results: In figure 1 exemplary datasets are displayed alongside the 3D average and an abnormal displacement map. In multivariate analysis, decreased motion in the proximal AAo was associated with RR (P<0.001), sex (P=0.033) and TI (P<0.001), in the distal AAo with TI (P=0.001), in the proximal DAo with age (P=0.001) and TI (P=0.013) and in the distal DAo with RR (P=0.01), LVF (P=0.03), age (P=0.02) and TI (P=0.02). Increased motion in the proximal AAo and DAo was associated with no parameters, in the distal AAo with TI (P=0.03), in the distal DAo with AoI (P=0.001). Incidence maps (figure 2) show that up to 85% of patients after RR had decreased motion in the proximal AAo and up to 45% increased motion in the proximal DAo, which was higher than non-RR patients.
Discussion: In this study we showed that systolic displacement of the aorta of Marfan patients presents higher and lower magnitude than healthy aortas depending on aortic region. Incidence maps show that RR surgery has an effect on motion in the aortic root and the proximal DAo, which are both locations associated with aortic dissection. Tortuosity has an effect on aortic motion as well. Motion was not associated with aortic diameter, and could therefore have added value in making treatment decisions for RR. Follow-up studies should indicate whether motion is associated with outcomes.

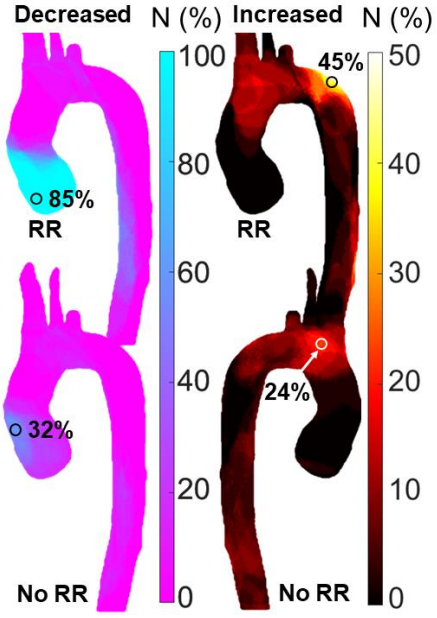

Figure 2. Incidence maps

References: [1] Bosshardt et al. submitted 2025. [2] Merton et al. Magn Res Med. 2024 [3] Isensee et al. Nat Methods 2021 [4] Merton at al. J Cardiovasc Magn Reson. 2024 [5] Franken et al. Int J Cardiol. 2015 [6] Farag et al. J Magn Reson Imaging 2018

Adverse Outcome Prediction in BAV patients with Machine-Learned Hemodynamic Estimates from Contrast-Enhanced MRA or Full Velocity Measurements from 4D flow MRI

Ethan Johnson[1], Haben Berhane[1], Aniket Dehadrai[1], Anthony Maroun[1], David Dushfunian[1], Bradley Allen[1], Michael Markl[1]
[1] Northwestern University, Chicago, USA

[*Purpose*] Bicuspid aortic valve (BAV) is a common disorder, carrying elevated risk of aortopathy and complications [1,2]. Stratifying risk is fundamentally challenging, and current standards monitor aortic diameter measurements from angiography. Altered aortic hemodynamics, e.g., regional peak velocity (V_{max}) and maximal wall shear stress (WSS), have involvement in BAV aortopathy [3,4], but these traditionally require time-consuming 4D flow MRI and as such are not routinely quantified [5]. Standard contrast-enhanced MR angiography (CEMRA) is less complex, with wider clinical adoption [6], but it does not provide hemodynamic information. Recent machine learning (ML) work has demonstrated velocity estimation directly from CEMRA by a fluid-physics informed cycleGAN network [7]. Here, we applied these methods to infer aortic velocities from CEMRA in a cohort of BAV patients, testing the hypothesis that ML-derived aortic hemodynamics can accurately predict adverse aortic outcome (dissection, surgical intervention). As reference, we compared to predictive performance of the same outcomes with hemodynamic estimates from 4D flow MRI.

[*Methods*] An institutional database was used to access CEMRA from 180 BAV subjects (no prior surgery). The electronic health record was queried to collate outcomes (diagnosis, procedure) for all subjects with MRA between 2011–2024. Lists were cross-referenced, yielding 146 subjects with both CEMRA available and outcomes collated. Imaging used 1.5T/3T (res. 0.6–2.2mm^3/tip 25°–40°/TE 0.9–1.2ms/TR 2.5–3.4ms). A cycleGAN network (fluid-physics-informed 3D dense-U-net generators/discriminators) was trained with paired 4D flow and CEMRA (*n*=775 BAV) to estimate peak systolic velocity vectors from CEMRA (Fig. 1) [7]. No data from network training was included in here. The MRA-to-velocity network was applied, and V_{max} and WSS were quantified. Additionally, 4D flow data for the same subjects was processed by an automated 4D flow MRI pipeline tool [8,9] to quantify V_{max} and WSS directly. Outcome data was filtered to find earliest occurrence of cardiovascular surgery or aortic dissection (Fig. 2). Patients were also grouped by time of adverse outcome relative to baseline CEMRA. Patients with outcomes occurring any time before or a limited time after imaging were excluded (surgery: 6 months, dissection: 1 month), as it was possible that imaging was due to another indication for the outcome. Patients with no adverse outcome were classified "stable"; those with adverse outcome after the threshold were classified intervened (Fig. 2).

The cycleGAN-derived V_{max} and WSS, patient age, and aortic diameter (mid-ascending) were used to fit linear models for predicting outcome (binomial: "stable" vs. "intervened"). For each hemodynamic parameter (V_{max} and WSS), two versions of the model were created, including or excluding aortic dimension as a variable. Additionally, a model using only diameter and age were also derived. Predictive performance of models was evaluated using receiver-operator characteristic (ROC) area-under-curve (AUC) as a performance metric. Finally, the same analysis was performed using quantifications of V_{max} and WSS from 4D Flow MRI.

[*Results*] The cohort had mean age 48.5y(±14.3y) with 75% male sex; mean follow-up duration was 6.1y(±3.7y) (Fig. 3). For surgery or dissection outcomes, 95 patients were stable, 26 had the outcome occur, and 25 were excluded (Fig. 2). Predicting adverse outcome from CEMRA hemodynamic estimates showed generally high performance (AUC=0.77–0.86; Fig. 3). The performance for predicting adverse outcome using 4D flow-derived parameters was similar (AUC=0.78–0.90; Fig. 3). Using hemodynamics alone (no diameter) to predict outcomes, V_{max} gave marginally better performance than WSS did for both imaging types (AUC=0.79 either V_{max} vs. 0.78, 0.77 for 4D Flow, CEMRA WSS). With diameter included for the model, WSS was more predictive than V_{max} (AUC=0.90,0.86 vs. 0.82,0.83). For both imaging types, either hemodynamic predictor was better than diameter alone (AUC=0.54).

[*Discussion*] Diameter-only prediction of adverse outcomes offered poor performance, marginally higher than random-chance. Introducing velocity information, whether inferred by cycleGAN from CEMRA or whether measured by 4D flow MRI, allowed markedly-improved prediction of surgery or dissection. The results here are consistent with a previous study showing 4D flow MRI-derived hemodynamic predictors for surgery in BAV [10], and those results translate to analysis of velocity estimates drawn from CEMRA images. The strong performance predicting adverse outcome using hemodynamic quantifications from easy-to-acquire CEMRA images suggests high potential clinical utility in management of BAV aortopathy, in particular to stratify risk in such patients.

[1] Masri A, et al. Heart. 2017. 103(17):1323. [2] Otto C, et al. JACC. 2021. 77(4):e25. [3] Liu J, et al. Front Physiol. 2018. 14(9):993. [4] Soulat G, et al. JACC:CVI. 2022 15(1):33. [5] van Schuppen J, et al. JMRI. 2024. 61(4)1618. [6] Reimer P, et al. Springer. 2006. [7] Berhane H, et al. JCMR. 2024. 26:100613. [8] Johnson E, et al. ISMRM. 2023. 933. [9] Johnson E, et al. ISMRM. 2024. 583. Dehadrai A, et al. SCMR. 2025.

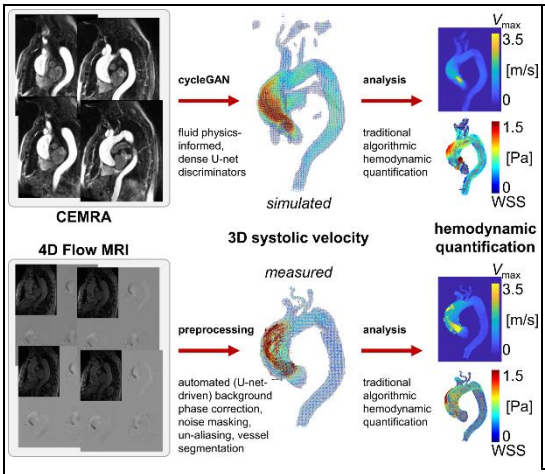

Figure 1. Schematic for data processing in this study, with a processing pipeline for CEMRA (*top*) using physics-informed cycleGAN to estimate velocities, or 4D flow MRI (*bottom*) with standard automatic preprocessing and algorithmic hemodynamic quantification.

	all subjects	surgery / dissection		
		stable	intervened	excluded
total subjects	146	95	26	25
male sex (%)	110 (75%)	68 (72%)	18 (69%)	24 (96%)
age [y]	48.5 ± 14.3	47.3 ± 13.9	50.0 ± 14.9	51.3 ± 15.1
aortic diameter [mm]	40.4 ± 8.2	39.0 ± 8.4	40.5 ± 7.4	45.3 ± 6.5
stenosis / regurg. (%)	105 (72%)	62 (65%)	21 (81%)	22 (88%)
follow-up duration [y]	6.1 ± 3.7	6.2 ± 3.6	7.0 ± 3.3	4.5 ± 3.9

outcome	procedure codes (CPT or ICD)
surgery	33120, 33130, 33256, 33265, 33266, 33300, 33300066, 33305, 33310, 33315, 33320, 33322, 33330, 33335, 33340, 33361, 33362, 33363, 33364, 33365, 33366, 33367, 33368, 33369, 33370, 33390, 33391, 33400, 33405, 33406, 33410, 33411, 33413, 33414, 33415, 33416, 33417, 33418, 33419, 33425, 33426, 33427, 33430, 33463, 33464, 33465, 33474, 33475, 33477, 33496, 33500, 33502, 33503, 33504, 33505, 33506, 33507, 33510, 33511, 33512, 33514, 33517, 33518, 33519, 33521, 33522, 33523, 33530, 33533, 33534, 33535, 33536, 33542, 33545, 33548, 33572, 33608, 33620, 33641, 33645, 33647, 33681, 33702, 33720, 33802, 33803, 33845, 33853, 33858, 33859, 33860, 33861, 33863, 33864, 33866, 33870, 33871, 33875, 33877, 33880, 33881, 33883, 33884, 33886, 33889, 33891, 33910, 33917, 33935, 33940, 33945, 33968, 33970, 33971, 33975, 33976, 33977, 33978, 34701, 34702, 34703, 34704, 34705, 34706, 34707, 34708, 34709, 34710, 34711, 34712, 34713, 34714, 34715, 34716, 34717, 34718, 34800, 34802, 34803, 34804, 34805, 34808, 34812, 34813, 34820, 34825, 34826, 34831, 34833, 34834, 34841, 34842, 34843, 34844, 34845, 34846, 34847, 34848, 34900, 35001, 35005, 35010659, 35010664, 35010671, 35011, 35021, 35045, 35081, 35082, 35091, 35092, 35102, 35103, 35112, 35121, 35131, 35141, 35142, 35151, 35221, 35251, 35281, 35472, 35500, 35506, 35510, 35512, 35531, 35556, 35558, 35565, 35566, 35570, 35571, 35572, 35600, 35601, 35606, 35616, 35621, 35623, 35626, 35631, 35632, 35633, 35634, 35637, 35646, 35647, 35654, 35656, 35661, 35663, 35665, 35666, 35671, 35682, 35694, 35695, 37215, 37216, 37217, 37220, 37221, 37222, 37223, 37236, 37237, 37616
dissection	I77.70, I71.00, I71.01, I71.010, I71.011, I71.012, I71.019, I71.02, I71.03

Figure 2. Summary of demographics for the overall cohort and the adverse-outcome subgroups (*top*), and electronic health record keys used to classify outcomes (*bottom*).

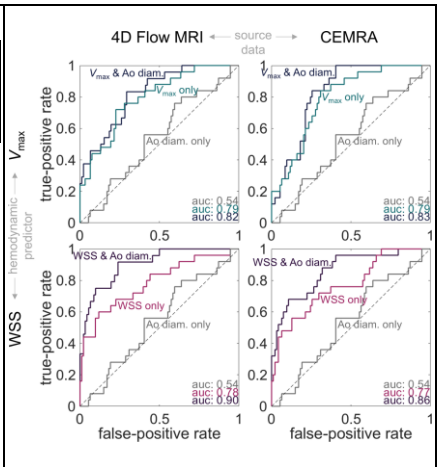

Figure 3. Receiver-operator characteristic curves show performance for prediction of adverse outcomes in BAV patients from CEMRA-based (*right*) or 4D flow MRI-based (*left*) hemodynamic parameter estimates.

Selective Hepatic artery and portal vein non-contrast Liver MR perfusion

Yoshiki Kuwatsuru[1,2], Vadim Malis,[1] Claude Sirlin,[1] Mitsue Miyazaki,[1]

1. Department of Radiology, University of California-San Diego, La Jolla, CA 2. Department of Radiology, Juntendo University, Tokyo, Japan

Introduction: This study aims to develop and validate non-contrast magnetic resonance (MR) perfusion techniques to assess hepatic artery (HA) and portal vein (PV) blood flow, separately. Current MR methods rely on the administration of contrast agents, which pose limitations for patients with allergies or renal insufficiency[1]. A recent report shows velocity selective ASL marking both HA and PV at one point using prospective respiratory motion compensation[2], being not able to separate HA and PV perfusion. We report here a new approach utilizing free-breathing interleaved stack-of-stars (iSoS) with time-spatial labeling inversion time (Time-SLIP) to selectively label HA and PV blood perfusion[3]. The Time-SLIP iSoS technique is radial in the horizontal (*kx-ky*) direction and Cartesian in the vertical (*kz*) direction, with interleaving segmented lines between slices with Time-SLIP tag-on and tag-off acquisitions[4], improving motion stability by oversampling the center of the k space with interleaving in the slice direction, without respiratory compensation. The methods improve the safety and accessibility of liver disease diagnosis and the possibility of assessing conditions such as hepatitis and portal hypertension without the risks of contrast agents.

Methods: All liver experiments were performed on a clinical 3T scanner (Vantage Galan 3T, Canon Medical Systems, Japan). Ten healthy subjects (23 to 80 years old, six males and four females) enrolled in the liver perfusion studies. In addition, one beta Thalassemia (BT) patient with mild fatty liver legions was examined. **Figure 1** shows the iSoS with Time-SLIP ASL using tag-on (non-selective-IR and spatial selective-IR pulses) and tag-off (only non-selective-IR pulse) for multiple TI (100, 500, 750, 1000, 1500, 2000, and 3000 ms). As shown in **Figure 1**, the HA perfusion was applied with a T2prep module with a TE of 65 ms to suppress the venous and background signals, and for the PV perfusion, T2prep was turned off to prevent excessive suppression of portal vein signals. Enhanced fat suppression (combination of STIR and CHESS)[5] was applied for uniform fat suppression. For the HA perfusion, a selective tag pulse is applied at the level of the aorta and heart on the diaphragm, while the oblique tag pulse is set to cover the splenic and mesenteric veins. A pre-saturation pulse was also applied to the heart to eliminate arterial signals for the PV perfusion. The HA and PV perfusion was evaluated as a whole area, as shown in **Figure 2** (A represents the ROI, B shows hepatic arterial blood flow, and C shows portal venous blood flow).

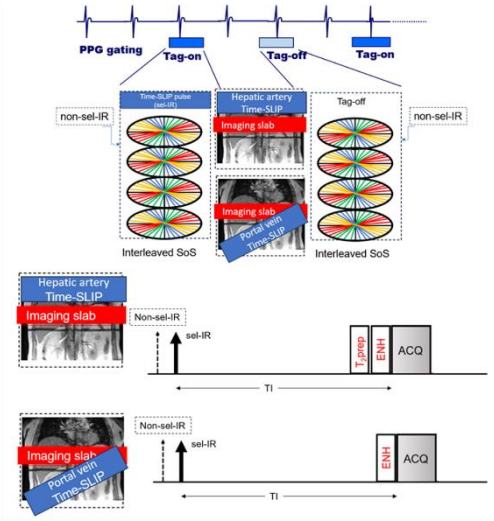

Figure 1

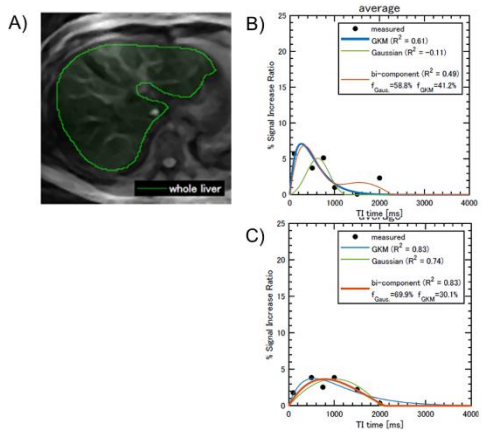

Figure 2

Results: The iSoS time-SLIP techniques allow evaluation of the blood flow of HA and PV to the liver segments in all six cases. **Figure 2** shows plots for the liver ROI for the HA and PV perfusion. The HA blood flow reaches an early time-to-peak (TTP) of around 250 ms, whereas that of PV is around 1000 ms. The HA peak diminishes quickly. In contrast, PV perfusion shows a broad curve with a slow diminishing signal. The evaluation results of each liver segment were generally similar in all healthy subjects.

Discussion: Using Time-SLIP iSoS, we observed an early blood flow TTP of 250 ms in the HA perfusion and a slow broad perfusion TTP of 1000 ms in the PV perfusion in all participants. This was consistent with previous HA and PV studies by dynamic contrast-enhanced CT (DCE-CT)[6]. Interestingly, the PV signals in DCE-CT rise slower than our PV perfusion. In the DCE-CT, the iodine contrast medium with blood flows vein via the systemic circulation before reaching at the PV, whereas our oblique PV tag by Time-SLIP labels the superior mesenteric vein (SMV) and splenic vein (SV). In the future, we also plan to investigate disease-specific changes in arterial and portal venous blood flow, as well as blood flow alterations induced by food intake.

Conclusion: By separately tagging the HA and PV using Time-SLIP iSoS, we successfully obtained HA and PV perfusion images without administration of contrast agents.

References: [1] McDonald RJ, et al. Radiology. 2015;275:772-782. [2] Zhang K, et al. in press Med Phys. 2024. [3] Miyazaki M, et al. Magnetic resonance imaging method. U.S. Patent No. 10,488,484. November 26, 2019. [4] Miyazaki M, et al. Microvasc. Res. 2015;98:94-101. [5] Miyazaki M, et al. JMRI2013; 38:981-986. [6] Ichikawa T, et al. Eur J Radiol. 2006;58(2):165-176.

Aortic Pulse Wave Velocity Measurements with a Simultaneous Multi-Slice Acquisition During Free Breathing and Valsalva

Tarun Naren[1]; Grant S. Roberts[1]; Kevin M. Johnson[1,2]; Oliver Wieben[1,2]
University of Wisconsin-Madison [1]Dept. of Medical Physics, [2]Dept. of Medicine, [2]Dept. of Radiology

Purpose: Pulse wave velocity (PWV) is an important biomarker that describes the propagation of blood pressure waves through a vessel. It is inversely related to arterial compliance and associated with cardiovascular disease with promise for early detection [1]. High frame rate cine 2D Phase Contrast (2DPC) MRI enables non-invasive aortic PWV assessment by assessing time delays in flow waveforms at multiple locations along the aorta and the vascular path lengths between them [1]. In prior work, we introduced a novel radial free-breathing Simultaneous Multi-Slice (SMS) 2DPC sequence with retrospective cardiac and respiratory gating that allows for flexible reconstructions while ensuring the physiological waveforms are synchronized across the slices, which can be compromised with sequential 2D acquisitions [2]. In this pilot study, we improve upon our sequence by increasing the SMS acceleration factor to 3 to acquire additional data points and improve the robustness of global PWV assessment. Additionally, we use this improved sequence to assess the influence of pleural pressure changes on aortic PWV measurements during free breathing [3] and, for the first time, we report MRI PWV measures under the Valsalva maneuver, which has complex hemodynamic effects and clinical uses [4].

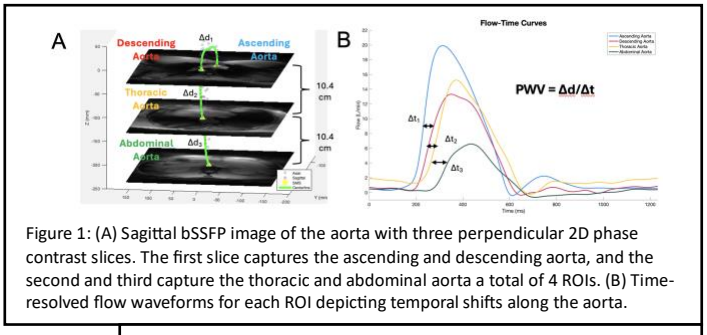

Figure 1: (A) Sagittal bSSFP image of the aorta with three perpendicular 2D phase contrast slices. The first slice captures the ascending and descending aorta, and the second and third capture the thoracic and abdominal aorta a total of 4 ROIs. (B) Time-resolved flow waveforms for each ROI depicting temporal shifts along the aorta.

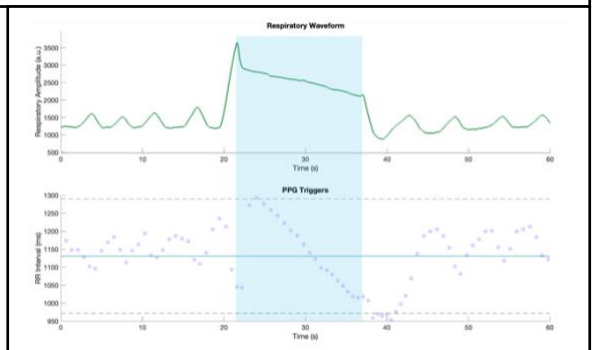

Figure 2: Respiratory bellows and RR interval length from PPG trigger signals during Valsalva maneuver. Reconstruction for Valsalva PWV only utilized radial projections acquired within blue region.

Methods: Subjects were scanned on a 3T scanner (SIGNA Premier, GE Healthcare) with a 30-channel chest coil. Peripheral pulse oximeter (PPG) and respiratory bellows signals were recorded for retrospective cardiac and respiratory gating. An SMS acceleration factor of 3 was used to acquire 3 axial planes along the aorta at: the aortic arch bisecting the ascending and descending aorta, the thoracic aorta, and the abdominal aorta (Figure 1A). Two acquisitions were performed: one free breathing (FB) and one with a 15 s Valsalva maneuver. Scan parameters include: TR/TE=7.5/4.3ms; flip angle=10˚; slice thickness=5mm; VENC=150cm/s; reconstructed cardiac frames=30; spatial res.=1mm; temporal res.=37.4-42.5ms; scan time=60s. The Valsalva acquisition was subsampled to only use projections acquired during the actual breath holds for reconstruction (Figure 2) and the FB acquisition was subsampled to match the same number of projections. FB data were reconstructed using a 50% threshold with a 5s sliding window to separate inspiration and expiration [2]. Ungated Cartesian free breathing anatomical FIESTA images (sagittal, coronal, and axial) were acquired for centerline calculations. A custom MATLAB tool (Mathworks) was used to trace centerlines and compute flow waveforms at each ROI (Figure 1B). The Time-to-Foot (TTF) method was used to calculate time shifts in flow waveforms [1]. Measured time shifts were plotted against centerline distances and linear regression was used to fit the 4 data points, where the inverse of the fitted slope is the estimated global aortic PWV.

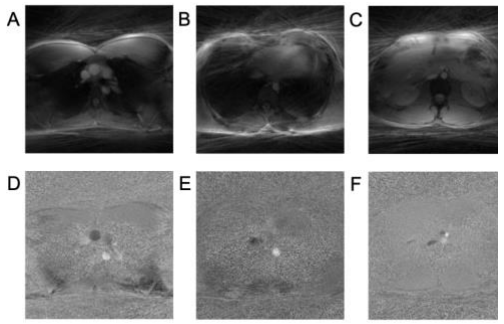

Figure 3: Example images from an SMS 2DPC acquisition. A), B), C) show time-averaged magnitude images from a 15 s free-breathing acquisition reconstructed during expiration for A) the aortic arch, B) thoracic aorta, and C) abdominal aorta. D), E), F) show the corresponding velocity images.

Results: Data were acquired for 2 subjects (1M/1F, age=25-28y). Reconstructed images for one subject are shown in Figure 3. Average global aortic PWV was calculated as 3.56 ± 0.67 m/s in expiration, 3.32 ± 0.46 m/s in inspiration, and 3.11 ± 0.50 m/s during Valsalva.

Discussion: Our prior work has shown that the reliability of global PWV calculations depends highly on the number of ROIs used to fit the regression curve [5]. Increasing the SMS factor allows for more points to be collected with no scan time penalty thereby improving the robustness of the method. Decreases in PWV between expiration and inspiration during FB are consistent with our previous findings [2,3]. A prior study utilizing a 1D MRI PWV method found an increase in PWV when comparing breath holds to the Valsalva maneuver [6], however we found there was a decrease compared to FB. This decrease is likely related to the complex effects the Valsalva maneuver can exert on heart rate, blood pressure, and hemodynamics [4]. More elastic aortas are less capable of transmitting fast pulse waves resulting from the "squeezing" of the heart during Valsalva. However, there are multiple physiological mechanisms at work during Valsalva and our pilot study has a small sample size, so a larger cohort is necessary to probe deeper trends. Future work will focus on exploring the potential clinical value of aortic PWV measurements in FB, Valsalva, and other breathing modes.

References: **[1]** Wentland AL, et al. Review of MRI-based measurements of PWV... Diagn. Ther. 2014 **[2]** Naren T, et al Feasibility of a radial SMS Acquisition. ISMRM 2024. **[3]** Roberts GS, et al. Effects of Respiration on Aortic PWV... ISMRM 2022. **[4]** Pstras, L., et. al. The Valsalva Manoeuvre… ActaPhysiol 2016. **[5]** Naren T, et al Comparing robustness of PWV methods... SMRA 2023 **[6]** Gaddum, N, et. al., Beat-to-beat variation in pulse wave velocity… MRM 2014
Acknowledgements: GE Healthcare, NIH (F31-AG071183)

Aortic wall enhancement using ultrasmall superparamagnetic particles of iron oxide on magnetic resonance imaging and fluorine-18 sodium fluoride uptake on positron emission tomography / computed tomography predict abdominal aortic aneurysm rupture, repair and future growth during long term follow up

Rachael O Forsythe, Olivia MB McBride, Jennifer MJ Robson, Alex T Vesey, Allison C Winarski, Callum Weston, Samuel Debono, Scott I Semple, Calum D Gray, Thomas J MacGillivray, Julie Brittenden, Giles Roditi, Wesley Stuart, Edwin JR van Beek, Andrew L Tambyraja, Michelle C Williams, Marc R Dweck, David E Newby

Edinburgh Vascular Unit, Edinburgh; Centre for Cardiovascular Science, University of Edinburgh; Ninewells Vascular Unit, Dundee; Leeds Vascular Institute; Department of Vascular Surgery, University Hospital Hairmyres; Department of Vascular Surgery, Queen Elizabeth University Hospital, Glasgow; Edinburgh Imaging Facility, Queen's Medical Research Institute, University of Edinburgh; School of Cardiovascular & Metabolic Health, Glasgow Cardiovascular Research Centre – all United Kingdom.

Purpose

We have previously shown that molecular and cellular imaging biomarkers of abdominal aortic aneurysms (AAA) are potential predictors of future clinical events in the medium term.[1,2] Assessment of aneurysm wall biology may provide incremental prognostic data when evaluated alongside clinical risk factors. Using ultrasmall superparamagnetic particles of iron oxide (USPIO) enhanced magnetic resonance imaging (MRI) and fluorine-18 sodium fluoride ([18F]NaF) positron emission tomography / computed tomography (PET/CT), we assessed the long-term clinical outcomes in patients with AAA enrolled in two prospective clinical imaging studies.

Methods

Patients with asymptomatic AAA underwent USPIO-enhanced MRI (n=338) and [18F]NaF PET/CT (n=72). Aneurysms were classified according to aortic wall USPIO enhancement and [18F]NaF uptake. Bespoke software was used to generate colour maps to depict the change in T2* 24 hours after intravenous USPIO administration, representing tissue resident macrophage-mediated inflammation. Scans were classified as USPIO positive if 10 contiguous voxels of USPIO enhancement was identified in the aortic wall or USPIO negative if not. Aortic wall microcalcification was assessed using [18F]NaF PET/CT after intravenous administration of a target dose of 125 MBq of ^{18}F-NaF on a hybrid 128-detector array PET-CT scanner. Patients were categorised into tertiles of [18F]NaF uptake in the most-diseased segment of the aneurysm, using maximum tissue-to-background ratio (TBRmax); Figure 1.

The endpoints of aneurysm expansion, composite of rupture or repair, and overall survival were compared.

Results

Aneurysm expansion was increased in patients with aortic wall USPIO enhancement (3.3±2.6 versus 2.5±2.2 mm/y; p=0.002) or high [18F]NaF uptake (4.0±2.0 versus 1.9±1.9 mm/y; p<0.001), and was greatest in those with both USPIO enhancement and high [18F]NaF uptake (5.1±1.7 *versus* 2.6 [1.2-3.6] mm; p=0.002) even after adjustment for clinical risk factors for disease progression including aortic diameter; Figure 1. During 102 months follow up, 62.7% patients met the composite primary endpoint of rupture or repair with high [18F]NaF uptake associated with more than two-fold higher risk (79.2% versus 36.2%; log rank p=0.003).

Discussion

Aortic wall USPIO enhancement on MRI and [18F]NaF uptake on PET/CT provide independent and additive measures of disease activity in patients under surveillance for AAA in the long term. These non-invasive imaging biomarkers provide an opportunity to identify those who are at greatest risk of AAA events.

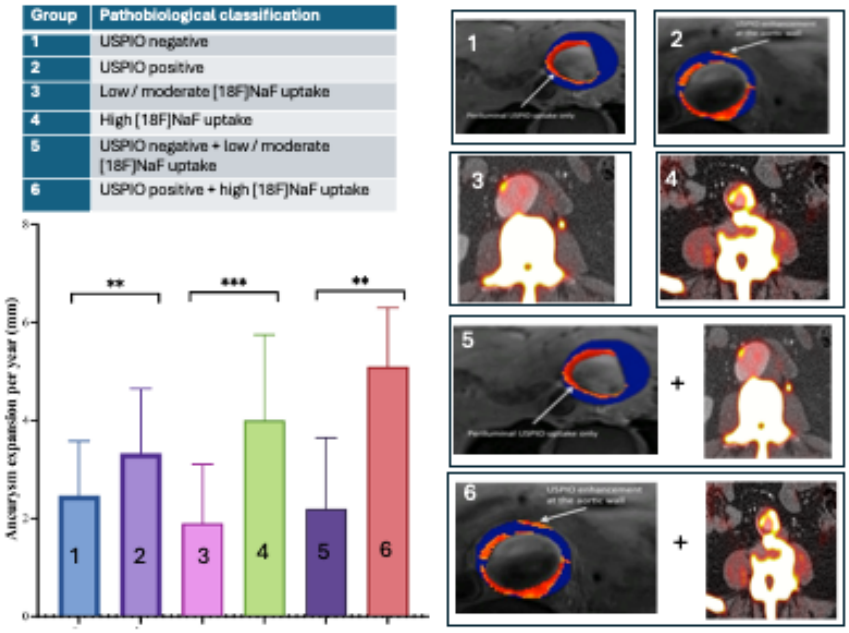

Figure 1

References

[1]The MARS Study Investigators, Newby D, Forsythe R, et al. Aortic Wall Inflammation Predicts Abdominal Aortic Aneurysm Expansion, Rupture, and Need for Surgical Repair. *Circulation*. 2017;136(9):787-797

[2]Forsythe RO, Dweck MR, McBride OMB, et al. 18F–Sodium Fluoride Uptake in Abdominal Aortic Aneurysms. *Journal of the American College of Cardiology*. 2018;71(5):513-523

Portal Vein Flow Measurements in Patients to Evaluate for Vascular Mesenteric Insufficiency

P Hall Barrientos, T Dockerty, G Roditi
Queen Elizabeth University Hospital, Glasgow, UK

Purpose: This study aimed to evaluate pre- and post-prandial portal venous flow in patients referred to confirm or exclude chronic mesenteric ischaemia (CMI). Previous work and our own pilot study [3] have shown that interrogation of the portal vein is a feasible method to measure these changes. This is an update of numbers on the clinical translation of this technique into clinical practice.

Methods: Patients in whom CMI required to be confirmed or refuted were identified through the vascular multidisciplinary team meeting at the Queen Elizabeth University Hospital, Glasgow, UK. Scans were performed on a 1.5 T Aera Siemens scanner with 2D phase contrast cine imaging applied for the supracoeliac abdominal aorta and over the portal vein (approximately 1 cm distal to the confluence). The imaging parameters were: TR/TE 4.2/3.1 ms, 1.8 x 1.8 cm in-plane resolution, slice thickness 6 mm, ECG gated, 30 cardiac phases, VENC 150 cm/s for arterial flow and 50 cm/s for portal flow (fig.1). All 2D flow images were acquired breath held. Baseline scans were acquired 8 hours fasting (including no caffeine) and post-prandial imaging was acquired at least an hour after a meal challenge consisting of two 200 ml bottles of Ensure Plus. Clinical CT angiography reports were used to record the degree of stenosis of the mesenteric arteries.

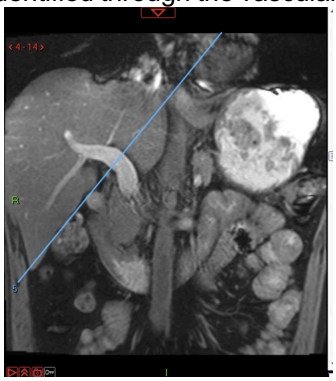

Fig1. Portal vein planning

Results: A total of 41 patients (9 male, age range 33–83 years), with varying degrees of mesenteric arterial steno-occlusive disease, were scanned between 2021 and 2024. Portal vein (PV) flow responses varied widely (-23% to 280%). Clinically significant PV flow increases (>60%), of which none developed postprandial symptoms, were observed in 10 patients and were not stented post-MR. The suspected CMI group was defined as having PV flow changes -23% to 40%. This included 26 patients of which 15 underwent stenting post-MR. Among the 9 not stented, 5 were managed conservatively due to the absence of postprandial pain, 3 were unsuitable for stenting and 1 died before the procedure. Intermediate PV flow increases (40–60%) were noted in 5 patients. Only one was stented due to severe abdominal pain, which was deemed consistent with CMI. Post-stenting follow-up was performed in 3 patients, with only 2 demonstrating a significant increase in flow.

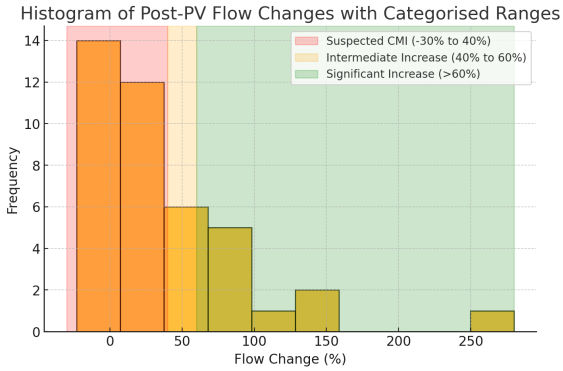

Discussion: Portal vein flow measurements in response to standard meal challenge can play a valuable role in aiding the clinical evaluation of patients with suspected CMI. We aim to continue to scan patients to improve our understanding of the wide range PV flow changes and their relationship to the patient health, age and degree of mesenteric stenosis. Further data collection is essential to improve clinical decision making.

References

1. Li KC, Whitney WS, McDonnell CH, et al. Chronic mesenteric ischemia: evaluation with phase-contrast cine MR imaging. Radiology 1994;190:175–179
2. Burkart DJ, Johnson CD, Reading CC, et al. MR measurements of mesenteric venous flow: prospective evaluation in healthy volunteers and patients with suspected chronic mesenteric ischemia. Radiology 1995;194:801–806
3. Hall Barrientos P, Knight K, Black D, Vesey A, Roditi G. A pilot study investigating the use of 4D flow MRI for the assessment of splanchnic flow in patients suspected of mesenteric ischaemia. Sci Rep. 2021 Mar 15;11(1):5914.

Cardiac MRI-Derived Pulmonary Arterial Stiffness Markers in Pre- and Post-Capillary Pulmonary Hypertension: A Comparison with Invasive Hemodynamics

Ipek Buber[1], MD, Paul Heerdt[4], MD, Inderjit Singh[4], MD, Cihan Ilyas Sevgican[5] MD, Jérôme Lamy[2], PhD, Jie Xiang[3], M.S., Joseph Philip[4], MD, **Dana C. Peters[1,3], PhD**

[1]Yale University, Department of Radiology and Biomedical Imaging, New Haven, CT

[2] Interdisciplinary University of Paris, Paris, France.

[3]Yale University, Department Biomedical Engineering, New Haven, CT

[4]Yale University, Department of Internal Medicine, Cardiovascular Division, New Haven, CT

[5]Private Health Hospital, Department of Emergency, Denizli, Turkey

Purpose: Pulmonary hypertension (PH) is a progressive disease with high mortality. Right heart catheterization (RHC) is the gold standard for diagnosing PH but is limited for routine monitoring due to its invasive nature[1]. Pulmonary arterial stiffness (PAS) has become a key marker for early detection of PH and could replace RHC indices[2].

This study investigates the relationship between CMR (cardiac magnetic resonance)-derived PAS and RHC hemodynamic measurements, assessing differences in PAS characteristics between pre-capillary, related to remodeling of the lung and post-capillary PH, related to left heart disease.

Methods: This study included 24 patients with PH, categorized into pre-capillary and post-capillary groups based on RHC criteria. Pulse wave velocity (PWV) and relative area change (RAC) were obtained from CMR to assess PAS (Figure 1a-d). The relationship between RHC-derived indices and PAS was analyzed and compared between the pre-capillary and post-capillary PH subtypes.

Results: Regression analyses showed that PWV was the most robust predictor of mPAP (R^2=0.42, p<0.001, Figure 1e; multivariate regression OR = 3.031, p = 0.027), while RVEF (right ventricular ejection fraction) was the primary predictor of PVR (OR = -0.173, p = 0.042). Notably, neither PWV nor RAC significantly differed among PH subtypes (p = 0.606 and p = 0.197).

Discussion: The non-invasive PWV, RAC, and RVEF were significant predictors of mean mPAP and PVR, demonstrating their potential for PH diagnosis and monitoring. The comparable PAS parameters between pre-capillary and post-capillary PH, suggest that vascular remodeling may follow similar patterns across PH subtypes irrespective of the underlying hemodynamic profile.

References:

1. Humbert, M., et al., *2022 ESC/ERS Guidelines for the diagnosis and treatment of pulmonary* hypertension. Eur Heart J, 2022. 43(38): p. 3618-3731.
2. Schafer, M., et al., Characterization of CMR-derived haemodynamic data in children with pulmonary arterial hypertension. Eur Heart J Cardiovasc Imaging, 2017. 18(4): p. 424-431.

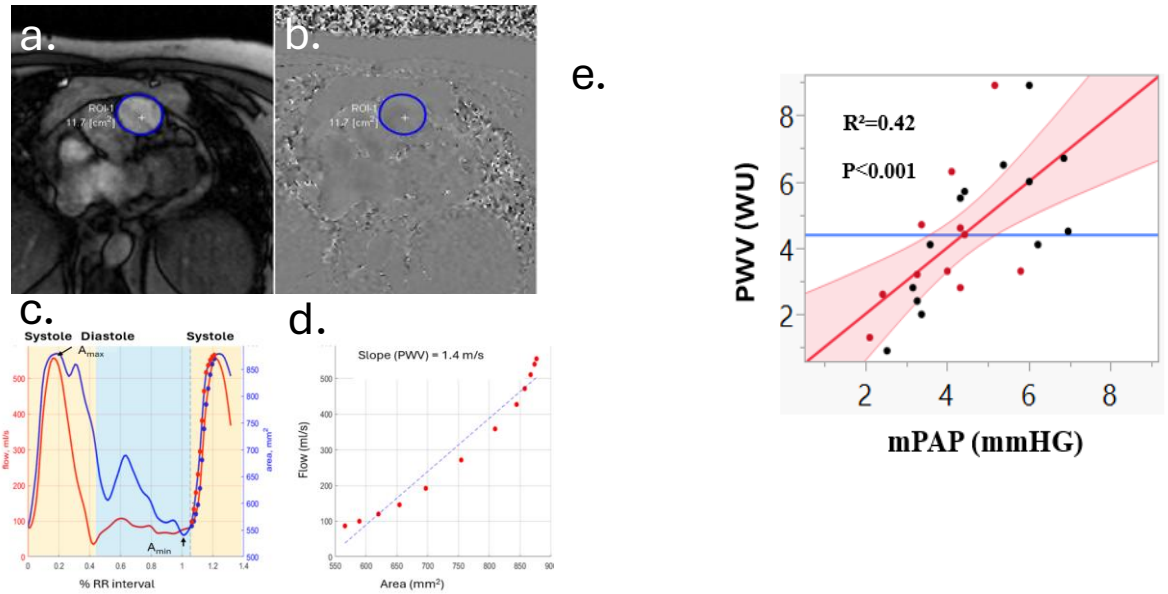

Figure 1: Measurement of PWV using 2d PC-GRE of the PA. A-B: PC-GRE magnitude and phase images. B:C: PA flow and area measured during the cardiac cycle. **D**: Plot of flow vs. Area during early systole (see region of indicated by dots in C) yields a slope which quantifies the PWV in this subject without PH to be 1.4 m/s E: Regression plot of PWV vs. mPAP, showing a strong correlation.

Image quality of QISS MRI with different stent types - preliminary results

Juhász Georgina[1], Dr. Gyánó Marcell[1], Dr. Csőre Judit[1], Dr. Suhai Ferenc Imre[1], Dr. Pataki Ákos[1], Dr.Fontanini Daniele Mariastefano[1], Dr. Bérczi Ákos[1], Dr. Csobay-Novák Csaba[1,3]

[1]Semmelweis Egyetem, Városmajori Szív- és Érgyógyászati Klinika, Intervenciós Radiológiai Tanszék, Budapest

[2]Semmelweis Egyetem, Városmajori Szív- és Érgyógyászati Klinika, Érsebészeti és Endovaszkuláris Tanszék, Budapest

[3]Semmelweis Egyetem, Semmelweis Aortacentrum, Budapest

Purpose: Image quality of lower extermity QISS-MRA can be affected by the implanted stents. The impact on the diagnostic value was investigated in iliac and femoro-popliteal region in our on-going study.

Materials and methods: Patients were included within 30 days of the stent implantation. First we performed Doppler ultrasound to exclude in-stent restenosis, after that QISS-MRA. We investigated a balloon expandable type (Dynetic), others were self-expanding stents. Three interventional, three diagnostic radiologists assessed the image quality of the affected regions on a 5-poin Likert scale. We calculated the mean, standard deviation and interrater agreement of the qualitative image quality.

Results: 15 iliac stents in 10 patients, 14 femoro-popliteal stents in 12 patients were evaluated. There were 4 Epic, 5 Astron and 6 Dynetic stents in the iliac, and 5 Supera and 9 Puslar 18-T3 stents in femoro-popliteal region. In the femoro-popliteal region the mean Likert-score was: 3,5 ±0,32; the interrater agreement was 14,3%. The mean Likert-score in iliac region was 1,9 ±0,19; interrater agreement was 11,1%. In femoral-popliteal region the signal intensity reduction wasn't significant at Supera, Pulsar-18-T3 stents ($p>0,05$). In iliac region balloon expandable stents achieved lower Likert-score than self-expandable stents, but the difference wasn't significant ($p>0.05$). Between iliac and femoro-popliteal group the difference was significant ($p<0,05$).

Conclusion: anatomical region, stent types influance the image quality of QISS-MRA, but in femoral-popliteal region the quality loss is insignificant with Supera, Pular-18-T3 stents. Further studies are needed to assess the impact of other stent types on the image quality of QISS-MRA.

Figure 1: Signal loss caused by the Epic (left), Astron (middle) and Dynetic (right) stents on QISS MRA images.

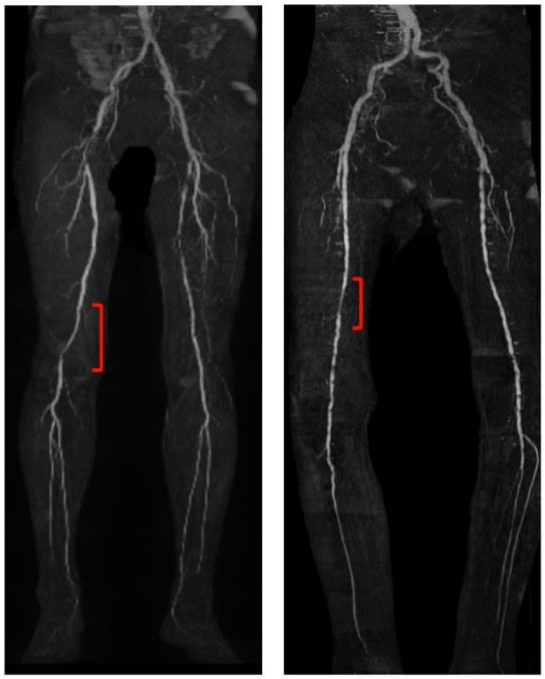

Figure 2: Signal loss caused by the Supera (left) and Pulsar-18-T3 (right) stents on QISS MRA images.

HiPath – A Multimodal deep learning tool for vessel segmentation and precision PAD diagnosis

E. Pomozi[1,2], A. B. Crichton[2], W. Chen[2], A. Tran[2], G. Wang[2], T. Roy[2,3]
1Semmelweis University, Budapest, Hungary, 2Houston Methodist Hospital, Houston, TX, USA, 3Weill Cornell Medical College, Houston, TX, USA

Introduction: Peripheral Artery Disease (PAD) is a progressive vascular disorder with significant cardiovascular morbidity and mortality worldwide, though its full pathophysiology remains poorly understood. To address this gap, we established the Houston Methodist Peripheral Arterial Disease Biorepository derived from 109 cadaveric legs from patients with chronic limb threatening ischemia (CLTI). This groundbreaking resource encompasses specimens that have been characterized with high-resolution MRI creating a unique three-dimensional visualization dataset. From this collection, selected specimens have undergone comprehensive histologic analysis, while others remain preserved for future investigations and experimental applications. Our study group has already demonstrated promising results in correlating MRI findings with histopathology, providing new insights into vessel wall and plaque characteristics [1] [2]. However, precise integration and automatization of these imaging modalities remain a challenge. To bridge this gap, we introduce HiPath, a deep-learning model leveraging contrastive learning and multimodal data fusion for improved tissue characterization.

Methods and Results: Our model, HiPath, a novel Vision Transformer (ViT)-based artificial intelligence (AI) model involves using algorithms and computational techniques to analyze medical images for studying tissue patterns by encoding images into an embedding space that reflects the different tissue components (Figure 1). The pre-training process employed a unique approach integrating natural language descriptions and omics data. Our model demonstrates superior performance compared to state-of-the-art (SOTA) models, including PLIP[3] and CONCH[4], showcasing its potential for advancing computational pathology and related applications.
We harvested 15 vessel samples from 15 amputated lower extremities of patients with terminal CLTI. For the detailed analysis, each sample underwent imaging in high-resolution preclinical 9.4T MRI scanner using ultra short echo time, and histological staining, to generate a multimodal dataset with a total of 114 vessel cross-sections which we use for the multi-step further teaching process of our deep learning model. The sequential steps include:

- Training the model to generate virtual histology images using real histology slices both with H&E and Movat stain.
- Aligning the virtual histology images with conventional and color-coded ultra-high resolution MRI cross-sections.
- Transcriptomics sequencing: we also process samples for further RNA sequencing.
- Combining all previous steps to generate virtual histology images using only MRI images, thereby enabling a fully automated, non-invasive histological analysis of PAD pathology.

Conclusions and Future directions: Our novel biorepository and ultra-high-resolution MRA imaging platform represent a significant step forward in AI-driven PAD diagnostics. By integrating deep learning and multimodal imaging, HiPath enables high-precision segmentation, automated tissue characterization, and improved diagnostic accuracy. This comprehensive Peripheral Arterial Disease Biorepository not only advances our understanding of PAD pathophysiology but also establishes a foundation for future AI algorithm development and integration with emerging technologies. As our tissue library expands, this method could pave the way for a standardized, non-invasive diagnostic framework that enhances clinical decision-making in vascular medicine.

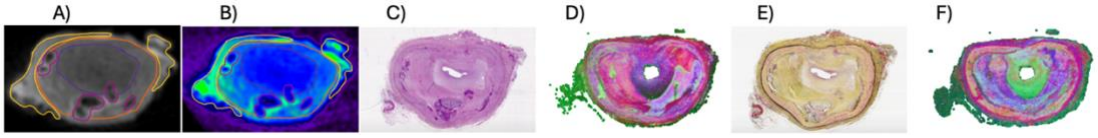

Figure 1. A) and B) Conventional and color-coded UTE MRI images –orange outline: thickened vessel wall with layered lipid rich and collagenous deposits (cholesterol clefts) typical in atherosclerosis, pink outline: hard calcium deposits, purple outline: central soft collagenous deposit causing luminal occlusion, yellow outline: fatty connective tissue, C) and E) paired histology cross sections with H&E and Movat staining, D) and F) HiPath generated colored virtual histology cross sections

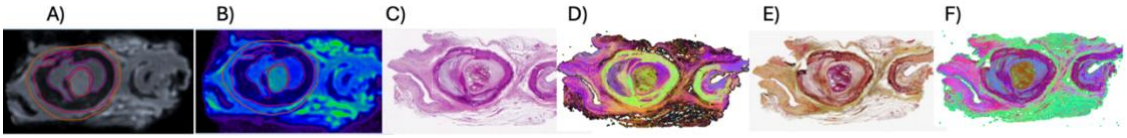

Figure 2. A) and B) Conventional and color-coded UTE MRI images – red outline: central luminal thrombus, purple outline: central collagenous deposits, pink outline: circumferential calcification, orange outline: : thickened vessel wall C) and E) paired histology cross sections with H&E and Movat staining, D) and F) HiPath generated colored virtual histology cross sections

References: [1] T. Roy et al. *J Endovasc Ther*. 24(1):35-46 (2017). [2] J. Csore et al. *J Vasc Surg*. 81(2):351-363.e3 (2025).
[3] M.Y. Ming et al. *Nature Medicine* 30.3 863-874 (2024).

Dynamic Glucose-Enhanced MRI of the Liver in a Mouse Model of Metabolic Associated Fatty Liver Disease at 3.0 T

Yuling Yang[1]; Lele Ma[2]; Chuyu Liu[2]; Rongrong Zhu[3]; Hao Liu[3]; Xiaolei Song[2]; Zhuozhao Zheng[1]

[1]Department of Radiology, Beijing Tsinghua Changgung Hospital, School of Clinical Medicine, Tsinghua Medicine, Tsinghua University, Beijing, China; [2]Center for Biomedical Imaging Research, Department of Biomedical Engineering, School of Medicine Tsinghua University, Beijing, China; [3]School of Information Sciences and Technology, Northwest University, Xian, China

Purpose: Dynamic glucose enhancement (DGE) imaging uses natural D-glucose as MRI contrast agent to observe glucose metabolism by detecting glucose-based chemical exchange saturation transfer (glucoCEST) signal changes after glucose injection. Based on the previously developed free-breathing abdominal CEST sequence[1], the study aims to investigate the feasibility of the free-breathing DGE MRI of liver in metabolic associated fatty liver disease (MAFLD).

Methods: The study included 6 MAFLD rats and 6 healthy rats aged 14-16 weeks. All imaging was performed at a 3.0T scanner with a dedicated 16-channel rat coil. The MR scanning sequences are shown in Figure 1. To minimize signal abnormalities, the water saturation shift referencing (WASSR) method was employed for B0 field correction. The WASSR sequence was configured with 21 frequency offsets using a step size of 0.1 ppm, covering a range of ±1 ppm. Each DGE sequence has a frequency offset step size of 0.25ppm and a coverage range of 0-3.5ppm. The other common imaging parameters for scan were: slice thickness = 4 mm, field of view = 150×102 mm^2, echo time (TE) = 4.9 ms, B1 of CEST preparation = 1.6μT, and duration of CEST saturation = 1 s. Data processing was performed using custom-written Matlab code, and DGE kinetic curves were generated under a single saturation offset of 1.2 ppm, 1.5ppm, 2.0ppm.

Results: Figure 2 presents the temporal signal curve in MAFLD rats and healthy rats following glucose administration. Notably, the signal of healthy rats exhibited significant enhancement post-glucose intake. In contrast, MAFLD rats showed no discernible signal alterations after glucose injection.

Discussion： We demonstrate the feasibility of the free-breathing DGE MRI of liver in MAFLD and found differences of DGE signals between the groups with and without MAFLD.

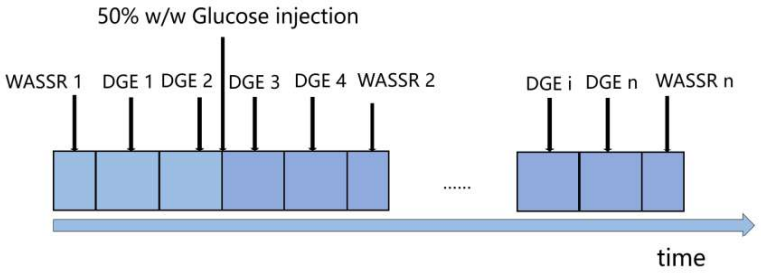

Figure 1. The workflow of dynamic glucose-enhanced MRI of the liver. Two baseline DGE scans are performed before glucose injection. B0 field correction was implemented using WASSR following every two DGE sequence acquisitions.

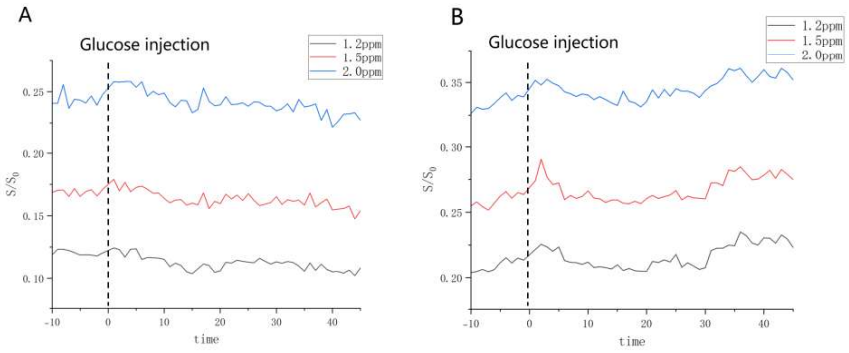

Figure 2. The temporal signal curve in MAFLD rats and healthy rats following glucose administration. A. MAFLD rat, B. healthy rat.

References: Chen Z et al. NMR Biomed. 2024 Aug;37(8):e5134.

Imaging and Clinical Impact of Cerebral Vascular Tortuosity: From Large to Small Arteries

Yulin Ge[1], Zhe Sun[1]

[1]Department of Radiology, NYU Grossman School of Medicine, New York, NY, United States

Purpose: Tortuosity in both large brain-feeding arteries and small medullary arteries is a key biomarker for cerebrovascular aging, impaired perfusion, white matter hyperintensities (WMHs), and neurodegeneration in the elderly. Twisted and elongated arteries cause hemodynamic disturbances, reducing blood flow efficiency and increasing the risk of hypoperfusion. Thus, early detection of such age-related vascular remodeling using advanced MR angiographic techniques is crucial for assessing vascular risk factors associated with aging and cognitive decline.

Methods: The tortuosity of large brain-feeding arteries, such as internal carotid arteries (ICAs) and vertebral (VAs) arteries, was assessed using time-of-flight (TOF) MRA at 3T at the neck level in a dataset of 247 healthy adults (ages 20-88 years; gender: 86M/161F)[1]. Among them, 144 participants were younger than 60 years. Blood flow and velocity associated with arterial tortuosity were evaluated with phase-contrast (PC) MRI. Using a centerline-tracking method, the vessels were segmented, and torturous severity was quantified using tortuosity index (TI), bending length (BL), and inflection count metric (ICM). The tortuosity of cerebral small medullary arteries was assessed with Ferumoxytol-enhanced high-resolution 3D susceptibility-weighted imaging (SWI) (in-plane resolution: 0.25x0.25mm) at 7T in 37 healthy individuals (ages 21-70 years; gender: 18M/19F)[2]. Ferumoxytol, an FDA-approved ultrasmall superparamagnetic iron oxide (USPIO) for treating iron-deficiency anemia, enhances the arterial blood susceptibility contrast on T2*-weighted imaging. Its blooming effect significantly improved the detection of small arteries.

Results: For large brain-feeding arteries, vessel tortuosity significantly increases across the adult lifespan. Quantitative analysis showed that in older subjects (>60 years), the tortuosity index (TI) of the ICAs was significantly higher than the TI, BL, and ICM measurements of younger subjects ($p < 0.001$) for all ICAs and VAs, indicating notable vascular changes when age 60 was used as a cutoff. For small cerebral medullary arteries (50–300 μm), which are undetectable with conventional imaging, high-resolution USPIO-enhanced 7T SWI enabled clear visualization of medullary artery tortuosity in the white matter. This represents the first in vivo demonstration of age-related microvascular topology changes using advanced imaging. The number of small tortuous arteries correlated with age, BMI, white matter atrophy, and the extent of perivascular spaces (PVS). Notably, significant age-related tortuosity changes in small vessels can begin as early as age 50, preceding similar changes in large arteries.

Discussion and Conclusion: Abnormal vessel tortuosity can contribute to localized hypoxia and ischemia, leading to microinfarcts and lacunar strokes, which are hallmark features of cerebral small vessel disease (SVD) and may play a critical role in age-related dementia. There is a growing clinical need for the quantitative characterization of early vascular morphological changes as an imaging biomarker to help prevention of age-related diseases associated with vascular dysfunction.

References:

1. Sun Z. et al. Front in Neurol 2022.
2. Sun Z. et al. Aging & Disease, 2023.
3. Brown WR. et al. J Neuro Sci 2022

Acknowledgement:

This work was partially supported by NIH grants: R01 NS108491; R01 AG077422, and U24 NS135568.

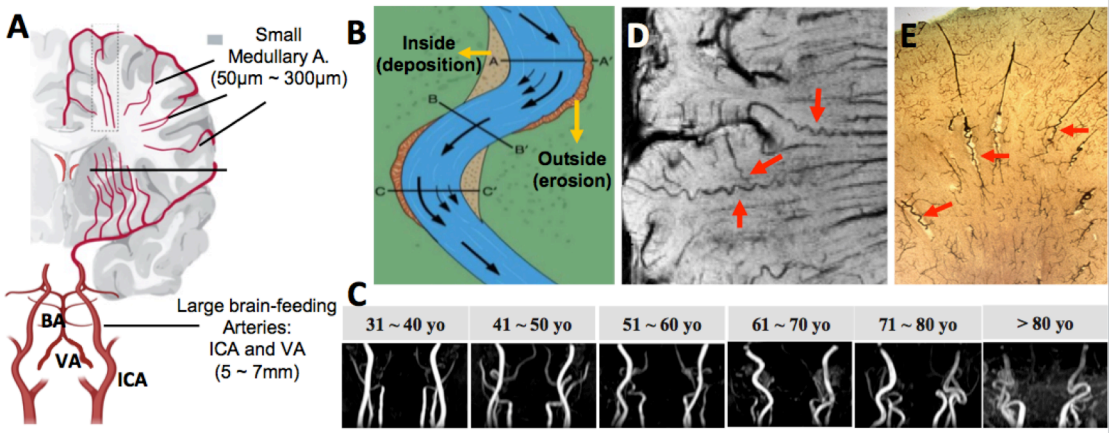

Figure 1. (A) Schematic illustration of large and small cerebral arteries. **(B)** The meandering of an aging river results from continuous or irregular flow, gradually altering its course and morphology over time. **(C)** TOF MRA showing increased tortuosity of ICAs and VAs over decades. **(D)** Small tortuous medullary arteries with corkscrew appearance (red arrows) detected with USPIO 7T SWI in a 68-year-old woman. **(E)** The cerebral medullary artery tortuous changes detected on MRI align with histology findings[3].

Quantitative Time-of-Flight MRA Improves Morphologic Agreement of the Intracranial Arteries with Respect to Dark-Blood Intracranial Vessel Wall MRI

Ioannis Koktzoglou[1,2], Zachary B. Bulwa[2,3], Elham Azizi[2,3], Fulvio R. Gil[2,3], William J. Ares[2,4]
[1]Department of Radiology, Endeavor Health, [2]Pritzker School of Medicine, University of Chicago, [3]Department of Neurology, Endeavor Health, [4]Department of Neurosurgery, Endeavor Health

Purpose: A limitation of conventional intracranial time-of-flight (cTOF) MRA is that it is sensitive to blood flow-related artifacts that can distort or obscure arterial morphology and affect precise structural evaluation of arterial pathology (1,2). In addition to providing hemodynamic data at no cost, the recently proposed method of quantitative time-of-flight (qTOF) MRA shows the potential to reduce flow-related artifacts that affect cTOF MRA (3). The aim of this study was to evaluate the morphologic agreement of the intracranial arteries as portrayed by qTOF and cTOF with respect to dark-blood intracranial vessel wall MRI (VWI).

Methods: This study was IRB approved and informed consent was obtained. 16 adult subjects with a history of arterial cerebrovascular disease (stenosis, aneurysm) were imaged with qTOF, cTOF and VWI protocols on a 3 Tesla MRI scanner (MAGNETOM Skyra^{fit}, Siemens Healthineers). qTOF and cTOF image data were rigidly registered to VWI data. The intracranial arteries were segmented, skeletonized, and cross-sectional reformations orthogonal to the arterial course were obtained every 1 mm. Ray-based full-width-at-half-maximum signal intensity analyses were done to define cross-sectional arterial lumen areas on acquired imaging volumes. Intracranial arterial cross-sections ≥1mm^2 that were reliably segmented on all scans were included in the final analysis. Intraclass correlation coefficient (ICC) and Pearson's correlation coefficient were used to evaluate agreement and correlation of lumen area measures. Dice Similarity Coefficient (DSC) was computed to evaluate morphologic correspondence of intracranial arterial lumen cross-sections as displayed by qTOF and cTOF with respect to VWI.

Results: **Figure 1** shows an example of registered qTOF, cTOF and VWI, where improved morphologic correspondence was observed between qTOF and VWI. **Figure 2** shows plots of arterial lumen cross-sectional area for qTOF and cTOF versus VWI**.** Compared with cTOF, qTOF improved ICC agreement (0.85 versus 0.76) and correlation (0.90 versus 0.88) with VWI. **Figure 3** shows plots of DSC values where larger (i.e., improved) DSC values were obtained with qTOF versus cTOF (mean values of 0.75 and 0.55).

Discussion: Compared to conventional head MRA, qTOF MRA improved agreement with VWI for evaluating intracranial arterial lumen area and morphology. Coupled with the hemodynamical data the method can also provide, future studies will evaluate whether the improved arterial morphology provided by the qTOF method can aid in the diagnosis and management of patients with cerebrovascular diseases and disorders.

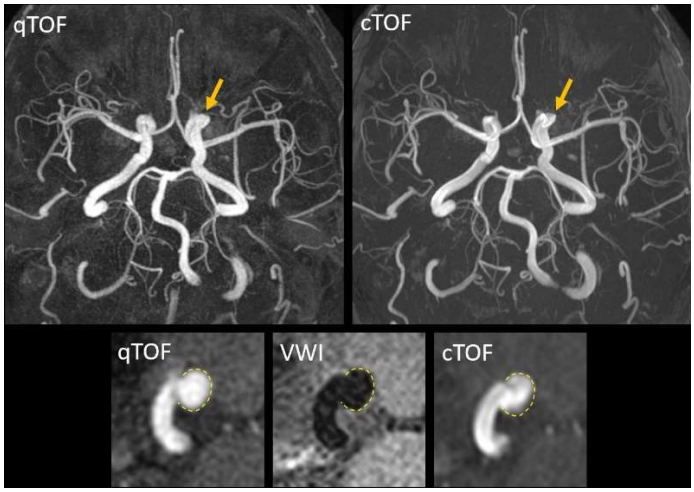

Figure 1. Top panel: qTOF and cTOF MR angiograms in a subject with left internal carotid artery aneurysm (arrow). Bottom panel: 1.25mm-thick maximum (qTOF, cTOF) and minimum (VWI) intensity projections showing the aneurysm and its outline as defined on VWI. Compared to cTOF, qTOF shows better morphologic agreement with VWI.

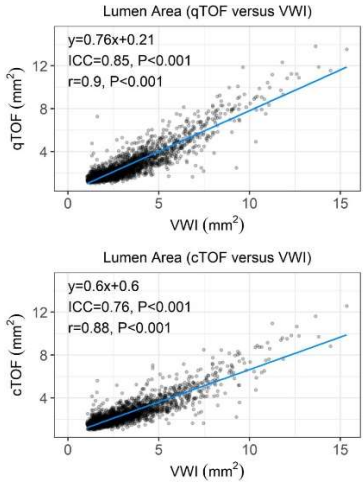

Figure 2. Scatter plots of intracranial arterial lumen area obtained with qTOF and cTOF versus VWI. qTOF shows better agreement with VWI (ICC of 0.85 versus 0.76).

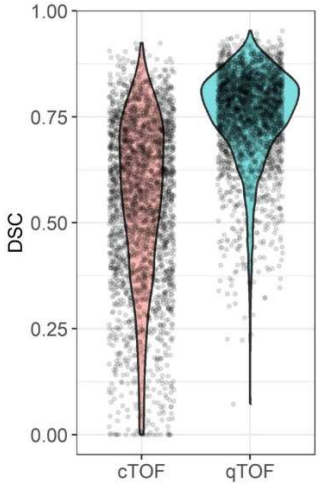

Figure 3. Violin plots of arterial DSC values for cTOF and qTOF with respect to VWI. Larger values indicate improved morphologic correspondence with VWI.

References: **1.** Nishimura et al. Magn Reson Med. 1991;22:481-492. **2.** You et al. European Radiology. 2022;32:2781-2790. **3.** Koktzoglou et al. J Magn Reson Imaging. 2025;61:404-412.

Acknowledgement: NIH R01EB027475, Endeavor Health Pilot Grant Program, Brain Aneurysm Foundation.

Correlation between characteristics of carotid vulnerable plaque and lacunar infarction

Decheng Meng[1], Ran Huo[1], Huimin Xu[1], Xihai Zhao[2], Tao Wang[1], Ying Liu[1]

[1]Peking University Third Hospital, Beijing, China

[2] School of Biomedical Engineering, Tsinghua University, Beijing, China.

Purpose: Lacunar infarction (LAC) refers to a small area of infarction (generally with a diameter of less than 15 mm) in the region of the deep perforating arteries of the brain, and is an independent predictor of stroke and transient ischemic attack[1]. Previous studies have found that increased carotid intima-media thickness and carotid stenosis are associated with the occurrence of lacunar cerebral infarction[2]. However, research evaluating the characteristics of high-risk carotid plaques and downstream LAC is still insufficient. Moreover, there is a lack of studies exploring the correlation between carotid plaque characteristics and LAC of varying severity. **This study aims to determine the relationship between carotid plaque characteristics and LAC using high-resolution magnetic resonance imaging (HR-MRI) of the carotid arteries.**

Methods: We collected clinical data from 194 patients with moderate to severe carotid atherosclerosis. All patients underwent HR-MRI of the carotid arteries and a non-contrast cranial MRI scan within 48 hours. The plaque characteristics were analyzed using the TSimaging Healthcare Vessel Explorer 2. Qualitative assessments were performed to evaluate the presence of lipid-rich necrotic cores (LRNC), intraplaque hemorrhage (IPH), ulceration, and calcification within the carotid plaques. Quantitative analyses were conducted to measure the volume and maximum area percentage of these features. The uAI Research Portal from United Imaging was utilized to assist in evaluating the LAC lesion levels in the patients. Based on the presence or absence of lesions, patients were categorized into a non-LAC group and an LAC group. Furthermore, patients were subdivided into mild (1–5), moderate (6–10), and severe (>10) groups according to the number of lesions.All statistical analysis was conducted using SPSS 27.0 (SPSS, Inc. Chicago, IL, USA). $P < 0.05$ was considered statistically significant.

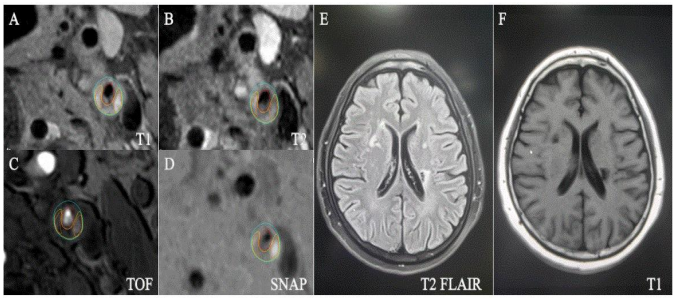

Figure 1 A patient with moderate stenosis in left carotid artery had mild LAC. **A-D** HR-MRI reveal a plaque with multiple components, including LRNC and IPH. **E-F** LAC can be clearly observed on T1 and T2 FLAIR images.

Results: Fig.1 presents a patient with carotid vulnerable plaque in left carotid artery who had mild LAC. Among the 194 patients, 163 (84.0%) were male, and the mean age was 65.3±8.0 years. There were 110 patients (56.7%) in LAC group, including 66 patients in mild group, 31 patients in moderate group and 13 patients in severe group. The levels of total cholesterol (TC) and triglyceride (TG) in LAC group were higher than those in non-LAC group (TC 3.9±1.0mmol/L vs 3.5±1.0mmol/L; TG 1.6±0.7mmol/L vs 1.3±0.7mmol/L). Univariate Logistic regression analysis showed that LAC patients with atherosclerosis had larger calcified plaque volume (OR 1.004, 95%CI 1.000-1.007) and calcified area (OR 1.052, 95%CI 1.017-1.089). Multivariate logistic regression analysis showed that patients with mild and moderate LAC also had larger calcified areas (OR 1.060, 95%CI 1.019-1.102 and OR 1.061, 95%CI 1.012-1.113, respectively). However, patients in the severe group had higher levels of LRNC and IPH (OR 1.002, 95%CI 1.000-1.003 and OR 1.003, 95%CI 1.001-1.006, respectively).

Discussion and Conclusion: Our findings are consistent with previous studies[3], indicating that elevated levels of triglycerides and total cholesterol are risk factors for LAC. Additionally, patients in the LAC group exhibited a higher burden of calcification in their carotid plaques. The increased calcification burden in carotid plaques can lead to greater arterial wall stiffness, which alters local hemodynamics[4]. This results in the transmission of high-pulse-pressure and high-velocity blood flow during systole to distal intracranial vessels, thereby causing ischemic damage to the cerebral microvasculatur[5]. Unlike patients with mild to moderate LAC, those in the severe group demonstrated higher levels of LRNC and IPH in vulnerable plaques. Histologically, plaques with larger LRNC are more prone to vulnerability[6]. A prior study has shown that larger LRNC are independently associated with thin or ruptured fibrous caps in carotid plaques, and such vulnerable plaques may experience asymptomatic micro-ruptures[7]. Moreover, IPH is also a critical risk feature of vulnerable plaques. Cui et al.[8] reported that the size of fresh IPH is independently associated with minor fibrous cap ruptures in carotid plaques, which can subsequently lead to downstream microcirculatory obstruction.

In summary, our results suggest that the pathogenesis of severe LAC may involve distinct pathophysiological processes, where micro-emboli from micro-ruptures of vulnerable plaques likely play a significant role. This highlights the need for clinicians to pay closer attention to the carotid plaque characteristics in patients with severe LAC and to actively consider the risk of plaque vulnerability in clinical management.

References: [1 MIWA K, et al.Intern Med. 2010. [2]LI Y, et al. Med Sci Monit. 2016. [3]Tirschwell, D L, et al.*Neurology* vol. 2004. [4]Edmonds, M E, *Zeitschrift fur Kardiologie*. 2000. [5]Kim, et al. *European neurology.* 2010. [6]Chen, et al. *Frontiers of neurology and neuroscience.* 2016. [7]Cappendijk, et al. *JMRI.* 2008. [8]Cui, et al. J*ournal of atherosclerosis and thrombosis*, 2018.

Utility of Vessel Wall Imaging in Clinical Practice at a Stroke Center.

Cristina Sanchez-Vizcaino[1], Ahmed Safwat[1], Mona Kharaji[1], Maouxue Wang[1], Mohammed Kanani[1], Noail Isho[2], Lauren Kim Sing[2], Nazem Akoum[3], Thomas S Hatsukami [4], Chun Yuan[5], Niranjan Balu[1], David Tirschwell[2], Mahmud Mossa-Basha[1].

[1]Department of Radiology, [2]Department of Neurology, [3]Department of Cardiology, [4]Department of Surgery and Vascular Surgery, University of Washington, USA. [5]Department of Radiology, University of Utah, USA.

Purpose: To assess the potential utility of vessel wall imaging (VWI) incorporation into stroke MRI protocols at a comprehensive stroke center in the etiological classification of patients with suspected stroke, and to describe the imaging features of the ESUS subgroup.

Methods: We retrospectively analyzed consecutive patients with suspected stroke who underwent stroke MRI (including pre- and post-contrast intracranial and extracranial VWI) at Harborview Medical Center (Seattle, WA, USA) between June 12, 2022, and November 13, 2023. Clinical, cardiac, and imaging data (MRI, VWI, CTA) were collected. Radiologic data were assessed by three neuroradiologists. Stroke etiology was classified using TOAST and ESUS criteria at three time points: pre-MRI/VWI, post-MRI/VWI, and at discharge; reflecting routine diagnostic progression, not solely MRI interpretation. Patients with poor image quality or incomplete data were excluded. Final etiological assignments were independently reviewed by a stroke neurologist. We performed a descriptive analysis of ESUS imaging features, and of diagnostic changes after MRI/VWI completion.

Results: Among 651 patients with VWI, 501 (77%) met quality standards, yielding 505 evaluable episodes. Ischemic stroke was confirmed in 61% (n=307); the remaining cases included TIA, stroke mimics, intracranial hemorrhage, and other conditions. In 176 patients initially categorized as undetermined ischemic stroke etiology, 46 (26%) were reclassified at the post-MRI/VWI time point: 8 as large artery atherosclerosis, 18 cardioembolic (influenced by additional clinical findings at the time), 10 small vessel disease, and 10 other specific causes (e.g., 4 dissections and 2 moyamoya disease).

In the ESUS subgroup (n=45; mean age 65 years; 53% male), cortical infarcts were observed in 73% of cases, with 20% involving multiple vascular territories. During follow-up, newly diagnosed atrial fibrillation was found in 16% of patients. High-risk carotid plaque (plaqueRADs≥3) was detected in 40%, with intraplaque hemorrhage (IPH) present in 10% (4/41) of ESUS patients. Among patients with anterior, uniterritorial ischemic strokes, ipsilateral high-risk plaque was identified in 33% (9/27) and contralateral high-risk plaque in 35% (9/26). Of those with ipsilateral high-risk plaque, 8 out of 9 had high-risk plaques bilaterally—6 with the same risk grade on both sides, and 2 with higher risk on the ipsilateral side, which were the two cases with ipsilateral carotid IPH. In the overall ESUS cohort, intracranially, non-calcified stenosis >30% was found in 26%, calcified stenosis >30% in 11%, and intracranial IPH in 7%.

Discussion: VWI enables the assessment of vessel wall pathology and may enhance etiological classification in stroke, particularly in vasculopathies such as dissection and moyamoya, as well as in ESUS[1-3]. Within our ESUS population, one in four patients experienced an ischemic event despite antiplatelet therapy, underscoring the importance of identifying underlying mechanisms. The heterogeneity of findings, including a proportion of patients with newly diagnosed atrial fibrillation and infarct patterns suggestive of embolic sources, as well as high-risk ipsilateral plaques, suggests overlapping mechanisms. Integrating vessel wall findings with MRI patterns may help reclassify some ESUS cases as large artery atherosclerosis, overcoming the limitations of TOAST classification and other angiographic methods based on luminal stenosis[1]. Further studies are needed to validate vessel wall findings for stroke classification and to assess their reclassification potential.

References: 1. Sannananja, B., Zhu, C., & Mossa-Basha, M. (2023). Vessel Wall Imaging in Cryptogenic Stroke. Radiologic clinics of North America, 61(3), 491–500. **2.** Xiao, J., Poblete, R. A., Lerner, A., Nguyen, P. L., Song, J. W., Sanossian, et al. (2024). MRI in the Evaluation of Cryptogenic Stroke and Embolic Stroke of Undetermined Source. *Radiology*, *311*(1), e231934. **3.** Mandell, D. M., Mossa-Basha, M., Qiao, Y., Hess, C. P., Hui, F., Matouk, C. et al. Vessel Wall Imaging Study Group of the American Society of Neuroradiology (2017). Intracranial Vessel Wall MRI: Principles and Expert Consensus Recommendations of the American Society of Neuroradiology. AJNR. American journal of neuroradiology, 38(2), 218–229.

Dynamic Velocity-Selective MRA (dynVSMRA)

Dan Zhu[1,2], Qin Qin[1,2]
1. F.M. Kirby Research Center, Kennedy Krieger Institute; 2. Department of Radiology, Johns Hopkins University

Purpose: The velocity-selective MRA (VSMRA)[1-3] can preserve the angiographic signal and suppress the tissue background within a single scan. We propose to exploit temporal sparsity afforded by VSMRA with multiple inflow times (TIs) using the Golden Angle rotated Spiral k-t Sparse Parallel imaging (GASSP) technique[4] to achieve high spatiotemporal resolution. Here, we implemented cerebral and perepheral applications of rapid large-FOV dynamic VSMRA (dynVSMRA) at 3T.

Methods: The cycle of the dynVSMRA sequence starts with a 1s pre-delay for signal recovery, followed by an adiabatic slab-selective inversion (SSI) pulse with an inversion delay (TI) for arterial inflow. The SSI module covers the imaging plane and extends 200ms distal to reduce venous contaminations. After that, a Fourier transform (FT) based VS saturation (VSS) pulse train was applied before image acquisition to suppress static tissue signal below the cutoff velocity (V_{cut}), followed by a non-selective saturation preparation with an identical acquisition to mitigate B0 and T_1-induced artifacts for large FOV scans. Images were acquired with 3D stack-of-spiral turbo FLASH (coronal). Multiple equally spaced TIs were sampled separately in consecutive cycles, with only one spiral arm for each TI, rotated by the golden angle (137.51°).

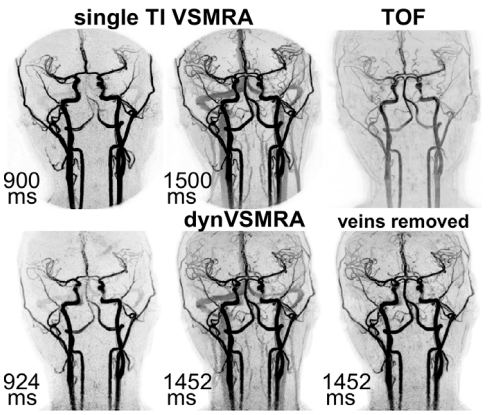

Fig. 1: Coronal MIPs of TOF, single-TI VSMRA and dynVSMRA (27yo Male).

IRB-approved scans were conducted on 4 healthy subjects (33±9yo, 2F) at 3T Philips on both the cerebral and peripheral. The brain dynVSMRA TIs range from 0ms to 2000ms (interval=132/100ms, scan time=2'46"/3'44" for 16/21 TIs). For comparison, fully sampled single-TI images were acquired at 900/1500ms (scan time=2'46"/3'12"). For all VSMRA scans, FOV=212(FH)×212(RL)×144(AP)mm, resolution=1mm isotropic, FA/TR/TE=12°/14/1.0ms, TFL factor=48, VSS V_{cut}=0.7cm/s. Spiral-based 3D TOF was also included, with 210ms FH coverage in 15 chunks, resolution=1mm isotropic, FA/TR/TE=18°/24/3.5ms (scan time=3'21"). For peripheral scans, 16 TIs range from 0ms to 3000ms (interval=200ms, scan time=4'16"), FOV=400(FH)×400(RL)×150(AP)mm, resolution=1.5 mm isotropic, FA/TR/TE=15°/17/2.7ms, TFL factor=48, VSS V_{cut}=0.5cm/s.

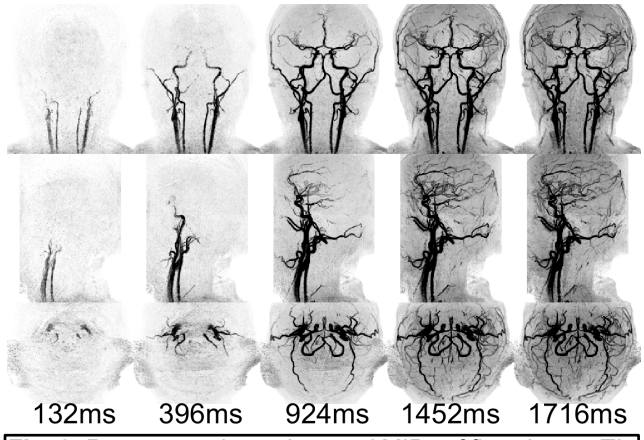

Fig. 2: Representative orthogonal MIPs of five chosen TIs from the 16-TI cereberal dynVSMRA (25yo Femmale).

The undersampled dynamic MRA data were reconstructed with GASSP with a reduction factor of 16. The mask of veins was calculated with both a shot TI image with nulled venous signal and a long TI image with recovered venous signal.

Results and Discussion: Fig. 1 compares the TIs closest to 900/1500ms from 16-TI cerebral dynVSMRA with single TI VSMRA and TOF. Compared to TOF and TI=~900ms images, TI=~1500ms images resulted in more distal and slow flow arteries (like vertebral/basilar artery) but were subject to recoved venous signal, which could be removed for dynVSMRA with multiple artery/vein contrasts. Fig. 2 and 3 demonstrated representative 16-TI and 21-TI cerebral dynVSMRA (veins removed), both showing great vessel contrast and clear small branches. Fig. 4 presents representative images of the 16-TI peripheral dynVSMRA images, clearly showing the inflow of the iliac and femoral arteries.

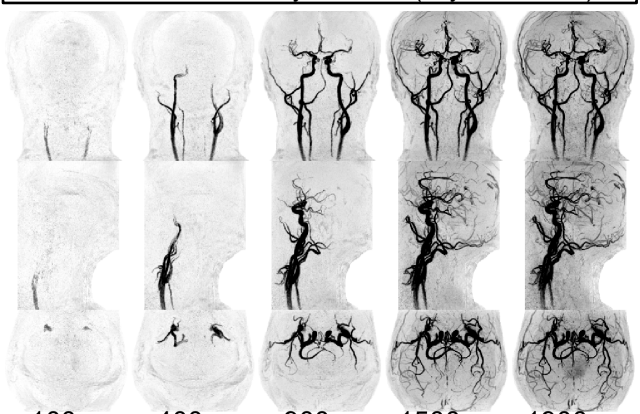

Fig. 3: Representative orthogonal MIPs of five chosen TIs from the 21-TI cereberal dynVSMRA (47yo male).

Conclusion: We demonstrated the feasibility of the proposed dynamic VSMRA using GASSP[4] for image acceleration in obtaining fast, large-FOV, high resolution, and high quality dynamic MRA images, for both the cerebral and peripheral areas. The time-resolved arterial inflow and venous separation are excellently depicted in healthy subjects.

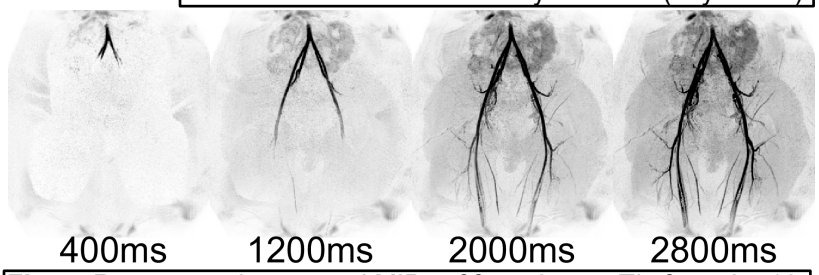

Fig. 4: Representative coronal MIPs of four chosen TIs from the 16-TI peripheral dynVSMRA (32yo Female).

References: 1. Qin Q, *MRM*, 2016;75:1232; 2. Li W, *MRM*, 2018;79:2014; 3. Zhu D, *MRM*, 2020;84:1173; 4. Zhu D, *MRM*, 2021;86:1929

Comparison of DANTE Blood Suppressed and Conventional T1-Weighted Post-Contrast SPACE Intracranial Vessel Wall MRI in Moyamoya Vasculopathy Patients

Dan Cheng, Cristina Sanchez-Vizcaino, Mona Kharaji, Beibei Sun, Mahmud Mossa-Basha
The Department of Radiology University of Washington School of Medicine, Seattle, Washington

Abstract

Purpose: To compare the wall enhancement characteristics between delay alternating with nutation for tailored excitation blood suppressed (DANTE) and conventional sampling perfection with application optimized contrasts (SPACE) postcontrast 3D T1-weighted imaging (T1WI) intracranial vessel wall MRI (IVW) in Moyamoya vasculopathy patients[1].

Methods: A total of 26 subjects who underwent both Dante and SPACE postcontrast 3D T1WI during the same IVW scanning session were included. 37 affected Moyamoya vasculopathy internal carotid artery segments were analyzed. Two neuroradiologists blinded to clinical data evaluated qualitatively evaluated imaging features including overall image quality, signal-to-noise (SNR), severity of artifacts, arterial and venous suppression, and lesion assessment by using 4-point or 5-point Likert scales[2] on DANTE and SPACE images independently and blinded to the acquisition, in a random order. Quantitative wall SNR and contrast-to-noise ratio (CNR) were determined for affected segments on both sequences.

Results: DANTE showed significantly reduced arterial (1.18 versus 2.36, p=0.001) and venous flow artifacts (1 versus 2.6, p=0.001) compared with SPACE. The intensity of vessel wall enhancement was less on DANTE compared to SPACE as well (1.33 verses 1.56, p=0.001). Affected segment SNR and CNR was not significantly different (SNR: Dante-40.3 versus SPACE-38.4, p=0.74; CNR: DANTE-24.6 versus SPACE-23.9, p=0.90).

Conclusion: DANTE blood suppression on T1-SPACE post-contrast IVW can significantly improve arterial and venous blood flow artifacts and reduce the intensity of wall enhancement without impact on quantitative SNR and CNR, relative to conventional post-contrast T1-SPACE. DANTE has the potential to improve image quality and improve IVW diagnostic assessment.

Evaluation of the process of aneurysm embolization after the bioabsorbable coil: A comparative study of high-resolution vessel wall Imaging and pathology

Bing Tian[1], Zhen Wang[1], Luguang Chen[1], Ying Zhou[2], Rui Zhao[3], Jianping Lu[1]

1. Department of Radiology, Changhai hospital of Shanghai, China
2. MicroPort Neurotech (Shanghai), China
3. Neurovascular Center, Changhai hospital of Shanghai, China

Purpose

The present study aimed to monitor the dynamic change of aneurysm embolization after treatment with bioabsorbable coils using HR-VWI in an experimental model and compare the results with histological results.

Methods

We conducted a newly bioabsorbable coil coated with polylactic/polyglycolic acid copolymerscc (PLGA) (Nufairy™, MicroPort). An experimental wide-necked aneurysm model was created by microsurgical suture of a venous pouch to the side wall of the bilateral cervical carotidal artery in one surgical session in 25 adult dogs weighing 15-21 kg. Each dog had two aneurysms created on each side of the carotid artery. DSA was employed after two weeks to confirm the aneurysm size and patency. After two weeks, the bioabsorbable coils were implanted into the aneurysm. All the dogs were fed with aspirin (15 mg/kg/day) and clopidogrel (15 mg/kg/day) by gavage for 5 days before and 3 months after the operation. There were 25 dogs with 50 aneurysms. HR-VWI, DSA, and histology were performed 14-, 90-, 270-, and 540 days after treatment. All dogs were scanned on a 3.0T whole-body MRI system Skyra, Siemens Healthcare, Erlangen, Germany). A 20-channel head/neck coil was used. 2D HR-VWI, including T2WI, pre-contrast T1WI, and post-contrast T1WI, were acquired in the axial plane with a spatially nonselective excitation. After the last follow-up, the aneurysm and the device-implanted parent artery were harvested at different times.

Results

On 14-day HR-VWI, the signals in the lumen and outside the outer wall of the aneurysm were mixed on T2WI and pre-contrast T1WI, and the aneurysm wall was significantly enhanced on post-contrast T1WI. There was no apparent enhancement of the aneurysm neck on 14-day HR-VWI. On 90-, 180-, and 540-days HR-VWI, the signals in the lumen and outside the outer wall of the aneurysm were uniform on T2WI and pre-contrast T1WI, and the aneurysm wall was not enhanced on post-contrast T1WI. The aneurysm neck can be seen enhanced on 90-, 270-, and 540-days HR-VWI. Pathology of 90-, 270-, and 540-days showed that the aneurysm neck was covered entirely by neointima with different thicknesses. The aneurysm lumen was filled with collagenous connective tissue. The fibrous tissue of the tumor body showed a large amount of collagen accumulation in the whole area.

Discussion

Previous studies revealed that aneurysm wall enhancement on MRI probably represents a normal healing response, and perianeurysmal edema represents an exaggerated inflammatory response during aneurysm healing. However, the aneurysm neck and wall change after treatment lacked pathological verification. In this experimental study, we created aneurysm models and placed the bioabsorbable coils. The HR-VWI was used to monitor the embolization process and compare the results with histological results. We found that the signal and enhancement changed during the regular follow-up. On 14 days of HR-VWI, the signals in the aneurysm cavity were mixed, and the wall of the aneurysm was strengthened after enhancement, suggesting the presence of inflammation in the wall. The signals of the surrounding soft tissue were mixed, and the enhancement showed noticeable uneven enhancement, indicating prominent edema of the surrounding soft tissue. The 14-day change after surgery suggested that the inflammation of the aneurysm wall and edema of the surrounding soft tissue were mainly caused by the aneurysm model. The 90-, 270-, and 540-day HR-VWI showed that the signals inside the aneurysm were relatively uniform, and there was no noticeable enhancement in the aneurysm wall after enhancement, suggesting that the inflammation of the aneurysm wall had subsided. The signal of the surrounding soft tissue was uniform, and no noticeable enhancement was observed after enhancement, suggesting that the surrounding soft tissue edema had subsided. The enhancement of the aneurysm neck on 90-, 270-, and 540-day HR-VWI suggested the endothelialization of the neck.

Conclusion

Aneurysm neck, lumen, and surrounding changes on HR-VWI can reflect the endothelialization, thrombus, and inflammatory process of aneurysms after coils, making HR-VWI an efficient tool for monitoring the embolization changes of aneurysms after bioabsorbable coils.

Reference

[1] Broeders JA, Ali UA, Molyneux AJ, et al. Bioactive versus bare platinum coils for the endovascular treatment of intracranial aneurysms: systematic review and meta-analysis of randomized clinical trials. J Neurointerv Surg. 2016 Sep;8(9):898-908.

[2] Kim S, Kang M, Kim DW, et al. Usefulness of Vessel Wall MR Imaging for Follow-Up after Stent-Assisted Coil Embolization of Intracranial Aneurysms. AJNR Am J Neuroradiol. 2018 Nov;39(11):2088-2094.

[3] Qiuji S, Qiang L, Qiaowei W, et al. Application of 3D T1-SPACE combined with 3D-TOF sequence for follow-up evaluation of stent-assisted coil embolization for intracranial aneurysm. J Interv Med. 2021 Feb 27;4(2):71-76.

Baseline Wall Permeability Derived from DCE-MRI Correlates with Growth of Non-Saccular Intracranial Aneurysms

Yan Li[1], Rui Li[1], Ziming Xu[1], Linggen Dong[2], Yajie Wang[1], Peng Liu[2], Ming Lv[2], Huijun Chen[1]
1. Center for Biomedical Imaging Research, Department of Biomedical Engineering, School of Medicine, Tsinghua University, Beijing, China. 2. Department of Neurosurgery, Beijing Tiantan Hospital, Beijing Neurosurgical Institute, Capital Medical University, Beijing, China

Purpose: Intracranial aneurysms (IAs), affect approximately 3.2% of the general[1]. The annual rupture rate is estimated at 1%, while growing aneurysms are at a higher risk of rupture compared to stable ones[2,3]. While the PHASES score (Population, Hypertension, Age, Size, Earlier Subarachnoid Hemorrhage, Site) provides validated clinical criteria for predicting aneurysm progression[4], its capacity to assess wall instability remains incomplete. Recent studies have suggested that wall permeability (K^{trans}), derived from dynamic contrast-enhanced magnetic resonance imaging (DCE-MRI), serves as a quantitative measurement of aneurysm wall permeability[5, 6]. This study investigates the predictive capacity of baseline K^{trans} for identifying growth propensity in non-saccular intracranial aneurysms.

Methods: Subjects: Patients with non-saccular IAs diagnosed by CTA, DSA, or MRA were included. Pregnant or breastfeeding women and those with MRI contraindications were excluded. All enrolled patients underwent at least 3 months of radiological follow-up. Imaging Protocol: Imaging protocols were executed on a 3T MRI system (Philips Ingenia CX). 3D black blood T1-weighted volume isotropic turbo spin echo acquisition (VISTA) sequences were used for capturing pre- and post-contrast aneurysm wall images. 3D T1-weighted spoiled gradient-echo sequences were utilized for obtaining DCE-MRI images. Imaging Analysis: Morphological confirmation of non-saccular architecture was achieved through 3D TOF. The region of interest (ROI) for the plasma contrast agent concentration (C_p) and the concentration in the tissue surrounding the aneurysm wall (C_t) were manually delineated (**Figure 1A, 1B**). Then K^{trans} map was calculated using the extended Kety/Tofts model[7] (**Figure 1C**). The wall enhancement index (WEI)[8] was utilized to quantify the degree of wall enhancement, calculated from pre- and post-contrast VISTA. Statistical Analysis: Aneurysm growth was defined as an increase of at least 0.5 mm in IA size[9], categorizing patients into growth and non-growth groups. Variables were expressed as mean ± SD, median (IQR) or number (percentage). The baseline demographic and imaging characteristics of the two groups were compared using the independent samples t-test. Significance was set at $P<0.05$.

Results: A total of 34 patients with non-saccular IAs were enrolled. The median follow-up time was 7.0 months (range: 6.0–10.0 months). The baseline demographic and imaging characteristics for the growth and non-growth groups, along with the results of the independent samples t-test, were shown in **Table 1**. Significant differences in baseline IA size (P = .015*), PHASES score (P = .011*), symptomatic (P = .043*) and K^{trans} (P = .012*) were observed between the growth and non-growth groups, whereas no significant differences were found in other demographic and imaging characteristics. **Figure 2** compared the distribution of baseline IA size, PHASES score, WEI, and K^{trans} between the growth and non-growth groups.

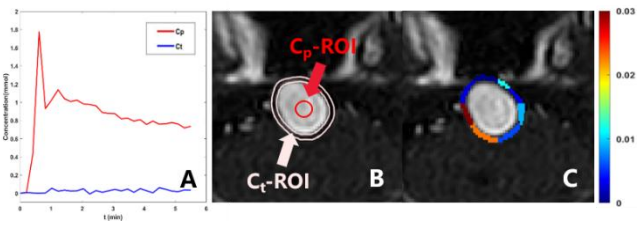

Figure 1. Measuring aneurysm wall permeability by DCE-MRI.

Discussion and Conclusion: Our results indicated that baseline K^{trans} showed a predictive ability for non-saccular IA growth, while WEI had no significant difference between the growth and non-growth groups. It suggested that K^{trans} may serve as a novel predictor for aneurysm growth.

Table 1. Comparative analysis of baseline clinical factors between the growth and non-growth groups.

	Growth (n = 16)	Non-growth (n = 18)	*P* Valuc
Follow-up period (month)	7.5 (5.5-10.5)	7.0 (6.0-9.8)	0.670
Age (yr)	53.4 ± 7.2	56.6 ± 7.9	0.230
Male sex	12 (75%)	13 (72%)	0.860
Current smoking	7 (44%)	11 (61%)	0.326
Hypertension	12 (75%)	13 (72%)	0.860
Diabetes	0 (0%)	2(11%)	0.163
Hyperlipidemia	5 (31%)	5 (28%)	0.831
Symptomatic	10 (63%)	5 (28%)	0.043*
Intramural Hematoma	5 (31%)	5 (28%)	0.831
Intimal flap	4 (25%)	3 (17%)	0.563
Double-Lumen sign	2 (13%)	1 (6%)	0.491
IA size (mm)	9.42 (8.52-11.50)	6.99 (6.12-9.06)	0.015*
PHASES score	8.0 (7.8-11.0)	6.5 (5.0-8.0)	0.011*
WEI	1.210 (0.993-1.392)	0.907 (0.693-1.336)	0.149
K^{trans} (min^{-1})	0.081 (0.049-0.110)	0.042 (0.030-0.064)	0.012*

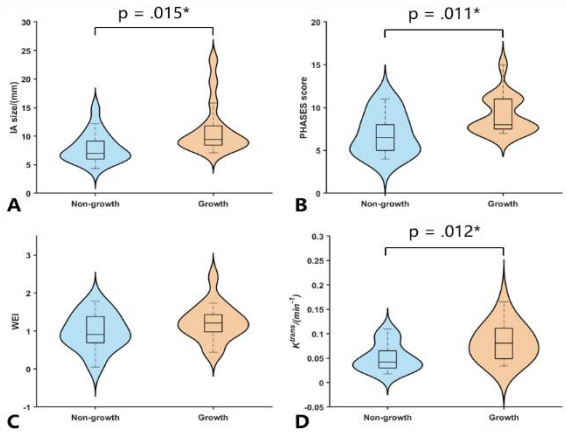

Figure 2. Comparison of baseline IA size (A), PHASES score (B), WEI (C) and K^{trans} (D) between growth and non-growth groups.

References: [1] Vlak, et al. Lancet Neurol. 2011. [2] Brinjikji, W, et al. AJNR. 2016. [3] Inoue, et al. J Neurosurg. 2012. [4] Backes, et al. Stroke. 2015. [5] Vakil, P, et al. AJNR. 2015. [6] Qi, H, et al. AJNR. 2019. [7] Tofts, Paul S, et al. JMRI. 1999. [8] Omodaka, S, et al. AJNR. 2016. [9] Matsubara, et al. J Neurosurg. 2004.

Multiparametric MRI Biomarkers for Early Diagnosis of Cognitive Impairment in Cerebral Small Vessel Disease

Wenli Lu[1], Li Yang[1], Ran Chen[1], Cheng Li[1]*, Dan Zhou[1*]

1.Department of Radiology, BenQ Medical Center, the Affiliated BenQ Hospital of Nanjing Medical University, Nanjing, China.

Purpose: This study aimed to evaluate the diagnostic utility of integrating the Diffusion Tensor Imaging Analysis along Perivascular Spaces (DTI-ALPS) index with quantitative measurements of enlarged perivascular spaces (EPVS) and choroid plexus volume (CPV) in patients with cerebral small vessel disease (CSVD) across different cognitive stages.

Methods: We retrospectively analyzed MRI data from 96 CSVD patients—divided into three groups (CSVD with normal cognition [CSVD-CN], n = 30; CSVD with mild cognitive impairment [CSVD-MCI], n = 26; and vascular dementia [VaD], n = 40)—and 55 normal controls (NCs). Quantitative assessments of the DTI-ALPS index, EPVS numbers/volume (particularly in the basal ganglia and centrum semiovale regions), and CPV were obtained using automated segmentation and manual region-of-interest analysis. Correlations with Montreal Cognitive Assessment (MoCA) scores were determined, and receiver operating characteristic (ROC) curve analyses were performed to evaluate the predictive performance of individual and combined imaging parameters.

Results: Compared with NCs, CSVD patients showed a significant decrease in the DTI-ALPS index (P < 0.001), with a progressive decline from CSVD-CN to VaD. Conversely, the number of EPVS in the basal ganglia and CPV significantly increased as cognitive impairment worsened (P < 0.001). MoCA scores were strongly and inversely correlated with both basal ganglia EPVS numbers (r = –0.66, P < 0.001) and CPV (r = –0.66, P < 0.001), while a moderate positive correlation was observed with the DTI-ALPS index (r = 0.45, P < 0.001). ROC analysis revealed that basal ganglia EPVS numbers discriminated CSVD patients from NCs with an AUC of 0.998, and a combined model of DTI-ALPS, EPVS metrics, and CPV achieved an AUC of 0.924 for detecting early cognitive impairment.

Discussion: Our study reveals that glymphatic dysfunction (reflected by reduced DTI-ALPS index), elevated EPVS numbers/volume, and enlarged CPV are closely linked to cognitive decline in CSVD. While basal ganglia EPVS numbers exhibit high sensitivity in distinguishing CSVD from NCs, their specificity for VaD diagnosis is limited. In contrast, CPV demonstrates balanced diagnostic accuracy. Integrating these biomarkers provides deeper insights into the vascular injury–glymphatic dysfunction–neuroinflammation pathway underlying CSVD-related cognitive impairment, improving early detection and subtype differentiation.

DANTE Module Optimization for 7T T1W SPACE with 0.5mm isotropic Resolution

Xiangzhi Zhou[1], Jun Ma[2], Erik H. Middlebrooks[1], Vishal Patel[1], Johnny Sandhu[1], Erin Westerhold[1], Shengzhen Tao[1]
[1]Department of Radiology, Mayo Clinic, Jacksonville, FL, United States, [2]Siemens Medical Solutions USA, Inc., Jacksonville, FL, United States

Purpose: For high resolution DANTE T1W SPACE at 7T, the scanner's SAR watchdog often imposed more restricted limitation. Therefore, SAR constraints, as well as more refined search in the DANTE parameter space are necessary to minimize SAR while still maintain the DANTE function on reducing the blood signal.

Method: In Bloch simulation, DANTE module was set to have RF pulse number = N_{RF}, flip angle= FA and duration =dur_{RF}. A "nominal SAR" is defined as $N_{RF}\times FA^2/dur_{RF}$ since it's proportional to DANTE SAR. A minimum M0 of 25.9 ms·mT/m is set to avoid banding artifacts. The minimization of blood signal with DANTE module is formulated as:

$$\underset{FA,\, dur_{RF},\, N_{RF},\, TR_{DANTE},\, G_{dephase}}{\operatorname{argmin}} |Blood_{DANTE}|$$

subject to 80 ms ≤ N_{RF} × TR_{DANTE} ≤ 180 ms, $G_{depahse}$ × (TR_{DANTE} - dur_{RF}) ≥ 25.9 ms·mT/m, Norminal SAR < 60000 (degree^2 /ms). The minimization was done through a grid search across the DANTE RF parameters (8° ≤ FA ≤ 14°, 1° increment; 0.1 ≤ dur_{RF} ≤ 0.4 ms, 0.01ms increment; 20 ≤ $G_{depahse}$ ≤ 35 mT/m, 1mT/m increment; 0.8 ≤ TR_{DANTE} ≤ 1.2 ms, 0.1ms increment).

In compliance with local institutional regulations, volunteer scans were performed on the investigational 7T Terra (Siemens Healthcare, Erlangen, Germany) equipped with the Nova 8Tx/32Rx head coil (Nova Medical Inc, Wilmington MA, USA) under TrueForm B1 shimming mode. The 0.5mm isotropic resolution T1 SPACE sequence with and without the optimized DANTE was tested on 4 volunteers (matrix size = 336 × 358, number of slices = 288, interpolated inplane resolution= 0.25mmx0.25mm, TR/TE = 650/13 ms, turbo factor = 22, echo train duration = 108 ms, bandwidth = 500 Hz/pixel; GRAPPA = 4×2). The total scan time was approximately 8.5 minutes.

Results: The simulation with SAR constraints identified the optimized DANTE module parameters as: FA=11°, dur_{RF}=0.40ms, N_{RF}=150, TR_{DANTE} =1.2ms, $G_{depahse}$ =30mT/m. This DANTE parameter set can be applied to the 0.5mm isotropic resolution T1W SPACE protocol without any SAR issue or banding artifacts. The signal reduction and relative contrast with and without DANTE are shown in Table 1. For the lumen, the DANTE module decreased the lumen signals in the ICA and the middle SSS by 67% and 72%, respectively. The DANTE module increased the relative contrast in both vessels, with p-values of 0.12 and 0.01 for the ICA and SSS. The relatively large p-value for the relative contrast in the ICA was likely due to the small sample size. Figure 1 shows a representative case acquired on a volunteer with the 0.5 mm isotropic resolution T1W SPACE. The slow flow blood signal was greatly reduced at SSS (arrows) and internal cerebral vein (arrowhead) by the DANTE preparation.

Discussion and conclusion: Running DANTE module at 7T is challenging for T1W SPACE due to SAR restrictions. The relatively short TR in T1W SPACE limits the length of the DANTE module and the number of RF pulses that can be applied. We use the same TR for T1W SPACE with and without DANTE, at the cost of slightly reduced T1 contrast with DANTE. Comparing to lower resolution DANTE T1W SPACE with the same SPACE readout, the higher resolution T1W SPACE's DANTE needs to further reduce flip angle and increase pulse duration to reduce the DANTE module SAR. The M0 also needs to be increased with increased spatial resolution.

		w/o DANTE	with DANTE	Signal ↓ (%)	
Signal ± σ	ICA Lumen	140.03 ± 38.07	43.03 ± 5.97	67 ± 10	P<0.05
	ICA VW	260.80 ± 32.22	134.47 ± 6.77	48 ± 6	
	SSS Lumen	256.50 ± 43.90	71.10 ± 1.72	72 ± 2	P=0.03
	SSS VW	474.30 ± 73.00	345.5 ± 94.12	29 ± 10	
	Splenium	402.40 ± 15.63	260.23 ± 6.31	35 ± 2	
				P value	
Relative Contrast ± σ	ICA	0.47 ± 0.09	0.68 ± 0.04	0.12	
	SSS	0.46 ± 0.01	0.78 ± 0.04	0.01	

Table 1: Signal and contrast with and without DANTE

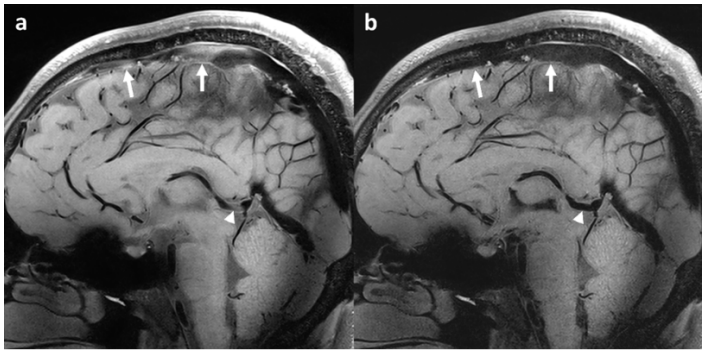

Figure 1: Images acquired with 0.5mm isotropic resolution T1W SPACE without (a) and with (b) DANTE.

Comparative Accuracy of BOOST MRA and CTA: A Novel Approach to Carotid Stenosis Assessment.

Ferenc Imre Suhai [1]; Judit Csőre [1], Bálint Szilveszter [1], Máté Kiss [2], Karl Kunze[3], Csaba Csobay-Novák [1]

1- **Semmelweis University Heart and Vascular Center**
2- **Siemens Healthcare, Budapest, Hungary**
3- **MR Research Collaborations, Siemens Healthcare Limited, Frimley, United Kingdom**

Introduction: Accurate determination of carotid stenosis is crucial for stroke risk assessment and treatment selection. While carotid computed tomography angiography (CTA) is the standard imaging modality, non-contrast magnetic resonance angiography (MRA) could be an alternative modality.

Objective: This study aimed to compare the accuracy of coronal T2-prep Bright-and-black blOOd phase-SensiTive (BOOST) MRA and axial Dixon-based BOOST MRA with carotid CTA in assessing the degree of carotid stenosis [1].

Methods: NASCET-based stenosis measurements were performed on both internal carotid arteries (ICA) in 15 patients (10 male, average age: 65 years) using CTA, and BOOST MRA on a 1.5T Magnetom Aera MRI scanner. Statistical analysis included the Wilcoxon test and Bland-Altman analysis.

Results: Stenosis measurement was not feasible in 2 cases with axial BOOST MRA and in 1 case with coronal BOOST MRA due to artifacts. The Wilcoxon test showed no significant difference between axial and coronal BOOST MRA measurements ($p=0.64$ and $p=0.25$, respectively). Both MRA sequences demonstrated a strong correlation with CTA measurements ($p<0.001$). Bland-Altman analysis indicated that axial BOOST MRA slightly overestimated stenosis (mean ± SD: 0.4%), whereas coronal BOOST MRA slightly underestimated it (mean ± SD: -2.5%).

Conclusion: To our knowledge, this is the first study to utilize BOOST MRA sequences for the assessment of carotid artery stenosis. Both axial and coronal BOOST MRA sequences accurately determine the degree of carotid stenosis and show good correlation with CTA. There is no significant difference in accuracy between the two MRA sequences. The clinical significance of the minimal over- and underestimations is likely negligible. Therefore, MRA represents a viable alternative to CTA, particularly for patients with contraindications to contrast agents.

References:

1. Correia T, Ginami G, Rashid I, Nordio G, Hajhosseiny R, Ismail TF, Neji R, Botnar RM, Prieto C. Accelerated high-resolution free-breathing 3D whole-heart T2-prepared black-blood and bright-blood cardiovascular magnetic resonance. J Cardiovasc Magn Reson. 2020 Dec 14;22(1):88. doi: 10.1186/s12968-020-00691-3. PMID: 33317570; PMCID: PMC7737390.

High resolution vessel wall imaging of intracranial arterial pathologies with multi-modal imaging correlation.

Jasmine Lijuan Chan, Yih Yian Sitoh, Hui Ping Oh, Wickly Lee, Wai-Yung Yu.

National Neuroscience Institute, Singapore

Purpose: Intracranial arterial disease is a major cause of neurological morbidity. The initial clinical workup will include computed tomography angiography (CTA) and/or magnetic resonance angiography (MRA) which provides information on arterial patency and luminal changes. Digital subtraction angiography (DSA) may be performed to assess the flow dynamics. However, these imaging modalities do not assess vessel wall morphology. High-resolution vessel wall imaging (HR-VWI) offers detailed assessment of vessel wall morphology and provides valuable insights into the underlying pathology with impact on clinical management.

Methods: We present a pictorial review of intracranial arterial pathologies, demonstrating their imaging features on HR-VWI, correlated with CTA, MRA and DSA where relevant. The diagnoses presented include atherosclerosis, vasculitis, dissection, Moyamoya disease and reversible cerebral vasoconstriction syndrome (RCVS).

Results: Imaging features assessed on HR-VWI include the pattern of wall involvement, wall enhancement and other disease-specific imaging features. Atherosclerosis may demonstrate eccentric wall thickening, intraplaque haematoma, and in cases of recent plaque rupture, thin enhancing fibrous cap can be seen. Vasculitis typically shows smooth concentric wall thickening and enhancement. In dissection, an intimal flap separating the true and false lumens, as well as eccentric wall thickening with intramural haematoma is observed. Features of Moyamoya disease include diseased segments at distal internal carotid arteries and/or middle cerebral arteries, with possible concentric wall enhancement and negative remodelling. RCVS usually shows concentric wall thickening with minimal or no enhancement, and subsequent normalisation within three months.

Discussion: HR-VWI is time and resource intensive, and typically not performed as the 1st line investigation in ischemic or vascular syndromes. The application of HR-VWI in clinically relevant cases increases diagnostic confidence in differentiating the various intracranial arterial pathologies, with subsequent impact on clinical management.

References: Mandell DM, Mossa-Basha M, Qiao Y, et al. Intracranial Vessel Wall MRI: Principles and Expert Consensus Recommendations of the American Society of Neuroradiology. *AJNR Am J Neuroradiol*. 2017;38(2):218-229. doi:10.3174/ajnr.A4893

Evaluating CSF Outflow Using Time-SLIP MRI and Bi-Component Modeling

V. Malis,[1] M. Miyazaki[1]

1. Dept. of Radiology, University of California-San Diego (UCSD), La Jolla, CA

Purpose: Cerebrospinal fluid (CSF) outflow is essential for clearing metabolic waste and maintaining brain health [1,2]. Existing ASL perfusion models like the General Kinetic Model (GKM) [3] may not adequately represent CSF outflow characteristics. This study proposes a novel bi-component model combining a fast, bulk flow component (Gaussian) and a slower, perfusion-like component (Γ-variate) to better characterize CSF dynamics using Time-SLIP MRI [4].

Methods: The Time-SLIP sequence is shown is shown in **Figure 1a**. A phantom study was conducted using a sealed water phantom with a computer-controlled pump to model bulk flow without perfusion (**Figure 1b**). We hypothesize that CSF outflow may exhibit a pass-through component similar to the one observed in the phantom, with tagged bolus passes through without perfusion. The images were acquired on a 3T clinical scanner (Vantage Galan 3T, Canon Medical, Japan). Parameters: a single-shot 2D Fast Spin Echo (FSE), TE/TR = 30/5000 ms, ETS = 5 ms, parallel imaging (SPEEDER) factor=2. The inversion times (TI) ranged from 1000 ms, with increments of 100 ms (**Figure 2a**). The calculated Signal Increase Ratio (SIR) was fitted using both a Γ-variate and Gaussian function (**Figure 2b**). Fit quality was assessed with Sum of Squares Error (SSE), Root Mean Square Error (RMSE), and R^2. *In-vivo* study was conducted on 5 healthy subjects using 3D Fast Spin Echo (FSE), superior sagittal sinus (SSS) region (**Figure 3a**) was used for quantitative analysis with General Kinetic Model (GKM) and a bi-component model (Eq. 1) fits:

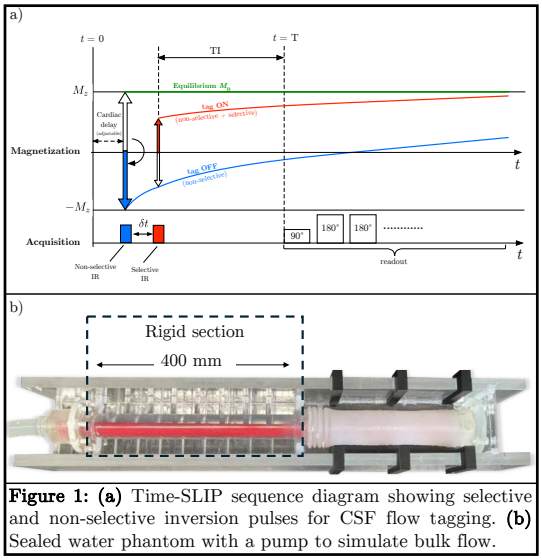

Figure 1: **(a)** Time-SLIP sequence diagram showing selective and non-selective inversion pulses for CSF flow tagging. **(b)** Sealed water phantom with a pump to simulate bulk flow.

$$\mathrm{SIR}(TI) = F_\Gamma\left(f\cdot(TI-\Delta t)\cdot\exp\left(-\frac{TI-\Delta t}{T_1}\right)\right) + F_{\mathrm{Gauss.}}\left(\exp\left(-\frac{((TI-\Delta t)-2\tau)^2}{2\tau^2}\right)\right) \quad [1]$$

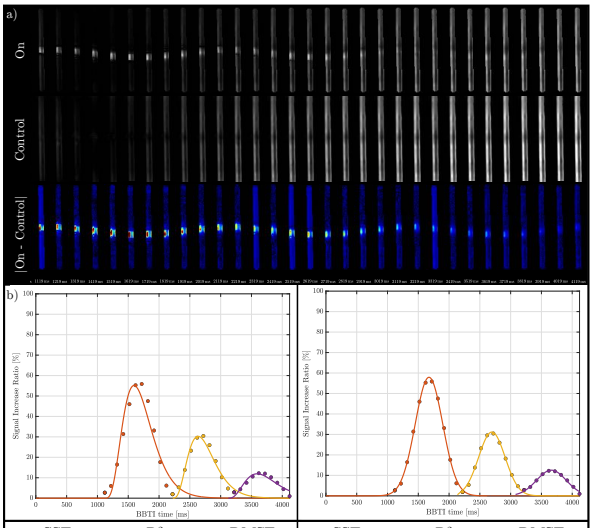

SSE	R^2	RMSE	SSE	R^2	RMSE
0.025	0.945	0.053	**0.002**	**0.995**	**0.017**
0.009	0.935	0.034	**0.001**	**0.994**	**0.010**
0.002	0.874	0.020	**0.000**	**0.975**	**0.008**

Figure 2: Phantom study results. In panel **(a)** - top row: Tag On images; Middle row: Control images; Bottom row: subtraction colormap showing bulk water motion. In panel **(b)** - comparison of Γ-variate (left) and Gaussian (right) fits for each oscillation cycle in the phantom study with fit metrics tables at the bottom, bold values indicate better fit.

Results: In the phantom study, the Gaussian consistently outperformed the Γ-variate fit across all metrics. In the *in-vivo* study, both the GKM and the proposed bi-component model provided good fits to the CSF Signal Increase Ratio (SIR) data. However, the bi-component model consistently achieved superior fit quality, with higher R^2 values across all subjects. The average signal ratio between the Gaussian (fast flow) and Γ-variate (perfusion) component was, on average, 5.3:1, reflecting a dominant fast outflow dynamic in healthy individuals (**Figure 3c**).

Discussion: The results demonstrate that the proposed bi-component model, combining a fast bulk flow and a slower component, more accurately represents CSF outflow than GKM alone. This suggests the presence of distinct pass-through and slow perfusion dynamics, in CSF outflow process. By decomposing the signal into separate components, the model enables more nuanced interpretation of outflow behavior. The observed dominance of the fast flow in healthy individuals suggests that it may play a primary role in CSF clearance under normal physiological conditions.

Conclusion: The proposed bi-component model improves CSF outflow characterization by capturing both fast and slow components, offering a more comprehensive framework for studying CSF dynamics. This approach may offer MRI-based biomarkers for detecting early alterations in CSF clearance associated with neurological disorders.

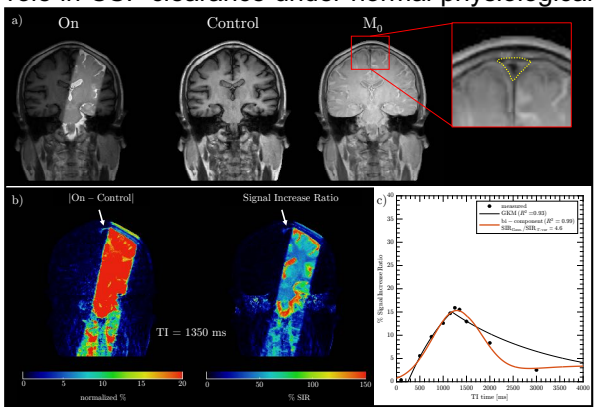

Figure 3: Panel **(a)** – Tag On image (left), Control image (center), and equilibrium image (M_0, right). Zoomed in is the superior sagittal sinus (SSS) region selected to assess CSF outflow. Panel **(b)** – Subtraction map (left) and Signal Increase Ratio (SIR) colormap (center) at TI=1350ms, with CSF outflow highlighted by an arrow. Panel **(c)** – SIR fits.

References:

[1] Miyazaki M., *et al*., *Magn Reson Med Sci.* 23(2), 171-83 (2024).

[2] Malis V., *et al*., *Magn Reson Med Sci*. 23(1), 66-79 (2024).

[3] Buxton RB., *et al*., *Magn Reson Med*. 1998;40(3)

[4] Yamada S., *et al*., *Radiology*. 2008;249(2)

Acknowledgements: Research grants to M.M. from NIH NIA RF1AG076692 and Canon Medical Systems Corp., Japan (35938).

Automatic segmentation and wall shear stress quantification of intracranial aneurysms from 4D flow using Convolutional Neural Networks

Patrick Winter[1,2], Haben Berhane[2], Maria Aristova[2], Sameer Ansari[2], Michael Markl[2] and Susanne Schnell[1,2]
[1]Department of MR Physics, University of Greifswald, Greifswald, Germany, [2]Northwestern University Feinberg School of Medicine, Chicago, Illinois, USA

Background: Intracranial 4D flow Magnetic Resonance Imaging (MRI) is a powerful imaging modality that enables 3D visualization and quantification of blood flow and related parameters[1,2]. Previous studies have demonstrated its successful application to various pathologies, including intracranial aneurysms. Notably, wall shear stress (WSS) has emerged as a potential marker for characterizing different aneurysm shapes[3]. However, WSS mapping in intracranial 4D flow MRI remains challenging due to the labor-intensive manual 3D segmentation of aneurysms. To streamline 4D flow post-processing and WSS analysis, an automated segmentation algorithm is needed. In this abstract, a convolutional neural network (CNN) was applied for fully automated 3D segmentation of the intracranial vascular tree in aneurysm patients, with the resulting 4D flow segmentations used to assess WSS values in the aneurysms.

Methods: A cohort of 130 intracranial 4D flow MRI scans (88 healthy controls, 16 with stenosis, 26 with aneurysms) was retrospectively selected. Data were acquired at 3T (Siemens, Germany) using a dual-venc sequence[4]. Manual segmentations (Mimics, Materialise, Belgium) served as ground truth for training a 3D Unet model[5]. Three additional aneurysm cases were used for testing (**Case 1**: Large saccular aneurysm in the anterior cerebral artery, **Case 2**: Large saccular aneurysms in both internal carotids, **Case 3**: Giant fusiform aneurysm in the left vertebral artery). Segmentation performance was evaluated via Dice Scores (DS) and Hausdorff Distances (HD) for the CoW and aneurysms. WSS was computed using the segmented 4D-flow data, Ensight (CEI Systems, USA) and a previously described algorithm[6]. Processing steps included lumen isosurface creation, surface normal vector calculation, and deformation tensor analysis[6]. The median and interquartile range (IQR) of temporally averaged WSS (TAWSS) were then determined for aneurysm sections of the CoW.

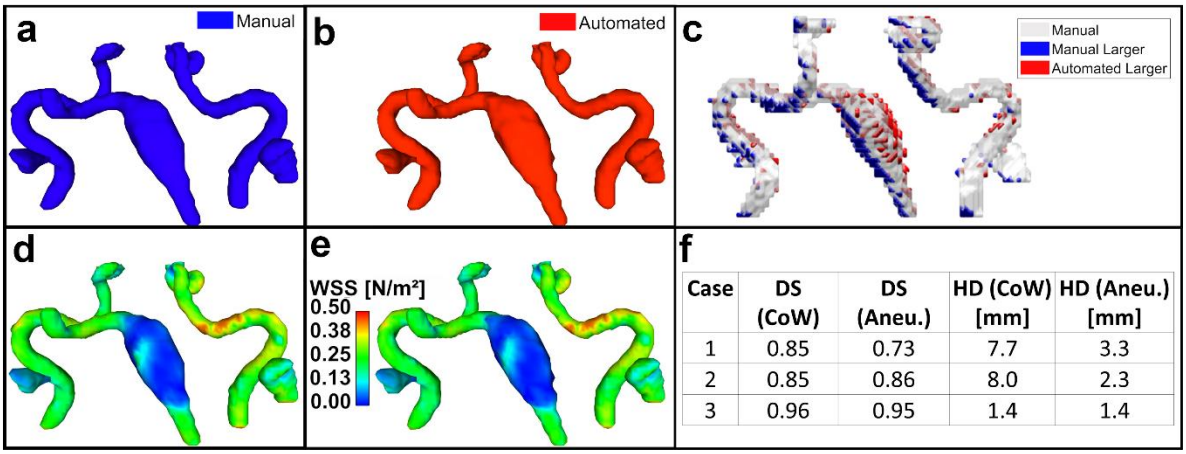

Case	DS (CoW)	DS (Aneu.)	HD (CoW) [mm]	HD (Aneu.) [mm]
1	0.85	0.73	7.7	3.3
2	0.85	0.86	8.0	2.3
3	0.96	0.95	1.4	1.4

Figure: *Manual* ***(a)*** *and automated* ***(b)*** *4D-flow segmentation of a patient with a giant fusiform aneurysm in the left vertebral artery. (c) Map illustrating the difference between both segmentations.* ***(d)*** *and* ***(e)***: TAWSS maps for both segmentations. **(f)** Table highlighting DS and HD values for all three aneurysm cases.

Results: Figures **(a)** and **(b)** show the manual and automated 4D-flow segmentation of **case 3**. The corresponding difference map shows very good agreement between both types of segmentation **(c)**. The DS was 0.96 for the whole CoW and 0.95 for the aneurysm while the HD was 1.4 mm. Figures **(d)** and **(e)** show the TAWS maps corresponding to the segmentations of **(a)** and **(b)**. The median (IQR) TAWSS values (N/m²) within the aneurysm for manual vs. automated methods are for all three aneurysm cases: **Case 1**: 0.42 (0.36) vs. 0.48 (0.44); **Case 2**: 0.52 (0.28) vs. 0.55 (0.25); **Case 3**: 0.05 (0.11) vs. 0.05 (0.10). The table in figure **(f)** shows the DS and HD values for all three aneurysm cases.

Discussion and Conclusion: In this study, a CNN was trained and applied for fully automated segmentation of intracranial aneurysms using 4D flow MRI data. DS and HD analyses demonstrated very good to excellent agreement with manual segmentations. Median TAWSS values derived from the automated approach closely matched those from manual analysis. To enhance robustness, additional manual segmentation data will be incorporated in future work. Furthermore, the performance of more generalized segmentation networks, including more cases of intracranial stenosis, will be evaluated.

Funding: NIH 1R01HL149787, NIH 1R21NS122511, NIH NIA P30AG059988, K01AG080070.

References: 1. Vali et al, MRM 82(2):749-762, 2019
2. Marlevi at al, MRM 86(6):3096-3110, 2021
3. Schnell et al, JMRI 39(1), 120-131, 2014
4. Schnell et al, JMRI 46(1), 102-114, 2017
5. Winter et al, Frontiers in Radiol., Vol 4, 2024
6. Winter et al., JCMR 21(1), 2019

Quantitative MRI relaxation time analysis of ex-vivo thrombus samples: Implications for mechanical thrombectomy and clot characterization

E. Pomozi[1,2], A.B. Crichton[2], C.D. Jordan[2], J. Csore[1,2], C. Karmonik[2], T. Roy[2,3]

1Semmelweis University, Budapest, Hungary, 2Houston Methodist Hospital, Houston, TX, USA, 3Weill Cornell Medical College, Houston, TX, USA

Introduction: Deep vein thrombosis (DVT), if untreated, can lead to pulmonary embolism, recurrent venous thromboembolism, and post-thrombotic syndrome. Anticoagulation is the first-line treatment but does not always fully resolve thrombi, leaving a risk of residual clot burden and chronic complications. Catheter-based interventions provide an alternative for patients unsuitable for anticoagulation, yet current guidelines remain limited due to a lack of reliable imaging biomarkers to differentiate acute and chronic thrombi. This study investigates MRI relaxation times (T_1, T_2, and T_2*) in ex vivo human thrombi to identify potential biomarkers for clot age estimation for optimization of treatment selection.

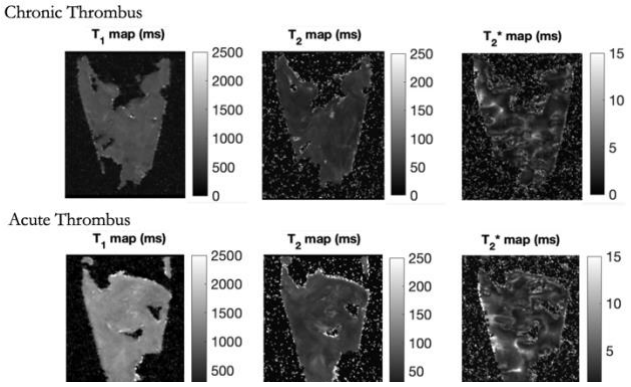

Figure 1. Visualization of fresh thrombus samples of different age using ex-vivo 9.4T MRI scanner

Methods: A total of 20 samples from 12 patients were collected post-thrombectomy and scanned using ultra-high-resolution ex-vivo 9.4T MRI. Of these, 15 samples were scanned fresh, then after formalin fixation (<6 hours: 8 samples and >24 hours: 10 samples). T_1, T_2, and T_2* relaxation times were measured to assess the effects of clot age (in days), formalin fixation, and clot type (deep vein thrombus, pulmonal embolus, arterio-venosus fistula thrombus). Pearson's correlation examined relationships between clot age and relaxation times. Repeated Measures ANOVA (RM-ANOVA) determined the impact of formalin fixation, with paired t-tests used for pairwise condition comparisons. One-way ANOVA assessed subgroup differences by clot type.

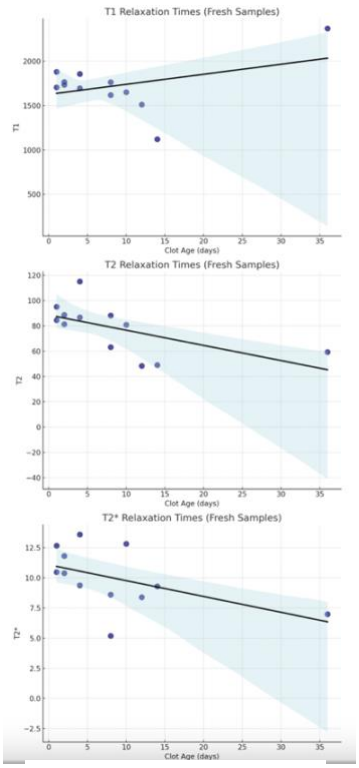

Figure 2. Relaxation times in fresh samples
T2 relaxation times shows a strong decreasing trend
T1 and T2* have high variability, making it less reliable for predicting the aging of clots.

Results:

1. Clot Age Effects: A significant negative correlation was observed between clot age and T_2 relaxation time ($r = –0.59$, $p = 0.04$), indicating that T_2 significantly shortens as thrombus ages. T_2* also trended downward with age ($p = 0.09$), while T_1 did not show a significant correlation.

2. Formalin Fixation Effects: T_2 was significantly reduced after formalin fixation ($p < 0.01$), with most changes occurring within the first 6 hours. T_1 also decreased significantly post-fixation ($p < 0.005$), while T_2* showed a moderate reduction, particularly after 24 hours ($p = 0.013$). Paired t-tests confirmed significant reductions in T_1 and T_2 between fresh and <6h fixation conditions ($p < 0.005$), with minimal additional changes between <6h and >24h.

3. Clot Type Effects: No significant differences in relaxation times were found between clot types (DVT, PE, AVF) ($p > 0.05$), suggesting that clot origin does not strongly influence MRI relaxation behavior.

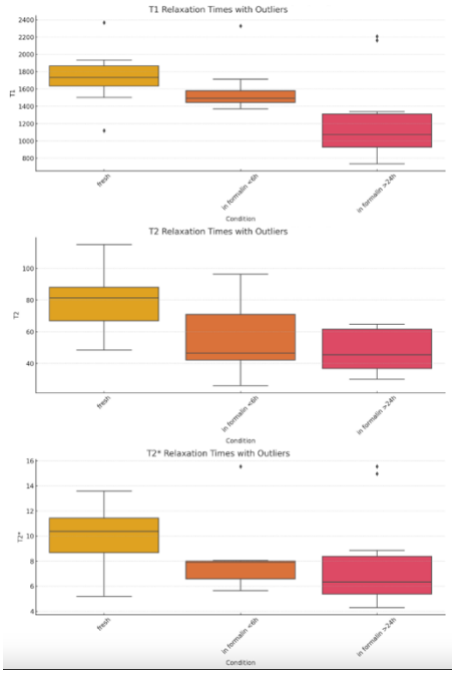

Figure 3. Formalin fixation effect

T1 is highly variable, indicating that formalin fixation affects water retention unpredictably.
T2 follows a stable decreasing trend, making it a better marker of clot age in formalin-fixed samples.
T2* with the most outliers suggesting formalin disrupts the usual iron breakdown process, leading to unexpectedly high T2* signal intensity in some samples.

Conclusions and Future Directions: This ex-vivo human thrombus study using ultra-high-resolution 9.4T MRI, offers unprecedented clot visualization, offering insights into clot characterization. This may optimize patient and treatment selection to minimize procedure errors, reduce unnecessary thrombolysis in chronic clots (lowering bleeding risk), and shorten hospital stays. The results highlight T_2 as the most sensitive marker for clot aging and also emphasize the need to account for fixation effects in MRI-based clot characterization. Our future work aims to integrate imaging findings with histological validation and extend relaxation time analysis to in vivo settings, thereby enhancing the clinical applicability of our findings.

References: [1] Shah, K.J.; Roy, T.L. *Life*. **12**, 1984 (2022). [2] Heit, J. A. *et al. Arch. Intern. Med.* **159**, 445 (1999). [3] Vedantham, S. *et al*. *N. Engl. J. Med.* **377**, 2240–2252 (2017).

Assessment of wide-coverage intracranial and extracranial vessel wall MRI at 5T

Xiancong Liu[1], Haoding Meng[1], Rui Li[1]

[1]Tsinghua University, Beijing

Purpose

Stroke is the second leading cause of death globally and is closely related to atherosclerosis [1]. 3D T1-weighted black blood Vessel Wall Imaging (VWI) has demonstrated its capability for vessel wall delineation and atherosclerotic plaque characterization [2]. However, high-quality VWI of both intracranial and extracranial arteries requires higher resolution and wider coverage. The recently introduced 5T MRI is expected to fulfill these requirements [3]. Therefore, this study aims to evaluate the performance of 5T MRI system in wide-coverage VWI using image quality analysis.

Methods

Study population and acquisition: 10 healthy volunteers were recruited in this study. All experiments were performed on a 5T MR scanner (United Imaging Healthcare, uMR Jupiter, Shanghai, China). For each healthy volunteer, we conducted two independent scans using a 48-channel head-neck coil and a carotid coil (HN-C coils) simultaneously, maintaining identical scan plane. Another scan was performed using only a 48-channel transmit-receive head coil (TR coil) for comparison. The VWI protocol is shown in Table 1.

Image quality analysis: All the analyses were performed at six locations, including Common Carotid Artery (CCA), Carotid Bifurcation (BULB), Internal Carotid Artery (ICA) C1, C2, C5, Middle Cerebral Artery (MCA) M1 segment. 2D cross-sectional slices at these bilateral locations were obtained from curved Multi-Planar Reconstruction (MPR) images. And the boundaries of the vessel wall and lumen were then segmented on these 2D images. In image quality analysis, Signal-to-Noise Ratio (SNR) and Contrast-to-Noise Ratio (CNR) at each location were calculated for statistical analysis under the two coil configurations.

Table 1. 5T black blood VWI protocol

Parameters	Values
FOV (FH×AP×LR mm^3)	260×232×150
Resolution (mm^3)	0.6×0.6×0.6
TE (ms)	14.82
TR (ms)	1200
Echo spacing (ms)	4.94
Echo train length	50
Scan time	4:50

Results

Good vessel wall delineation and blood suppression over the entire arteries were found on images using HN-C coils, while images of CCA showed almost no discernible vessels when using TR coil (Fig. 1). Image quality analysis indicated that images of HN-C coils can achieve good vessel wall delineation in both intracranial and extracranial arteries (Fig. 2).

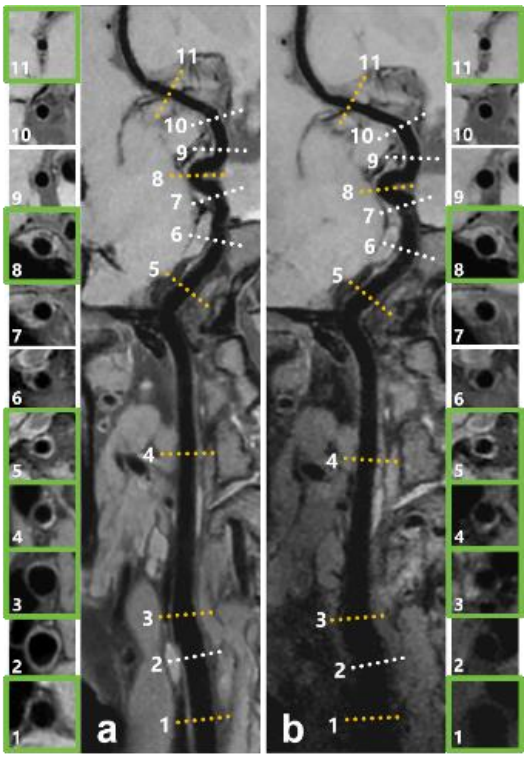

Fig. 1 The curved MPR images of 5T VWI when using HN-C coils (a) and TR coil (b).

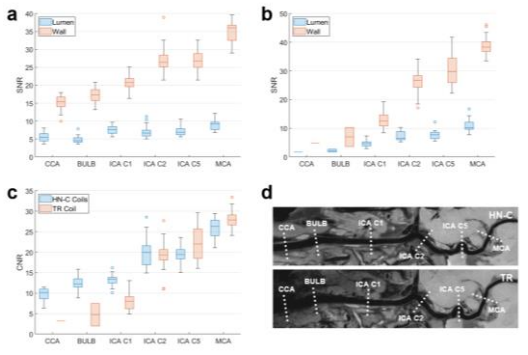

Fig. 2 Results of SNR measurement on lumen and wall for HN-C coils (a) and TR coil (b). CNR at different locations for each coil setup (c).

Discussion

5T black blood VWI can achieve high resolution, wide coverage, and rapid acquisition simultaneously, which are challenging to realize with either 3T or 7T alone. Future research should focus on optimizing 5T VWI sequence design and comparing performance across different field strengths and manufacturers in larger populations.

Reference

[1] Brauer M et al. The Lancet. 2024.

[2] Mandell DM, et al. American Journal of Neuroradiology. 2017.

[3] Shi Z, et al. Radiology 2023.

Quantitative Intracranial Vessel Wall Imaging Features in Differentiating Intracranial Vasculopathies

Mona Kharaji[1], Yin Guo[2], Mohamad H. Mosi[1], Dan Cheng[1], Beibei Sun[1], Gador Canton[1], Xin Wang[3], SeyyedKazem HashemizadehKolowri[4], Chun Yuan[4], Niranjan Balu[1], Mahmud Mossa-Basha[1]

1. Department of Radiology, University of Washington; 2. Department of Bioengineering, University of Washington; 3. Department of Electrical Engineering, University of Washington; 4. Department of Radiology, University of Utah

Purpose: Intracranial vasculopathy differentiation is a common clinical indication for intracranial vessel wall MRI (IVW)[1]. Multi-contrast IVW has led to the development of qualitative criteria to help diagnose vasculopathies such as atherosclerosis (ICAD) and vasculitis (VAS)[2]. However, these qualitative markers often differ across studies, lack consistency, and depend on the interpreter's experience. This study introduces a newly developed semi-automated quantitative IVW tool designed to evaluate whether IVW features can reliably distinguish between ICAD and VAS.

Methods: Twenty patients with established intracranial vasculopathies based on clinical evaluation underwent multi-contrast IVW with and without contrast. Each imaging dataset was processed using the MOCHA pipeline[3]: multi-contrast IVW were registered, each arterial segment was independently traced on TOF-MRA and then displayed in a multi-planar view. A deep-learning algorithm automatically segmented the vessel lumen and outer wall boundaries from which wall thickness and volume were derived. Three radiologists reviewed each arterial segment, adjudicated the presence of ICAD and VAS lesions, and corrected any segmentation errors. A contrast enhancement color map was generated by normalizing the vessel wall signal intensity on post-contrast IVW with the intensity measured in the genu of the corpus callosum. Quantitative measures of contrast-enhancement were derived based on the contrast enhancement map. For each lesion, maximum wall thickness and lesion length were extracted. The eccentricity index was computed as (maximum wall thickness–minimum wall thickness)/maximum wall thickness. The mean enhancement ratio was the mean signal intensity on the normalized post-contrast IVW. Enhancing volume was defined as the volume of the vessel wall with an enhancement ratio>1, and percent enhancing volume was calculated as (enhancement volume/wall volume)×100.
Quantitative IVW features from ICAD and VAS lesions were compared using generalized estimating equation-based univariate regression to account for multiple lesions identified within the same patient.

Results: Among the twenty patients, six were clinically diagnosed with VAS and sixteen with ICAD. There were a total of 30 arterial segments affected by VAS and 89 with ICAD. Comparing the 30 VAS lesions to the 89 ICAD plaques, significant differences were observed in lesion length (VAS, 14.2±7.6 mm vs. ICAD, 6.7±5.1 mm, p=0.003), maximum wall thickness (VAS, 1.52±0.29 mm vs. ICAD, 1.93±0.43 mm, p<0.001), and eccentricity (VAS, 0.58±0.05 vs. ICAD, 0.63±0.08, p=0.001). Contrast enhancement was observed in 83.1% (74/89) of ICAD compared to 93.3% (28/30) of VAS lesions. VAS lesions demonstrated a significantly higher mean enhancement ratio (VAS, 1.26 ± 0.47 vs. ICAD, 0.67 ± 0.22, p=0.001) and higher percent enhancing volume (VAS, 59.7±32.0 vs. ICAD, 13.0±17.3, p<0.001) (Figure1).

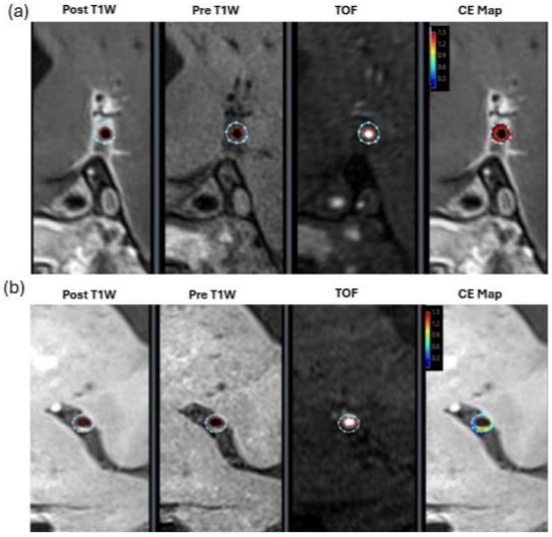

Figure 1. Examples of MI MCA analyzed using MOCHA, showing multi-contrast IVW in cross sections with lumen (red) and outer wall (blue) contours, along with a contrast enhancement (CE) color map. (a)Vasculitis lesion showing diffuse concentric enhancement, and (b) atherosclerotic plaque showing eccentric wall thickening and less enhancing volume.

Conclusion: Quantitative IVW features revealed that VAS is characterized by longer lesions, lower wall thickness, lower wall eccentricity, and more intense and diffuse contrast enhancement compared to ICAD. Our results suggest that quantitative IVW features may be useful to differentiate between ICAD and VAS. Future large-scale studies should focus on developing predictive models to improve the differentiation of intracranial vascular diseases using quantitative IVW features.

References

[1] Mossa-Basha M, et al. AJNR 2022;43:951–7.
[2] Mossa-Basha M, et al. Stroke 2015;46:1567–73.
[3] Guo Y, et al. JMRI 2022;56:944–55.

Deep-Learning based Reconstruction of Highly Accelerated 4D Flow MRI using >1000 Datasets

Haben Berhane[1], David Dushfunian[1], Justin Baraboo[1], Ning Jin[2], Bradley Allen[1], Michael Markl[1]
[1]Radiology, Northwestern University, Chicago, IL, [2]Cardiovascular MR R&D, Siemens Medical Solutions USA Inc, Chicago, IL

Purpose: 4D flow MRI provides spatiotemporally-resolved information on 3D blood flow dynamics enabling comprehensive hemodynamic evaluation. However, 4D flow MRI is still hindered by long scan times. Recently, multiple studies demonstrated the feasibility of a Compressed Sensing (CS)-accelerated 4D flow MRI of the thoracic aorta in under 2 min [1]. However, CS-accelerated 4D flow MRI has shown significant underestimation in hemodynamics quantifications compared to conventional, GRAPPA accelerated 4D flow [1,2]. Alternatively, deep learning based techniques have shown great promise reconstructing highly accelerated 4D flow MRI by k-space sub-sampling or abbreviated velocity encoding schemes [3,4]. We seek to expand on these advances by developing a fluid-physics informed convolutional neural network (CNN) for highly accelerated 4D flow MRI reconstruction to improve hemodynamic quantifications.

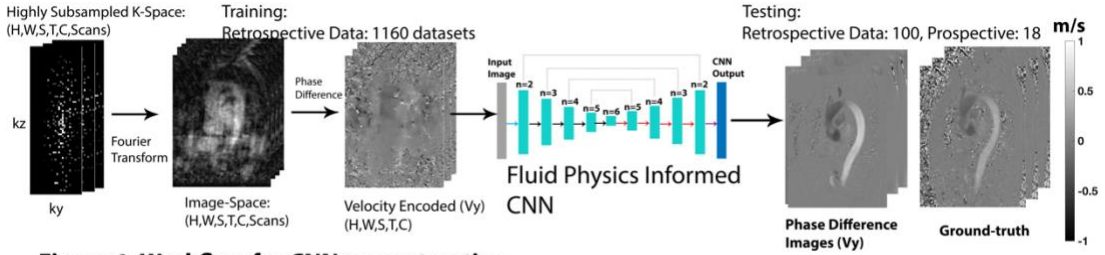

Figure 1: Workflow for CNN reconstruction

Methods: For this study, we used 1: 1260 (median age: 53 years) 4D flow of the thoracic aorta datasets from a prototype sequence to retrospectively generate subsampled data (spatial res=1.7-5.0mm^3 and venc=100-500cm/s) and 2: 18 prospectively acquired aortic 4D flow MRI scans in patients (median age: 58 years) with aortic disease for additional testing. For the prospective data, all subjects underwent four 4D flow MRI scans: (1) GRAPPA, R=2, (2) CS, R=5.7, (3) CS, R=7.7, (4) CS, R=10.2, with identical parameters (2.4-4.2 mm^3 and venc=150-350cm/s). Training was performed on N=1160 datasets with retrospectively generated subsampled data. The data was converted to kspace, and a pseudo-random phyllotaxis sampling pattern was applied along the ky-kz directions to simulate undersampling. R-factors 5.7, 7.7, and 10.2 were used. The CNN used was a hybrid 3D DenseNet/U-Net as previously described here [5], with Navier-Stokes-based and vector magnitude and angular loss functions incorporated in the training. The ground-truth was either the original 4D flow data (retrospective data) or the GRAPPA, R=2 4D flow data (prospective data). Figure 1 provides an outline for the CNN-based 4D flow image reconstruction. CNN testing was on 100 retrospective and 18 prospective datasets. Peak velocity, net flow, and peak flow were obtained for the ascending aorta (AAo), aortic arch, and descending aorta (DAo) and compared to the fully sampled 4D flow ground truth data using Bland-Altman analysis, with the bias and limits of agreement (LOA), as the percent different from the mean, reported.

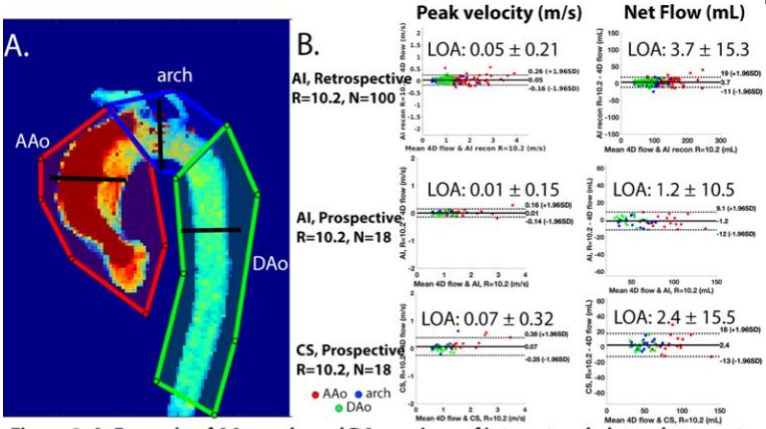

Figure 2: A. Example of AAo, arch, and DAo regions of interest and plane placement on MIP. B: Bland-Altman results for R=10.2 Retrospective data, AI-reconstructed prospective data, and CS-reconstructed prospective data

Table 1

		peak velocity			net flow			peak flow		
		Aao	arch	Dao	Aao	arch	Dao	Aao	arch	Dao
AI recon Retrospective, N=100	5.7	0.03 ± 12.1%	0.06 ± 14.2%	0.04 ± 13.3%	0.41 ± 14.1%	3.2 ± 11.0%	2.3 ± 10.6%	1.4 ± 14.1%	5.7 ± 13.3%	3.2 ± 10.8%
	7.7	0.02 ± 13.3%	0.02 ± 14.6%	0.03 ± 13.5%	0.81 ± 14.2%	0.56 ± 13.8%	-2.6 ± 11.6%	-1.8 ± 15.4%	1.5 ± 15.6%	.03 ± 15.1%
	10.2	**0.05 ± 13.8%***	0.04 ± 12.6%	0.06 ± 14.8%	5.7 ± 14.6%	1.3 ± 13.3%	3.6 ± 13.8%	2.7 ± 13.7%	4.8 ± 13.3%	3.5 ± 13.0%
AI recon Prospective. N=18	5.7	0.03 ± 11.1%	0.0 ± 9.6%	0.02 ± 11.5%	1.8 ± 11.5%	1.5 ± 13.6%	0.88 ± 15.3%	2.9 ± 12.6%	8.8 ± 11.8%	5.0 ± 11.4%
	7.7	0.02 ± 12.8%	0 ± 12.1%	0.1 ± 15.4%	1.2 ± 11.8%	0.03 ± 15.3%	0.04 ± 16.1%	3.7 ± 13.6%	7.6 ± 13.6%	4.0 ± 14.4%
	10.2	0.02 ± 13.3%	0.02 ± 9.9%	0.02 ± 10.7%	2.2 ± 13.0%	0.88 ± 18.2%	0.72 ± 18.0%	2.8 ± 14.7%	**6.9 ± 15.4%***	**7.3 ± 15.1%***
CS recon Prospective. N=18	5.7	**0.1 ± 15.0%***	**0.04 ± 20.2%***	0.07 ± 23.0%	2.1 ± 20.7%	6.3 ± 11.5%	0.88 ± 16.4%	1.2 ± 18.2%	**4.4 ± 19.6%***	-4.9 ± 17.5%
	7.7	**0.14 ± 15.6%***	0.05 ± 26.3%	0.1 ± 14.6%	**2.5 ± 27.6%***	**-2.9 ± 22.3%***	**0.29 ± 21.2%***	3.6 ± 15.0%	3.7 ± 22.8%	6.7 ± 15.8%
	10.2	0.14 ± 19.4%	**0.08 ± 32.7%***	0.02 ± 17.5%	-3.3 ± 24.1%	3.4 ± 20.2%	0.84 ± 23.1%	2.5 ± 21.2%	**5.4 ± 17.5%***	**9.4 ± 21.1%***

Results: 4D flow image reconstruction time for the CNNs was 75±8 seconds, compared to ~240-360 seconds for CS reconstruction. Figure 2 shows strong to excellent agreement in Bland-Altman comparisons between in the R=10.2 data between the AI and ground-truth across all aortic regions. Notable, AI reconstruction resulted in improved performance compared to CS. This can further be seen in Table 1, with AI reconstruction showing strong to excellent agreement to the ground-truth in both the retrospective and prospective data across all R-factors, with no significant differences found in R=5.7 or 7.7. We found significant differences in the arch and DAo peak flow for R=10.2 prospective data, while CS reconstruction showed a larger bias, wider LOA and more significant differences across all comparisons and R-factors.

Discussion: The CNN-based reconstruction of 4D flow MRI showed strong-to-excellent agreement with conventional GRAPPA, R=2 4D flow MRI. Future direction of this study is to explore AI reconstruction on higher acceleration factors.

References: [1] MA, L. et al. *MRM*. 2019. [2] Pathrose, A. et al. *MRM*. 2020. [3] Vishnevskiy V. et al. *Nature Machine Intell*. 2020. [4] Kim et al. *MRM*. 2022 [5] Berhane, H. et al. *MRM*. 2020

Imaging relative pressure fields through turbulent flow domains - combining ICOSA6 4D Flow MRI and physics-based full-field pressure estimators

Vincent Lechner[a], Mia Bonini[b], Tino Ebbers[c], David Nordsletten[b], David Marlevi[a,d]

[a] Karolinska Institutet, Sweden, [b] University of Michigan, USA, [c] Linköping University, Sweden, [d] Massachusetts Institute of Technology, USA

Purpose: 4D Flow MRI with six-directional flow encoding (ICOSA6) allows for direct quantification of turbulent flow fluctuations within different cardiovascular settings, opening up comprehensive hemodynamic mapping across a wide range of pathologies. A central variable of interest in this regard is relative pressure. However, although methods to derive *global* pressure differences in turbulent flows have been explored[1,2], extensions of methods to derive complete three-dimensional relative pressure *maps* remain much more scarce, leaving exploration of spatial pressure changes through turbulent flow domains comparably unexplored. The aim of this study is therefore to present and explore the extension of two state-of-the-art methods for full-field relative pressure recovery[3,4], explicitly including turbulent flow fluctations in their formulations: the Pressure Poisson Estimator with turbulent flows (PPE-t), and the Stokes Estimator with turbulent flows (STE-t).

Methods: STE-t and PPE-t both originate from a Reynolds-Averaged Navier Stokes (RANS) formulation with the acquired velocities separated into phase-averaged mean and fluctuating components $\boldsymbol{U}$,$\boldsymbol{u}$. As per **Fig 1.A**, the RANS momentum equations are rearranged to isolate the sought after pressure gradient. For PPE-t, the divergence of this expression is taken and a Poisson equation obtained. For STE-t the momentum equations are perturbed by the Laplacian of a divergence-free auxiliary velocity field $\boldsymbol{w}$. To assess the effect of including turbulent contributions on method performance, two different test cases were considered: first, non-pulsatile data from a previously published *in-vitro* stenotic flow phantom setup were explored, with ICOSA6 4D Flow MRI acquired across various stenotic configurations including reference pressure port data[1]. Second, pulsatile data from a physiologically realistic *in-silico* flow simulation of an aortic stenosis case were assessed, with synthetic ICOSA6 4D Flow MRI generated by sampling mean and fluctuating simulation outputs onto a spatial image grid and comparing to reference pressure fields.

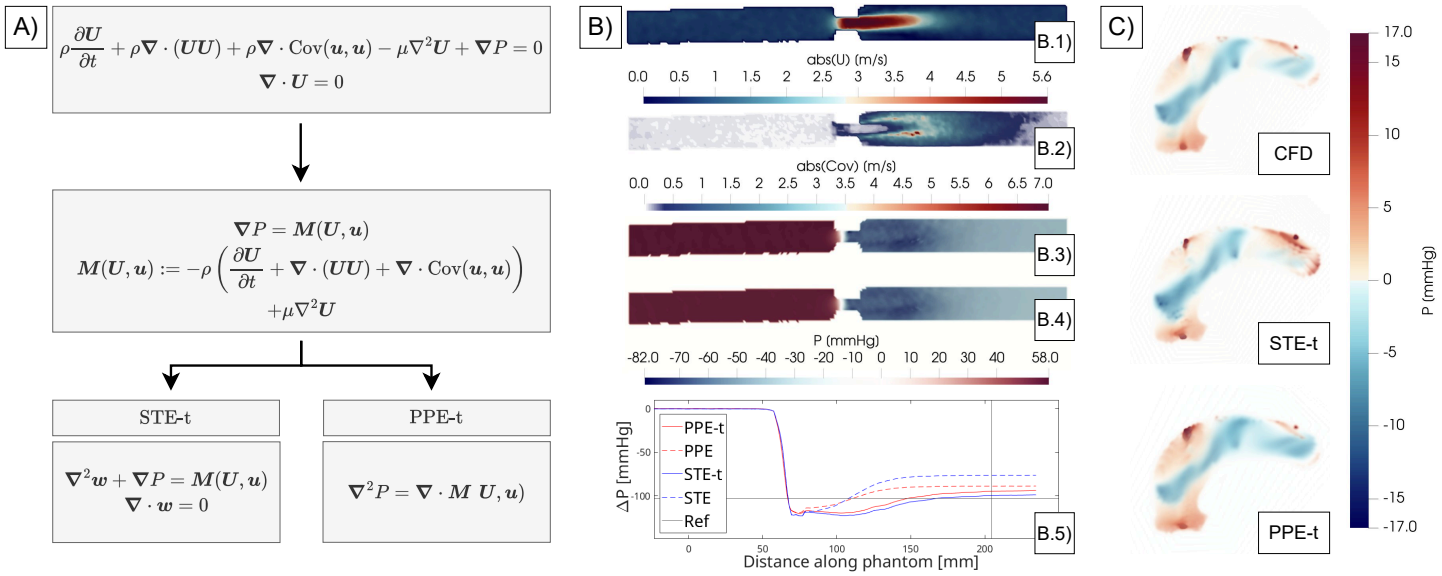

Figure 1: A) Methodological derivation of the two relative pressure field estimators. B) Evaluation of *in-vitro* phantom flow case, showing slices of the B.1.) velocity magnitude, B.2.) covariance magnitude, and pressure fields obtained by B.3) STE-t and B.4) PPE-t. B.5) Relative pressure drop between inlet and outlet plane along phantom. C) Pressure fields obtained by PPE-t and STE-t compared to the CFD solution for a stenotic in-silicio phantom of the ascending aorta around peak systole.

Results: *In-vitro* flow phantom results indicate improved accuracy for turbulence-including approaches, with a strong correlation to reference pressure port estimates (linear regression k = 0.96 and 0.94 for PPE-t and STE-t vs. 0.90 and 0.78 for PPE and STE; mean bias of -3.1 and 2.9 mmHg for PPE-t and STE-t vs -4.3 and -6.3 for PPE and STE). **Fig. 1.B.1-5)** showcase velocity, covariance and the derived relative pressure fields, together with the transversely averaged pressure change along one of the flow phantoms: distinct pressure change occurs at the stenotic narrowing, followed by the turbulence-including methods converging closer to the reference end-to-end pressure change ('*Ref*'). As a complementing preliminary result, **Fig. 1.C)** shows derived relative pressure fields from the *in-silico* aortic stenosis, qualitatively highlighting alignment between derived approaches and the underlying reference pressures (*'CFD'*).

Discussion: Using a RANS formulation with ICOSA6-based covariance-imaging, this study highlights how full-field relative pressure mapping is enabled through physiologically relevant turbulent flow domains. Results across *in-vitro* and *in-silico* setups indicate improved accuracy with turbulence inclusion. Further analysis in the simulated setup, with complementing *in-vivo* assessments are planned to further clarify the impact and clinical relevance of the presented method extensions.

References:[1]Ha et al. MRM 2019. [2]Marlevi et al. MedIA 2020. [3]Krittian et al. MedIA 2012. [4]Švihlová et al. IJES 2016.

Deep Learning Image-to-Image Translation from CEMRA to CTA via Conditioned Diffusion

Sebastian Cohn[1], William Dong[1], Bradley Allen[1], Michael Markl[1]

[1]Northwestern University, Department of Radiology

Purpose: Generative AI has potentially powerful applications in healthcare, ranging from data augmentation to cross-modality image synthesis. In this paper, we explore the use of a diffusion deep learning model to create a synthetic computed tomography angiography (CTA). We guide the diffusion process by conditioning the network on a patient's contrast-enhanced magnetic resonance angiography (CEMRA) to preserve patient-specific anatomy.

Methods: The 2D Denoising Diffusion Probabilistic Model (DDPM) implementation in Project MONAI[1] was originally used to generate synthetic hand X-ray images from noise. In this project, the model architecture was modified to generate synthetic CTA images by adding a second input channel to the model to accept a conditional input, the CEMRA. We used pairs of chest CEMRA and CTA data for n = 53 patients. CEMRA data were used as input data to the AI model and CTA images served as ground truth data for the CEMRA to CTA image translation. All CEMRA and CTA images were first resampled to have a voxel size of 2.5 mm x 2.5 mm x 3 mm using MATLAB. The CTA images were cropped to only include the thoracic aorta region and zero-filled to a matrix size of 100 x 104 x 175. The resampled CEMRA images were registered to corresponding CTA images using the ANTs package in 3D Slicer (the CTA served as the fixed image while the CEMRA was the moving image). We used a combination of 3 registration algorithms (called QuickSyN in 3D Slicer): rigid, then affine, then SyN. Rigid transformation only involves translation and rotation; affine transformation is rigid with the addition of shear and scaling (12 parameters); symmetric normalization (SyN) is affine plus a deformable transformation, which is iteratively optimized based on mutual information between the CTA and CEMRA images. After the registration process, all images were normalized to have an intensity range of [-1,1] to allow the network to better compare CEMRA and CTA values. Additionally, sagittal slices toward the edge (15 on each side of every volume) were discarded as they included mostly blank images (resulting in a total of 70 slices per image). Finally, the 3D images were broken up into 2D sagittal slices with matrix sizes of 104 x 175 to be inputted into the training model. The results of the registration process were visually inspected and rated by 2 researchers to be either sufficient or poor. Registrations with poor performance were repeated until improved results were obtained, poor results were still yielded after 10 repetitions. 13 of 53 CTA/CEMRA pairs failed to yield satisfactory registration results. Overall, we had 40 sets of image pairs * 70 imaging slices/volume. We used 38 patients (2660 slices) for model training and 2 patients (140 slices) for testing. The model was trained for 75 epochs, using a batch size of 8, a timestep T set to 1000, the ADAM optimizer, and a mean square error loss function. To evaluate the performance of our network, we calculate the signal intensity difference in average intensity of a small (7 mm diameter circle) region of interest in the aorta and spine for both the AI-generated and original ground-truth CTA images.

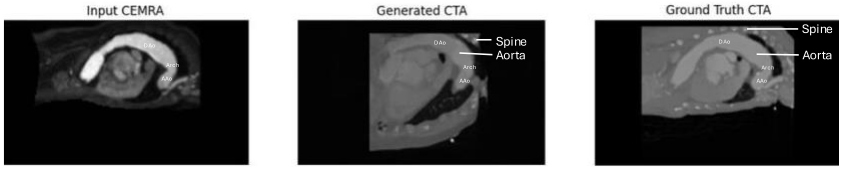

Figure 1. Example inference. The network does not see the ground truth. AAo = Ascending Aorta. DAo = Descending Aorta.

Results: Out of the 140 generated CTA imaging slices for testing (Fig. 1), 27 were noisy and 85 do not contain both the aorta and spine for intensity evaluation. This left 28 images suitable for analysis. As seen in Table 1, the mean intensities of the aorta and spine were similar between the AI-generated and ground truth CTA images, but the intensity variance was higher in the AI-generated images compared to ground truth CTA.

AI Generated CTA mean +- STD intensity			Ground Truth CTA mean +- STD intensity			Paired t-test p-value		
Aorta SI	Spine SI	Aorta - Spine SI	Aorta SI	Spine SI	Aorta - Spine SI	Aorta SI	Spine SI	Aorta - Spine SI
-0.38 +- 0.10	-0.29 +- 0.13	-0.08 +- 0.07	-0.33 +- 0.01	-0.27 +- 0.06	-0.06 +- 0.06	0.02	0.38	0.18

Table 1. Statistics for generated and ground truth CTA intensity mean and standard deviation. SI = signal intensity.

Discussion: Our work shows the potential for implementing deep learning based cross-modality synthesis in chest imaging using a CEMRA to generate a CTA for a patient. A limitation of our work is our small training and testing set. Another limitation is that the paired data from each patient was not aligned fully (different fields of view and time of acquisition) resulting in failed image registration for some patients. In addition, we do not include a quantitative assessment of our registration error. Next steps will include training the model on a larger dataset and implementing further evaluation metrics. If successfully developed, this technology could provide physicians with CTA-equivalent insights without requiring patients to undergo an additional scan if they already have a CEMRA.

References: [1] Pinaya WH, Graham MS, Kerfoot E, Tudosiu PD, Dafflon J, Fernandez V, Sanchez P, Wolleb J, Da Costa PF, Patel A, Chung H. Generative AI for Medical Imaging: extending the MONAI Framework. arXiv preprint arXiv:2307.15208. 2023 Jul 27.

Susceptibility-Enhanced Vascular Imaging at 5T: A Feasible Approach To Decode Cerebral Small Vein Networks And Cerebral microbleeds

Wushi Shao[1,2], Jun Li[2], Fan Liu[1], Yafeng Peng[2], Cinian Lv[3], Yixu Zhao[1], Zuoxiang He[2], Hua Guo[1]

[1]*Center for Biomedical Imaging Research, School of Biomedical Engineering, Tsinghua University, Beijing, China*

[2]*School of Clinical Medicine, Tsinghua University, Beijing, China*

[3]*School of Biomedical Engineering, Tsinghua University, Beijing, China*

Purpose: To investigate the diagnostic potential of 5 Tesla (5T) MRI with high-resolution susceptibility-weighted imaging (SWI) and quantitative susceptibility mapping (QSM) in detecting cerebral microbleeds (CMBs) and small venous structures[1]. By combining SWI and QSM, we seek to enhance the visualization of microvascular abnormalities and enable differentiation between hemorrhagic iron deposition and calcification, thereby complementing conventional MR angiography (MRA) and MR venography (MRV) techniques.

Method: Whole-brain SWI and QSM images were acquired using a 5T MRI system with a multi-echo gradient-echo sequence and a 48-channel head coil. The study included five healthy volunteers and five patients with Parkinson's disease. SWI and QSM images were automatically using the vendor's processing pipeline. The imaging parameters are shown in **Table 1**.

Parameter Type	5T Scan (United Imaging)
	3D multi echo GRE
Repetition Time (TR)	36.1ms
1st Echo Time (TE)	6.6ms
2nd Echo Time (TE)	14.4ms
3rd Echo Time (TE)	22.2ms
Flip Angle	13°
Spatial Resolution	0.51 x 0.51 x 2 mm³
Matrix	432 x 352 x 64(slices)
Field of View (FOV)	220 x 180 x 128 mm³
Readout Bandwidth	350 Hz/pixel
SENSE/Acceleration	2.2
Acquisition Time	8m 6s

Table 1. 5T Imaging Parameters

Results: Three cerebral microbleeds were detected in one patient, as shown in **Fig.1**, one located in the left Corona radiata and the other two in the cerebellum. All three lesions are clearly visible across all imaging modalities: magnitude, SWI_C, miP_C, and QSM. Meanwhile, miP_C provided the most stable observation of lesion size. What's more, QSM revealed that all three lesions had positive susceptibility values, confirming their nature as hemorrhagic deposits. High-resolution SWI allowed clear visualization of small veins, which were otherwise undetectable with conventional MRA/MRV. **Fig.2** showing a healthy volunteer, demonstrating the high-resolution imaging capabilities of 5T SWI for visualizing small venous structures throughout the brain.

Discussion: SWI captures susceptibility changes due to venous deoxygenation and blood product deposition, addressing the limitations of conventional angiographic techniques. The detection of microbleeds as small as 0.98 mm demonstrates the feasibility of high-resolution full-brain imaging with this method. Enhanced venous imaging also supports microvascular pathology studies in conditions like cerebral small vessel disease and Parkinson's disease. However, several limitations must be considered. The sample size in this study was small, including only five healthy volunteers and five patients with Parkinson's disease, which limits the generalizability of the findings. A larger sample size is needed to validate the findings and establish diagnostic thresholds. The lack of statistical analysis is a limitation, and future studies should include statistical methods to assess group differences.

Conclusion: High-resolution 5T SWI with QSM is an effective tool for detecting and characterizing cerebral microbleeds and small venous structures. It improves submillimeter lesion detection and provides diagnostic specificity by quantifying lesion composition, offering potential for advanced cerebrovascular imaging in clinical use.

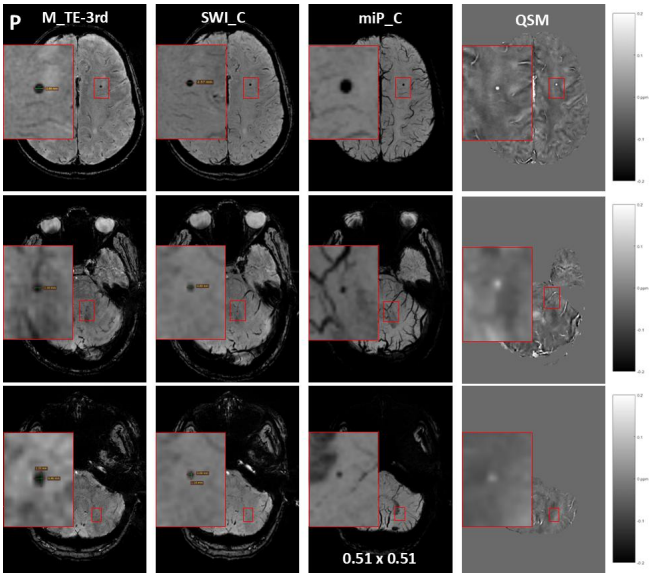

Fig.1 This figure illustrates the detection of three cerebral microbleeds in a Parkinson's disease patient using SWI, miP, and QSM images. The smallest lesion, located in the cerebellum, has a short diameter of 0.98 mm.

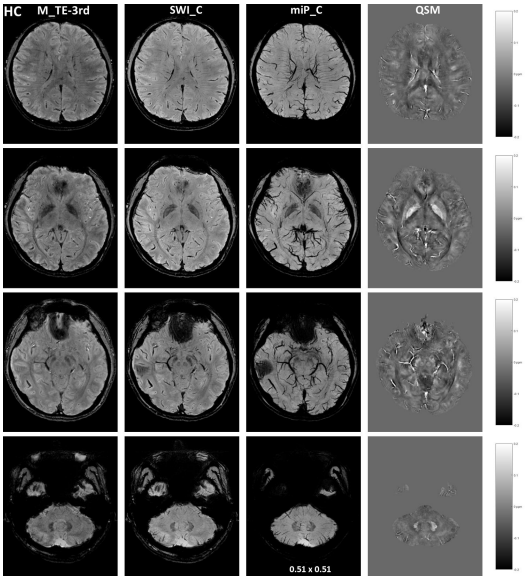

Fig.2 HC = Healthy Control. The image, with a resolution of 0.51 × 0.51 mm², highlights the enhanced contrast of small venous structures.

Reference:

[1] Greenberg S M, et al. The Lancet Neurology, 2009, 8(2): 165-174.

Development of a Clinical Tool for LSA Segmentation: Leveraging 3T Data for 7T LSA Segmentation with nnU-Net and Swin-UNETR

Diantong Xie[1], Haokun Li[1], Yixu Zhao[2], Xue Zhang[3], Yuanbin Zhao[3], BinBin Sui[4] and Huijun Chen[1]

[1]Center for Biomedical Imaging Research, School of Biomedical Engineering, Tsinghua University, Beijing, China; [2]Key Laboratory for Biomechanics and Mechanobiology of Ministry of Education, Beijing Advanced Innovation Center for Biomedical Engineering, School of Biological Science and Medical Engineering, Beihang University, Beijing, China; [3] Department of Radiology, Beijing Tiantan Hospital, Capital Medical University, Beijing, China; [4]Department of Radiology, Beijing Hospital, National Center of Gerontology, Institute of Geriatric Medicine, Chinese Academy of Medical Sciences, Beijing, China.

Purpose: The lenticulostriate artery (LSA) plays a critical role in several neurological conditions, such as stroke, cerebral ischemia, and Alzheimer's disease[1]. However, LSA is not visible in 3T magnetic resonance angiography (MRA) data. While 7T MRA can clearly visualize the LSA[2], it is not easily accessible and hard to segment manually. This study aims to demonstrate that LSA segmentation, trained on 3T data, can successfully segment the LSA in 7T data, thus providing a clinically useful automatic segmentation tool.

Methods: We used the CAS 2023 challenge dataset (https://codalab.lisn.upsaclay.fr/competitions/9804) containing 3T TOF MRA data from 100 patients with symptomatic intracranial artery stenosis, along with corresponding segmentation masks. We employed two deep learning models for training: nnU-Net and Swin-UNETR[3][4]. Data augmentation included spatial cropping, flipping, intensity normalization, and for Swin-UNETR, resampling was performed to a resolution of 0.3mm x 0.3mm x 0.6mm. To assess segmentation accuracy, we used recall as the primary metric. The loss function was Dice Loss and the curve of training process are shown below(**Fig1**). For testing, we used 7T TOF MRA data from two patients at Beijing Tiantan Hospital, with LSA segmentation annotated by a junior radiologist under the supervision of a senior radiologist.

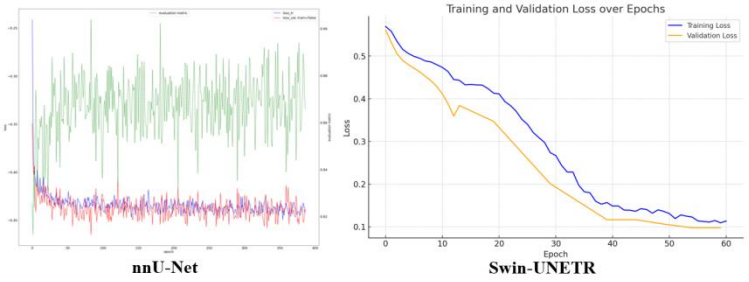

Figure1. The training process of nnU-Net and Swin-UNETR on 3T TOF MRA dataset.

Table1. Recall Values of Two Methods on Two Cases

Methods	Case 1	Case 2	Average
nnU-Net	0.553	0.524	0.539
Swin-UNETR	0.947	0.878	0.912

Results:

The models trained on 3T data demonstrated reasonable segmentation performance on 7T data. Detailed results of recall value are presented in **Table 1** and visual outcomes in **Figure 2** and **Figure 3**. Notably, the Swin-UNETR model outperformed nnU-Net, likely due to its refined resampling strategy during data augmentation.

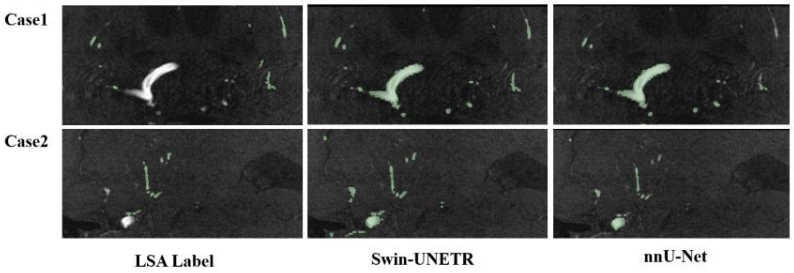

Figure2. Comparison of LSA Labels and Segmentation Results of nnU-Net and Swin-UNETR.
This figure compares the segmentation results of different methods on two cases. The LSA labels are used as the ground truth for evaluation, and the segmentation performance of each method is visually compared to the true labels.

Discussion and conclusions:

The models trained on 3T data demonstrated promising generalization capabilities when applied to 7T test data, although the results are still preliminary due to the limited number of test cases. Swin-UNETR outperformed nnU-Net, likely because of its more advanced resampling strategy in data augmentation. Future work will focus on increasing the test sample size to improve the model's robustness and exploring new network architectures to enhance segmentation results.

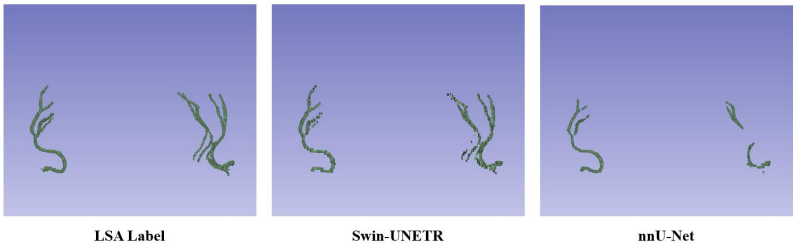

Figure3. 3D Comparison of LSA Labels and Segmentation Results of nnU-Net and Swin-UNETR.
This figure compares the segmentation results of different methods of a same case. We captured the ROI (LSA voxels) of whole brain segmentation results for display.

References:

[1]Zang-Hee Cho et al., Stroke, 2008;[2]Chang-Ki Kang et al., Hypertension, 2009 [3]Ali Hatamizadeh et al., BrainLes, 2021; [4]Fabian Isensee et al., Nat Methods 18, 203–211 (2021)

Automated Cardiovascular MRI Protocoling for Common Cardiac Indications using Natural Language Processing

Melika Shafeghat[1], Blair Tilkens[1], Daniel J Pittman[2], Adrienne Sarah Kline[2],James Carr[1]

[1]Radiology, Feinberg School of Medicine, Northwestern University, IL, USA

[2]Surgery, Cardiac Surgery Division, Feinberg School of Medicine, Northwestern University, IL, USA

Purpose:
Traditionally, radiologists and imaging specialists manually review clinical documentation to determine the most suitable imaging sequence and parameter set, a method that is not only time-consuming but also prone to variability and potential human error.

To harness natural language processing (NLP) for the automated selection of cardiovascular MRI protocols using common clinical indications as input. This system will enhance workflow efficiency and diagnostic accuracy, and reduce inter-observer variability and errors.

Methods:
Utilizing NLP techniques, including named entity recognition, part-of-speech tagging, and syntactic parsing, the system extracts from clinical notes a patient's history, symptoms, and suspected pathologies. System performance and accuracy of clinical entity extraction are evaluated using precision, recall, and F1-score. A decision-support algorithm maps data to a curated database of MRI protocols, flexibly accommodating diverse documentation styles and multiple protocol selections.

Results:
Initial findings indicate that key clinical indicators are identified with high accuracy, showing a 30% reduction in protocol selection time compared to conventional manual methods.

Discussion:
MRI is essential for modern diagnostics, but selecting the appropriate protocol remains a complex, expert-driven task (1). Automating the extraction of critical clinical information standardizes protocol selection, leading to improved patient care and optimized radiological resource utilization. In the future, we plan to deploy our algorithm for use in other cardiac imaging modalities including CT.

References:

1. Kalra A, Chakraborty A, Fine B, Reicher J. Machine Learning for Automation of Radiology Protocols for Quality and Efficiency Improvement. J Am Coll Radiol. 2020;17(9):1149-58.

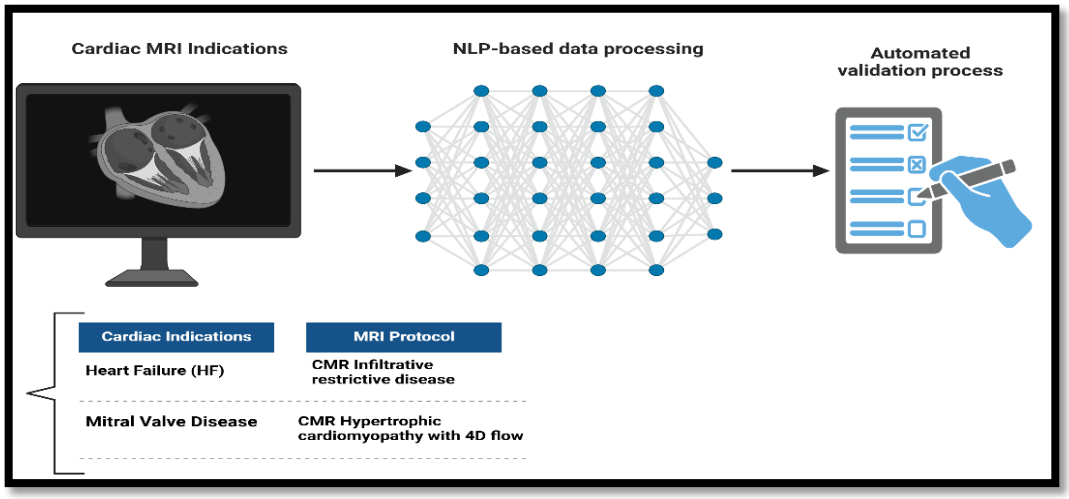

Intravoxel incoherent motion and diffusion kurtosis imaging can be used to assess the differentiation degree of non-small cell lung cancer

Mingyu Tan [1], Peijun Wang[1]

[1] Department of Medical Imaging, Tongji Hospital, School of Medicine, Tongji University, Shanghai, China

Purpose

This study aims to investigate the potential of intravoxel incoherent motion (IVIM) and diffusion kurtosis imaging (DKI) as non-invasive biomarkers for evaluating tumor differentiation degree in non-small cell lung cancer (NSCLC), given their unique capabilities in characterizing water diffusion heterogeneity and tissue microstructural complexity

Methods

Forty-one consecutive patients with NSCLC were enrolled in this study. MRI was performed within 1 week after finding lung lesions on CT. All Protocols were performed on a 3T MR scanner (GE Premier, GE Healthcare, Milwaukee, Wisconsin, USA). The lung images obtained included coronal T2WI, axial IVIM (repetition time/echo time, 7500/63ms; slice thickness, 4.0mm; interslice gap, 1mm; field of view, 512 ×512mm; and matrix, 256×256) and axial DKI (repetition time/echo time, 7200/70.8ms; slice thickness, 4.0mm; interslice gap, 1mm; field of view, 512 ×512mm; and matrix, 256×256). IVIM in three orthogonal directions was measured by using b values of 0, 20, 60, 100, 150, 200, 400, 600, 800, and 1000s/mm^2. DKI in three orthogonal directions was measured by using b values of 0, 1000, and 2000s/mm^2. Two radiologists independently analyzed the IVIM and DKI parameters for each lesion using post-processing software. The intraclass correlation coefficient (ICC) was generated to assess interobserver agreement. The parameters were compared between the poorly differentiated group and the moderately and highly differentiated group. Receiver operating characteristic analysis was performed to evaluate the diagnostic efficacy.

Results

Intraobserver agreement was from good to excellent. Excellent interobserver agreement between the two observers was obtained for D, Dapp, Kapp and f with ICC of 0.931, 0.878, 0.840, and 0812 respectively. Good interobserver agreement was obtained for D* with ICC of 0.712. There were statistically significant differences in D and Dapp values between the poorly differentiated group and the moderately and highly differentiated group (p < 0.05), but D*, f, and Kapp showed no statistically significant differences between the two groups . ROC curve analysis showed that the D value had the highest area under the curve (AUC = 0.773), followed by Dapp (AUC = 0.745)(Fig.1 and Table 1). Nevertheless, the difference in diagnostic efficacy among the two parameters was not statistically significant (p > 0.05).

Discussion and Conclusion:

In this study, we found that ADC and D values of moderately and highly differentiated group were significantly higher than those of poorly differentiated group, Theoretically, as the differentiation degree of NSCLC decreases, the tissue atypia and the degree of malignancy increases, the proliferation of tumor cells will become more vigorous, leading to increased cell density and reduced extracellular space[7]. In this study, the perfusion-related parameters D* and f were not significantly different between the poorly differentiated group and the moderately and highly differentiated group. The reason may be that the repeatability of D* and f values in pulmonary diffusion imaging is poor and has great variability, which is affected by the shape, size and location of the lesion[8]. In this study, the ICC of D* was lower than other parameters. This study demonstrated that the diffusion parameter (D and Dapp) derived from IVIM and DKI could be used to noninvasively identify the differentiation degree of NSCLC.

Table1: Comparison of IVIM and DKI Parameters in NSCLC with Different Differentiation Grades

Parametes	Poorly differentiated group (n=24)	Moderately and highly differentiated group (n=17)	*p*
D(x10^{-3}mm^2/s)	0.88 ± 0.23	1.14 ± 0.29	0.003
D*(x10^{-3}mm^2/s)	20.34 ± 12.72	18.65 ± 7.41	0.626
f(%)	29.77 ± 15.45	29.96 ± 15.84	0.968
Kapp	0.78 ± 0.20	0.71 ± 0.17	0.190
Dapp(x10^{-3}mm^2/s)	1.29 ± 0.34	1.64 ± 0.43	0.006

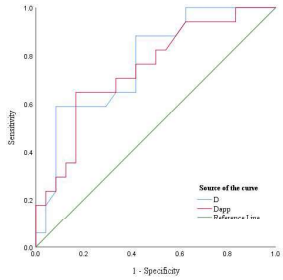

Fig.1. The ROC analysis compares the diagnostic performance of diffusion parameters D and Dapp .